ZZ Production in Proton-Proton Collisions at $\sqrt{s} = 13\,\text{TeV}$ in Four-Lepton Events Using the CMS Detector at the LHC

by

Nathaniel Woods

A dissertation submitted in partial fulfillment of

the requirements for the degree of

Doctor of Philosophy

(Physics)

at the

University of Wisconsin – Madison

2017

Defended on 25 October 2017

Dissertation approved by the following members of the Final Oral Committee:

Wesley Smith · Bjorn Wiik Professor of Physics

Sridhara Dasu · Professor of Physics

Matthew Herndon · Professor of Physics

Lisa Everett · Professor of Physics

Pupa Gilbert · Professor of Physics

Abstract

Several studies of four-lepton production in proton-proton collisions are presented. The dataset used corresponds to an integrated luminosity $35.9\,\text{fb}^{-1}$ at a center-of-mass energy of 13 TeV, collected by the CMS detector at the LHC. All reported measurements use the $2\ell 2\ell'$ final states, where $\ell, \ell' =$ e or μ. The total ZZ cross section for all events with two Z bosons in the mass range 60–120 GeV is measured and found to be $\sigma(\text{pp} \to \text{ZZ}) = 17.2 \pm 0.5\,(\text{stat}) \pm 0.7\,(\text{syst}) \pm 0.4\,(\text{theo}) \pm 0.4\,(\text{lumi})$ pb. The Z branching fraction to four leptons is found to be $\mathcal{B}\,(\text{Z} \to 4\ell) = 4.8 \pm 0.2\,(\text{stat}) \pm 0.2\,(\text{syst}) \pm 0.1\,(\text{theo}) \pm 0.1\,(\text{lumi}) \times 10^{-6}$ for events with $80 < m_{4\ell} < 100$ GeV and $m_{\ell\ell} > 4$ GeV for all opposite-sign, same-flavor lepton pairs. Differential cross sections are measured as functions of a number of kinematic and jet-related observables. All these results agree with standard model predictions. A search for fully electroweak ZZ + 2jets production is performed, and an excess consistent with standard model vector boson scattering is found at the 2.7σ level. Searches for anomalous triple and quartic gauge couplings are performed, and the four-lepton invariant mass distributions are used to set the most stringent limits to date on a number of parameters affecting neutral gauge boson interactions.

Acknowledgements

They say it takes a village to raise a child, and a grad student is just a toddler whose grape juice has fermented, so I have many people to thank. I am indebted to too many advisors, colleagues, friends, and family members to name them all here, so I will highlight just a few for particular appreciation; the many omissions are solely for the purpose of keeping this document under 200 pages.

I must first thank the members of the Wisconsin CMS group, who have, understandably, played a central role in my life over the past five and a half years. The professors, Wesley Smith, Sridhara Dasu, and Matt Herndon, are great physicists and master tacticians, and their clear-eyed advice has been extremely valuable throughout my time here. Sascha Savin has been a great guide in the day-to-day business of being a physicist, and he has taught me an enormous amount about physics, data analysis, work habits, intracollaboration politics, and just about everything else. The postdocs, Evan Friis, Maria Cepeda, Senka Duric, Isobel Ojalvo, Bhawna Gomber, and Cécile Caillol, are uniformly brilliant and endlessly helpful. Everything would grind to a halt and nothing would ever get done if not for Dan Bradley, Ajit Mohapatra, Carl Vuosalo, and the rest of the computing team, to whom I should also apologize for all the times I completely broke everything. Pam Klabbers and Aleš Svetek are founts of knowledge about the CMS trigger, and are fully responsible for any competence I appeared to display while on shift. I would never have accomplished anything without the other UW CMS grad students. Tom Perry, Aaron Levine, Laura Dodd, Devin Taylor, Tyler Ruggles, Nick Smith, Kenneth Long, James Buchanan, and Usama Hussain, and others with whom I overlapped more briefly, have been great friends and comrades-in-arms. The intelligence, collective knowledge, and snark on continuous display in the group chat and in our office chats were invaluable to both

my work and my mental health.

Ivan Furic and Darin Acosta helped me get my foot in the door during my REU at the University of Florida and taught me a lot when I had essentially no knowledge base to work from.

The friends I made in Madison and Geneva are far too numerous to mention individually, but they are wonderful people and I'm lucky to have them in my life. A special shoutout goes to my flatmates, Laser Kaplan, Svet Hristozkov, Heather Russell, and Tessa Carver, for not just putting up with my idiosyncrasies but actively making home a place I wanted to go.

I never would have gone anywhere in life without my smart, funny, supportive family: my parents Anne and David, my siblings Julia and Peter, a small army of extended family, and a clowder of cats led by The Boss, Gadget. I could not ask for a stronger foundation on which to build my future.

Contents

List of Figures

List of Tables

Chapter 1

The Standard Model

The mission of fundamental particle physics is an audacious one. An exercise in reductionism taken to its logical extreme, the goal of the field is to find the minimal set of mathematical precepts that underlie all interactions of matter and energy and from which everything else in the universe is, in principle, an emergent property. Despite the loftiness of its goals, the program has been extraordinarily successful, yielding the standard model (SM), a remarkable theory which is elegant in its mathematical formulation yet expansive and powerful in its predictions, most of which have been verified in exquisite detail. Calculations done in the framework of the SM have matched data within the precision of essentially every experiment over roughly four decades, making it arguably the best-confirmed theory in the history of science. It is generally believed to be self-consistent; future advances will likely add to it, explain its free parameters, or find some deeper underlying structure, not contradict it.

And yet work remains. There are a few known phenomena that the SM does not cover, and some of its features seem for now to be surprising coincidences (see Section 1.5). One area of particular interest is the physics of the electroweak interaction, which was the last piece to fall into place. Its final major component, the existence of

the Higgs boson, was definitively confirmed only as recently as 2012 and some details remain hazy or unverified, from an experimental perspective.

Chapter 1 gives an overview of the SM with a focus on its electroweak sector, and describes some of the shortcomings that motivate continued searches for new physics even now that it is complete. Chapter 1 also describes diboson and multi-boson processes, interactions involving multiple instances of the particles underlying electroweak physics, which are valuable tools for understanding how the bosons interact with each other. This thesis presents several studies of the ZZ diboson process, intended to illuminate the behavior of the neutral part of electroweak interactions. In particular, the focus of this work is the case in which two Z bosons each decay to a pair of charged leptons. Such events are rare but experimentally appealing. Two of the three charged leptons, electrons (e) and muons (μ) can be reconstructed with high precision, and few physics processes aside from ZZ result in four-lepton final states, so they provide an unmistakable experimental signature that can be easily identified over small backgrounds. Details of ZZ physics are described in Chapter 2, along with a review of previous literature.

High-energy particle collisions in a laboratory provide a way to investigate ZZ production and other fundamental interactions in a controlled setting. CERN's Large Hadron Collider (LHC), a proton-proton collider in tunnels running beneath the Swiss-French border near Geneva, provides collisions at record-breaking energies and rates, which are used by the Compact Muon Solenoid (CMS) detector to study diboson processes in unprecedented detail. These apparatus are described in Chapter 3. Accurate simulations of physics and particles' interactions with the detector are vital to obtaining valid results; this process is described in Chapter 4. Chapter 5 describes how physics objects are built from the detector signals, and how those appropriate for analysis are selected. The strategy for performing the ZZ measurements presented

in this thesis is given in Chapter 6. New studies of four-lepton events in a sample of proton-proton collisions are presented in Chapter 7.

1.1 Introduction

The standard model is a set of related theories that together describe matter and its interactions at a fundamental level. The following sections give a general overview of the SM and related topics that serve as background material for the four-lepton processes described in more detail in subsequent chapters. This includes discussions of the particle content of the SM and the gauge structure that leads to particle interactions, the spontaneous symmetry breaking mechanism that leads to the specific structure of the electroweak sector of the SM, diboson processes, and the SM's limitations and how they might be addressed. Some details are also given about the proton-proton collisions used to probe particle interactions at high energies. More complete information may be found in a number of texts, including Refs. [1–5]. Everything that follows uses units such that $c = \hbar = 1$, where c is the speed of light and $\hbar$ is the reduced Planck's constant $\hbar = h/2\pi$.

1.2 Matter and Forces

In the SM, matter is made of fermions (particles with half-integer spin; all SM fundamental fermions have spin $\frac{1}{2}$) which interact by exchanging gauge bosons (integer spin; spin 1 for the SM force carriers). Table 1.1 lists the fundamental particles and some of their properties. With the exception of the neutral bosons, all particles have a corresponding antiparticle which is the same except that all its quantum numbers have opposite sign. The fermions come in two categories, leptons and quarks. All

the quarks and half the lepton types carry electric charge and are therefore subject to interactions through the electromagnetic force, described by quantum electrodynamics (QED) [2]. In a QED interaction, two charged particles exchange a photon, which carries the momentum transferred from one to the other. The photon is a spin-1 gauge boson that is massless and electrically neutral itself, explaining why electromagnetic forces are long-range.

There are six types of quarks which fall into three "generations:" up and down (u and d, first generation); charm and strange (c and s, second generation); and top and bottom (t and b, third generation)[1]. Quark masses increase with each successive generation. Up-type quarks (u, c, t) have electric charge $+2/3$ (in units of the positron charge e) while down-type quarks have $-1/3$. Quarks are the building blocks of hadrons, including $\mathrm{q\bar{q}'}$ bound states called mesons and $\mathrm{qq'q''/\bar{q}\bar{q}'\bar{q}''}$ bound states called baryons, of which protons (uud) and neutrons (udd) are the most familiar. Top quarks are too heavy to form bound states; the toponium ($\mathrm{t\bar{t}}$ meson) weak decay width is larger than the spacing between its energy levels and its mean lifetime is an order of magnitude shorter than its orbital period so no resonance may form [5]. Hadrons are bound by the strong nuclear force, described by the theory of quantum chromodynamics (QCD).

The mediator for the strong force is the gluon, which like the photon is a massless spin-1 gauge boson. The analog of electric charge is "color", a notion originally introduced [6] as an ad hoc explanation of how identical quarks could exist in the symmetric bound state of a hadron despite the Fermi exclusion principle and later found to be the charge underlying the strong force [1, 7]. Unlike electric charge, there are three types of color charge, typically called red, green, and blue, though these names are arbitrary[2]. The analogy with visible color comes primarily from

[1] Top and bottom quarks are sometimes called truth and beauty.

[2] Antiquarks carry negative color charges, typically called antired, antigreen and antiblue.

Table 1.1: The particles of the standard model, and some of their properties. All fermions have a corresponding antiparticle with opposite sign for all quantum numbers. Quarks and leptons are grouped by generation. Note that the listed T^3 (the measured component of the weak isospin, described below) applies only to left-handed fermions; right-handed fermions have $T^3 = 0$ and do not couple to the $W^{\pm}$ (right-handed neutrinos, if they exist, do not couple to the Z either).

Particle	Mass (GeV)	Charge (e)	T^3	Gauge couplings
Scalar boson (spin 0)				
H	125	0		$W^{\pm}$, Z
Fermion (spin 1/2)				
u	0.023	+2/3	+1/2	g, γ, Z, $W^{\pm}$
d	0.048	−1/3	−1/2	g, γ, Z, $W^{\pm}$
e	5.11×10^{-4}	−1	+1/2	γ, Z, $W^{\pm}$
ν_e	$< 2.2 \times 10^{-9}$	0	−1/2	Z, $W^{\pm}$
c	1.28	+2/3	+1/2	g, γ, Z, $W^{\pm}$
s	0.95	−1/3	−1/2	g, γ, Z, $W^{\pm}$
μ	0.105	−1	+1/2	γ, Z, $W^{\pm}$
ν_μ	$< 1.7 \times 10^{-4}$	0	−1/2	Z, $W^{\pm}$
t	172	+2/3	+1/2	g, γ, Z, $W^{\pm}$
b	4.2	−1/3	−1/2	g, γ, Z, $W^{\pm}$
τ	1.77	−1	+1/2	γ, Z, $W^{\pm}$
ν_τ	< 0.018	0	−1/2	Z, $W^{\pm}$
Vector boson (spin 1)				
g	0	0	0	g
γ	0	0	0	$W^{\pm}$
Z	91.2	0	0	$W^{\pm}$
$W^{\pm}$	80.4	± 1	± 1	γ, Z, $W^{\pm}$

the heuristic that natural states must be "colorless," i.e. a hadron may have equal parts color and corresponding anticolor as in a meson, but it may also be "white," containing red, blue, and green in equal measures as in a baryon. This implies that a color charged object cannot exist on its own, a property known as confinement.

Confinement arises from the structure of QCD interactions and gluons themselves. Among fermions, only quarks interact through the strong force, but gluons also carry color charge and interact with each other. Because gluons self-interact, have no distinct antiparticle, and are massless, they can split and radiate infinitely. The resulting soft gluon interactions around quarks lead to an anti-screening effect that causes the strength of the strong force to change as a function of the distance between interacting quarks, with close quarks interacting less strongly as far as a single gluon exchange is concerned. As quark separation gets larger, the potential energy of strong interactions rises rapidly, until it is energetically favorable for the gluon connecting them to split into a $q\bar{q}$ pair that screens them and effectively breaks off the interaction. A single colored particle will thus cause more colored particles to be produced from vacuum until only colorless bound states remain, enforcing confinement. This process is known as hadronization, and causes single quarks or gluons leaving a hard scattering interaction to produce "jets" of many hadrons, each carrying a fraction of the original parton momentum, that enter the detector in a conical shower. This is why a free quark has never been observed, and is not expected to be found, and why the strong interaction is short-range even though gluons are massless. It is also why, for example, $qq\bar{q}$ bound states are not seen in nature. Conversely, close-range QCD is relatively feeble, leading to "asymptotic freedom," the property of partons within hadrons that they may be considered independent in high-energy collisions, because their interactions are weak enough that bound state effects may be neglected (see Section 1.6).

Leptons may be electrically charged or neutral, and come in three generations, each containing one lepton of each type, a charged lepton and a corresponding neutrino. In order of charged lepton mass, the generations are the electron and its neutrino (e and ν_{e}), muon and its neutrino (μ and ν_{μ}), and tau and its neutrino (τ and ν_{τ}). Taus decay quickly, with a mean lifetime of $2.9 \times 10^{-13}\,\mathrm{s}$ in their rest frame; muons also decay, but their lifetime ($2.2\,\mu\mathrm{s}$) is long compared to other time scales involved in particle collider experiments, so they are considered stable particles for the purposes of this work. Neutrinos are known to have mass [8–10], and the masses are known to be small but they have not been measured. All leptons and quarks interact via the weak nuclear force, which is best known for causing the nuclear beta decay reaction $\mathrm{n} \to \mathrm{p} + \mathrm{e}^{-} + \bar{\nu_{\mathrm{e}}}$. Neutrinos are notable for coupling to the rest of the SM only through weak interactions, making them difficult to detect in practice. Detectors at particle colliders make no attempt to detect neutrinos, and their presence is inferred only through the apparent momentum imbalance resulting from the fact that they are not detected.

The weak force operates through two mechanisms, charged-current and neutral-current interactions. Neutral-current interactions proceed through exchange of a Z boson, an electrically neutral spin-1 mediator, and are analogous to electromagnetic interactions except for two important differences. Unlike the γ, the Z has mass—in fact, one of the largest known masses at 91 GeV [11]—giving it longitudinal polarization modes [2] and limiting the range of the force because it decays with a halflife on the order of $10^{-25}\,\mathrm{s}$ [11]. Also unlike QED, weak interactions do not respect parity (P) symmetry. The Z boson couples more strongly to left-handed fermions (those with helicity opposite their direction of motion) and right-handed antifermions than to their opposite-spin counterparts. The degree of asymmetry varies by fermion type; notably, the Z does not couple at all to right-handed neutrinos. Neutral-current inter-

actions are still symmetric under combined charge conjugation (C) and parity (CP) transformations, because processes that are odd under P are also odd under C.

Charged-current interactions proceed through exchange of an electrically charged boson, the $W^{\pm}$, which has a mass around 80 GeV [11]. Leptons couple to W^- bosons in $\ell^-, \bar{\nu}_\ell$ pairs (W^+ bosons likewise with their antiparticles), causing μ and τ decays. Lepton flavor is conserved in the sense that charged leptons couple to the W only in conjunction with the (anti-)neutrino from the same generation, so the total lepton number $N_\ell = n_{\ell^-} - n_{\ell^+} + n_{\nu_\ell} - n_{\bar{\nu}_\ell}$, where n_{X} is the number of X particles in existence, is conserved separately for $\ell \in (\mathrm{e}, \mu, \tau)$. Flavor conservation does not hold for quarks undergoing charged weak interactions. An up-type quark always couples to the W in conjunction with a down-type quark, as it must to obey conservation of electric and color charge. The pairings are in general described by a unitary 3×3 matrix known as the Cabibbo–Kobayashi–Maskawa (CKM) matrix which defines the inter-generational mixing [12, 13]. Flavor-changing currents allow heavy quarks to decay to lighter ones, and are thus responsible for the decay of hadrons that do not contain the $\mathrm{q\bar{q}}$ pair necessary for strong or electromagnetic decays.

Charged-current interactions also do not respect parity symmetry, and in fact are maximally parity violating: the W couples only to left-handed fermions and right-handed antifermions. Because neutrinos interact only through the weak force[3], and the Z also couples only to left-handed neutrinos, it is not clear that right-handed neutrinos even exist. If they do, they have no way to interact with other matter and they are not part of the SM. Unlike neutral-current interactions, charged-current interactions violate CP symmetry at a small but measurable rate. CP violation was first observed in neutral kaon mixing before the theory of the weak force was fully worked out [14]. After flavor-changing charged currents were formalized it was

[3]Aside from gravity, presumably, but this interaction is not experimentally accessible and is not covered by the standard model.

realized that CP violation could arise from a complex phase in the CKM matrix, which arises in models with at least three generations of quarks[4] [13]. CP violation was subsequently confirmed by observation in a number of meson decays [15–20].

The quantum number analogous to electric charge and color charge for the weak interaction is the three-component weak isospin T^i, which is typically defined such that the measured component is T^3. Left-handed fermions have $|T| = \frac{1}{2}$, the $\mathrm{W}^{\pm}$ has $|T| = \pm 1$, and all other particles have $|T| = 0$. Weak isospin is conserved in all electromagnetic, strong, and fermion-fermion weak interactions, but is not conserved in general because the Higgs boson (see below) carries weak isospin. Electric charge is always conserved, and is related to the measured component of the weak isospin by the weak hypercharge Y, which is

$$Y = 2\left(Q - T^3\right), \tag{1.1}$$

where Q is the electric charge. This connection between the electromagnetic and weak forces, and the parallels between the weak neutral-current interaction and QED, are not coincidental. In fact, in the SM, they are unified into a single *electroweak* force. The differences we observe between electromagnetic and weak interactions, including the masses of the weak gauge bosons, arise from the mechanism of electroweak symmetry breaking, which defines much of the structure of the SM and is described in more detail in the next section.

[4] At the time, only the first two generations were known, so the observed CP asymmetry was taken as an early indication of the existence of top and bottom quarks.

1.3 Electroweak Unification and Symmetry Breaking, and the Higgs Boson

The structures of the fundamental forces arise from symmetries in the underlying fields, specifically gauge invariance of the relevant terms in the SM Lagrangian. Much of the phenomenology of QCD, for example, arises from the $SU(3)$ symmetry of invariance under local color phase transformations, and the fact that the symmetry is non-Abelian (i.e. the transformation operators do not commute). Charges are the generators of the relevant symmetry group, the conserved currents of Noether's first theorem [21]. A full treatment of the SM's symmetry group structure and its connections to the theory's phenomenology is given in a number of books, including Refs. [2, 4, 5, 22]. The relevant point here is that the weak force arises from an $SU(2)$ symmetry generated by the weak isospin T, and the electromagnetic force from a $U(1)$ symmetry generated by the electric charge Q, so a unified electroweak force should obey an $SU(2)_L \times U(1)$ symmetry, where the L indicates that only left-handed fermions transform nontrivially under the $SU(2)$ symmetry. The resulting unified electroweak theory is known as the Glashow–Weinberg–Salam (GWS) model [23–25].

An unbroken $SU(2)_L \times U(1)$ symmetry implies four massless vector gauge fields: a triplet $W_\mu^i (i \in 1, 2, 3)$ which couple to fields with weak isospin (but only for left-handed particles), and a singlet B_μ which couples to weak hypercharge currents. This looks like the weak and electromagnetic forces discussed above, except that the weak gauge fields are massless and all three weak bosons are maximally P-violating. The gauge bosons can be given mass if the underlying symmetry is somehow broken in the theory's vacuum state. Symmetry breaking occurs via the Higgs mechanism[5] [26–28],

[5]The Higgs mechanism is also called the Englert–Brout–Higgs–Guralnik–Hagen–Kibble mechanism to acknowledge more of the theorists who developed it, with Anderson and 't Hooft sometimes included as well.

which introduces an isospin doublet of complex scalar fields

$$\phi = \begin{pmatrix} \phi^+ \\ \phi^0 \end{pmatrix}, \tag{1.2}$$

with a Lagrangian of the form

$$\mathcal{L}_H = (D_\mu \phi)^\dagger (D^\mu \phi) + \mu^2 \phi^\dagger \phi - \lambda^2 \left(\phi^\dagger \phi\right)^2 \tag{1.3}$$

where μ and λ are nonzero real numbers, D_μ is the covariant derivative invariant under $SU(2)_L \times U(1)_Y$,

$$D_\mu = \partial_\mu + igT_i W_\mu^i + i\frac{g'Y}{2} B_\mu, \tag{1.4}$$

and g and g' are the W_μ^i and B_μ coupling strengths. Because the potential in Eq. (1.3) is not minimized at 0, for small excitations around the vacuum expectation value (VEV) $v = \frac{\mu}{2\lambda} = 246\,\text{GeV}$, in appropriately chosen coordinates, the doublet of complex scalar fields is reduced to

$$\phi = \frac{1}{\sqrt{2}} \begin{pmatrix} 0 \\ v + h(x) \end{pmatrix}. \tag{1.5}$$

Substituting Eq. (1.5) into Eq. (1.3) introduces mixing terms between the W_μ^i, B_μ, and h fields The new Lagrangian has mass eigenstates

$$\begin{aligned} W_\mu^\pm &= \frac{1}{\sqrt{2}} \left(W_\mu^1 \mp W_\mu^2\right) \\ Z_\mu &= \frac{gW_\mu^3 - g'B_\mu}{\sqrt{g^2 + g'^2}} = W_\mu^3 \cos\theta_W - B_\mu \sin\theta_W \\ A_\mu &= \frac{g'W_\mu^3 + gB_\mu}{\sqrt{g^2 + g'^2}} = W_\mu^3 \cos\theta_W + B_\mu \sin\theta_W \end{aligned} \tag{1.6}$$

where θ_W is the Weinberg electroweak mixing angle

$$\tan\theta_W = \frac{g'}{g}. \tag{1.7}$$

The newly defined fields are the gauge fields for the weak and electromagnetic forces, and in this basis, the Lagrangian has terms

$$\mathcal{L}_{m_{\mathrm{V}}} = -\frac{v^2 g^2}{4} W_\mu^+ W^{-\mu} - \frac{v^2(g^2+g'^2)}{8} Z_\mu Z^\mu, \tag{1.8}$$

which imply boson masses

$$\begin{aligned} m_{\mathrm{W}} &= \frac{1}{2} v g \\ m_{\mathrm{Z}} &= \frac{1}{2} v \sqrt{g^2+g'^2} \\ m_A = \ & m_\gamma = 0, \end{aligned} \tag{1.9}$$

and

$$\cos\theta_W = \frac{m_{\mathrm{W}}}{m_{\mathrm{Z}}}. \tag{1.10}$$

The original Higgs doublet in Eq. (1.2) had four degrees of freedom (two complex scalars), of which only one remains in the final Higgs field $H = h - v$, which is now a physical field with a corresponding massive scalar boson. The other three became the longitudinal polarization modes of the vector bosons.

Electroweak symmetry breaking thus explains the observed structure of the electromagnetic and weak forces. Three bosons become massive, while one stays massless. Because the photon is massless, the theory retains the $U(1)_{EM}$ gauge symmetry observed in electromagnetic interactions and electric charge is conserved, while the $SU(2)$ symmetry is broken and its generator T^i is not. The $\mathrm{W}^\pm$ bosons still couple only to left-handed fermions, while the Z couples right- and left-handed fermions but not equally. The nonzero VEV even gives a convenient mechanism for generation of fermion masses in Yukawa couplings with Lagrangian terms of the form

$$\mathcal{L}_{m_{\mathrm{f}}} = \sqrt{2}\frac{m_{\mathrm{f}}}{v}\left(\bar{\mathrm{f}}_L \mathrm{f}_R + \bar{\mathrm{f}}_R \mathrm{f}_L\right). \tag{1.11}$$

It also controls off-diagonal terms in the Lagrangian that cause interactions between the electroweak bosons, the primary focus of this research.

1.4 Diboson and Multiboson Physics

In addition to the previously discussed boson mass terms introduced into the SM Lagrangian by electroweak symmetry breaking, boson interaction terms appear for trilinear gauge boson couplings

$$\begin{aligned}\mathcal{L}_{WWV} = &- ig\left[\left(W^{+}_{\mu\nu}W^{-\mu} - W^{+\mu}W_{\mu\nu}\right)\left(A^{\nu}\sin\theta_W - Z^{\nu}\cos\theta_W\right)\right. \\ &\left. + W^{-}_{\nu}W^{+}_{\mu}\left(A^{\mu\nu}\sin\theta_W - Z^{\mu\nu}\cos\theta_W\right)\right],\end{aligned} \tag{1.12}$$

which results in the vertices shown in fig 1.1; quartic gauge couplings

$$\begin{aligned}\mathcal{L}_{WWVV} = &- \frac{g^2}{4}\left\{\left[2W^{+}_{\mu}W^{-\mu} + \left(A_\mu\sin\theta_W - Z_\mu\cos\theta_W\right)^2\right]^2\right. \\ &- \left[W^{+}_{\mu}W^{-}_{\nu} + W^{+}_{\nu}W^{-}_{\mu}\right. \\ &\left.\left. + \left(A_\mu\sin\theta_W - Z_\mu\cos\theta_W\right)\left(A_\nu\sin\theta_W - Z_\nu\cos\theta_W\right)\right]^2\right\},\end{aligned} \tag{1.13}$$

(Fig. 1.2); Higgs couplings to the massive vector bosons

$$\mathcal{L}_{HV} = \left(gm_{\mathrm{W}}H + \frac{g^2}{4}H^2\right)\left(W^{+}_{\mu}W^{-\mu} + \frac{Z_\mu Z^\mu}{2\cos^2\theta_W}\right), \tag{1.14}$$

(Fig. 1.3); and Higgs self-interactions

$$\mathcal{L}_{HH} = -\frac{gm^2_{\mathrm{H}}}{4m_{\mathrm{W}}}H^3 - \frac{g^2m^2_{\mathrm{H}}}{32m^2_{\mathrm{W}}}H^4, \tag{1.15}$$

(Fig. 1.4).

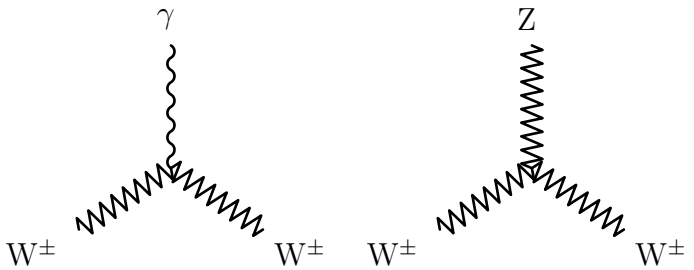

Figure 1.1: Vertex for the trilinear gauge boson couplings allowed at tree level in the SM.

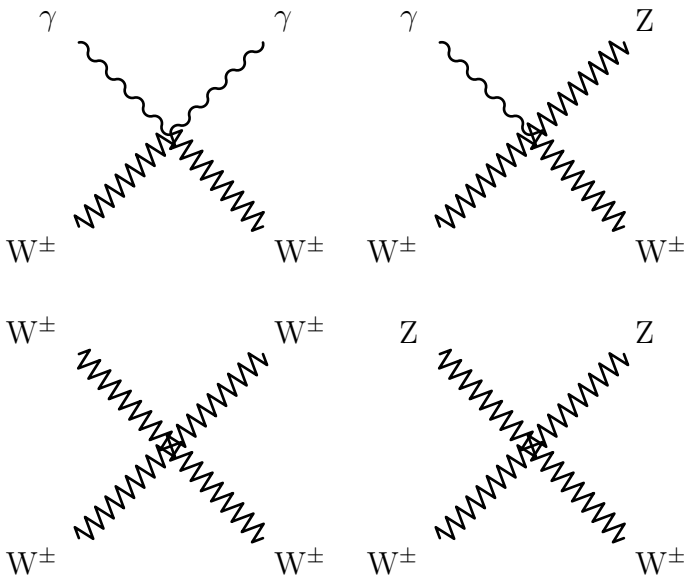

Figure 1.2: Vertices for the quartic gauge boson couplings allowed at tree level in the SM.

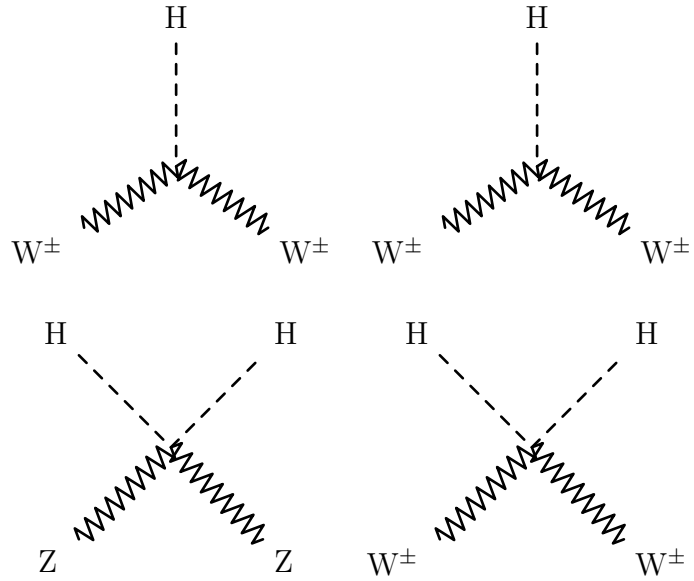

Figure 1.3: Vertices for Higgs boson couplings to gauge bosons allowed at tree level in the SM.

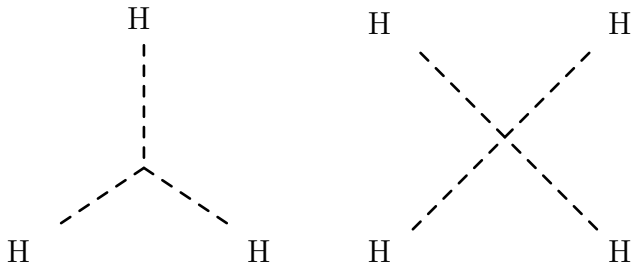

Figure 1.4: Higgs boson trilinear and quartic self-coupling vertices.

The structure of the interactions shown in Figs. 1.1–1.4 depends on the details of the GWS model and spontaneous symmetry breaking, making multiboson interactions excellent probes of the SM electroweak and Higgs sectors. One can confirm the basic validity of the Higgs mechanism by observation of a Higgs boson, and its interactions with the massive gauge bosons can be probed in decays to ZZ^* and $W^{\pm}W^{\mp *}$, which were in fact used in its discovery (see Section 2.2.2.1). The SM makes a number of other testable predictions about the behavior of the electroweak bosons, the most easily testable of which are the multiboson production cross sections, i.e. the rates at which particle collisions result in final states with two or more electroweak gauge bosons. The tree-level diagrams for general diboson production in fermion-antifermion collisions ($f\bar{f} \rightarrow VV$) are shown in Fig. 1.5. The cross section for such a process will be strongly dependent on the gauge bosons' couplings to fermions, in the first diagram in Fig. 1.5, and their couplings to other gauge bosons in the second diagram (which does not contribute at all for neutral gauge bosons in the SM). Diboson production in gg collisions does not occur at tree level but may proceed through a quark loop as in the so-called box diagram of Fig. 1.6.

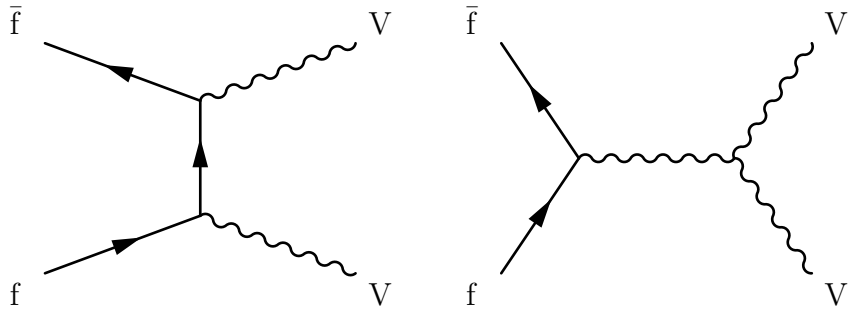

Figure 1.5: Tree-level Feynman diagrams for diboson production in fermion-anti-fermion collisions. The second diagram does not contribute for neutral gauge bosons in the SM.

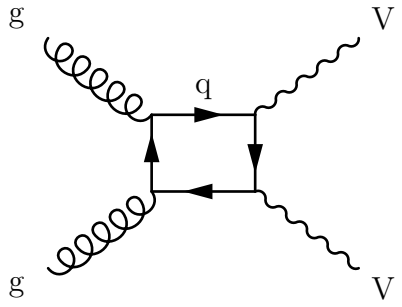

Figure 1.6: Leading order "box" diagram for diboson production through a quark loop in a gluon-gluon fusion event.

1.4.1 Vector Boson Scattering

Quasielastic vector boson scattering (VBS) interactions (VV $\rightarrow$ VV) are sensitive to a number of features of the SM electroweak sector. If only the vector bosons are considered, the scattering amplitude for the process grows quadratically with the center-of-mass energy, violating unitarity [29]. Interference from diagrams involving the Higgs boson restores unitarity, as shown in Fig. 1.7. The VBS cross section is therefore sensitive to both the four-point gauge boson couplings of Fig. 1.2 and the structure of the Higgs field, and can be used to distinguish the SM from models without a Higgs boson and models with multiple particles that play its role.

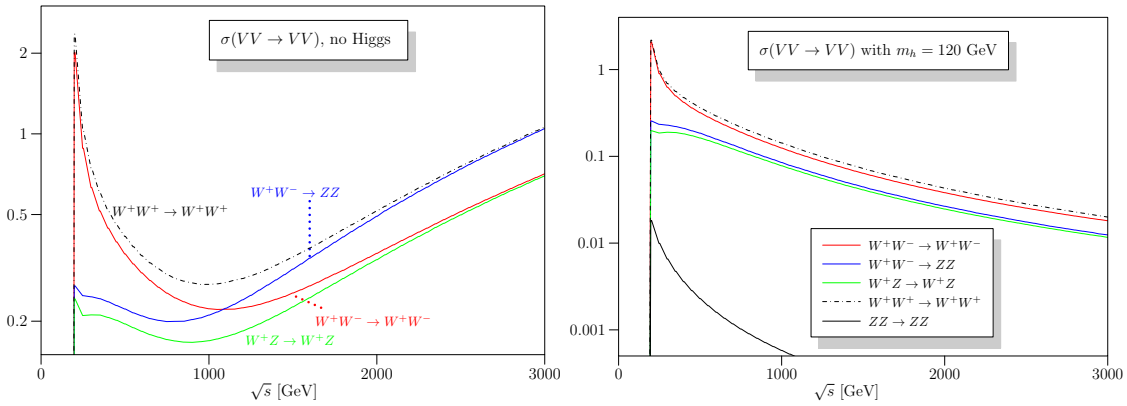

Figure 1.7: VV $\to$ VV scattering cross sections as a function of center-of-mass energy for the SM with no Higgs boson (left) and a Higgs boson with $m_{\mathrm{H}} = 120\,\mathrm{GeV}$ (right), reproduced from Ref. [29]. The model with no Higgs violates unitarity.

1.5 Limitations and Possible Extensions

As noted above, the SM is believed to be fully self-consistent, but it has several notable omissions. It makes no mention of gravity, which is too weak to be probed at the level of individual particles at energies available in collider experiments. Neutrinos in the SM are massless, but they are found experimentally to oscillate between the three flavors in flight, which implies that the flavor eigenstates are not mass eigenstates, and thus that they have mass. Dark matter, the unidentified substance that makes up roughly 80% of the universe's gravitationally interacting material [11, 30–32], is also not described. Some consider the SM to be "ad hoc" in the sense that the fermion masses, and a number of other parameters—19 in all—are completely unconstrained, and a more aesthetically satisfying theory would make predictions for all of them. A nicer theory would also offer thorough explanations for what seem now like remarkable coincidences. For example, the so-called hierarchy problem: it is intuitively surprising that the strengths of the fundamental forces vary by many orders of magnitude, and do so in such a way that large quantum corrections to the effective Higgs potential cancel almost exactly, causing the Higgs boson mass to be nonzero but much smaller

than the scale of the corrections ($\mathcal{O}(10^{19}\,\mathrm{GeV})$) [33–35].

A number of theories have been proposed which modify or extend the SM [11, 32], adding new symmetry groups, unifying the existing ones further, adding new particles, etc. A fourth generation of fermions would be a simple extension, but the fourth neutrino would have to have a mass more than half the Z boson mass to have escaped detection so far, which would be surprising given the small masses of the first three [11, 36]. Supersymmetric models, for example, posit a symmetry between bosons and fermions, such that each particle would have a "superpartner" with the opposite spin statistics which would provide an opposite correction to the effective Higgs potential and thus a clean solution to the hierarchy problem [11, 37]. Despite extensive searches, no evidence of such models has been found [38].

1.5.1 Anomalous Gauge Couplings

Another simple extension to the SM would be a new force, with mediator gauge bosons analogous to the W and Z above the masses accessible at existing colliders. Such a force would originate from a previously undiscovered symmetry, which in many models could result from a higher symmetry which unifies all the fundamental forces at high energy but is broken and effectively reduces to the SM in the low-energy limit [11, 33, 35, 39]. This, and several other possible extensions to the SM, would appear in practice as small deviations from the expected couplings of the gauge bosons. Such deviations from standard model interactions are called anomalous gauge couplings (aGC), and may involve anomalous trilinear (aTGC) or quartic (aQGC) vertices. Of particular interest here are the anomalous neutral couplings, which correspond to the vertices shown in Fig. 1.8. These interactions are forbidden in the SM. Their existence would increase the cross section for diboson production, and affect the cross section for $\mathrm{ZZ} \to \mathrm{ZZ}$ scattering, changing the requirements on the Higgs field needed

to preserve unitarity.

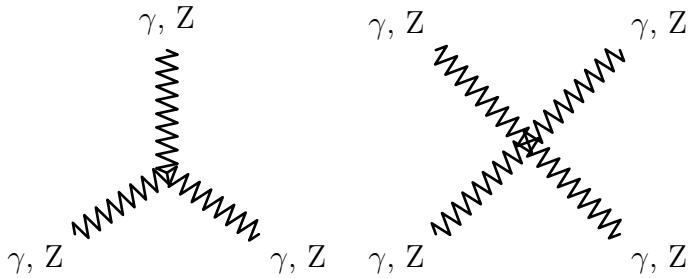

Figure 1.8: Fully-neutral gauge coupling vertices, for aTGCs (left) and aQGCs (right). These are forbidden in the SM.

Several theoretical frameworks exist for describing aGCs. For aTGCs, we use the effective Lagrangian approach described in Ref. [40–42]. In this parameterization, a ZZV coupling (where V may be Z or γ) has a vertex function corresponding to the vertex shown in Fig. 1.9 of the form

$$\Gamma_{\mathrm{V}}^{\alpha,\beta,\delta}\left(q_1,q_2,P\right)=i\frac{\hat{s}-m_{\mathrm{V}}^2}{m_{\mathrm{Z}}^2}\left(f_4^{\mathrm{V}}\left(P^{\alpha}g^{\delta\beta}+P^{\beta}g^{\delta\alpha}\right)+f_5^{\mathrm{V}}\varepsilon^{\delta\alpha\beta\lambda}\left(q_1-q_2\right)_{\lambda}\right), \tag{1.16}$$

where $\hat{s}$ is the center of mass energy squared, $g^{\mu\nu}$ is the Minkowski metric and $\varepsilon^{\alpha\beta\gamma\delta}$ is the fully antisymmetric tensor with $\varepsilon^{0123}=1$. Neutral aTGCs are then described by two parameters $f_4^{\gamma,\mathrm{Z}}$ associated to CP-odd terms and two parameters $f_5^{\gamma,\mathrm{Z}}$ associated to CP-even terms.[6] The effective Lagrangians in use here are taken to be low-energy approximations invalid at high energy, and are not unitary at high $\sqrt{\hat{s}}$. In some previous literature (see Section 2.3.1), unitarity is enforced with a generalized dipole for factor [42, 43], such that the vertex factor takes an energy dependence,

$$f_i^{\mathrm{V}}\left(\hat{s}\right)=\frac{f_{i,0}^{\mathrm{V}}}{\left(1+\hat{s}/\Lambda^2\right)^n}, \tag{1.17}$$

where Λ is the energy scale of the new physics process. No such form factor is applied in this work, to avoid adding unnecessary model dependence, so Λ is taken to be much larger than the energies accessible in the experiment and no form factor is applied.

[6] There are, of course, analogous terms for all anomalous VVV couplings, where V may be any of the electroweak bosons, but only the ZZZ and ZZγ terms are relevant to this work.

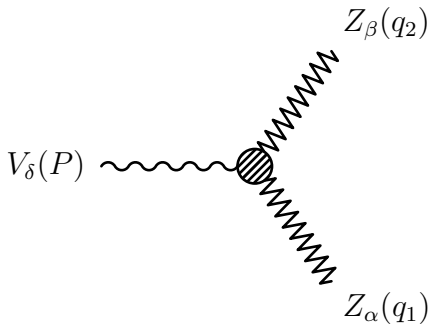

Figure 1.9: An anomalous neutral triple gauge coupling vertex, with momentum labels corresponding to Eq. (1.16).

For aQGCs, we adopt an effective field theory approach [44] which parameterizes the effects of new physics as a set of field operators [45]. The operators are chosen to be dimension-8, because this is the lowest dimension that can yield neutral quartic couplings, and the lowest dimension that can produce a theory with aQGCs but no aTGCs. Out of the large class of operators which control aQGCs in general, ZZ VBS is sensitive to five,

$$\begin{aligned}
\mathcal{L}_{\mathrm{T0}} =& \frac{f_{\mathrm{T0}}}{\Lambda^4}\mathrm{Tr}\left[\hat{W}_{\mu\nu}\hat{W}^{\mu\nu}\right] \times \mathrm{Tr}\left[\hat{W}_{\alpha\beta}\hat{W}^{\alpha\beta}\right] \\
\mathcal{L}_{\mathrm{T1}} =& \frac{f_{\mathrm{T1}}}{\Lambda^4}\mathrm{Tr}\left[\hat{W}_{\alpha\nu}\hat{W}^{\mu\beta}\right] \times \mathrm{Tr}\left[\hat{W}_{\mu\beta}\hat{W}^{\alpha\nu}\right] \\
\mathcal{L}_{\mathrm{T2}} =& \frac{f_{\mathrm{T2}}}{\Lambda^4}\mathrm{Tr}\left[\hat{W}_{\alpha\mu}\hat{W}^{\mu\beta}\right] \times \mathrm{Tr}\left[\hat{W}_{\beta\nu}\hat{W}^{\nu\alpha}\right] \\
\mathcal{L}_{\mathrm{T8}} =& \frac{f_{\mathrm{T8}}}{\Lambda^4}B_{\mu\nu}B^{\mu\nu}B_{\alpha\beta}B^{\alpha\beta} \\
\mathcal{L}_{\mathrm{T9}} =& \frac{f_{\mathrm{T9}}}{\Lambda^4}B_{\alpha\mu}B^{\mu\beta}B_{\beta\nu}B^{\nu\alpha},
\end{aligned} \tag{1.18}$$

where

$$\hat{W}_{\mu\nu} = \sum_j W^j_{\mu\nu}\frac{\sigma^j}{2}, \tag{1.19}$$

and $\Lambda \gg \sqrt{\hat{s}}$ is again the scale of the new physics causing the change in the effective couplings.

1.6 Proton-Proton Collisions

Our experimental probe of all these interactions is proton-proton collisions. As discussed above, protons are bound states of three quarks (uud), known as the valence quarks, held together by virtual gluon exchange. The proton constituents, quarks and gluons, are collectively called partons. The gluons carry roughly half the total proton momentum [2]. Because the number of gluons is not conserved, and they self-interact, the gluon structure of the proton is constantly evolving, and gluons produce virtual $q\bar{q}$ "sea quark" pairs which annihilate again on time scales of order $t_{virt} \sim 1/\Delta E$ [3]. A sufficiently energetic color-charged particle colliding with a proton may therefore interact with any kind of quark or with a gluon, and interesting physics in a pp collision may be initiated by $qq, q\bar{q}, qg$, or gg scattering. A particle that scatters with a proton of energy P has a probability of interacting with a parton of a given type with momentum xP given by the parton distribution function (PDF) $f(x, Q^2)$, where x is the fraction of the proton momentum carried by the parton and Q is the momentum transfer of the interaction [3]. Heuristically, the PDF is a function of Q because it sets the wavelength of the mediating gauge boson and thus the scale on which the interaction can resolve constituent partons. PDFs are nonperturbative and have not been calculated from theory, so they are built from fits to experimental data from fixed-target and symmetric $e^{\pm}p$ deep inelastic scattering (DIS) data, and from hadron collider data [46]. The most recent PDFs from the NNPDF collaboration [46] are shown in Fig 1.10.

As mentioned previously, the rate at which a scattering process occurs is called its cross section σ, typically given in barns, a unit of area $\mathrm{b} = 10^{-24}\,\mathrm{cm}^2$. The number of collisions is characterized by the luminosity $\mathscr{L}$ such that the rate of events with

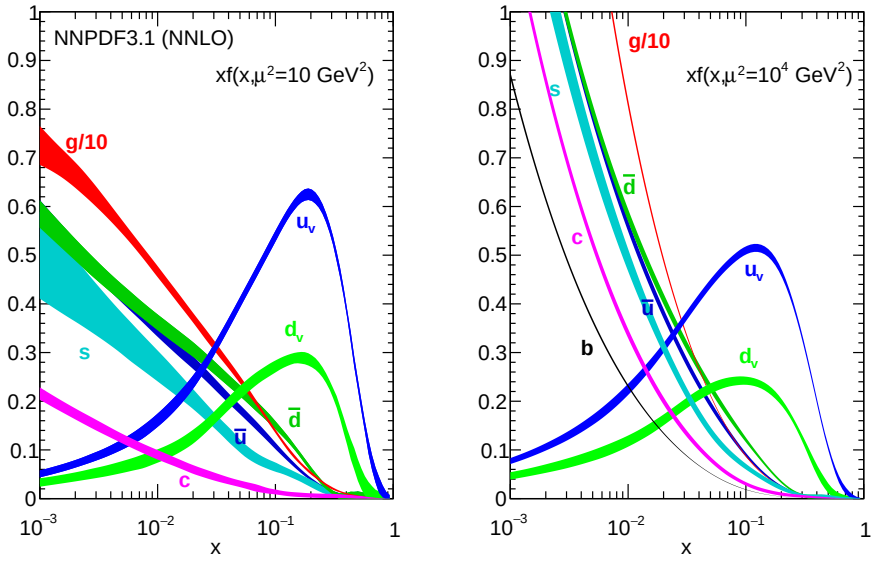

Figure 1.10: Parton distribution functions from NNPDF3.1, reproduced from Ref. [46], which used μ for the momentum transfer denoted Q in the text.

final state X will be given by

$$\frac{\mathrm{d}N_X}{\mathrm{d}t} = \sigma\left(\mathrm{pp} \to X\right)\mathscr{L} \tag{1.20}$$

as described in more detail in Section 3.1. If the initial protons each have momentum P and collide head on, such that their center-of-mass energy is $\sqrt{s} = 2P$, the interacting partons will have total energy $\sqrt{\hat{s}} = \sqrt{2x_1x_2}P$ where x_1 and x_2 are the fraction of its proton's momentum each incoming parton carried. The cross section is given by

$$\sigma\left(\mathrm{pp} \to X\right) = \sum_{p_1,p_2 \in \mathrm{q},\bar{\mathrm{q}},\mathrm{g}} C_{p_1,p_2} \int \mathrm{d}x_1 \mathrm{d}x_2 f_{p_1}(x_1, Q^2) f_{p_2}(x_2, Q^2) \sigma_{\mathrm{ME}}(p_1 + p_2 \to X), \tag{1.21}$$

where σ_{ME} is the matrix element-level cross section for the bare partons to scatter to final state X and C_{p_1,p_2} is a combinatoric factor based on the number of possible color combinations that varies based on the initial state particles p_1 and p_2. This

factorization into perturbative hard process physics and the nonperturbative PDF greatly simplifies calculations.

1.7 ZZ Measurements in Context

This is the context for the work described in the following chapters: the SM is incomplete, but it has been tested extensively and no discrepancies have been found (a partial review of studies that did not exclude the SM can be found in Chapter 2). Because the electroweak sector was the last to be confirmed experimentally and is generally best explored at high energies, a number of aspects await detailed confirmation and remain a potential area where new physics might be found. This thesis presents several studies of diboson events with $\ell^+\ell^-\ell'^+\ell'^-$ $(\ell, \ell' \in \mathrm{e}, \mu)$ final states designed to probe the interactions of the neutral electroweak bosons. In particular, as one can deduce from Eqs. (1.12)–(1.14), ZZ production processes are sensitive to the details of the couplings between the gauge bosons and can therefore be used to investigate the GWS model and the Higgs model and spontaneous symmetry breaking. Measurements of ZZ production have been made before, but measurements in a new energy regime and with a very large dataset allow stringent new tests of the SM and allow the potential observation of previously unseen phenomena within and beyond it. The results presented here substantially expand our understanding of ZZ production, with inclusive and differential cross section measurements at the record-breaking center-of-mass energy of 13 TeV, the most precise measurement of the $\mathrm{Z} \to 4\ell$ branching fraction to date, and searches for vector boson scattering and anomalous neutral gauge couplings.

Chapter 2

ZZ Phenomenology and Previous Results

Four-lepton final states originate primarily from three physics processes: nonresonant diboson production, resonant Higgs boson production, and resonant single-Z production. Multi-Z triboson production (WZZ and ZZZ) occurs at negligible rates [47, 48]. Single-Z triboson production (WWZ) [48, 49] and $t\bar{t}Z$ production result in final states with four prompt leptons, but are considered background (see Section 2.4). The three signal processes can be distinguished by kinematics, such as the four-lepton invariant mass distribution.

The signal processes all involve on- or off-shell Z bosons. The Z was first indirectly observed in 1973 when the Gargamelle bubble chamber experiment at CERN recorded an elastic muon antineutrino-electron ($\bar{\nu_\mu}+e^- \rightarrow \bar{\nu_\mu}+e^-$) scattering event [50]. Direct observation in leptonic decays came roughly a decade later, from the UA1 experiment, also at CERN [51]. Clean e^+e^- collisions at LEP and SLAC, where the center-of-mass energy could be adjusted to produce Z bosons copiously, allowed its properties—and a number of other parameters of the electroweak theory—to be measured with per-mille

precision or better [52]. Of particular importance to this study, its mass is

$$m_{\mathrm{Z}} = 91.1876 \pm 0.0021\,\mathrm{GeV}, \tag{2.1}$$

its full width is

$$\Gamma_{\mathrm{Z}} = 2.4952 \pm 0.0023\,\mathrm{GeV}, \tag{2.2}$$

its width in leptonic decays is

$$\Gamma_{\mathrm{Z}}(\ell^{+}\ell^{-}) = 83.984 \pm 0.086\,\mathrm{MeV}, \tag{2.3}$$

and it decays to a pair of charged leptons 3.3658% of the time for each lepton flavor [11].

2.1 Nonresonant ZZ/Zγ^{*} Production and Decay

Leading-order ZZ production is q$\bar{\mathrm{q}}$-initiated and proceeds through t-channel quark exchange, as shown in Fig. 2.1. At next-to-leading order (NLO; several representative diagrams are shown in Fig. 2.2), production may have a gluon in the initial state and may have a quark or gluon in the final state which hadronizes and appears experimentally as a jet [53–55]. Next-to-next-to-leading order (NNLO) adds gluon-gluon fusion box diagrams (Fig. 2.3), as well as q$\bar{\mathrm{q}}$-initiated production with two loops, one loop and a final state jet, and two jets [56, 57]. The NLO and NNLO corrections are generally large, outside the scale uncertainties of the calculations at previous orders, because diagrams with new initial states contribute only positively to the cross section. Quark-gluon scattering diagrams introduced at NLO and gluon-gluon fusion diagrams introduced at NNLO have large amplitudes—the gg $\rightarrow$ ZZ process accounts for roughly 60% of the total NNLO correction, for example—due to the high effective gluon luminosity in multi-TeV proton collisions [56]. Because

of the box diagrams' large contribution, "NLO + gg" simulations are often used, in which NLO $q\bar{q}/qg/\bar{q}g \to ZZ$ and LO $gg \to ZZ$ samples are summed even though they formally contribute at different orders in α_s.

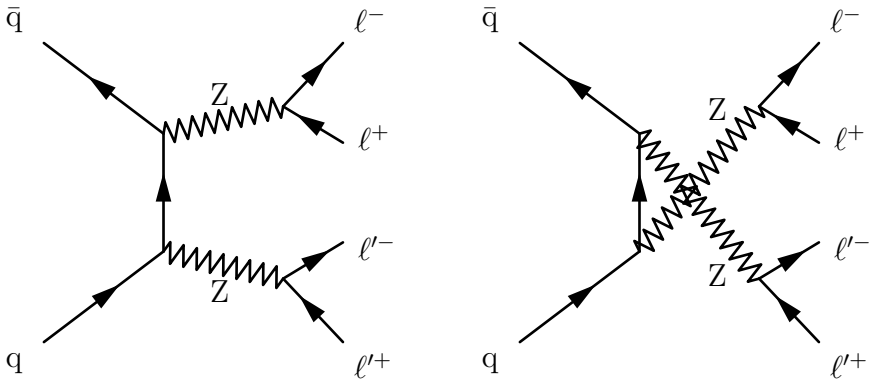

Figure 2.1: Leading order Feynman diagrams for $ZZ \to 4\ell$ production in pp collisions.

Production of pairs of on-shell Z bosons[1] turns on sharply at the kinematic threshold $\sqrt{\hat{s}} = 2m_Z = 182.4\,\text{GeV}$, and in proton-proton collisions at $\sqrt{s} = 13\,\text{TeV}$, peaks around $m_{ZZ} \approx 200\,\text{GeV}$ before falling steeply at higher invariant masses. Continuum production occurs below the kinematic threshold when one or both Z bosons are replaced by a Z^*/γ^* admixture, typically in the form of a $q\bar{q} \to Z$ event in which one of the incoming quarks emits a virtual photon as initial state radiation (ISR). Events of interest in this analysis (see Sections 5.4 and 6.3) generally have one on-shell Z, and a Z^*/γ^* at a lower mass. Nonresonant $Z\gamma^*$ production is generally flat as a function of invariant mass between roughly 100 GeV and the doubly resonant threshold.

[1]Events with two on-shell Z bosons are often called "doubly resonant," but are a subset of "nonresonant" production in the sense that the ZZ system is not produced by a resonance. Either term may be used to distinguish "continuum" production from "singly resonant" production from $Z \to 4\ell$, $H \to ZZ^*$, or a potential new particle which decays to ZZ.

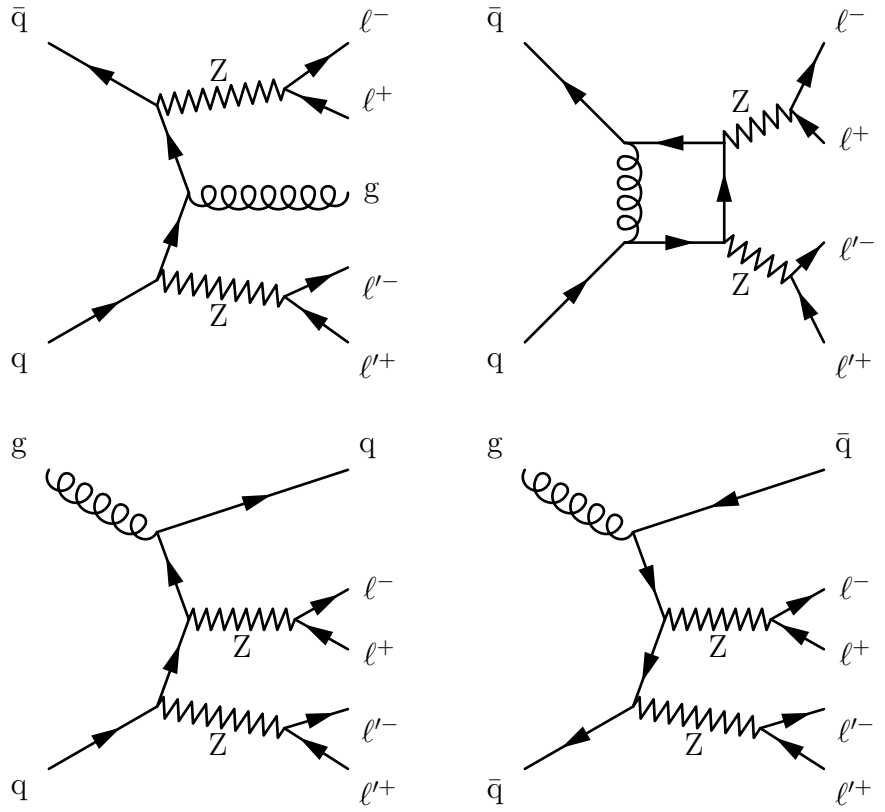

Figure 2.2: Four representative Feynman diagrams that contribute to $ZZ \to 4\ell$ production in pp collisions at NLO. Clockwise from the top right, the diagrams are examples of one-loop diagrams, real antiquark and quark emission, and real gluon emission. The loop diagram (top right) is formally NNLO, but contributes at NLO through interference with NLO $q\bar{q} \to ZZ$ diagrams.

2.1.1 Vector Boson Scattering

Vector boson scattering proceeds at hadron colliders through the diagrams shown in Fig 2.4, resulting in a ZZjj final state. This fully electroweak (EWK) production must be distinguished from the background of QCD-initiated ZZ + jets events (see Section 2.4). The hallmark of the EWK process is a pair of high energy, high rapidity jets from the quarks, which retain a high boost along the z-axis even after electroweak boson emission and are thus deflected through a small angle in the lab frame. At the same time, the ZZ system is produced with low transverse boost compared to QCD-

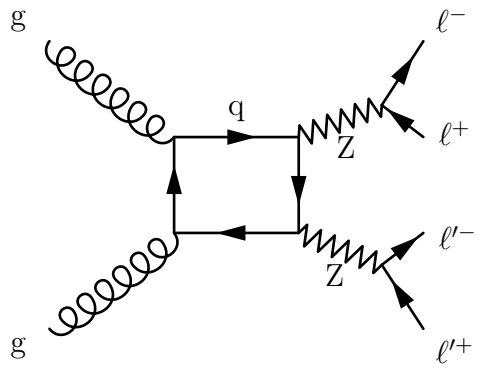

Figure 2.3: A LO box diagram for ZZ $\rightarrow 4\ell$ production through a quark loop in a gluon-gluon fusion event. This is formally an NNLO diagram for ZZ production overall, but is often included in NLO calculations because it accounts for a large fraction of the NNLO correction and its contribution to the ZZ cross section has a similar magnitude to that from the NLO corrections. The gg $\rightarrow$ ZZ amplitude is so large due to the high effective luminosity of gluons with enough energy to produce a Z boson pair in proton collisions at high Q^2,

initiated ZZjj events, in which the ZZ system recoils against the jets, and somewhat higher invariant mass on average [58]. Because the hard scattering interaction involves no color exchange or reconnection [58–60], VBS events are much less likely to have less energetic jets between the two high-energy quark jets. Useful variables to discriminate between EWK and QCD production therefore include the angle between the jets, the jet energies, the dijet invariant mass, the ZZ invariant mass and rapidity, and the number of central jets (see Section 6.5 for a full list and definitions).

2.1.2 Prior Measurements

Doubly resonant ZZ production was first observed in e^+e^- collisions at LEP by the ALEPH, OPAL, L3, and DELPHI experiments, from 183 GeV, just above the threshold center-of-mass energy, to the LEP maximum of 209 GeV [61–66]. Because the ZZ cross section is very small, these measurements used all possible final states except those in which all Z decay products were neutrinos or taus. This was possible because

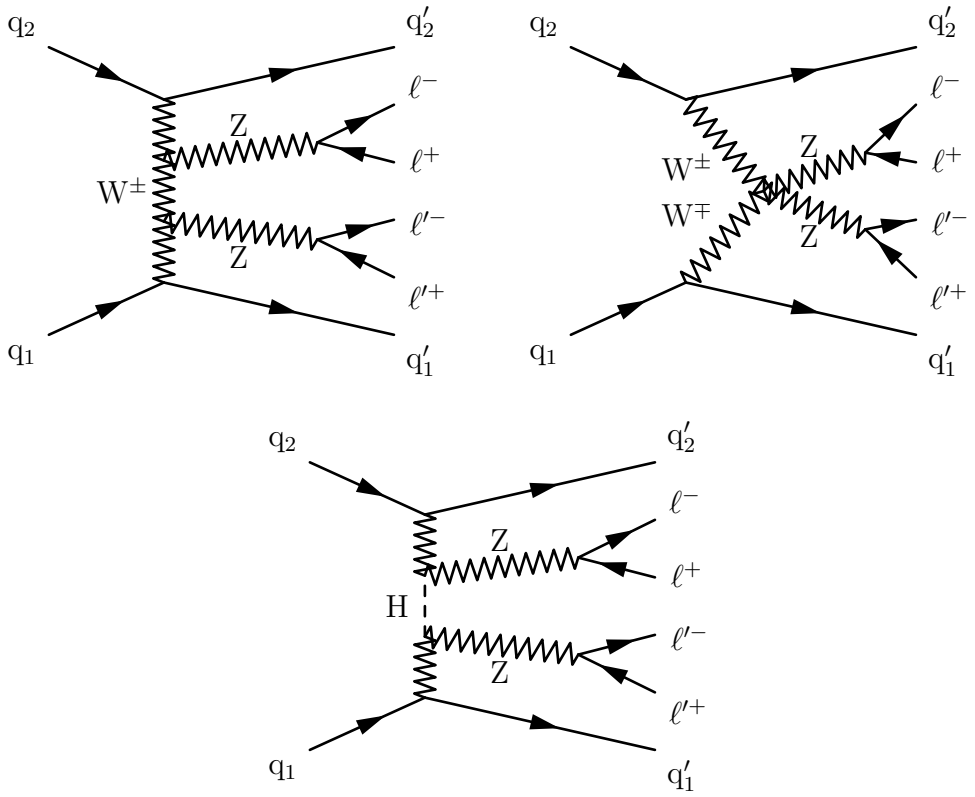

Figure 2.4: The primary ZZ VBS diagrams at hadron colliders. Diagrams also exist with antiquarks and with permutation and crossing of the final state particles. The interaction is only unitary to arbitrarily high energy when all diagrams are considered.

jets in e^+e^- collisions can be reliably matched to a hard scattering process, allowing identification of $Z \to q\bar{q}$ decays. The measurements agreed with the SM, but were dominated by statistical uncertainties. Example measured cross sections from OPAL are shown in Fig 2.5 [65].

Production in hadron collisions was first observed by the CDF and D0 experiments, in 1.96 TeV $p\bar{p}$ events at Tevatron [67–71]. In contrast to the LEP measurements, $p\bar{p}$ colliders cause too many extraneous jets for the hadronic channels to be seen above the background, so only the 4ℓ and $2\ell 2\nu$ ($\ell = e, \mu$) final states were used. These fully leptonic decay modes have small branching fractions on top of the small ZZ cross section of around 1.6 pb [53], but the total Tevatron dataset of roughly 6 fb^{-1}

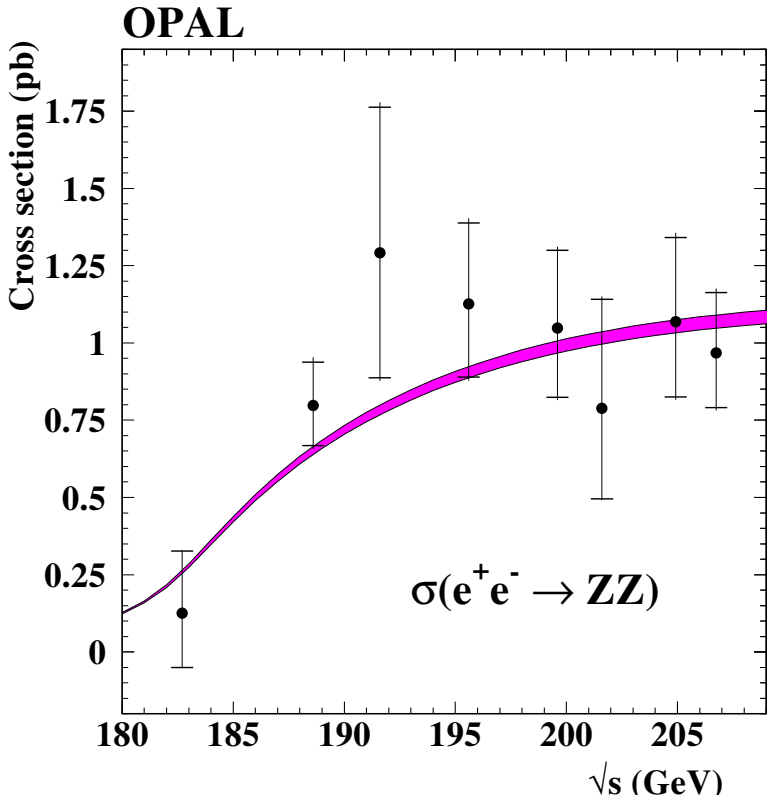

Figure 2.5: Measured $e^+e^- \to ZZ$ cross sections from the OPAL experiment, reproduced from Ref. [65]. Points represent the measured values. Vertical bars are the total uncertainty with horizontal bars indicating the statistical uncertainties, which dominate. The band is the SM prediction with a 2% theoretical uncertainty.

was large enough for CDF and D0 to find a few dozen events each. Results were again fully consistent with the SM but the statistical uncertainties were large, as can be seen in the example $m_{4\ell}$ shown in Fig. 2.6 [70].

The first run of the LHC (see Section 3.1) produced large datasets of pp collisions at $\sqrt{s} = 7$ and 8 TeV, producing ZZ events with a higher cross section than at Tevatron [56] and with a greater integrated luminosity. The primary measurement channels were again the fully leptonic 4ℓ and $2\ell 2\nu$ decays, and the cross sections were measured at $\sqrt{s} = 7$ and 8 TeV by both CMS [72–75] and ATLAS [76–78]. With a dataset of roughly $20\,\text{fb}^{-1}$ and signal event counts in the hundreds even for the

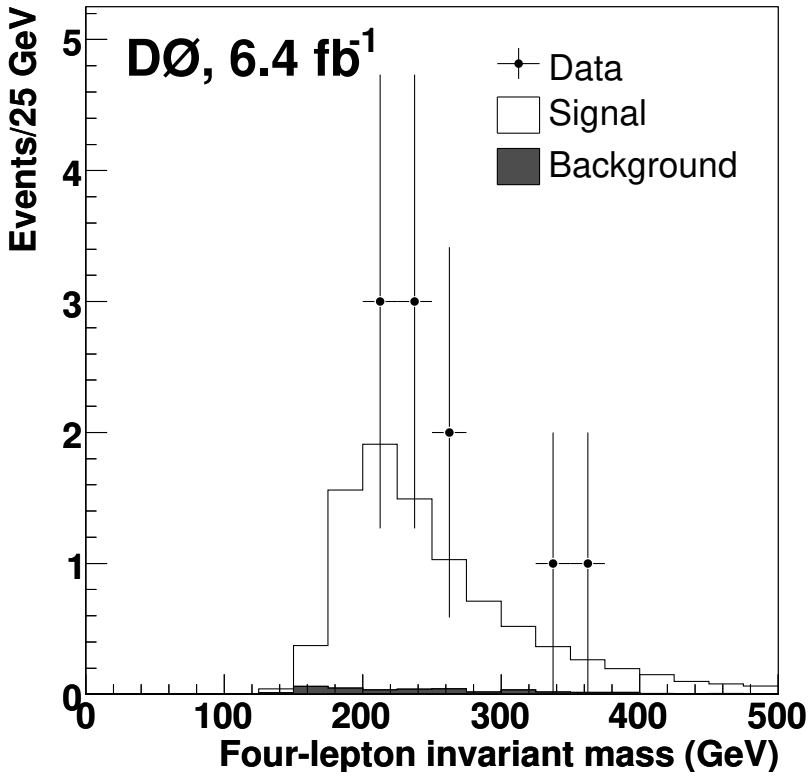

Figure 2.6: Measured $m_{4\ell}$ distribution from ZZ events collected by D0, reproduced from Ref. [70]. Points represent data with vertical bars showing statistical uncertainties, while the histograms show the SM expectation.

low-rate 4ℓ channel, the 8 TeV measurements had the statistical power to include differential cross sections as functions of kinematic observables for the ZZ system and the associated jets. Statistical uncertainties were still larger than the systematic uncertainties, but they were at the level of 5–10% for the total cross section, compared to 30–50% at Tevatron and 15–150% at LEP depending on the experiment and center-of-mass energy[2]. The four-lepton mass spectra from the CMS and ATLAS ZZ cross section measurements at 8 TeV are shown in Figs. 2.7 and 2.8, respectively [73, 77]. A measurement was also performed on CMS data in the $\mathrm{ZZ} \to \ell^+\ell^-\mathrm{b\bar{b}}$ and $\mathrm{ZZ} \to \nu\bar{\nu}\mathrm{b\bar{b}}$ channels [79].

[2]Most LEP ZZ cross section measurements had statistical uncertainties around 20–40%; see references given in the text for details.

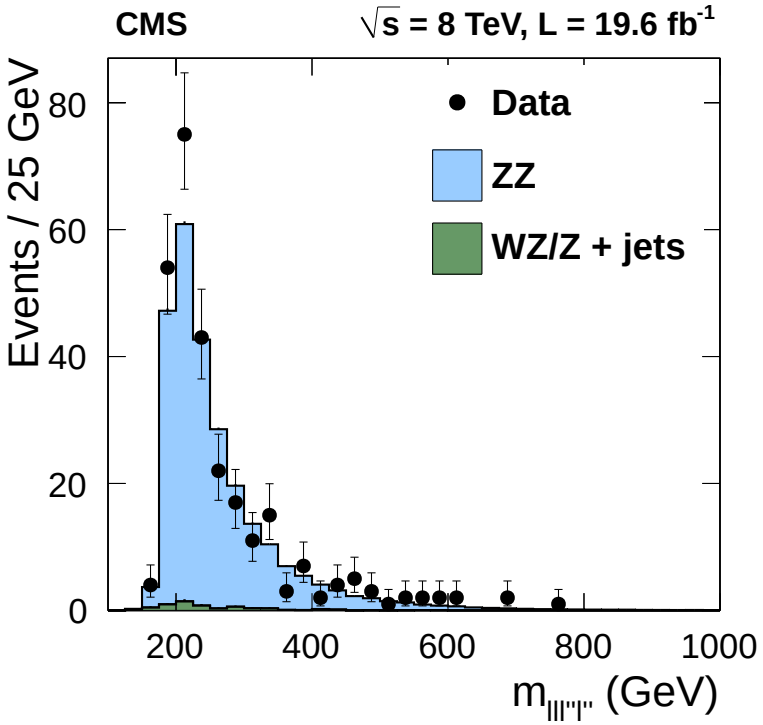

Figure 2.7: Measured $m_{4\ell}$ distribution from ZZ events collected by CMS at $\sqrt{s} = 8\,\text{TeV}$, reproduced from Ref. [77]. Points represent data with vertical bars showing statistical uncertainties, while the histograms show the SM expectation. The grey hatched band represents the total uncertainty on the prediction.

CMS found that the total ZZ cross sections, defined as the cross sections of all events with two Z bosons in the mass range 60–120 GeV, to be

$$\begin{aligned}\sigma_{\text{ZZ}}(7\,\text{TeV}) &= 6.24^{+0.86}_{-0.80}\,(\text{stat})^{+0.41}_{-0.32}\,(\text{syst}) \pm 0.14\,(\text{lumi})\,\text{pb} \\ \sigma_{\text{ZZ}}(8\,\text{TeV}) &= 7.7 \pm 0.5\,(\text{stat})^{+0.5}_{-0.4}\,(\text{syst}) \pm 0.4\,(\text{theo}) \pm 0.2\,(\text{lumi})\,\text{pb},\end{aligned} \tag{2.4}$$

when measured with 4ℓ final states [73, 76], and

$$\begin{aligned}\sigma_{\text{ZZ}}(7\,\text{TeV}) &= 5.1^{+1.5}_{-1.4}\,(\text{stat})^{+1.4}_{-1.1}\,(\text{syst}) \pm 0.1\,(\text{lumi})\,\text{pb} \\ \sigma_{\text{ZZ}}(8\,\text{TeV}) &= 7.2 \pm 0.8\,(\text{stat})^{+1.9}_{-1.5}\,(\text{syst}) \pm 0.2\,(\text{lumi})\,\text{pb}\end{aligned} \tag{2.5}$$

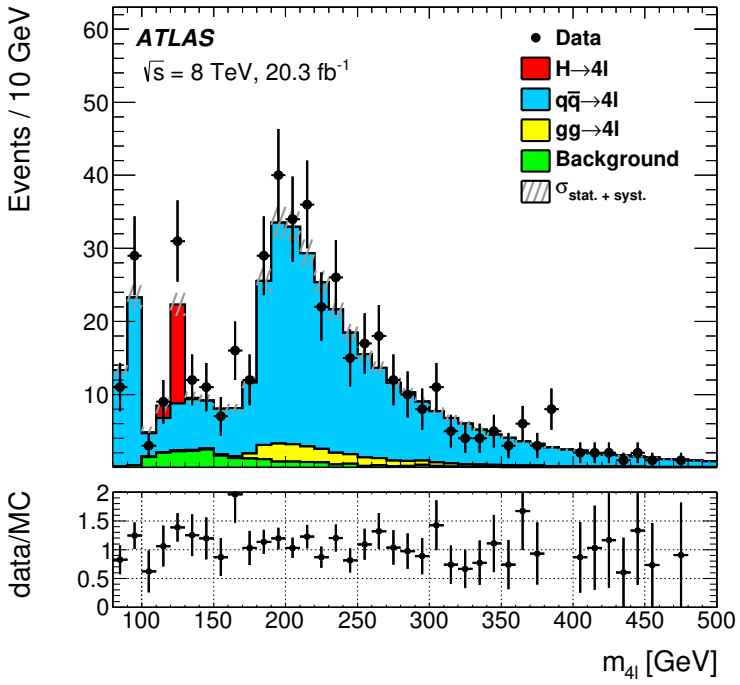

Figure 2.8: Measured $m_{4\ell}$ distribution from ZZ events collected by ATLAS at $\sqrt{s} = 8\,\text{TeV}$, reproduced from Ref. [70]. Points represent data with vertical bars showing statistical uncertainties, while the histograms show the SM expectation.

when measured with $2\ell 2\nu$ final states [74]. ATLAS found

$$\begin{aligned}\sigma_{\text{ZZ}}(7\,\text{TeV}) &= 6.7 \pm 0.7\,(\text{stat})^{+0.4}_{-0.3}\,(\text{syst}) \pm 0.3\,(\text{lumi})\,\text{pb} \\ \sigma_{\text{ZZ}}(8\,\text{TeV}) &= 7.3 \pm 0.4\,(\text{stat}) \pm 0.3\,(\text{syst}) \pm 0.2\,(\text{lumi})\,\text{pb},\end{aligned} \tag{2.6}$$

using 4ℓ final states at 7 TeV [76] and a combination of 4ℓ and $2\ell 2\nu$ events at 8 TeV [78]. ATLAS used a slightly different definition of the Z, considering it to have mass in the range 66–116 GeV, which reduces the SM expected cross section by 1.6% [80]. Measured cross sections from both experiments are again consistent with SM predictions of $6.7 \pm 0.2\,\text{pb}$ at 7 TeV and $8.3 \pm 0.2\,\text{pb}$ at 8 TeV, both calculated at NNNLO in QCD with MATRIX, with factorization and renormalization scales $\mu_{\text{F}} = \mu_{\text{R}} = m_{\text{Z}}$.

Searches for vector boson scattering were first performed at $\sqrt{s} = 8\,\text{TeV}$. The first

process examined was the low-background same-sign WW process pp $\rightarrow W^{\pm}W^{\pm}jj$ studied at ATLAS, where evidence for electroweak production was observed at the level of a 3.6 standard deviation excess over the null hypothesis [81], and at CMS, where a 2.0σ excess was found [82]. Subsequent searches for electroweak $Z\gamma jj$ production found a 3.0σ excess above the null hypothesis at CMS [83] and no significant excess at ATLAS [84]. A CMS measurement of $W\gamma jj$ production found a 2.7σ excess above the null hypothesis consistent with electroweak production [85]. Searches for photon-photon VBS were performed as searches for exclusive and quasi-exclusive $\gamma\gamma \rightarrow W^+W^-$ production pp $\rightarrow p^{(*)}W^+W^-p^{(*)}$, in which the protons do not collide but instead both radiate photons, which scatter. CMS found evidence at the level of 3.4σ above the null hypothesis [86], and ATLAS saw a 3.0σ excess [87]. Roughly contemporaneously with this work, electroweak same-sign WW production was observed at CMS in 13 TeV collisions, with a significance of 5.5σ [88]. No searches for Electroweak ZZ production had been performed prior to the analysis described in the following chapters.

2.2 Resonant $ZZ^*/\gamma^*\gamma^*$ Production

Resonant production appears as a sharp peak in the four-lepton invariant mass distribution over the broad spectrum from nonresonant production. There are two known four-lepton resonances: single-Z decays to four leptons around 91 GeV, and Higgs decays to ZZ^* around 125 GeV. Another resonance, caused by a new particle, could still be discovered at high mass, or at low mass but with a very small cross section.

2.2.1 Z Boson Decays to Four Leptons

A single Z boson may decay to a four-lepton final state when a lepton from a normal $\mathrm{Z} \to \ell^+\ell^-$ decay radiates a virtual photon, as shown in Fig 2.9. In a window around the Z mass of $80 < m_{4\ell} < 100\,\mathrm{GeV}$, t- and u-channel production (the diagrams of Fig 2.1 with γ^* for both bosons) contribute at the few-percent level (4% at $\sqrt{s} = 13\,\mathrm{TeV}$). Four-fermion decays were studied in detail at LEP [89]. This included four-lepton decays, but used all $\ell^+\ell^-\mathrm{f}\bar{\mathrm{f}}(\ell = \mathrm{e}, \mu, \tau)$ final states, where f could be any fermion except the neutrinos. $\mathrm{Z} \to 4\ell$ decays were also observed at 7 and 8 TeV at CMS, where the branching fraction was found to be $\mathcal{B}(\mathrm{Z} \to 4\ell) = 4.2^{+0.9}_{-0.8}\,(\mathrm{stat}) \pm 0.2\,(\mathrm{syst}) \times 10^{-6}$ [90], and at ATLAS, where it was found to be $3.20 \pm 0.25\,(\mathrm{stat}) \pm 0.13\,(\mathrm{syst}) \times 10^{-6}$ in a slightly different phase space [91]. After correcting for phase space differences, the measurements are compatible with each other and with the SM.

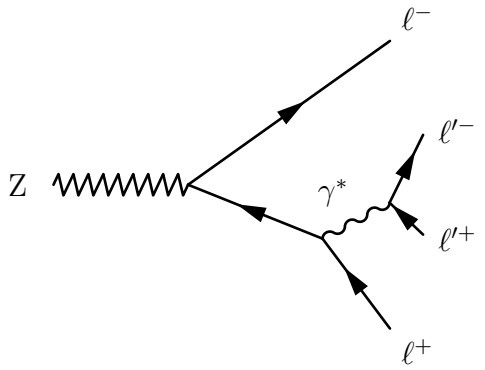

Figure 2.9: Tree-level Feynman diagram for $\mathrm{Z} \to 4\ell$ production. Either initial lepton may radiate the γ^*.

2.2.2 Higgs Boson Production

The primary Higgs production mechanism in multi-TeV hadron collisions is gluon-gluon fusion through a quark loop, because of the gluon's high effective luminosity and the top quark's strong Yukawa coupling. Other mechanisms, in decreasing order by

cross section, include vector boson fusion (VBF), vector boson associated production (VH or "Higgsstrahlung"), and top-antitop associated production ($t\bar{t}H$). Tree-level Feynman diagrams for all four are shown in Fig. 2.10. The SM cross sections for the various production mechanisms, and the Higgs branching fractions, are shown as functions of m_H near the measured mass of 125 GeV in Fig. 2.11. Gluon-gluon fusion has roughly an order of magnitude higher rate than the others. The VBF process contributes to the unitarization of vector boson scattering along with the diagrams in Fig. 2.4. Decays to four leptons are heavily suppressed by the fact that, since $m_H < 2m_Z$, energy conservation requires at least one of the Z bosons to be far off its mass shell. Decays to four charged leptons are further suppressed by the small $Z \to \ell^+\ell^-$ branching fraction. However, the distinctive signature of four high-energy charged leptons in a single event is easy to detect with high efficiency and background rejection, and the momentum of electrons and muons can in general be measured with high precision, allowing the Higgs resonance to be easily seen as a sharp peak over a small, relatively flat background. $H \to 4\ell$ became the most attractive channel for Higgs discovery and measurement of its properties in spite of its low rate.

2.2.2.1 Prior Measurements

Higgs boson searches at LEP were for Z-associated production, which has the highest cross section in e^+e^- collisions. The maximum LEP center-of-mass energy, 209 GeV, was just under the ZH threshold around 216 GeV. The LEP combined 95% confidence level (CL) lower limit on m_H was 114.4 GeV [93], and a combination of LEP data and electroweak precision measurements set an upper limit of 193 GeV [94]. Searches at the CDF and D0 experiments at the Tevatron were combined to find a 3.0σ local excess (2.8σ global) consistent with $m_H = 125$ GeV [95], with the $H \to b\bar{b}$ search alone finding a local excess of 3.3σ (3.1σ local) [96]. Results from all the Tevatron

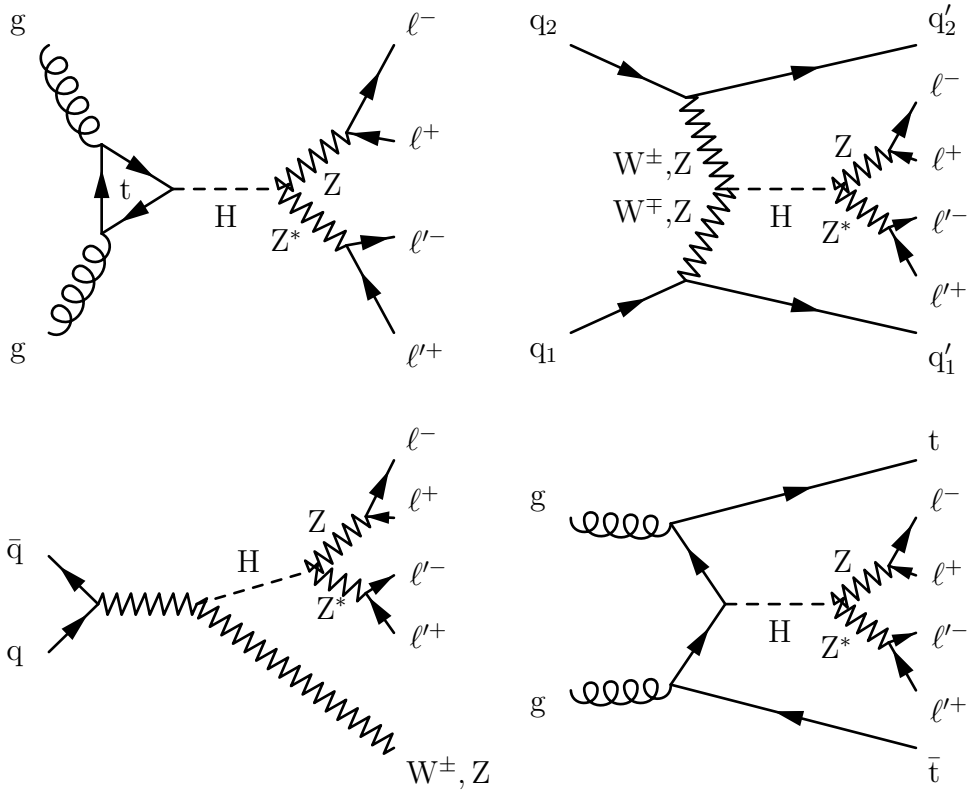

Figure 2.10: Tree-level Higgs production diagrams for gluon-gluon fusion (top left), VBF (top right), VH (bottom left), and $t\bar{t}H$, decaying to four leptons.

and LEP measurements and electroweak precision measurements were combined to place an upper mass limit of 158 GeV at 95% CL [97]. The Higgs was finally discovered simultaneously by the CMS and ATLAS collaborations with a combination of 7 and 8 TeV data [98, 99]. The four-lepton channel was, as anticipated, one of the most important [98, 100]. Its properties were subsequently investigated in detail at both experiments. The Higgs mass was found to be

$$m_{\mathrm{H}} = 125.09 \pm 0.21\,(\mathrm{stat}) \pm 0.11\,(\mathrm{syst})\,\mathrm{GeV} \tag{2.7}$$

based on a combination of data from the two experiments [101], and SM predictions of its properties have been confirmed by a number of measurements [102].

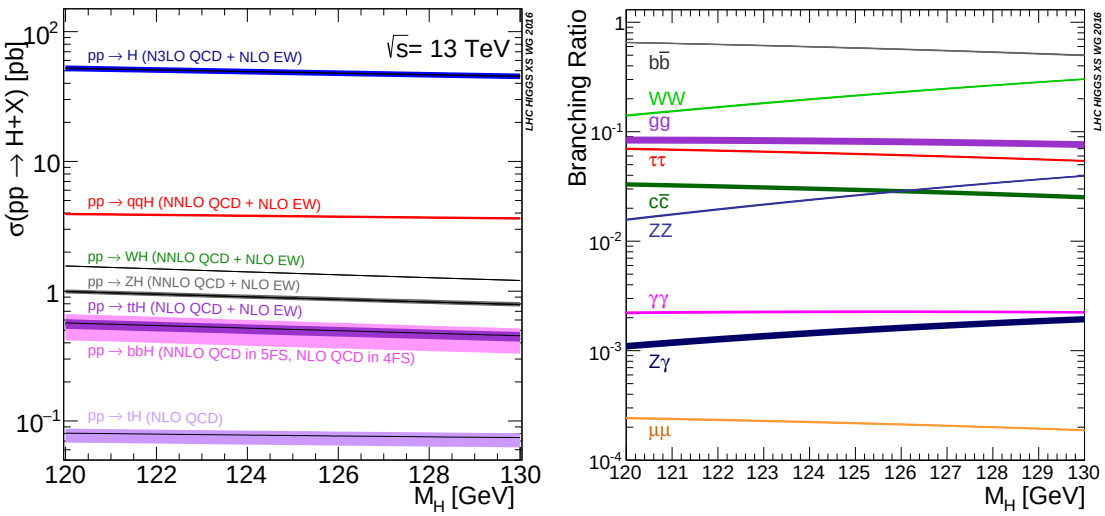

Figure 2.11: The SM cross sections for each Higgs boson production mode (left) and the Higgs branching fraction to several important final states (right), as a function of Higgs mass near the measured mass of 125 GeV. Both plots are reproduced from Ref. [92].

2.3 Anomalous Gauge Couplings

The most visible characteristic of anomalous couplings is an enhanced cross section at center-of-mass energies of order 1 TeV [42]. The increase in cross section at high $m_{4\ell}$ implies higher transverse momentum for the outgoing Z bosons and leptons, as shown for two example aTGC models in Fig. 2.12. Searches for high-mass ZZ events are attractive because SM continuum production cross sections are extremely small above a few hundred GeV and all other sources of prompt or nonprompt four-lepton events are negligible, so even a handful of events would be an unambiguous sign of new physics. The search for nonzero aTGCs is performed using inclusive ZZ events, because the aTGC parameters should not have a large effect on jet distributions. The aQGC search is performed in ZZjj events because it would specifically enhance the VBS cross section at high mass.

The neutral aTGC parameters f_4^{V} and f_5^{V} are expected to have almost identi-

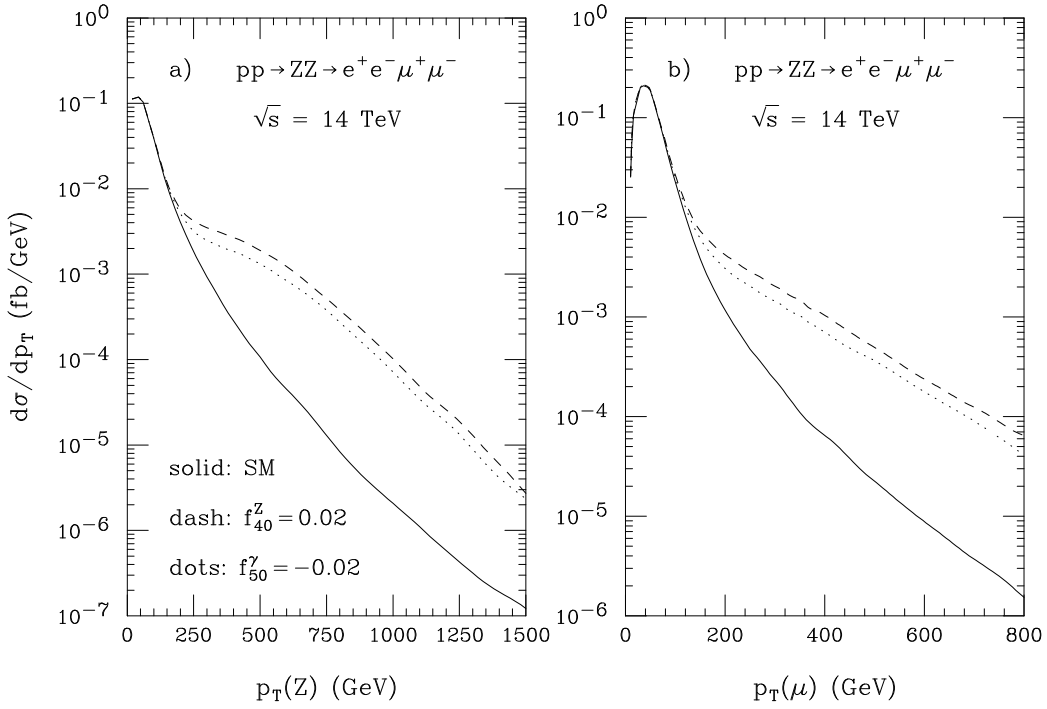

Figure 2.12: Cross section enhancements at high Z and μ momenta caused by example nonzero aTGCs. Reproduced from Ref. [42].

cal effects at high energy, so the search variables cannot be used to determine the relative strengths of the possible anomalous couplings [42]. However, because the terms governed by f_4^{V} have opposite behavior to the terms governed by f_5^{Z} under parity transformations, they affect the helicity amplitudes of the Z bosons and alter the angular distributions of the final-state leptons. Figure 2.13 shows the cross section as a function of total angular distance and the azimuthal angular difference between muons from the same Z decay for several example nonzero aTGCs and for the SM. These distributions could be used to distinguish between the possible aTGC parameters and determine the sign of the CP-conserving f_5^{V} terms.

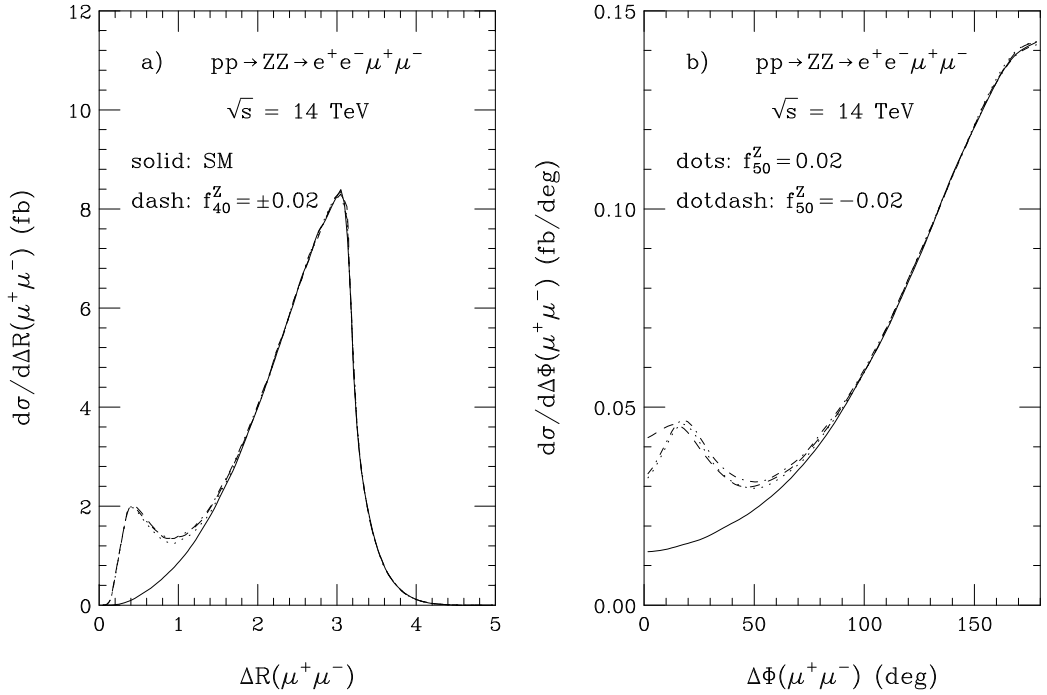

Figure 2.13: Total angular distance and azimuthal angular difference between muons from the same the same Z decay caused by several example nonzero aTGCs. Reproduced from Ref. [42].

2.3.1 Previous Limits

The first neutral aTGC searches were performed at LEP using ZZ and Zγ events [65, 66, 103, 104]. Depending on the experiment and parameter, 95% CL limits were generally $\mathcal{O}(\pm 1)$, and the statistical combination set limits around 0.2–0.4 [94]. The first searches in hadron collisions were performed at Tevatron the by CDF collaboration, which set symmetric 95% CL limits in the range ± 0.10–0.13 for all parameters [105], and the D0 collaboration, which set symmetric limits around ± 0.20–0.31 for all parameters [106]. Both Tevatron experiments used a unitarity-preserving cutoff of $\Lambda = 1.2\,\text{TeV}$. CMS and ATLAS set 95% CL limits at 7 TeV at $\mathcal{O}(\pm 0.1)$ [72, 76, 107], and $\mathcal{O}(\pm 0.005)$ at 8 TeV [73, 108]. ATLAS presented limits from 7 TeV data with and without a unitarizing form factor; their 8 TeV results, and all CMS results,

did not use one. Prior to this work, the most stringent limits on all four neutral aTGC parameters were set by CMS with a combination of 7 and 8 TeV data [74],

$$\begin{aligned} -0.0022 < f_4^{\mathrm{Z}} < 0.0026, \quad -0.0023 < f_5^{\mathrm{Z}} < 0.0023, \\ -0.0029 < f_4^{\gamma} < 0.0026, \quad -0.0026 < f_5^{\gamma} < 0.0027. \end{aligned} \tag{2.8}$$

The two-dimensional aTGC limits set by CMS with the 8 TeV dataset are shown in Fig. 2.14 [73].

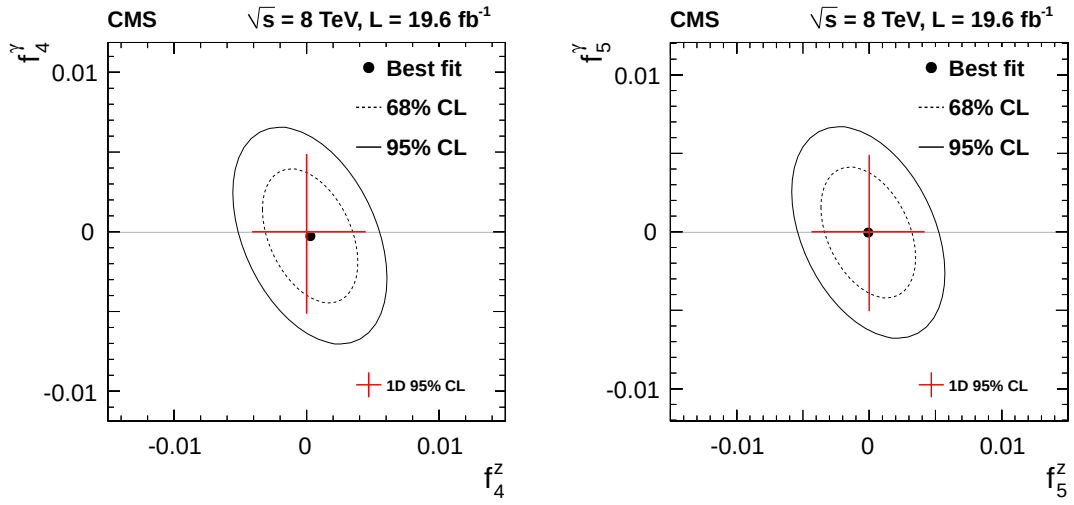

Figure 2.14: Two-dimensional 95% CL aTGC limits set by CMS, reproduced from Ref. [73].

No prior aQGC searches were performed using ZZ processes, but both LHC experiments set limits on the ZZ-sensitive effective field theory operators using other channels. The most stringent limits on f_{T0} were from $\sqrt{s} = 8\,\mathrm{TeV}$ Zγqq events at ATLAS [84], found to be

$$-3.4 < f_{\mathrm{T0}}/\Lambda^4 < 2.9\,\mathrm{TeV}^{-4} \tag{2.9}$$

at 95% CL, with similar results produced by CMS [83]. The most stringent limits on f_{T1} and f_{T2} were set by CMS at 8 TeV using same-sign WWqq events [82], and were

found to be

$$-2.1 < f_{\mathrm{T1}}/\Lambda^4 < 2.4\,\mathrm{TeV}^{-4} \tag{2.10}$$

and

$$-5.9 < f_{\mathrm{T2}}/\Lambda^4 < 7.1\,\mathrm{TeV}^{-4}. \tag{2.11}$$

CMS and ATLAS produced nearly identical limits on f_{T8} and f_{T9} in the same $\mathrm{Z}\gamma\mathrm{qq}$ searches that set limits on f_{T0},

$$-1.8 < f_{\mathrm{T8}}/\Lambda^4 < 1.8\,\mathrm{TeV}^{-4} \tag{2.12}$$

and

$$-3.9 < f_{\mathrm{T9}}/\Lambda^4 < 3.9\,\mathrm{TeV}^{-4}. \tag{2.13}$$

2.4 Background Processes

Spurious events are categorized as irreducible backgrounds, i.e. those that are expected to have four prompt leptons, and reducible backgrounds, which have two or three prompt leptons and another object that is misidentified as a prompt lepton. The only nontrivial irreducible backgrounds to inclusive $\mathrm{ZZ}/\mathrm{Z}\gamma^*$ production are WWZ triboson events in which all three bosons decay leptonically, and $\mathrm{t\bar{t}Z}$ events in which both top quarks and the Z all decay leptonically as shown at tree level in Fig. 2.15. The most prominent reducible backgrounds are $\mathrm{WZ} \to 3\ell\nu$ events in which a jet fragment is misidentified as a prompt lepton, Z + jets events in which two jet fragments are misidentified, and leptonic $\mathrm{t\bar{t}}$ events with two misidentified fragments from the secondary b-jets. For the VBS search, the background is real ZZ events which have two jets, but the jets originate from QCD interactions instead of the fully electroweak processes of Fig. 2.4. An example non-VBS ZZ + 2jets diagram is also shown in Fig. 2.15.

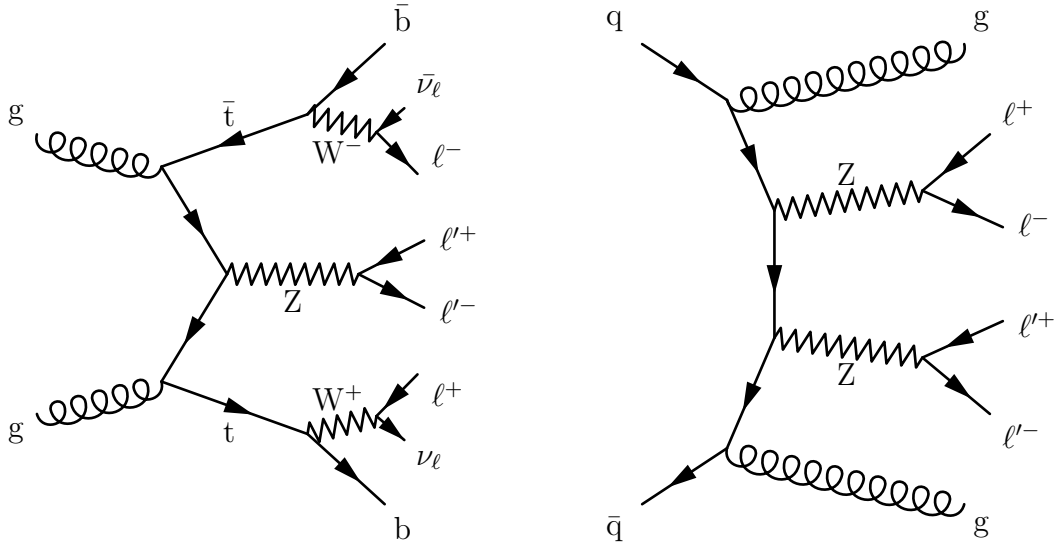

Figure 2.15: An example tree-level $t\bar{t}Z$ diagram (left), which is an irreducible background for inclusive $ZZ/Z\gamma^*$ production, and an example non-electroweak ZZjj diagram (right).

Chapter 3

The CMS Experiment and the CERN LHC

Production of controlled high-energy particle collisions, and detection of particles created in those collisions, are monumental technical challenges. The apparatus used to obtain the results presented in this thesis are the result of decades of work by thousands of scientists and engineers, making use of many techniques developed in the course of building and operating previous experiments. The LHC [109, 110] accelerates pairs of charged hadron (proton or lead ion) beams and collides them to provide a source of high energy particle interactions for several fully independent detectors, including CMS [111], which collected the data used in the studies presented here. Detailed descriptions of the LHC and CMS follow.

3.1 The CERN Large Hadron Collider

The LHC, the most powerful particle accelerator and collider ever built, is a 26.7 km circumference ring of superconducting magnets running through tunnels roughly

100 m below the suburbs and countryside near Geneva, Switzerland. It first produced collisions suitable for collecting physics data in 2010 before generating large datasets with beam energies of 3.5 TeV in 2011 and 4 TeV in 2012. Following a shutdown for upgrades and repairs, it operated in 2015 and 2016 to deliver beam energies of 6.5 TeV. Beams collide head-on so that the center-of-mass frame of the proton-proton system is the rest frame of the detectors, giving proton-proton center-of-mass energies of 7, 8, and 13 TeV respectively for collisions in 2010–2011, 2012, and 2015–2016. Each successive energy was the highest ever acheived in controlled hadron-hadron collisions, giving unprecedented access to extremely high-energy processes at every step.

In addition to increasing collision energies, the LHC increased its rate of collisions with each new machine configuration. The average event rate $\mathrm{d}N/\mathrm{d}t$ for a process with production cross section σ is determined by the instantaneous luminosity $\mathscr{L}$ of the collider,

$$\frac{\mathrm{d}N}{\mathrm{d}t} = \mathscr{L}\sigma \tag{3.1}$$

so a high instantaneous luminosity enables the observation of rare processes like Higgs boson production. The LHC's unprecedented luminosities have allowed collection of the largest physics datasets in history.

The desire for high luminosities drove the decision to collide protons with other protons instead of with antiprotons as was done at Tevatron, LHC's predecessor at Fermilab in Batavia, IL. Antiprotons simply cannot be produced in sufficient quantities for a collider on this scale. Tevatron was designed to study many processes that are $\mathrm{q\bar{q}}$-initiated, so it is useful to have valence antiquarks available in the collisions. The LHC was designed with Higgs boson production in mind, and the two most important Higgs production modes are proton/antiproton agnostic. Even for $\mathrm{q\bar{q}}$-initiated processes, valence antiquarks are less critical at the LHC because, for the

same center of mass energy, the effective $q\bar{q}$ luminosity is higher for proton-proton collisions at LHC energies than at Tevatron energies (1.98 TeV center-of-mass energy) as discussed in Section 1.6.

In addition to protons, the LHC can accelerate beams of lead nuclei to 2.51 TeV per nucleon, also the highest ever achieved. All studies presented in this thesis were performed on proton-proton collision data, rendering the details of so-called "heavy ion" beams beyond the scope of this document.

Beams are maintained and manipulated with magnets, most of them made of superconducting niobium-titanium (NbTi) windings cooled to 1.9 K by superfluid helium. Dipole magnets with fields up to 8.33 T bend the beam around the ring, interspersed with quadrupoles for focusing. More quadrupoles and higher-moment magnets keep the beams focused, squeeze them for collisions, and apply a number of corrections. Superconducting radio frequency (RF) cavities operating at 400 MHz accelerate the beam, maintain it at its final energy, and maintain bunch shape and spacing.

3.1.1 Accelerator Chain, Layout, and Detectors

The LHC was built in tunnels originally constructed for the Large Electron-Positron Collider (LEP), an e^+-e^- collider that operated from 1989 to 2000. Using existing caverns, tunnels, and infrastructure was a substantial cost-saving measure, but imposed several important constraints on the LHC's design. In LEP, the electron and positron beams could be accelerated in opposite directions by the same magnets, because they are oppositely charged. Conversely, proton beams require opposite magnetic fields for the two beams. Because the tunnels were not wide enough to accommodate two completely separate beam lines, most of the magnets in the LHC use a twin-bore design, shown schematically in Fig. 3.1, in which the pipes and windings for the two beams

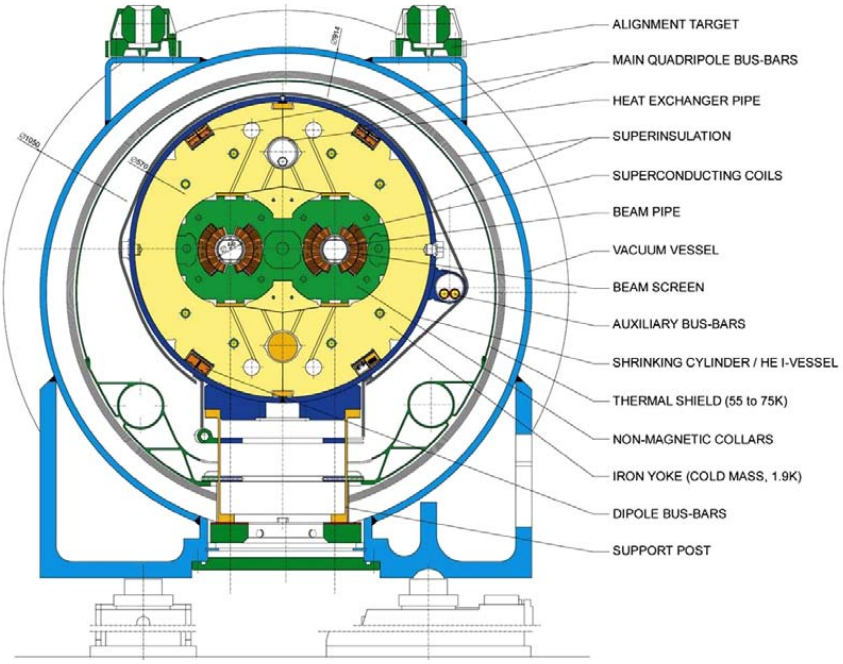

Figure 3.1: Schematic cross section of an LHC dipole and its attendent electrical and cryogenic infrastructure, reproduced from Ref. [109].

share a common cryogenic system. The electromagnetic, mechanical, and cryogenic coupling of the two beamlines represents a significant engineering challenge [109, 110].

Because no single accelerator has the dynamic range necessary to take a stationary proton to TeV-scale energies, a chain of smaller accelerators repurposed from previous experiments feeds moderate-energy protons into LHC. Protons are obtained by ionizing hydrogen atoms, then accelerated to 50 MeV by the Linac 2 linear accelerator and injected into the Proton Syncrotron Booster (PSB), the first of several circular accelerators. The PSB feeds 1.4 GeV protons into the Proton Synchrotron (PS), which in turn injects them into the Super Proton Synchrotron (SPS) at 26 GeV. The protons are then accelerated to 450 GeV in the SPS before being injected into LHC. A diagram of the entire accelerator chain is shown in Fig. 3.2.

The LHC ring is divided into eight sectors, each of which features a 528 m straight section connected to the adjacent sections by 2.45 km arcs. The straight section length

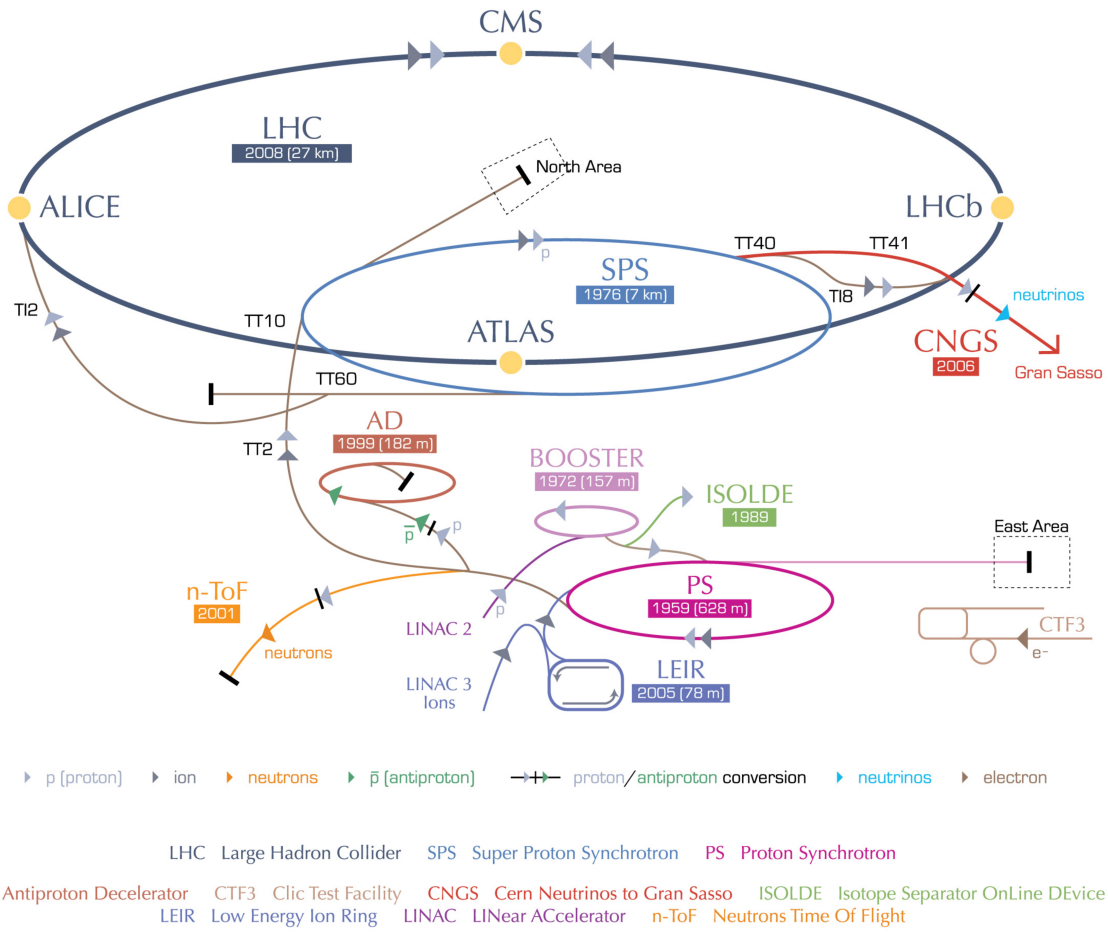

Figure 3.2: A schematic of the LHC accelerator chain and peripheral experiments, reproduced from Ref. [112].

was set by the need for RF cavities to accelerate LEP beams to counteract synchrotron radiation, which is a primary factor limiting electron and positron beam energy. This is not ideal for proton beams; protons' much higher mass means they radiate less and need fewer RF cavities. The straight sections feature access points numbered with Point 1 at the main CERN site in Meyrin, Switzerland, and the rest numbered 2–8, increasing in the clockwise direction when viewed from above. Points 1, 2, 5, and 8 have beam crossing points and host detectors to study the resulting proton-proton collisions. Points 3 and 7 feature collimators to reduce momentum and betatron nonuniformities in the beams. The RF cavities are at Point 4 and the beams are

dumped after use or in the event of a magnet quench at Point 6. Beams are disbursed and deflected into an 8 m long water-cooled graphite absorber by fast kicker magnets which activate in a 3 μs-long bunch-free region of the beam known as the abort gap.

The CMS detector is at Point 5 in Cessy, France, the furthest point on the ring from the Meyrin site and Point 1, which houses ATLAS [113], a similar but fully independent general-purpose particle detector. CMS and ATLAS use complementary detector technology so that any measurement or discovery by one can be made concurrently or verified by the other. The other two experimental insertions feature specialized detectors studying collisions at lower-luminosity beam interaction points. The LHCb detector [114], at Point 8, studies hadronic physics with an emphasis on b-hadrons, and ALICE [115] studies heavy ion collisions at Point 2. Three smaller experiments share interaction points with the larger detectors, with TOTEM [116] studying proton structure and the total proton-proton interaction cross section next to CMS; LHCf [117] studying the π^0 energy spectrum and multiplicity near ATLAS; and MoEDAL [118] searching for magnetic monopoles or other heavy, stable, ionizing particles at Point 8 with LHCb.

3.1.2 Operating Parameters

With the beam energy set by the radius of the ring and the strength of available magnets, the number of interesting physics events produced in LHC collisions depends only on the integrated luminosity

$$\mathscr{L}_{int} = \int \mathscr{L} \mathrm{d}t, \tag{3.2}$$

where $\mathscr{L}$ is the instantaneous luminosity defined in Eq. (3.1) and the integral runs over the time the machine spends in collisions mode. LHC's availability for collisions depends on the electrical and mechanical stability of the accelerators and their

support systems, including the cryogenics and the vacuum in the beam pipe. The instantaneous luminosity while running depends only on the beam parameters. For symmetric beams which each have n_b colliding gaussian bunches of intensity (i.e. number of protons in the bunch) N_b, orbiting the ring with frequency f_{rev} and relativistic factor $\gamma = E_p/m_p$, the instantaneous luminosity is given by

$$\mathscr{L} = f_{rev}\frac{n_b N_b^2 \gamma}{4\pi\beta^*\epsilon_N}R, \tag{3.3}$$

where β^* is the amplitude of the beams' betatron oscillations around the nominal ring path at the interaction point, the normalized emittance ϵ_N is a measure of the beams' spread in both position and momentum space, and R is a geometrical factor accounting for the beam crossing angle,

$$R = \sqrt{1 + \left(\frac{\theta_c \sigma_z}{2\sigma^*}\right)^2}. \tag{3.4}$$

Here θ_c is the beams' crossing angle, and σ_z and σ^* are respectively the longitudinal and transverse RMS widths of the bunches in the lab frame.

3.1.2.1 Design

The machine parameters in the LHC design specification can be seen in the first column of Table 3.1. Machine parameters during data taking have in general been quite different, due to both technological advances and technical challenges. In particular, beam energy and number of colliding bunches are both lower than designed due to commissioning issues with the magnets and their safety systems [119], but increases in the number of collisions per bunch crossing ("pileup") have more than compensated, leading to a peak instantaneous luminosity in 2016 that was more than 50% higher than designed. Operating parameters have changed frequently during data taking and upgrades are always ongoing.

Table 3.1: LHC beam parameters as designed and in practice. As stated in the text, n_b is the number of colliding bunches, N_b is the number of protons in each bunch, β^* is the betatron amplitude at the interaction point, ϵ_N is the normalized emittance, and $\mathscr{L}_{(int)}$ is the instantaneous (integrated) luminosity.

	Design	Run I			Run II	
Year		2010	2011	2012	2015	2016
Energy per beam (TeV)	7	3.5	3.5	4	6.5	6.5
Bunch spacing (ns)	25	150	50	50	25	25
n_b	2808	348	1331	1368	2232	2208
$N_b\,(10^{11})$	1.15	1.2	1.5	1.7	1.15	1.25
β^* (m)	0.55	3.5	1.0	0.6	0.8	0.4
ϵ_N (mm mrad)	3.75	2.2	2.3	2.5	3.5	3.0
Peak pileup		4	17	37	22	49
Peak $\mathscr{L}\,(10^{34}\mathrm{cm}^{-2}\mathrm{s}^{-1})$	1	0.02	0.35	0.77	0.52	1.53
$\mathscr{L}_{int}\left(\mathrm{fb}^{-1}\right)$		0.04	6.1	23.3	4.2	41.1

3.1.2.2 Run I

The LHC came online in 2010 with a beam energy of 3.5 TeV, which was increased to 4 TeV in 2012. Bunches were spaced 50 ns apart instead of 25 ns to allow full exploitation of excellent injection chain performance [120]. Beams exiting the SPS had bunch intensity as much as 50% higher than anticipated in the original LHC design and beam emittance as low as 67% of nominal. This allowed the LHC to achieve 77% of its design instantaneous luminosity in 2012 despite having roughly half as many bunches in each beam.

Machine availability was overall good considering the complexity and relative newness of the LHC, with about 36% of scheduled time spent in stable beams. In all, LHC delivered 6.1 fb^{-1} to CMS and ATLAS in 2011 and 23.3 fb^{-1} in 2012, enough to allow discovery of the Higgs boson. The integrated luminosity for each year of LHC operation is shown as a function of calendar month and day in Fig. 3.3.

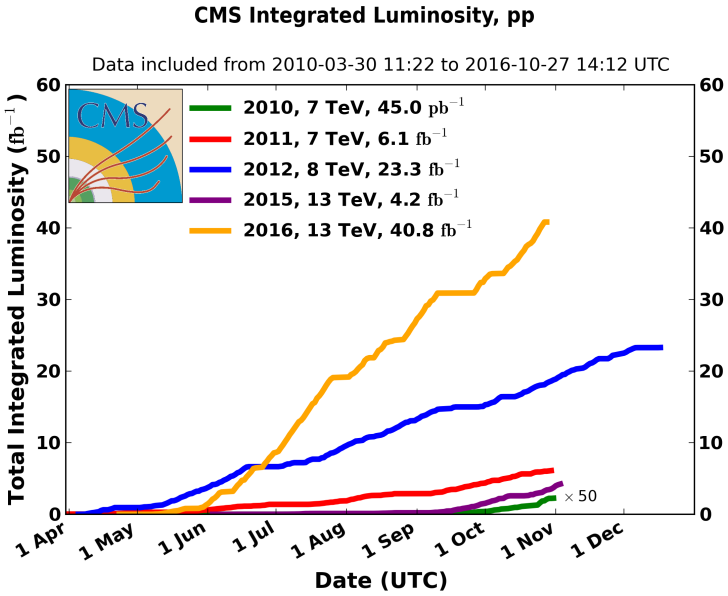

Figure 3.3: The integrated luminosity delivered to CMS in each year of LHC operation, shown as a function of the date within the year.

3.1.2.3 Run II

The LHC shut down for 2013 and 2014 to allow a number of repairs and upgrades, including measurements, repairs and upgrades on the electrical connections and cryogenic safety systems. Beam energies were increased to 6.5 TeV, close to the nominal 7 TeV. The bunch spacing was decreased to 25 ns while maintaining low emittance and high bunch intensity with the implementation of the beam compression merging and splitting (BCMS) scheme in which bunches are merged in the PS before they are split for injection into SPS, allowing higher bunch intensity [121]. This was offset by vacuum problems in the SPS beam dump, which limited the total number of colliding bunches to around 2200 [122]. Improvements in collimators and beam optics reduced β^* to 40 cm in 2016, lower than the design β^* of 55 cm. Overall instantaneous luminosities were substantially higher than originally designed.

Machine availability in Run II was excellent, with over 60% of planned time spent in stable beams [122]. The world's first 13 TeV collisions in 2015 were the subject of

a number of measurements and searches, though the $4.2\,\text{fb}^{-1}$ integrated luminosity delivered to Points 1 and 5 in 2015 was less than planned due to several mechanical issues. The integrated luminosity acheived in 2016, $41.1\,\text{fb}^{-1}$, was far above the roughly $25\,\text{fb}^{-1}$ expected and more than all previous runs combined, allowing measurements and searches of unprecedented sensitivity and reach, including those presented in this Thesis.

3.2 The Compact Muon Solenoid Detector

The CMS detector [111] is a general-purpose particle detector located in a cavern roughly 100 m below the surface at LHC Point 5. Though designed to do a wide range of physics analyses, CMS was designed specifically with Higgs boson discovery in mind. Primary design goals include

- High-efficiency reconstruction of charged particles with precise measurement of their trajectories and momenta
- Good electromagnetic energy resolution, including diphoton and dielectron mass resolution
- Hermetic calorimetry for good missing transverse energy and dijet mass resolution
- Good muon identification, momentum resolution (including dimuon mass resolution), and charge determination over a broad range of energies

To this end, CMS features a silicon tracker, a scintillating crystal electromagnetic calorimeter (ECAL), and a hermetic hadronic calorimeter (HCAL) inside a 3.8 T solenoid magnet surrounded by ionized gas muon tracking devices, all of which can

be seen as part of the whole detector in Fig. 3.4. Decisions on which events to read out are made on-line by a two-level trigger system. Descriptions of these systems follow.

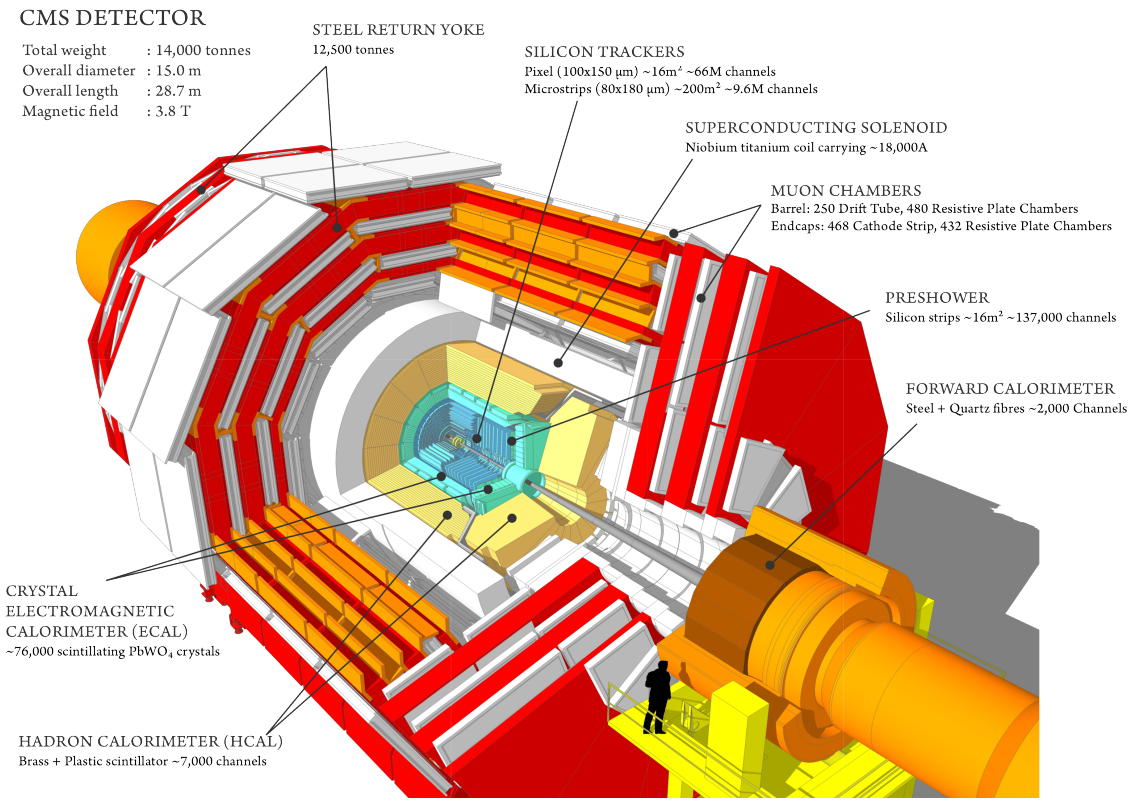

Figure 3.4: Cutout schematic of CMS with all major subdetectors, the beamline, the magnet, and the return yoke visible. Reproduced from Ref. [123].

3.2.1 Terminology and Geometry

The CMS detector systems are arranged in cylindrical layers with the interaction point at the center, serving as the origin for the coordinate system. The coordinate system is defined with the positive-x direction pointing toward the center of the ring, positive-y pointing vertically up, and positive-z pointing parallel to the beam in the counterclockise direction when the LHC ring is viewed from above. Particle

momenta are typically expressed in quasicylindrical coordinates $(p_{\mathrm{T}}, \eta, \phi)$. Here p_{T} is the magnitude of the particle's momentum transverse to the beam

$$p_{\mathrm{T}} \equiv \sqrt{p_x^2 + p_y^2}, \tag{3.5}$$

and ϕ is the azimuthal angle, i.e. the angle from the x-axis to the particle's trajectory in the x-y plane. The pseudorapidity η is defined as

$$\eta \equiv -\ln\left[\tan\left(\frac{\theta}{2}\right)\right] \tag{3.6}$$

where θ is the polar angle measured from the z-axis. The relativistic rapidity

$$y \equiv \frac{1}{2}\ln\left(\frac{E + p_z}{E - p_z}\right), \tag{3.7}$$

converges to the pseudorapidity in the limit of massless particles. Pseudorapidity is preferred to rapidity because it is purely geometrical, with no dependence on the particle energy. Both are preferred over θ because rapidity differences are invariant under longitudinal boosts, and because hadron flux at colliders is roughly constant as a function of rapidity. The transverse energy E_{T} is the the magnitude of the particle's four-momentum transverse to the beam, equal to p_{T} in the limit of massless particles. Spatial coordinates are expressed as (r, η, ϕ), where r is the distance from the beam in the x-y plane.

3.2.2 Magnet and Inner Tracking System

A particle of charge q moving through a uniform magnetic field of strength B that points in the z direction will travel in a helix of radius R, given by

$$R = \frac{p_{\mathrm{T}}}{|q|B}, \tag{3.8}$$

with the chirality of the helix determined by the sign of q. Thus one can determine the transverse momentum of the particle by measuring its path through the magnetic field

and finding the radius of curvature. In practice, all but the lowest-energy particles leave too short an arc in the detector for direct measurement of the radius, so the sagitta of the arc is used instead, given by

$$s = \frac{qBL^2}{8p_{\mathrm{T}}} \tag{3.9}$$

where L is the length of the chord spanning the arc (typically equal to the radius of the tracking system). The transverse momentum resolution varies as

$$\frac{\delta p_{\mathrm{T}}}{p_{\mathrm{T}}} \propto \frac{p_{\mathrm{T}}}{BL^2}, \tag{3.10}$$

so a strong field and a large tracking volume are vital to keeping measurements precise even at high energies.

To this end, CMS contains the world's largest superconducting magnet[1], a solenoid 13 m long and 6 m in diameter, which generates a nearly-uniform 3.8 T field in the centralmost part of the detector [124]. To measure the paths of charged particles in the field, the volume closest to the interaction point contains layers of silicon sensors that detect hits from charged particles with high efficiency and excellent position resolution, between 4.4 cm and 1.1 m from the beam for 2.7 m on either side of the interaction point. This system, called the inner tracker and shown schematically in Fig. 3.5, consists of an inner pixel detector surrounded by a larger silicon strip detector. Both consist of concentric cylinders of sensors covering the barrel of the detector capped by discs covering the high-η region, up to $|\eta| < 2.5$. With a total of roughly 200 m^2 of silicon, the inner tracker is the largest silicon tracker in the world. Tracks may be reconstructed with hits in as many as 14 layers. The downside of this is that the tracker and its mechanical support structure represent a substantial amount of material for electrons and photons to interact with before they reach the

[1]Largest in the sense of having the largest stored energy when at constant full field. The largest by size is the ATLAS barrel toroid.

calorimeters, with total material budget between 0.4 radiation lengths ($\eta = 0$) and 1.8 radiation lengths ($|\eta| \approx 1.4$), as shown in Fig. 3.6. The tracker-only p_{T} uncertainty is around 1.2% at 200 GeV and 15% at 1 TeV. Tracker readout is too slow for it to be used in the L1 trigger (see Section 3.2.6.1), the first set of trigger decisions must be made using only information from the calorimeters and outer muon system.

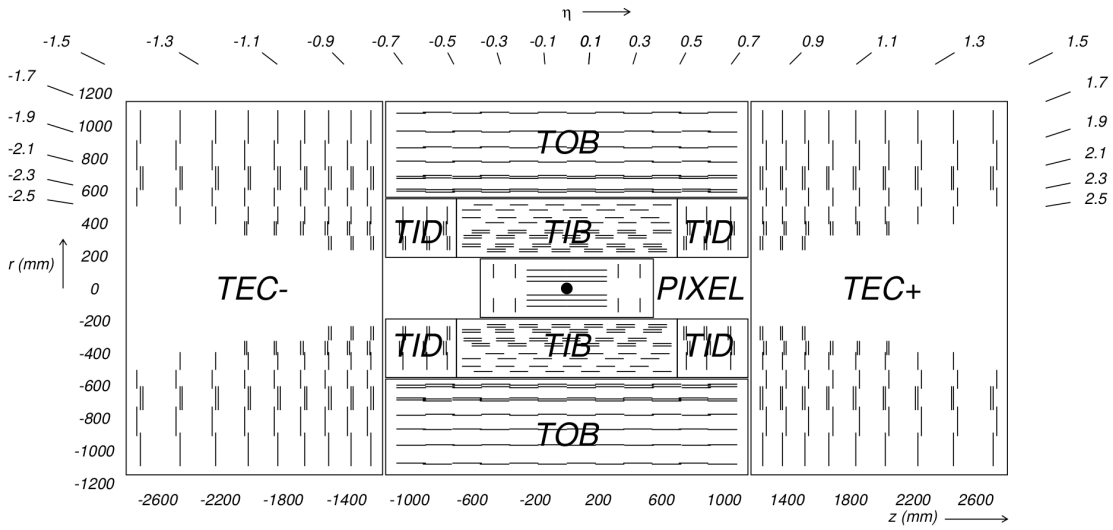

Figure 3.5: Diagram of the inner tracker layout, reproduced from Ref. [111].

As the system closest to the interaction point, the inner tracker is subject to extremely high radiation doses, equivalent to 840 kGy for the innermost pixel layer over an integrated luminosity of $500\,\mathrm{fb}^{-1}$, so radiation tolerance is a major design constraint for both the sensors and readout electronics [125]. Leakage currents in the sensors, which degrade sensor performace, increase linearly with radiation fluence and exponentially with temperature. Because leakage currents cause self-heating in the silicon, they can create a dangerous positive thermal feedback loop if the sensors are not cooled below -10° C during operation. Reverse annealing, a process by which radiation-induced defects in the silicon can cause further damage months after the radiation dose is received, can be mitigated by keeping the sensors below 0° C at all times except for brief maintenance periods [111]. Therefore, to improve tracker

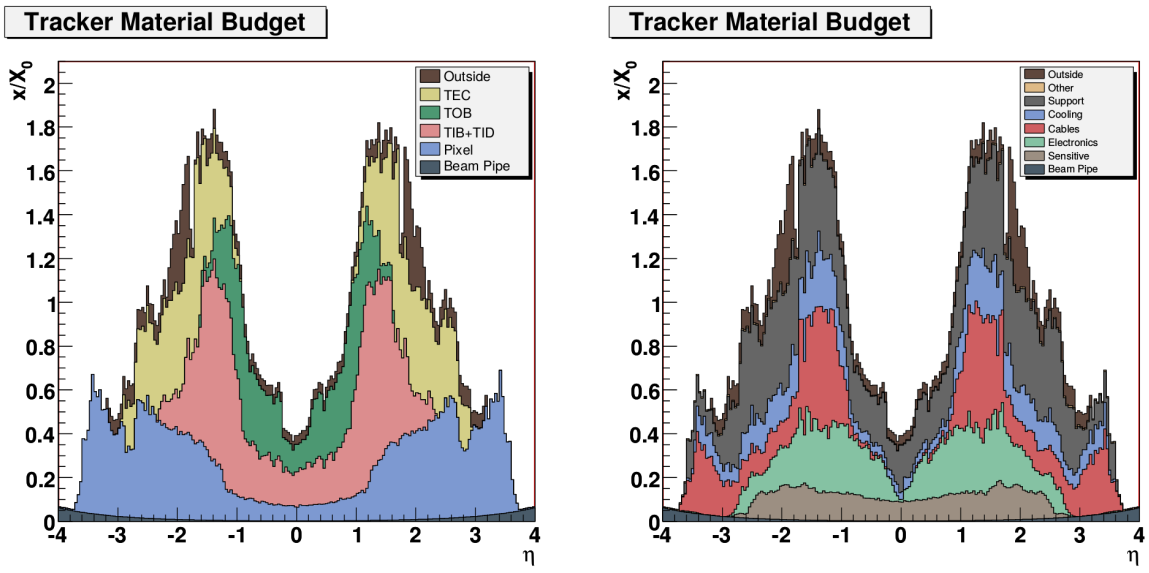

Figure 3.6: Total tracker material budget in units of electromagnetic radiation lengths, as a function of pseudorapidity. At (left) the total is divided by detector subsystem, at (right) by the function of the material. Reproduced from Ref. [111].

performance and increase the detectors' lifetimes, a gas cooling system is used to keep the strip tracker around -15° C and the pixel detector around -20° C during operation.

3.2.2.1 Pixel Detector

The pixel detector [125], consisting of three layers in the barrel and two in the endcap, is responsible for accurate reconstruction of primary proton-proton interaction vertices and secondary vertices from decays of b-hadrons or other long-lived particles, as well as providing "seed" tracks that may be used in strip tracker reconstruction. As the system closest to the interaction point, the pixel system experiences the highest charged-particle flux and therefore must have extremely fine granularity to differentiate between nearby particles. The 66 million pixels in the system have a cell size of $100 \times 150\,\mu\text{m}^2$. Interpolation of the analog signals from the individual pixels allows a final spatial resolution of $15\,\mu$m in each direction. The outermost barrel layer is

10.2 cm from the beam, and the second endcap disk is 46.5 cm from the interaction point. The sensor modules are arranged such that at least three sensors cover the solid angle within the pixel detector's acceptance.

3.2.2.2 Strip Tracker

Outside the pixels is the silicon strip tracker [125], extending out to 1.1 m in the r direction and ± 2.8 m in the z direction. The tracker is divided into inner and outer subdetectors, each of which has both barrel cylinders and endcap discs. In total, there are ten layers in the barrel and nine in each of the endcaps. The inner tracker uses 320 μm-thick sensors with a typical strip cell size of 10 cm $\times$ 80 μm, leading to hit resolutions of 23–35 μm. The outer tracker uses 500 μm-thick sensors with typical strip sizes up to 25 cm $\times$ 180 μm, leading to hit resolutions of 35–53 μm.

3.2.3 Electromagnetic Calorimeter

Outside of the tracker is the electromagnetic calorimeter (ECAL), which is designed to absorb and measure the energy of electrons and photons. ECAL is made of 68,524 radiation tolerant lead tungstate ($PbWO_4$) crystals arranged in a cylindrical barrel (EB) covering $|\eta| < 1.444$ and two endcap discs (EE) covering $1.566 < |\eta| < 3.0$. The geometry of the ECAL barrel and endcap can be seen in Fig. 3.7; the small gap between the barrel and endcap is necessary to accommodate cabling and support structures for the tracker. $PbWO_4$ crystals scintillate blue-green light and are optically transparent, so the resulting light can be read out by avalanche photodiodes (APDs) in the barrel and vacuum phototriodes (VPTs) in the endcap. ECAL's granularity is set by $PbWO_4$'s small Molière radius of 2.2 cm, which is also the size of the square front faces of the barrel crystals, which flare out to 2.6 cm at the back, giving

them a truncated pyramid shape covering a roughy 0.0174×0.174 area of η-ϕ space. The endcap crystals go from 2.86 cm squares at the front to 3.0 cm at the back.

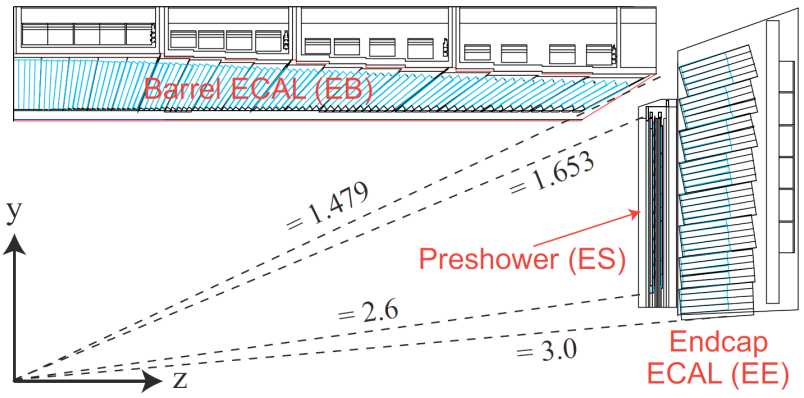

Figure 3.7: Diagram of ECAL geometry, reproduced from Ref. [126].

One of the primary design innovations of CMS—the eponymous compactness—was to place the calorimetry inside the magnet so that tracks can be unambiguously associated with energy deposits in the calorimeters without interference from scattering in the magnet coils. This is possible in part thanks to the high density ($8.28\,\mathrm{g/cm^3}$) and short radiation length (0.89 cm) of $PbWO_4$, which allow ECAL crystals to be only 23 cm long in the barrel and 22 cm long in the endcap while still spanning 25.8 and 24.7 radiation lengths, respectively. This is enough to ensure that few electrons or photons escape ECAL with any appreciable remaining energy.

The total scintillation light yield is relatively low, averaging just 4.5 photons per MeV deposited. This is partially compensated by the fact that virtually all of ECAL is active material and no energy is lost to uninstrumented absorbers, but Poisson fluctuations in the yield are still the largest contribution to ECAL energy resolution for most electron and photon energies. This statistical uncertainty is represented by the first term in the full resolution equation,

$$\left(\frac{\delta E}{E}\right)^2 = \left(\frac{2.8\%}{\sqrt{E/\mathrm{GeV}}}\right)^2 + \left(\frac{0.12}{E/\mathrm{GeV}}\right)^2 + (0.30\%)^2\,. \tag{3.11}$$

The second term comes from electronic noise and noise from pileup, and the last term represents intrinsic differences between crystals. The upside to $PbWO_4$'s scintillation is that it is fast: roughly 80% of the light is emitted in the 25 ns between bunch crossings, so energy measurements require integration over only a few bunch crossings.

3.2.4 Hadronic Calorimeter

Between ECAL and the magnet is the hadronic calorimeter (HCAL), responsible for measuring the energy of hadronic jets. HCAL is a sampling calorimeter, meaning that the hadrons pass through dense, uninstrumented material and the products of the resulting interactions deposit energy in scintillators which are used to measure the total energy of the original incoming particles. The HCAL barrel (HB, $|\eta| < 1.305$) and endcap (HE, $1.305 < |\eta| < 3.0$) are made of layers of brass absorber interleaved with plastic scintillating tiles. The energy resolution in HB and HE is given by

$$\left(\frac{\delta E}{E}\right)^2 = \left(\frac{90\%}{\sqrt{E/\mathrm{GeV}}}\right)^2 + (4.5\%)^2 . \tag{3.12}$$

The first term is from the stochastic evolution of hadronic showers in the absorber, the second is from calibration uncertainties.

The geometry of HB, HE, and HO is shown in Fig. 3.8. The thickness of HB and HE is constrained by the size of the magnet, varying from 5.4 nuclear interaction lengths in the central barrel to more than 10 in the endcaps. Because HB is not thick enough to absorb all hadrons in the barrel, there is an extra outer HCAL component (HO) outside of the magnet, consisting of two more layers of scintillator on either side of a 20 cm-thick iron "tail catcher" covering $|\eta| < 1.3$. With HO and the 1.1 interaction lengths in ECAL considered, no part of the calorimeter system spans fewer than 11.8 interaction lengths except in the gaps between barrel and endcap, minimizing the flux of hadronic "punchthrough" interacting with the muon system.

The total material budget in front of the layers of the muons systems is shown in Fig. 3.9.

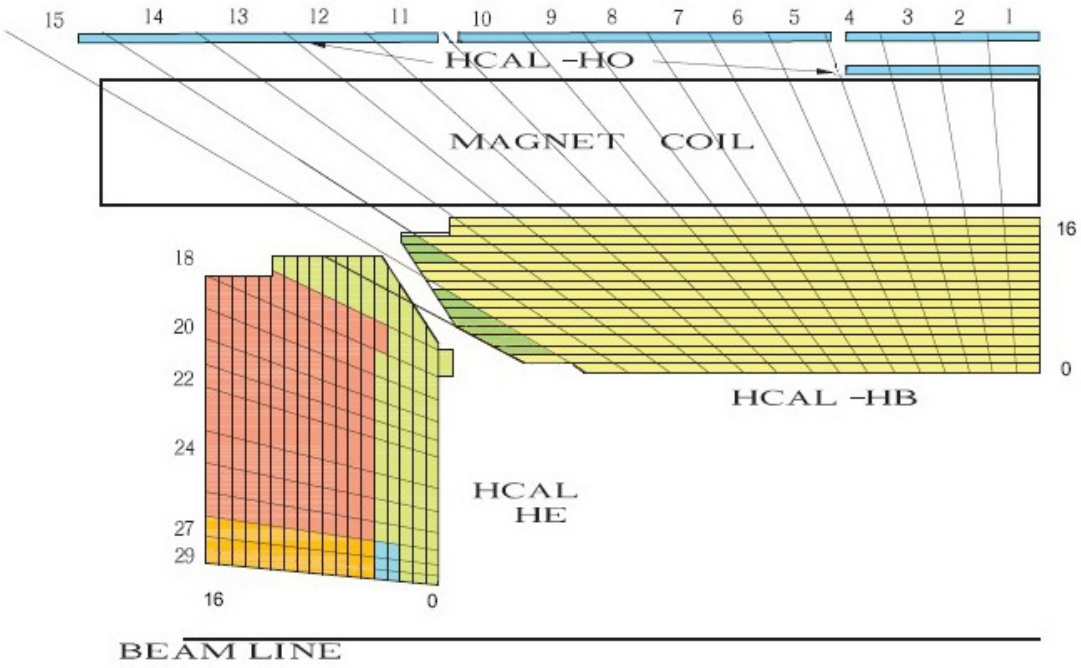

Figure 3.8: Diagram of HCAL geometry, reproduced from Ref. [111].

Closer to the beam line on each side, the forward hadronic calorimeter (HF, $3.0 < |\eta| < 5.2$) is made of iron and quartz fibers instead of brass and plastic scintillator to maximize radiation hardness. It acts as a Cherenkov detector with the quatz fibers as the active detection element. Half the fibers extend the entire depth of HF, while the other half start after the hadrons have traversed 22 cm of iron, allowing some differentiation between electromagnetic and hadronic energy. The energy resolution in HF is given by

$$\left(\frac{\delta E}{E}\right)^2 = \left(\frac{172\%}{\sqrt{E/\mathrm{GeV}}}\right)^2 + (9\%)^2\,, \tag{3.13}$$

where the terms have the same physical interpretation as those in Eq. (3.12). HF improves CMS's missing energy resolution by roughly a factor of three.

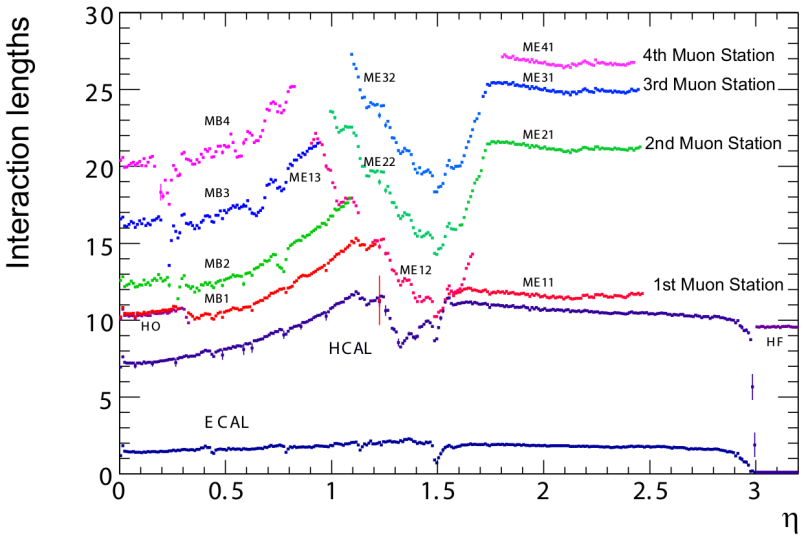

Figure 3.9: Total material budget in units of nuclear interaction lengths, as a function of pseudorapidity, reproduced from Ref. [111].

3.2.5 Muon Spectrometer

Many of the most interesting physics processes at the LHC involve high energy muons, so muon identification, triggering, and momentum measurement are important design goals. Muons leave very little energy in the calorimeters, so ECAL and HCAL cannot be used for triggering and identification as they are for electrons, photons and hadrons, or to improve momentum measurements of high-p_{T} muons whose tracks are too straight to allow good measurements of their curvature. Instead, these functions are provided for muons by three gas-based systems surrounding the rest of the detector [127, 128]. In all three, ionizing gas chambers provide hits which form a track. The magnetic field for this is provided by the return yoke, a set of steel plates interleaved with the muon chambers which confine the solenoid's magnetic return field. The yoke plates weigh a total of $10,000\,\mathrm{t}$ and are fully saturated by the solenoid.

Unlike the inner tracker, the muon systems can be read out fast enough to provide triggering. Because muons above $3\,\mathrm{GeV}$ generally traverse the muon system while most other measurable particles are stopped in the calorimeters, magnets, or return

yoke, the muon system provides high efficiency, low-background muon identification. The muon system's momentum measurements are not competitive with the inner tracker's at low p_{T}, but a combined fit of the inner track and the muon system ("standalone") track improves muon p_{T} resolution above roughtly 200 GeV. The geometry of all three muon systems and the return yoke can be seen in Fig. 3.10.

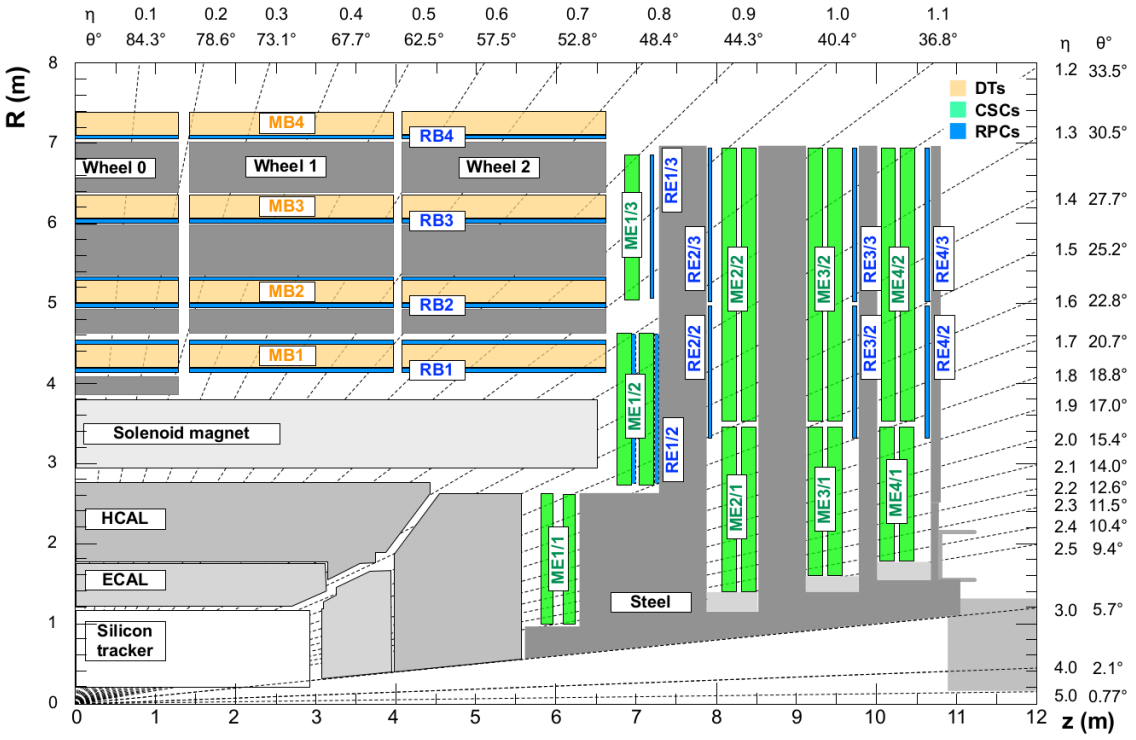

Figure 3.10: Diagram of muon system and return yoke geometry, reproduced from Ref. [128]. The magnet, calorimeters, and inner tracker are also visible.

3.2.5.1 Drift Tubes

In the barrel ($|\eta| < 1.2$), drift tube (DT) chambers are arranged in four "stations" separated by the steel layers of the yoke. Stations are made of two or three superlayers (SLs) of four layers of rectangular drift cells. Adjacent layers are staggered latterally by half a drift cell width to avoid gaps. Each station has two SLs with wires running parallel to the beam to measure muon tracks in the r-ϕ plane, separated by an

aluminum honeycomb lattice to provide mechanical rigidity and act as a spacer. The inner three stations contain an extra SL on the outer side of the spacer with wires perpendicular to the beam line, to measure muon position along the z-axis.

Each drift cell contains a roughly 2.4 m-long wire in gas (85% Ar, 15% CO_2). The electric field in the cell is proveded by aluminum tape glued to the top and bottom of the cell and held at +1.8 kV relative to the grounded aluminum plates above and below. Aluminum tape cathodes on the side of the cell are held at −1.2 kV, while the wires act as +3.6 kV anodes. The width of each cell perpendicular to muon motion, 42 mm, was chosen for a maximum drift time of 380 ns, sufficient to obviate the need for double-hit readout logic in this low-occupancy region of the detector. The height of 13 mm set by mechanical and space constraints. Track timing resolution in each SL is a few nanoseconds when all cells are allowed to read out all deposited charge. The r-ϕ position resolution available for online use in the trigger is about 1.5 mm in each SL; offline, for a single wire it is roughly 250 μm, leading to an overall offline resolution of 100 μm at each station.

3.2.5.2 Cathode Strip Chambers

Muons with $1.2 < |\eta| < 2.4$ are detected by the cathode strip chambers (CSCs).[2] The CSC system's trapezoidal chambers are arranged on discs interleaved with the endcap yoke in four layers. Chambers close to the beamline each cover 20° sections in ϕ while outer chambers cover 10° sections, with overlap to avoid gaps.

A CSC chamber is made of seven panels sandwiched together to make six gaps filled with a gas mixture (40% Ar, 50% CO_2, 10% CF_4). Six of the plates have cathode strips milled into one side, varying in pitch from 8.4 mm at the narrow end of the trapezoid to 16 mm at the wide end, with 0.5 mm gaps between strips. Three panels

[2]Where the CSCs and DTs overlap ($0.9 < |\eta| < 1.2$), tracks are formed from hits in both.

are wrapped with anode wires, alternating with the other panels so that every gas gap has a plane of wires. Wires are spaced 3.2 mm apart and run azimuthally around the detector, except for the innermost chamber closest to the interaction point, which are inside the magnet and must have their wires tilted 29° so that charge collected by the wires moves parallel to them despite the Lorentz forces from the solenoid.

A typical muon will deposit charge in 3–4 cathode strips and a similar number of anode wires per gas gap, allowing hit position to be interpolated using all these signals as well as timing information. The single-plane spatial resolution can be as good as 80 μm but depends strongly on where in the width of the strip the muon hits. The strips in alternating planes are therefore offset by half their width. Measurements from all six gas gaps in a chamber are combined into a segment with position resolution in the 30–80 μm range, which depends on the chamber but not where in the chamber the muon hit.

Anodes and cathodes are held 3.6 kV from each other, leading to a drift time of roughly 300 ns. Single anode planes have an RMS timing resolution of around 11 ns, insufficient for assigning a hit unambiguously to an individual bunch crossing, as required for triggering. However, information from all six anode planes in a chamber can be combined to yield a segment timing resolution around 5 ns. Segments are therefore the unit of information sent to the trigger. Segment position resolution at trigger level is 1–2 mm.

3.2.5.3 Resistive Plate Chambers

To provide a redundant set of muon momentum measurements, as well as precise timing of muon hits, CMS has six layers of resistive plate chambers (RPCs) in the barrel and four in the endcap up to $|\eta| < 1.6$. RPC chambers consist of two thin layers of intert gas (95.2% $C_2H_2F_4$, 4.5% C_4H_{10}, 0.3% SF_6) each between a pair of

Bakelite electrodes held at 9.3 kV. The two "gas gaps" are placed on either side of a plane of copper strips. When a passing muon ionizes the gas, the high voltage causes a fast electron avalanche read out by the strips. The narrow gap allows the RPCs to have single-hit timing resolution around 1 ns, but the spatial resolution is limited to about 1 cm by the size of the readout strips. The DTs and CSCs both have better momentum resolution than the RPCs, but RPCs are a simple, robust auxiliary system and the timing resolution can be used in conjunction with the other systems to improve overall muon measurements. The gaps between RPC chambers do not align with the gaps in the other outer muon systems, increasing the muon spectrometer's geometrical acceptance.

3.2.6 Data Acquisition and Trigger

With a bunch crossing rate of 40 MHz and over 40 collisions possible in each crossing, the collision rate can exceed 1.6 GHz. Event sizes on disk of 1–2 MB mean that the raw data generation rate of CMS is around 40 TB/ s, which could potentially be several PB/s with full reconstruction, substantially more than can be read out, stored or analyzed with current technology. However, most events consist only of low-energy, well-understood QCD interactions, so the data rate can be drastically reduced by reading out and storing only events likely to have interesting physics content. CMS reduces the event rate with a two-level trigger system.

The level-1 (L1) trigger uses custom hardware operating on trigger primitives (TPs) containing lower-granularity detector information to reduce the event rate to 100 kHz or less. The inner tracker's readout is too slow for use in the trigger, so only the calorimeters and muon systems generate TPs. Events accepted at level-1 are fully read out, digitized, and sent to the high level trigger (HLT), where they are partially reconstructed in software and filtered further, reducing the final rate of stored events

to roughly 1 kHz.

3.2.6.1 Level-1 Trigger

LHC beams collide at too high a rate for trigger decisions to be made in software, so the L1 trigger is instead implemented in custom hardware, with processing done using field-programmable gate arrays (FPGAs) as much as possible for flexibility, and application-specific integrated circuits (ASICs) where required. Hardware limitations of other CMS subsystems—in particular, the inner tracker's readout speed and buffer capacity—impose strict constraints on the system. The rate of events passing at level-1 cannot exceed 100 kHz and the system's overall latency cannot exceed roughly 4.2 μs from the proton-proton interaction to data storage at level-1. These goals are achieved while maintaining high efficiency for interesting physics events by using low-granularity detector information, to reduce the bandwidth needed within the trigger system. Information flows through several processing steps, with the data throughput reduced at each step. Calorimeter and muon information are processed in parallel and combined only in the final step. Optical links between systems provide high-bandwidth data transfer and allow flexibility in the overall trigger architecture. The calorimeter trigger was upgraded with respect to the Run I configuration in 2015, and the whole trigger system was overhauled in 2016 [129]. Both configurations will be described here.

Calorimeter information is compressed into TPs for use in the trigger by trigger primitive generators (TPGs). Each TP represents a "tower" consisting of a 5×5 cluster of barrel or endcap ECAL crystals and the HCAL tower behind them, or a section of the HF. The TP contains an 8-bit transverse energy sum and a quality bit for each calorimeter, and six bits of error checking and bookkeeping information. In 2015, TPs were sent to the Regional Calorimeter Trigger (RCT) [130], which processed

18 portions of the detector (segmented in ϕ with $+\eta$ and $-\eta$ treated separately) in parallel in separate crates of electronics, using several ASICs and one FPGA in each crate for processing [131]. Each RCT crate summed the TPs with $|\eta| < 3.0$ into 4×4 tower regions, and found isolated and non-isolated 2×1 tower e/γ and τ candidates. These objects were sent to Stage 1 Layer 2, which selected the best e/γ and τ candidates from the entire detector, clustered regions into 3×3 region jet candidates, and computed global quantities like missing transverse energy and the scalar sum of transverse momentum for all particles in the event. Pileup subtraction was performed with a lookup table (LUT) based on the number of regions in the detector with no energy.

In 2016, the whole calorimeter trigger was replaced with a new two-tiered system. Stage 2 Layer 1 ("CaloL1") consists of 18 FPGA-based Calorimeter Trigger Processor 7 (CTP7) cards [132], which calibrate and reformat the TPs before forwarding them to Stage 2 Layer 2 ("CaloL2") [131], an FPGA-based time-multiplexed system which finds e/γ, τ, and jet candidates and computes global quantities for whole events in parallel using tower-level information.

In 2015, the DTs and CSCs fed track segments into track finders (DTTF [133] and CSCTF [134]) which used pattern recognition algorithms to reconstruct tracks and measure their p_{T}, sharing information between the track finders to avoid inefficiency in the overlap region. The RPCs made their own tracks. Since the 2016 upgrade, track finding has been done by geometrical region of the detector rather than detector subsystem alone, with separate track finders for the barrel (BMTF, $|\eta| < 0.85$) using DT and RPC information [135], the endcap (EMTF, $1.25 < |\eta| < 2.4$) using CSC and RPC information [129], and the overlap region (OMTF, $0.85 < |\eta| < 1.25$) using all three muon systems [136]. The track finders feed into the Global Muon Trigger (GMT, upgraded to μGMT in 2016) [137, 138], which merges and sorts tracks, analyzes their

quality and selects the best ones.

The calorimeter and muon trigger systems, which have up to this point worked entirely in parallel, both send their selected candidates and global quantities to the Global Trigger (GT, upgrated to μGT) [139, 140]. The Global Trigger contains the trigger menu, the configurable set of algorithms used to determine whether an event is accepted or not. These algorithms can use combinations of the objects from the calorimeter and muon trigger systems, including imposing topological requirements, e.g. requiring a large $\Delta\eta$ between muons in a pair. The final decision is a logical OR of all triggers in the menu, but each trigger may be prescaled, i.e. only included in the final decision a fraction of the time in order to reduce its rate. When an event is accepted, a level 1 accept (L1A) signal is sent to all CMS subsystems instructing them to read out information collected in the accepted event, which is stored in buffers until it can be read out or safely discarded. A diagram of the whole 2016 L1 trigger system and its information flow is shown in Fig. 3.11.

3.2.6.2 High-Level Trigger

After an accepted event is read out and digitized, it must undergo another level of screening before being stored. The High Level Trigger (HLT) uses full detector information reconstructed with versions of the normal CMS reconstruction algorithms specially optimized for speed, running on a large farm of commercial computers [141]. Much of HLT's power comes from having tracker information, allowing more precise momentum measurements, isolation calculations and identification algorithms than are available at L1. For example, the pixels can be used to reconstruct vertices and tag b-quark jets, and requirements can be placed on the invariant mass of a lepton pair. However, track reconstructions is slow, so it is typically only done as one of the last steps in the filtering process, allowing the event to be rejected based on more

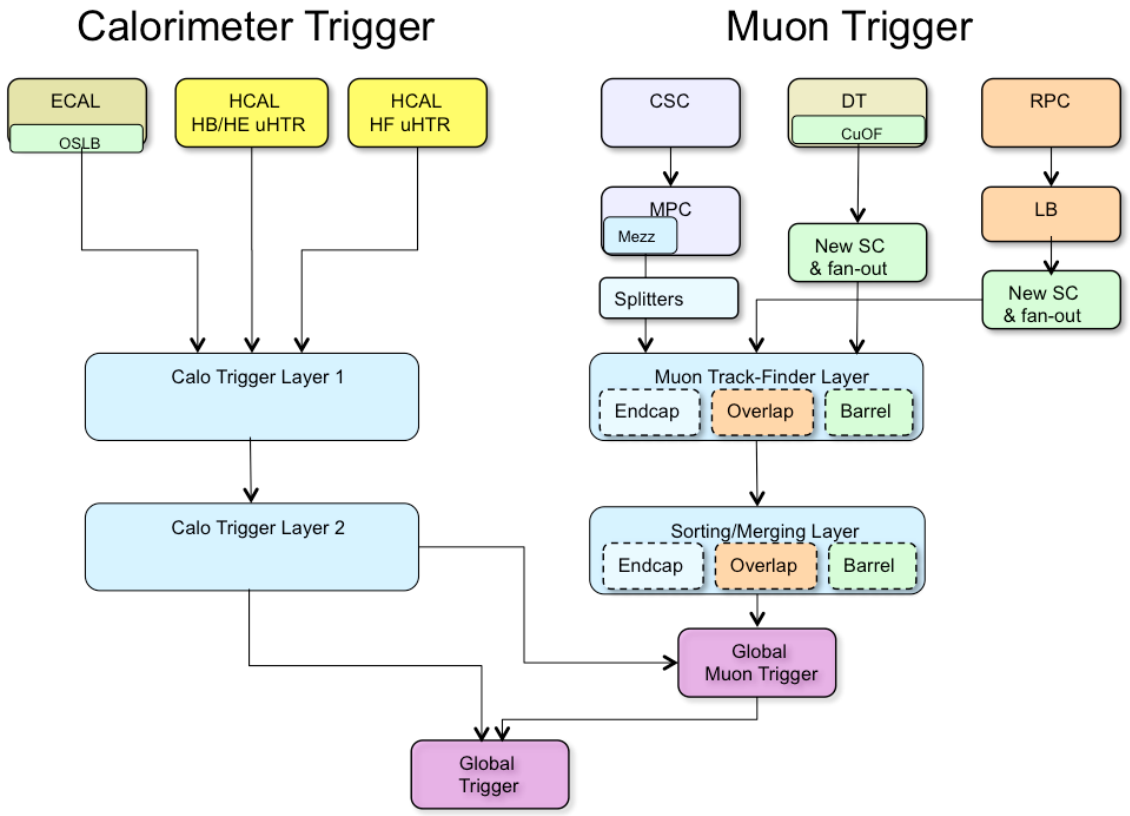

Figure 3.11: Data flow diagram for the CMS L1 trigger after the 2016 overhaul, reproduced from Ref. [129].

easily reconstructed objects like tracks in the muon system. Other optimizations include only reconstructing tracks near objects passed in by the L1 Global Trigger. The final result is that the rate of events saved for later analysis is around 1 kHz.

3.2.7 Luminosity Determination

A precise measurement of the luminosity delivered by the LHC is critical to precisely measuring any cross section. The instantaneous luminosity for n_b colliding bunch pairs with intensity N_b and orbit frequency f_{rev} is given by

$$\mathscr{L} = \frac{n_b N_b^2 f_{rev}}{A_{\text{eff}}} \tag{3.14}$$

where A_{eff} is the effective area of the beam-beam overlap. If beam i has a gaussian density profile in the u direction of width $\sigma_{i,u}$, and the beam densities are uncorrelated in each direction, then

$$A_{\text{eff}} = 2\pi\sqrt{\sigma_{1,x}^2 + \sigma_{2,x}^2}\sqrt{\sigma_{1,y}^2 + \sigma_{2,y}^2}. \tag{3.15}$$

The beam widths $\sigma_{i,u}$, the only unknowns in Eq. (3.14), are purely geometrical and can be found with the Van de Meer (VdM) scan method [142, 143]. In a VdM scan, for which LHC has a special run mode, one beam is held fixed while the position of the other is scanned in the x-y plane, and detector activity is measured as a function of beam displacement. Because the width of the interaction rate distribution is independent of its overall normalization, the detector activity metric may be any quantity linearly proportional to the interaction rate.

Over the course of an LHC run, n_b, N_b, and A_{eff} are all subject to change, and in fact the VdM scans are performed regularly, so in practice the procedure outlined above provides a calibration and overall scale for luminosity measurements during physics collisions. For a given detector metric labeled Q with rate R^Q that peaked at R_0^Q with no beam displacement, the VdM scan yields a visible cross section, the constant of proportionality between the rate and the instantaneous luminosity,

$$\sigma_{\text{vis}}^Q \equiv \frac{R^Q}{\mathscr{L}} = \frac{A_{\text{eff}} R_0^Q}{f_{rev}}. \tag{3.16}$$

CMS has several such metrics; the primary one used for measuring integrated luminosity is the number of pixel hit clusters [144, 145]. The instantaneous luminosity is given by

$$\mathscr{L} = \frac{\langle N_c \rangle f_{rev}}{\sigma_{\text{vis}}^{\text{PCC}}} = \frac{\langle N_c \rangle f_{rev}}{A_{\text{eff}} \langle N_c \rangle_0} \tag{3.17}$$

where $\langle N_c \rangle = R^{\text{PCC}}/f_{rev}$ is the average number of pixel hit clusters at each bunch crossing and $\langle N_c \rangle_0$ is its peak value during the VdM scan.

A number of complications must be accounted for or included in systematic uncertainty estimates. Beam-beam interation effects, correlations between the proton density distributions in the x and y directions, drifts in the beam orbit, and normalization uncertainties on the bunch intensity and absolute distance scale from the beam spot must all be handled with care. The result is a total integrated luminosity uncertainty of 2.3% in 2015 [144] and 2.5% in 2016 [145].

Chapter 4

Simulation

Comparing data collected by CMS to theoretical predictions is a complex task. The theories described in Chapter 1 are understood in great detail, but using this knowledge to calculate observables is a nontrivial enterprise. Once calculated, observables must be compared to data from a detector with finite resolution and subject to a number of experimental effects that do not exist in the rarefied world of quantum field theory. The general strategy is to employ numerical simulations of individual collision events that involve a physics process of interest, and apply accurate simulations of the detector's response to these events to obtain samples that are directly comparable to data. The success of all steps in this process at a high-luminosity hadron collider is one of the triumphs of the LHC era, with many observables in interesting processes simulated accurately to the level of a few percent.

4.1 Monte Carlo Event Generation

Even in trivial cases, it would be impossible to integrate over the phase space of hard scattering outcomes determined from theory, convolved with matter interactions, de-

tector effects, and other experimental factors, to calculate observables analytically. Particle interactions are well-understood on a microscopic scale, but it is extremely difficult to extrapolate from this first-principles understanding to a description of the macroscopic behavior of an ensemble of particles as needed to make predictions about fundamentally stochastic processes. Observable spectra are therefore modeled with the Monte Carlo (MC) method [11, 146], a numerical integration technique so named because, like a casino, it relies heavily on random numbers[1]. The scattering amplitudes for a process are calculated from theory at a chosen perturbative order [148], and for each simulated event a configuration of final state particles is selected at random from this phase space. The final state particles are propagated through decays, radiation, hadronization, and interaction with other matter—such as the detector—based on well-understood physics principles, and the outcome of any stochastic process is chosen at random from a realistic set or distribution of possibilities. In the limit of a large number of simulated events, the distributions from the simulated detector will converge to be directly comparable to aggregated data. Individual steps in this process are detailed in the following sections.

4.1.1 Matrix Element and Hard Process Generation

Event generator programs start by calculating the scattering amplitudes for a process at a chosen order in perturbation theory. For example, the generator MadGraph5_aMC@NLO [149] generates all the relevant Feynman diagrams up to NLO and calculates the matrix elements for them. Others, like POWHEG [150–152], SHERPA [153] and MCFM [53, 54, 154], are not fully general but have a broad range of physics processes implemented at NLO; SHERPA and MCFM can do some calculations

[1]Pseudorandom numbers are actually used, but there is no difference in practice as long as a good pseudorandom number generator (PRNG) is chosen and seeded properly. The Mersenne Twister algorithm [147] is the modern standard among general-purpose PRNGs in physics and elsewhere.

at NNLO [155]. Events are generated across the entire allowed phase space, either uniformly or with the specific distribution dictated by one of several "importance sampling" techniques [11, 156] which ensure appropriate statistical coverage in regions where the distribution has a large slope or value. Each event is assigned a weight $w \in (0, 1)$ based on the scattering amplitude in that region of phase space and the probability of having an appropriate initial state based on the PDFs discussed in Section 1.6. The sample is then "unweighted" to a subset that is directly comparable to data by removing events with a probability proportional to $1 - w$.

4.1.2 Parton Shower, Hadronization, and Underlying Event

Processes generated beyond leading order may have extra radiation, as in the real emission diagrams of Fig. 2.2. In the case of calculations at higher orders in QCD, the emissions are quarks and gluons which fragment, hadronize, decay, etc. This process is handled by a parton shower (PS) MC program such as PYTHIA8 [59] (used for most simulations used in this analysis), HERWIG [157, 158], or SHERPA [153]. In PYTHIA8, parton showering is simulated with the Lund string model [11, 159–161], which treats gluons as strings connecting color charged particles whose tension increases as the quarks move apart. When a string stretches too far, it breaks, producing a quark pair at the new string ends.

Parton shower programs also handle radiation of soft gluons from color charged particles and photons from electrically charged particles [162]. The emitter may be an incoming parton (initial state radiation, ISR), a virtual particle exchanged during the interaction, or an outgoing particle (final state radiation, FSR). The distinction between "soft" radiation that should be handled by the PSMC and "hard" emission present in the matrix element is not well defined, so it is important to avoid double-counting regions of phase space at the boundary between the processes. This is done

with jet matching [11, 149]. At tree level, matching may be achieved by enforcing a jet energy cutoff: partons from the matrix element must have energy $E > E_{\text{cut}}$, and the PSMC is responsible for any softer radiation. At NLO, loop diagrams carry divergences that must be canceled by divergences of opposite sign in the infrared radiation regime, which the cutoff would prevent, so a more sophisticated scheme must be used which weights some events negatively to handle destructive interference [149] or modifies the shower development algorithm [150, 151].

When combining showered samples that have different jet multiplicities at the hard process level, the task becomes even more difficult because the phase space of events with n jets in the matrix element that gain another from the PS overlaps with the phase space of events with $n + 1$ jets at matrix element level. This problem can be solved with one of several jet merging algorithms [149, 163–165]. The MLM [166] and CKKW [167] algorithms implement merging for tree-level diagrams of different jet multiplicities by cutting (MLM) or weighting (CKKW) events based on the probability that such an event would originate from the matrix element or PS. The FxFx algorithm implements merging when one-loop diagrams are included [168], and therefore plays the same role in NLO calculations that the MLM and CKKW algorithms play in LO calculations.

PSMC programs provide several more features that are vital in obtaining a faithful reproduction of data, especially in events with only soft hadronic activity. The radiation described above affects the p_{T} of the hard scatter system, so PSMCs must "retroactively" adjust the kinematics generated by the matrix element MC. The underlying event and further QCD interactions that happen below the regime that can be calculated perturbatively are modeled phenomenologically [11, 59]. This includes soft color exchange between fragments of the colliding hadrons that sends proton remnants into the detector in the form of extra soft hadrons [169]. There

is also a possibility that multiple pairs of partons will undergo hard interactions in the same proton-proton collision, essentially combining two quasi-independent hard scatters [162, 170].

4.1.3 Pileup Simulation

The high per-bunch luminosity of the LHC causes multiple proton-proton collisions to occur in each bunch crossing. The extra interactions are called pileup. To account for this effect, CMS simulations include extra minimum-bias collision events overlaid on top of the primary collision [171, 172]. This includes simulated pileup interactions that are time evolved to reproduce the effects of "out-of-time" pileup from previous bunch crossings, because detector electronics generally have relaxation times longer than a single bunch crossing time so signals overlap. Because MC samples are produced before the pileup profile can be measured in data, simulated events are reweighted based on the number of pileup interactions such that the distribution of the number of reconstructed vertices becomes similar to that in data.

4.1.4 Samples Used in this Analysis

The $q\bar{q} \to ZZ$, $qg \to ZZ$, $gg \to H \to ZZ^*$, and $q\bar{q} \to Z \to 4\ell$ samples are produced at NLO with POWHEG 2.0 [55, 150–152, 173] and scaled to the NNLO total cross section with K factors of 1.7 for the Higgs sample and 1.1 for the others [56]. The non-Higgs POWHEG samples include ZZ, Z/γ^*, and $\gamma^*\gamma^*$ production with a generator-level constraint of $m_{\ell\ell'} > 4\,\text{GeV}$ for all opposite-charge lepton pairs, to limit the generated phase space to only regions of interest and far from infrared divergences. For the inclusive cross sections and differential cross sections in fully leptonic observables, this POWHEG sample is considered the primary theory prediction. For the differential

cross sections in jet-related variables, MadGraph5_aMC@NLO 2.3.3 [149] is used for the nominal sample, because it has an extra jet at matrix-element level, merged with the PS jets using the FxFx scheme. Box diagram gg $\rightarrow$ ZZ samples are generated with MCFM 7.0 at LO [174]; these are scaled to NLO with a K factor of 1.7 [57].

Background WZ events are produced with POWHEG with the same settings as the ZZ sample while $t\bar{t}Z$ and WWZ samples are generated at LO with MadGraph5_aMC@NLO. Electroweak and non-VBS ZZjj samples are produced with MadGraph5_aMC@NLO for the VBS and aQGC searches and with Phantom 1.2.8 for the cross section measurements [175]. Samples with nonzero aTGCs are generated at LO with SHERPA 2.1.1 [153] and scaled such that the total yield from the SM SHERPA sample is the same as the yield from the POWHEG ZZ sample. Signal samples for the aQGC search are made with MadGraph5_aMC@NLO.

All samples use the NNPDF3.0 PDF sets [176]. Parton showing, hadronization, and underlying event simulation are done with Pythia8 using the CUETP8M1 tune [177] for all samples except the aTGC samples, for which SHERPA performs these tasks.

4.2 Detector Simulation

To incorporate experimental effects into MC samples, the detector and the final state particles' interactions with it are simulated with the highest possible level of detail [171, 172]. The detector geometry and material, including both instrumented and non-instrumented components, are modeled with the Geant4 package [178], which describes microscopic particle interactions with matter over a wide range of energies and propagates the effects of these interactions to their macroscopic consequences. Stochastic effects are again implemented with Monte Carlo methods that

select outcomes at random from realistic distributions of possibilities. The GEANT4 simulation includes a detailed model of the magnetic field, so particle trajectories are calculated correctly, and the generation of secondary particles like e^+e^- pairs from photons interacting with tracker material. Charge deposition in silicon, scintillation in clear crystals, hadronic showers from nuclear interactions, and ionization, are all included, among many other processes. Detector signals are derived from microscopic interactions, and GEANT4 simulates signals in the analog front end detector electronics and has signal digitization capabilities which ensure that the signals coming out of the simulated detector are exactly those that would be produced by the real detector in the same situation.

The simulated signals are fed into the same reconstruction software as is used for data (see Chapter 5). The same analysis strategy may then be used for MC samples and data, and comparing the results is meaningful. Though every effort is made to model the detector accurately, no simulation can incorporate all real effects with perfect fidelity. Monte Carlo samples must be produced before data are actually collected, so the final detector alignment cannot be known exactly, and conditions and calibrations may change mid-run if—for example—a subdetector channel goes dead or LHC beam conditions change. Residual corrections for these small effects are applied to final physics objects in the final steps of the analysis to make distributions of interest, such as dilepton mass around the Z resonance or the overall jet p_{T} spectrum, match in aggregate. The overall level of agreement between data and simulation may be seen in Fig. 4.1, which shows the invariant mass of e^+e^- events around the Z resonance for simulated samples and data, and their ratio.

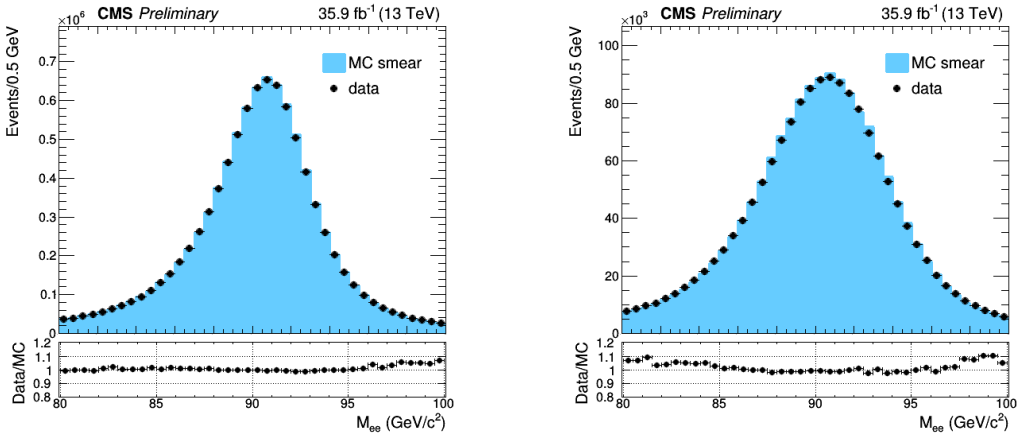

Figure 4.1: The invariant mass of e^+e^- events with both electrons in the barrel (left) and both electrons in the endcaps (right) in the whole 2016 dataset after all corrections are applied. The lower plots show the ratio of data and simulation to show the level of agreement achieved.

Chapter 5

Object Reconstruction and Selection

The raw detector information stored on disk after an event passes trigger selections is not yet suitable for physics analysis. Hits in the tracker and muon systems, and energy deposits in the calorimeters, require significant processing to build physics objects that are interpretable in terms of the physics of the hard scatter. Patterns in the tracker and muon system hits are found and used to construct charged particle and muon tracks, and energy deposits in the calorimeters are grouped into clusters. Final state particles that interact with CMS are reconstructed from the tracks and calorimeter clusters, final state particles are clustered into jets, charged particles are clustered by track origin to find proton-proton collision vertices, and visible particle momenta are summed to find the transverse momentum imbalance from undetectable particles (in the SM, neutrinos). The resulting physics objects undergo selection to determine which represent real particles of interest for the analysis. Selected particles are used to reconstruct the hard interaction from the collision—in the analyses presented here, leptons are paired to form Z/γ^* boson candidates which may be paired

to form Higgs or Z boson candidates or nonresonant ZZ candidates, and jets are used to construct hadronic observables and to distinguish electroweak and QCD ZZ production.

5.1 Track Reconstruction and Vertex Identification

Tracks are reconstructed in the inner tracker by iterative application of a combinatorial Kalman filter algorithm [179–182]. At each iteration, tracks found in the pixel detector are used as "seeds", track segments which serve as the initial trajectories on which strip tracker hits from the same particle are expected. The pixel seed supplies the initial parameters for the combinatorial Kalman filter. At each tracker layer, the algorithm predicts where the particle will hit the next layer based on the track's current parameters, taking into account the effects of particle interaction with tracker material. The extrapolated trajectory is used to find compatible hits in the next layer with a χ^2 test, and if possible the most compatible hit is added to the track and its parameters are updated accordingly. If no hits are compatible, a "ghost" hit which does not contribute to the track parameters may be added to account for the possibility of a missing hit in the corresponding layer. This procedure is repeated recursively at each tracker layer, from the innermost layer past the seed to the outermost layer of the silicon strip tracker. If two tracks found in an iteration share too many hits, they are assumed to be from the same particle and the one with fewer hits is rejected, using the total χ^2 of all hits as a tiebreaker. The first iterations of the track finding algorithm searches for high-p_{T} tracks from primary proton-proton interactions, which are easier to find because they are close to straight and originate from the beam line. When a track is found, its constituent hits are removed from consideration in future

iterations, reducing the computational complexity of finding the more difficult tracks from lower-p_{T} particles and products of b hadron decays which happen away from the beam line.

Because the Kalman filter obtains the final track parameters only at the outermost tracker layer, each track is refit and smoothed with further Kalman filters, improving track quality and reducing fake rate. Spurious tracks are rejected from the final collection with requirements on the number of layers hit, the χ^2 of the fit, and compatibility with a primary vertex. The efficiency for reconstructing tracks of all prompt charged particles with $p_{\mathrm{T}} > 900\,\mathrm{MeV}$ is around 94% in the barrel and 85% in the endcap; for isolated muons, it is virtually 100% in the whole tracker acceptance [182].

Electrons lose substantially more energy to interactions with the tracker material than other charged particles, often breaking the assumption of Gaussian energy loss inherent to the Kalman filter. To mitigate the impact of the resulting poor track fits, tracks with many missing hits or a poor χ^2 are refit using a Gaussian sum filter (GSF) [183]. Any Kalman filter or GSF tracks with trajectories that intersect ECAL energy clusters (see below) are considered electron track candidates and refit with a second, more complicated GSF. This GSF track collection is used as inputs to the PF electron reconstruction described below.

Proton-proton interaction vertices are found by clustering tracks by minimizing the figure of merit

$$\chi^2 = \sum_i \sum_j p_{ij} \frac{\left(z_j^t - z_i^V\right)^2}{\sigma_j^2}, \tag{5.1}$$

where z_i^V is the z position of vertex i, z_j^t is the z position of track j at its closest point to the beamline, and σ_j^2 is its uncertainty. The track-vertex association matrix p_{ij} maps tracks to their associated vertices, i.e. $p_{ij} = 1$ if vertex i and track j are associated, $p_{ij} = 0$ if they are not. Rather than minimize Eq. (5.1) directly with an

unknown number of vertices, the CMS clustering algorithm [182, 184] uses a technique known as deterministic annealing [185], which treats the system as a statistical ensemble of associations between the tracks and an unknown number of vertices. The association matrix p_{ij} is then the probability that vertex i and track j are associated. If every possible set of assignments, for every possible number and arrangement of vertices, is considered equally probable, this is analogous to a thermodynamic system at high temperature, with χ^2 playing the role of energy. The system is simulated at high "temperature" and the analog of free energy is minimized to determine p_{ij}. The temperature is then lowered in steps, with track-vertex associations deterministic in the limit of zero temperature.

Among the interaction vertices in an event, the one whose associated charged particles have the highest sum of p_{T}^2 is labeled the primary vertex (PV). A PV must be less than 24 cm from the nominal beam spot in the z direction and less than 2 cm from it in the x-y plane. Many commonly-used analysis observables are strongly dependent on the number of secondary proton-proton interaction vertices in the event, colloquially called the pileup. The pileup distributions used in Monte Carlo samples are not the same as the distribution in data, biasing sensitive quantities. Monte Carlo events are therefore reweighted based on the number of simulated pileup vertices such that the overall N_{vtx} (number of proton-proton interaction vertices) distributions match.

5.2 Particle Flow Reconstruction

The simplest conceivable algorithm would reconstruct each type of particle mostly with information from single subsystems: muons with the outer muon system, electrons and photons with ECAL (using HCAL to differentiate them from hadrons), jets

with the calorimeters aided by inner tracker information to handle b jet vertexing, etc. This approach is sufficient for many analyses and sophisticated versions of the general principle have performed admirably at a number of experiments, but it is suboptimal. It fails to exploit the full detector information for many objects—for example, not using the inner tracker's precise measurements of low-energy charged hadrons in jets made by clustering calorimeter deposits—and misses significant correlations between detector systems. The CMS collaboration takes a different approach, using a particle flow (PF) algorithm combining subdetector signals for optimal particle reconstruction and identification [186–188].

Several features of CMS facilitate PF reconstruction, as described in Section 3.2. The most important is that the calorimeters are inside the magnet and close to the tracker, so charged particles are much less likely to interact with material between them. The inner tracker's precise position measurement and ECAL's fine segmentation thus allow tracks to be associated to calorimeter clusters even for individual charged hadrons of modest energy.

5.2.1 PF Candidates

The inputs to the PF algorithm are inner tracker tracks, muon system tracks, and clusters of energy deposits in the calorimeters, all of which are calibrated beforehand. Calorimeter clusters are built independently for each subsystem, with ECAL and HCAL barrel and endcaps considered separately. Topological clusters are built by combining adjacent cells with energy deposits over a threshold, using cells that are local energy maxima as seeds. Within the topological clusters, the final calorimeter clusters are built by fitting the energy deposits with the sum of several two-dimensional Gaussians, one Gaussian for each seed in the topological cluster.

The first step of the PF algorithm is to link tracks and clusters across subdetec-

tors. Tracks are linked to calorimeter clusters by extrapolating from the track to the calorimeter cells the particle would be expected to hit. To account for bremsstrahlung photons from electron interactions with tracker material, GSF tracks are linked with ECAL clusters compatible ($\Delta\eta < 0.05$) with a tangent to the track where it hit the tracker. Overlapping ECAL and HCAL clusters are linked outside the inner tracker acceptance. Inner tracks are linked to muon system tracks if their hits can be propagated onto a common surface and merged into a single track within the resolution of the muon system (see Section 3.3 of Ref. [188]). The groups of linked objects, called "PF blocks", usually originate from one or a few particles and are the basic unit of PF reconstruction.

5.2.1.1 Muons

Muon candidates in CMS [189] come in three flavors: "standalone", "tracker", and "global" muons. Standalone muons use only the track from the muon spectrometer (the "standalone track"), built with a fit to track segments made of clusters of hits in the DTs, CSCs, and RPCs. Tracker muons use only the inner track, identified as a muon because the track is compatible with one or more track segments in the muon system within 3 cm transverse to the track direction, or four standard deviations of the track's angular position uncertainty. Global muons use a combined "global track" made by fitting the hits in an inner track and a compatible standalone track to a common muon trajectory through the whole detector. By construction, global muons have corresponding standalone and tracker muons. Tracker muons are merged into their corresponding global muons, which use the inner track momentum for muons with $p_{\mathrm{T}} < 200\,\mathrm{GeV}$ and the momentum of the track with the best normalized χ^2 otherwise. When a muon candidate is reconstructed, its constituent tracks are removed from the PF block and are therefore not used in further reconstruction.

5.2.1.2 Electrons and Prompt Photons

Electron reconstruction uses GSF tracks linked with ECAL clusters [183, 190]. The cluster associated with a track and the bremsstrahlung candidate clusters on tangents to the track are collectively called the "supercluster". Prompt photons are reconstructed from superclusters without associated tracks except displaced track pairs consistent with photon-initiated electron-positron pair production in the tracker material [191]. In both cases, the HCAL energy near the supercluster cannot be more than 10% of the supercluster energy. Non-isolated photons, i.e. those with substantial nearby tracks or calorimeter deposits or a high ratio of HCAL energy to ECAL energy, are assumed to be from π^0 decays and are described with neutral hadrons in the next section. Tracks and clusters used to reconstruct electrons and photons are removed from the PF block and are not used in hadron reconstruction.

5.2.1.3 Charged and Neutral Hadrons

With muon, electron, and prompt photon constituents removed, remaining detector signals are taken to be from charged and neutral hadrons (including non-prompt photons) [186, 188]. Clusters in ECAL without associated tracks are taken to be photons from π^0 decays, because neutral hadrons deposit very little energy in ECAL. Trackless clusters in HCAL are taken to be neutral hadrons. Both are removed from the PF blocks, so all that remain are linked clusters and tracks. Paired tracks and clusters with compatible energies are taken to be charged hadrons. If the track p_{T} is much less than the calorimeter-measured p_{T}, the pair is labeled as overlapping charged and neutral hadrons.

5.2.2 Jets

Effective clustering of hadrons, non-prompt photons, and non-prompt leptons into jets is critically important for many physics analyses, including the ZZ + jets differential cross section measurements and the ZZ VBS search (see Sections 6.5 and 5.4.3). Clustering must be efficient, to ensure the tagging jets in VBS events are found, but the clustering algorithm should not tag spurious jets, as the number of jets in an event is sensitive to higher-order QCD corrections and therefore an interesting quantity to compare to theoretical predictions. Similarly, the algorithm should not erroneously cluster particles from the same initial parton into multiple jets or merge jets from multiple original partons, because the kinematics of the original quarks and gluons are also of theoretical interest and the detector-level jet kinematics should accurately reflect them. A clustering algorithm is said to be "infrared safe" if the presence of low-energy hadrons from soft gluon radiation does not change the number of jets or have a qualitatively significant effect on jet shapes and kinematics. This fits with the intuition that a single 1 GeV pion should have essentially no effect in an event with multiple jets with energies on the order of hundreds of GeV [192]. An algorithm is said to be "collinear safe" if the jets are not changed substantially by splitting one hadron into two nearly collinear hadrons with the same total four-momentum. This also fits with physical intuition in that jets deposit energy over an area significantly larger than the spatial resolution of the detector, so increasing the detector granularity enough to resolve two very close particles (without changing their total four-momentum) should have little or no effect on the jet.

Infrared and collinear (IRC) safety are critically important for comparing data to theoretical predictions [193]. Collinear splittings and soft gluon radiation during jet fragmentation should not affect the dynamics of the TeV-scale hard scattering processes we wish to probe, but they are nonperturbative and difficult to model

(see Section 4.1.2), and experimental analysis can only probe the underlying hard interaction if it is insensitive to this kind of mismodeling. Experimental detectors' finite resolution and inability to measure arbitrarily soft particles enforces some level of IRC safety on any algorithm, but the results of an analysis methods that uses an IRC unsafe clustering will depend on the complex, detector-dependent details of this partial IRC regularization. In any case, the most meaningful comparisons between data and theory should use the same definition of a jet in the experimental analysis and the perturbative calculation, and perturbative calculations require IRC safe observables to preserve unitarity.

These considerations, and the desire for conical jets with a well-defined area in the η-ϕ plane, lead most CMS analyses (including this one) to use jets clustered with the anti-k_{T} algorithm [194, 195]. The anti-k_{T} algorithm defines the distance between two particles i and j as

$$d_{ij} = \min\left(p_{\mathrm{T}i}^{-2}, p_{\mathrm{T}j}^{-2}\right)\frac{\Delta_{ij}}{R}, \tag{5.2}$$

where Δ_{ij} is the distance in the rapidity-polar angle plane,

$$\Delta_{ij}^2 \equiv (y_i - y_j)^2 + (\phi_i - \phi_j)^2, \tag{5.3}$$

and R is a parameter setting the size of the resulting jets. The algorithm proceeds iteratively. At each iteration, if the smallest d_{ij} between any pair of particles in the event is smaller than the smallest p_{T}^{-2} of any single particle, the particles in the pair are merged into a single particle with their total four-momentum. If the minimum single-particle p_{T}^{-2} is smaller than the minimum d_{ij}, the single particle is labeled a jet and removed from further consideration. Iteration proceeds until all particles are part of a jet. In this analysis, the size parameter used is $R = 0.4$.

Charged hadrons whose tracks originate in pileup interactions are not included in jet clustering [196]. The contribution of neutral hadrons from pileup is estimated with

a jet area technique [197–199] in which the energy density of neutral hadrons from pileup is calculated event-by-event and multiplied by the area of the jet to estimate the neutral pileup contribution, which is subtracted from the jet energy. Jets in Monte Carlo samples have their energy shifted and stochastically smeared such that the overall energy scale and resolution match that of jets in data [197, 200].

5.2.3 Missing Transverse Energy

Neutrinos—or, hypothetically, WIMP dark matter or other new particles that do not decay or interact directly with the detector—escape and cannot be directly measured. Because the beams have no momentum in the x-y plane, the transverse momentum of the visible particles must balance the transverse momentum of the invisible ones. The missing transverse momentum is thus

$$\vec{p}_{\mathrm{T}}^{\,\mathrm{miss}} = -\sum_{\mathrm{visible}} \vec{p}_{\mathrm{T}}, \tag{5.4}$$

where the sum runs over the transverse momenta of all PF candidates in the event. The missing transverse energy, $E_{\mathrm{T}}^{\mathrm{miss}}$, is its magnitude. The $E_{\mathrm{T}}^{\mathrm{miss}}$ is calibrated by propagating the jet energy scale corrections to the $E_{\mathrm{T}}^{\mathrm{miss}}$ calculation [201–203]. All PF candidates are included in the sum in Eq. (5.4), including those originating from pileup interactions, because these soft collisions are very unlikely to produce neutrinos, so including them biases the measurement less than trying to determine which neutral particles should be considered pileup and which should not.

5.3 Object Identification and Selection

The reconstruction algorithms described above are general purpose in the sense that they can be used in nearly any analysis, but do not address the specific needs of

any, so further selections are essentially always required to optimize object efficiency and purity for studying a specific physics process. The leptons used in this analysis are required to pass identification requirements on top of those imposed during PF reconstruction, and are required to be isolated from other particles in the event, to reject fake objects from jet fragmentation. Four-lepton processes have low reducible backgrounds, so the selections presented here are generally loose, optimized for high efficiency compared to most CMS analyses.

5.3.1 Electrons

Electrons are required to have $p_{\mathrm{T}} > 7\,\mathrm{GeV}$ and to be in the tracker acceptance, $|\eta| < 2.5$. They must be compatible with the PV, with minimum track-PV distance $d_z < 1\,\mathrm{cm}$ in the z direction and $d_{xy} < 5\,\mathrm{mm}$ in the plane transverse to the beam. Each electron's 3-dimensional impact parameter (IP) $d_{3\mathrm{D}}$ must satisfy a requirement on its significance,

$$\mathrm{SIP}_{3\mathrm{D}} \equiv \frac{d_{3\mathrm{D}}}{\sigma_{d_{3\mathrm{D}}}}, \tag{5.5}$$

where $\sigma_{d_{3\mathrm{D}}}$ is the uncertainty on the IP. The $\mathrm{SIP}_{3\mathrm{D}}$ requirement is $\mathrm{SIP}_{3\mathrm{D}} < 10$ for the ZZ and $\mathrm{Z} \to 4\ell$ cross section measurements and the aTGC search, and $\mathrm{SIP}_{3\mathrm{D}} < 4$ for the Higgs boson measurement and the VBS and aQGC searches. Distributions of $\mathrm{SIP}_{3\mathrm{D}}$ are shown for electrons and muons in Fig. 5.1. To remove fake electrons arising from muon tracks being associated to photons or other incidental ECAL energy clusters, electrons within $\Delta R < 0.05$ of a muon are vetoed.

To further reduce photon and jet fragment backgrounds while maintaining high prompt electron efficiency, a further selection is applied using a multivariate discriminator made with a boosted decision tree (BDT) [204, 205]. The BDT uses 21 input variables, which fall into three broad categories:

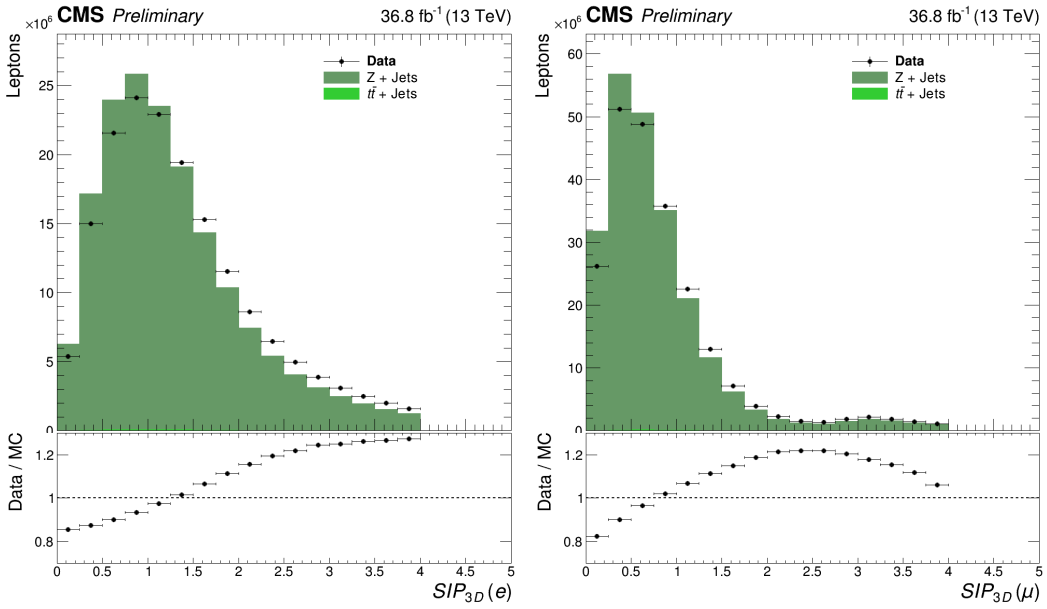

Figure 5.1: Vertex compatibility in the form of the $\mathrm{SIP}_{3\mathrm{D}}$ distribution for electrons (left) and muons (right) in a single-Z sample. The distribution extends only to 4 because these events were used for Higgs boson measurements.

- Track-related observables like the number of hits and normalized χ^2 of the Kalman and GSF tracks and the energy lost to bremsstrahlung according to the GSF fit. These are intended to discriminate between electrons and charged hadrons.

- Calorimetric information including a number of supercluster shape observables and the amount of HCAL energy near the supercluster, to discriminate electrons from electromagnetically rich jets.

- Track-cluster observables comparing the positions and momenta of the particles seen in the tracker and by ECAL.

The BDT training and working point selection are done separately for electron candidates with p_{T} above and below 10 GeV and in three bins of $|\eta|$ (0–0.8, 0.8–1.479,

and 1.479–2.5). The working points are chosen to correspond to 98% efficiency for single signal electrons in each bin.

To ensure that electron candidates are not part of a jet, they are required to be isolated from other particles in the event. The relative isolation is defined as

$$R_{\text{Iso}} = \left(\sum_{\text{charged}} p_{\text{T}} + \max \left[0, \sum_{\text{neutral}} p_{\text{T}} + \sum_{\text{photons}} p_{\text{T}} - p_{\text{T}}^{\text{PU}} \left(\ell \right) \right] \right) \Big/ p_{\text{T}}^{\ell} \tag{5.6}$$

where the sums run over the p_{T} of PF hadrons and photons in a cone of $\Delta R < 0.3$ around the electron trajectory. To mitigate the contribution of pileup to the isolation calculations, charged hadrons are included only if they originate from the event's PV. The estimated neutral contribution to isolation from pileup, $p_{\text{T}}^{\text{PU}} \left(\ell \right)$, is defined for electrons as

$$p_{\text{T}}^{\text{PU}} \left(\text{e} \right) \equiv \rho \times A_{\text{eff}}, \tag{5.7}$$

where the average transverse-momentum flow density ρ is calculated in each event using the jet area method described above. The effective area A_{eff} is the geometric area of the isolation cone times an η-dependent correction factor that accounts for the residual dependence of the isolation on pileup. Electrons are considered isolated if their relative isolations satisfy $R_{\text{iso}} < 0.35$. Relative isolation distributions are shown for electrons and muons in Fig. 5.2.

Efficiencies for GSF track reconstruction, electron reconstruction and identification, and electron isolation criteria, are found with a "tag-and-probe" method [206]. In this technique, events are selected which contain at least one high-p_{T} "tag" electron passing strict ID and isolation requirements, and a "probe" track with the opposite sign that combines with the electron to have an invariant mass close to the Z boson mass. The resulting sample is enriched with $\text{Z} \to \text{e}^{+}\text{e}^{-}$ events, so the track is likely to correspond to a real prompt electron. Unlike all background processes, $\text{Z} \to \text{e}^{+}\text{e}^{-}$ production forms a distinct resonance peak in the $m_{\ell\ell}$ distribution, so shape fits can

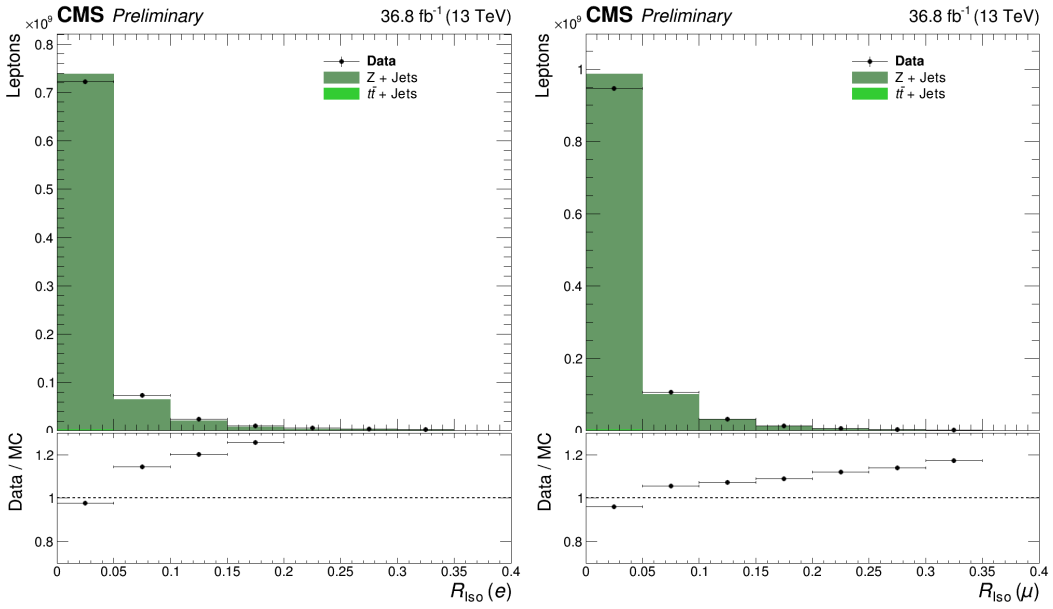

Figure 5.2: Relative isolation for electrons (left) and muons (right) in single-Z events.

be used to find the overall purity of the sample, and thus the number of prompt electrons among the probes. The selection efficiency is then the number of passing probes divided by the total number of prompt probes. This procedure is performed in bins of p_{T} and η for data and Monte Carlo events, and residual differences in efficiency in Monte Carlo samples are corrected to match data by weighting events by the ratio of data and Monte Carlo efficiency for each electron candidate. Overall electron efficiency varies between roughly 85% in the inner endcap ($|\eta| > 2.0$) to around 95% in the central barrel ($|\eta| < 0.8$).

5.3.2 Muons

Muon selection is similar to electron selection, but simpler because muon backgrounds are much smaller. Candidate muons are required to be tracker or global muons with $p_{\mathrm{T}} > 5\,\mathrm{GeV}$ within the muon system acceptance ($|\eta| < 2.4$). They are subject to the same PV compatibility criteria as electrons, $d_z < 1\,\mathrm{cm}$, $d_{xy} < 5\,\mathrm{mm}$, and $\mathrm{SIP}_{3\mathrm{D}} < 10$

or 4 depending on the analysis. Muon candidates are further subject to the so-called "PF ID" criteria, which require them to be isolated from calorimeter deposits or to have high-quality tracks with good fits [188].

Isolation is defined as in Eq. (5.6), the same as for electrons except for the definition of the neutral pileup contribution, which for muons is based on using the known charged pileup density to estimate the neutral pileup based on the average charge composition of pileup jets,

$$p_{\mathrm{T}}^{\mathrm{PU}}(\mu) \equiv 0.5 \sum_{\text{charged}} p_{\mathrm{T}}^{\mathrm{PU}}, \tag{5.8}$$

where the sum runs over the charged particles from all pileup vertices. As for electrons, the radius of the isolation cone is 0.3 in the η-ϕ plane and the selection criterion is $R_{\mathrm{iso}} < 0.35$. Muon efficiencies are measured and corrected with the same tag-and-probe technique as used for electrons, and found to be around 97%.

5.3.3 Final State Photon Radiation

Final-state radiation (FSR) photons emitted by muons are not included in the PF momentum reconstruction, and some photons emitted by electrons may be missed, degrading Z boson reconstruction. Photons are considered FSR candidates if they have $p_{\mathrm{T}} > 2\,\mathrm{GeV}$, $|\eta| < 2.4$, relative isolation $R_{\mathrm{iso}} < 1.8$ as defined in Eq. (5.6) (with no neutral pileup correction), and $\Delta R(\ell, \gamma) < 0.5$ with respect to the nearest lepton. To avoid double counting, photons in electron superclusters are not considered. Because FSR has a higher energy spectrum than photons from pileup and is expected to be quasi-collinear with the emitting leptons, a photon is accepted as FSR and included in the ZZ final state if $\Delta R(\ell, \gamma)/E_{\mathrm{T}\gamma}^2 < 0.012$. The performance of this algorithm is tuned and evaluated with comparisons to generator-level information in MC samples, and is found to have efficiency around 60% for a purity around 80%.

FSR photons are omitted from the isolation determination for emitting leptons. In the rest of this thesis, the momentum of any FSR photons found is included in Z/γ^* and ZZ four-momenta unless otherwise stated.

5.3.4 Jets

Jets are considered for analysis if they have $p_T > 30\,\text{GeV}$ and $|\eta| < 4.7$. Loose criteria are applied to reject spurious jets by requiring they contain multiple particles, and the particles be a mix of charged and neutral consistent with hadronic jets. Jets are removed from consideration in the event if a lepton or FSR photon is in its cone ($\Delta R < 0.4$ with respect to the jet's total momentum vector).

5.3.5 Misidentified Objects

The reducible background estimation method described in Section 6.1 requires the use of "loose" lepton candidates which are similar to candidates passing the full selection but much more likely to be jet fragments or other non-prompt objects. Loose lepton candidates pass the p_T and η cuts and vertex compatibility criteria, but the other identification criteria are reduced. The electron BDT discriminator is not applied to loose electrons. Loose muons must still be tracker or global muons, but the PF ID is not applied. Isolation requirements are not applied to loose candidates. Depending on their use, loose candidates may have no further requirements applied, or may be required to fail the tight ID and/or isolation requirements, as detailed in Section 6.1, where the fake rates for electrons and muons are shown in Fig. 6.1. Aside from the ID and isolation criteria, loose leptons are treated the same as their tight cousins, with FSR recovery performed with the same algorithm. Jets near loose leptons are only removed if the loose lepton is taken to be one of the four in the ZZ candidate in

the final event interpretation.

5.4 ZZ Candidate and Event Selection

Online event selections used single, double, and triple lepton triggers. The double lepton triggers were the primary paths, with single and triple lepton triggers correcting for residual inefficiencies to bring the overall trigger efficiency above 99%. Exact HLT parameters changed over the course of datataking as instantaneous luminosities changed and trigger rates rose, so many thresholds are shown here as ranges.

- Single muon p_{T} thresholds were between 20 and 24 GeV for isolated muons. Nonisolated single muons were required to have $p_{\mathrm{T}} > 50\,\mathrm{GeV}$ or $p_{\mathrm{T}} > 45\,\mathrm{GeV}$ and $|\eta| < 2.1$. Single electron p_{T} thresholds were 25 or 27 GeV depending on ID criteria applied.

- Leading lepton p_{T} thresholds in double lepton paths were 17 or 23 GeV. Trailing lepton thresholds were 12 GeV and 8 GeV for electrons and muons, respectively. Isolation requirements and requirements on the z-axis distance between lepton track origins were added part way through datataking.

- The p_{T} requirements in triple lepton paths varied between 5 and 16 GeV, with no isolation or vertex requirements.

An event is considered for the analysis is any of these triggers fires.

Several distinct analyses fall under the four-lepton umbrella, each with different requirements and therefore different selection criteria. The sets of selections will be listed here with brief descriptions of their uses, and detailed in full below.

- The *full spectrum selection* picks a phase space that encompasses all four-lepton events, and all other selection sets yield strict subsets of the full spectrum phase space.

- The *singly resonant* ($Z \to 4\ell$) *selection* picks events with four-lepton mass around the Z boson resonance.

- The *Higgs selection* is that used for the Higgs boson discovery and properties measurements. It is similar to the full spectrum selection but with slightly tighter requirements on the second Z/γ^* candidate, because $Z \to 4\ell$ events are of less interest and some backgrounds may be reduced by excluding events with an on-shell Z boson and a low mass lepton pair that could be a decay of an Υ or similar meson.

- The *on-shell* or *doubly resonant selection* requires both Z candidates to be compatible with a resonant Z boson. It is used for the ZZ and ZZ + jets cross section measurements and the aTGC search.

- The *dijet* (ZZjj) *selection* uses the on-shell selection for the four-lepton system, and additionally requires at least two jets. It is used for the VBS and aQGC searches.

5.4.1 Z/γ^* Candidate Selection

A Z/γ^* candidate is built from a pair of opposite-sign, same-flavor leptons with invariant mass between 4 and 120 GeV. The Z/γ^* candidate with mass closest to the nominal Z boson mass is labeled Z_1, the other is labeled Z_2. Mass requirements on the Z/γ^* candidates are among the primary differences between the various analysis selections. The full spectrum, $Z \to 4\ell$, and Higgs selections require $m_{Z_1} > 40\,\text{GeV}$.

The Higgs selection additionally requires $m_{Z_2} > 12\,\text{GeV}$. The on-shell and dijet selections require both Z_1 and Z_2 to have $m_{Z_i} > 60\,\text{GeV}$. The mass range thus allowed, $60 < m_{Z_{1,2}} < 120\,\text{GeV}$, serves as the definition of an on-shell Z boson for purposes of this analysis.

Table 5.1: The number of events in data reconstructed as having two pairs of opposite-sign, same-flavor leptons, at several points in the analysis flow. Best candidate selection is done only with the full spectrum selection, and an event may have candidates in multiple channels, so channel yields do not sum to the total yield in early steps.

Selection	4e	2e2μ	4μ	Total
Trigger	580633	645640	399212	1598705
Lepton ID	2195	6760	11614	20563
Lepton Isolation	597	1189	1548	3334
Full Spectrum	440	1111	838	2389
$Z \to 4\ell$	78	206	225	509
$H \to 4\ell$	19	41	34	94
$ZZ \to 4\ell$	220	543	335	1098

5.4.2 ZZ Candidate Selection

Four-lepton candidates are built from pairs of Z/γ^* candidates. Among the four leptons in the candidate, all opposite-sign pairs must have invariant mass $m_{\ell^+\ell'^-} > 4\,\text{GeV}$ regardless of flavor, to remove events in which decay products of a light, leptonically decaying particle like a J/ψ are erroneously paired with the two leptons from a real Z boson to form two false Z/γ^* candidates by chance when paired incorrectly. The requirement on all pairs does not include FSR photons, because the mesons that would cause such a problem are generally found in jets which include photons from π^0 decays, whcih are likely to be misidentified as FSR. All lepton pairs must have $\Delta R > 0.02$ to avoid "ghost" leptons with shared tracks. The leading and lepton among the four

must have $p_{\mathrm{T}} > 20\,\mathrm{GeV}$, and the subleading lepton must have $p_{\mathrm{T}} > 10\,\mathrm{GeV}$ if it is an electron or $p_{\mathrm{T}} > 12\,\mathrm{GeV}$ if it is an electron. The $\mathrm{Z} \to 4\ell$ selection requires the candidate to have $80 < m_{4\ell} < 100\,\mathrm{GeV}$, consistent with resonant single-Z production.

All allowed pairings of leptons into Z/γ^* candidates are examined separately, so an event with two electrons and two positrons, for example, will yield two possible ZZ candidates, with the only difference being how the electrons are paired into Z_1 and Z_2. In the case that multiple interpretations of the same event pass the full selection, the one with Z_1 closest to the nominal Z mass is chosen. In the rare case of further ambiguity, which may arise in events with five or more leptons, Z_2 is chosen to maximize the scalar p_{T} sum of the four leptons. This best candidate selection is done after the full selection is applied, and the other analysis selections are applied to the disambiguated events in the full spectrum phase space. Like the mass cut on all opposite-sign lepton pairs, this prevents events with one on-shell Z and one lower-mass γ^* from passing the on-shell Z mass cuts with an erroneous lepton pairing.

The number of events found in data after several analysis steps is shown in Table x. Specifically, the numbers in Table x include events with four objects reconstructed as two opposite-sign, same-flavor lepton pairs. Early in the analysis flow, most of these objects are fakes later removed by lepton ID and isolation requirements. The total signal efficiency of all selections is estimated by finding the fraction of events in the POWHEG and MCFM ZZ samples which pass both the fiducial cuts at generator level and the full analysis selection after detector simulation and reconstruction. For the doubly on-shell selection ($60 < m_{\ell\ell} < 120\,\mathrm{GeV}$), the efficiency is 54% for 4e events, 65% for 2e2μ events, and 78% for 4μ events. For $\mathrm{Z} \to 4\ell$ events, the efficiencies for the 4e, 2e2μ, and 4μ channels are, respectively, 24%, 36%, and 73%.

5.4.3 Dijet and VBS Signal Selection

The dijet selection, used for the VBS and aQGC searches, requires the event to contain two or more jets. The two highest-p_{T} jets are called the "tagging jets." The tagging dijet system must have $m_{\mathrm{jj}} > 100\,\mathrm{GeV}$. This criterion is not intended to preferentially select the EWK signal, which is concentrated at much higher dijet masses, but rather to provide a minimal selection for the sample on which to perform the multivariate VBS analysis described in Section 6.5 and the shape-based aQGC analysis described in Section 6.6. No further selections are applied, and the VBS signal efficiency is therefore close to 100%.

Chapter 6

Analysis Strategy

Four-lepton signal processes are generally well modeled, and backgrounds are small, so most analyses can use simple "cut and count" comparisons between data and Monte Carlo samples' yields after applying the selections described in Chapter 5. The comparisons include the contribution from reducible backgrounds, which is estimated with a data-driven technique. Inclusive and differential cross sections are extracted from the observed yields with maximum likelihood estimation techniques. The search for vector boson scattering extracts the signal yield with a multivariate discriminator, and the searches for anomalous couplings use a profile likelihood method to extract limits from the bin-by-bin yields in the $m_{4\ell}$ distribution. These techniques are all described in this chapter, as are the relevant systematic uncertainties, which are taken into account by varying the input parameters to the yields and observing the resulting changes in yield and spectrum shape.

6.1 Background Estimation

Reducible backgrounds for four-lepton events typically have two or three prompt leptons and two or one other objects—typically jet fragments, sometimes photons—which are misidentified as prompt leptons. The largest source of background contamination is from events in which a Z boson is produced in association with a photon and a jet, a leptonically-decaying W boson and a jet, or two jets. There is also a contribution from $\mathrm{t\bar{t}}$ events in which both top quarks decay to a lepton, a neutrino, and a b quark jet. For simplicity, the two sets of processes are not treated separately in what follows, and are collectively labeled "Z + X" events[1].

The contributions of the reducible backgrounds to the selected four-lepton signal samples are evaluated using the tight-to-loose "fake rates" method, described in Ref. [207]. In this procedure, the likelihood of a nonprompt ("fake") object to be misidentified as a prompt lepton is estimated and applied to control regions enriched with Z + X events to estimate their contribution to the signal region. The lepton misidentification rate $f_\ell\left(p_{\mathrm{T}}^{\ell}, \eta^{\ell}\right)$ is measured from a sample of $\mathrm{Z} + \ell_{\mathrm{fake}}$ events, where the Z boson candidate is selected as in the signal region but with $|m_{\ell\ell} - m_{\mathrm{Z}}| < 10\,\mathrm{GeV}$, and the ℓ_{fake} object is a lepton candidate that passes relaxed ID requirements as defined in Section 5.3.5, with no isolation or tight ID requirements applied.

The misidentification rate is defined as the fraction of ℓ_{fake} candidates which pass full lepton identification and isolation critera, in bins of p_{T} and η. One should note that the misidentification rate cannot be interpreted as a probability in the usual sense, and if fact there is no simple physical interpretation of it. Events with three prompt leptons can contaminate this control region and bias the misidentification rate, because the non-Z lepton is falsely assumed fake. To mitigate this bias, the

[1] This is a bit of a misnomer, as "Z + X" does not accurately describe $\mathrm{t\bar{t}}$ events, but the terminology is retained here for consistency with the CMS papers on these analyses.

$WZ \to 3\ell\nu$ yields in the numerator and denominator in each bin are estimated from a simulated sample and subtracted before the ratio of yields is taken. Figure 6.1 shows the misidentification rates for electrons and muons separately as a function of p_T and η.

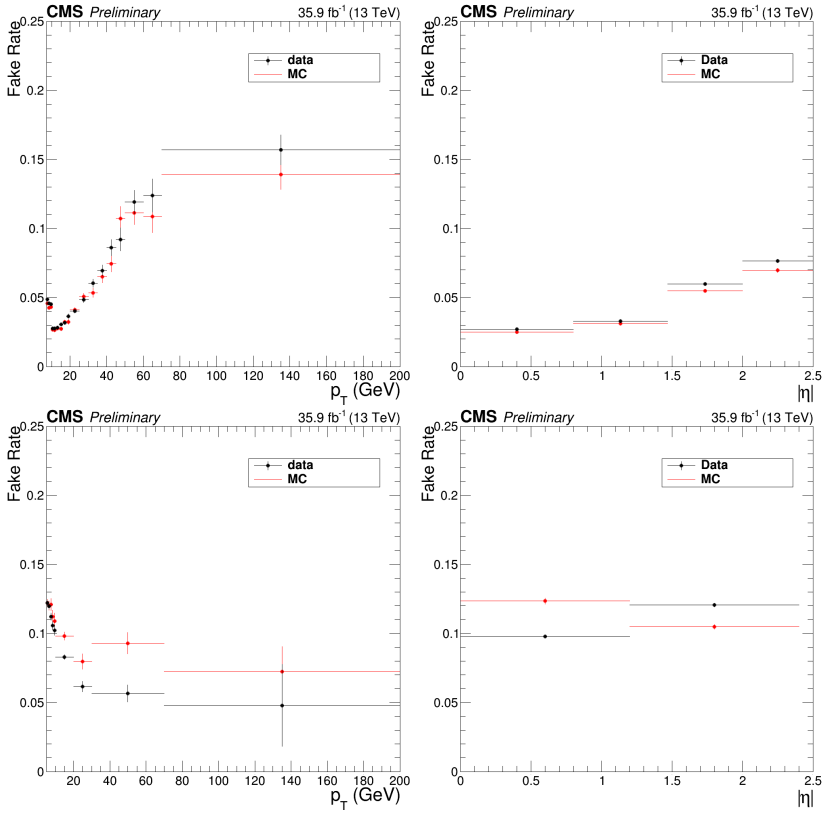

Figure 6.1: Fake rate for electrons (top) and muons (bottom) as a function of p_T (left) and η (right).

To estimate the total reducible background yield, the misidentification rates are applied to two Z + X enriched control samples, each containing a Z boson candidate passing all signal region requirements plus two more lepton candidates which pass the relaxed identification criteria and would make a second Z boson candidate according to Section 5.4.1 except that one or both fail the full identification or isolation criteria. The sample with one failing lepton, called the "3P1F" sample for "3 prompt 1 fake,"

covers the contribution from WZ events, while the sample with both leptons in the second Z boson failing ("2P2F") covers Z + jets, Zγ + jets, and $t\bar{t}$ events. The fake object transfer factor

$$F_\ell\left(p_{\mathrm{T}}^{\ell}, \eta^{\ell}\right) = \frac{f_\ell\left(p_{\mathrm{T}}^{\ell}, \eta^{\ell}\right)}{1 - f_\ell\left(p_{\mathrm{T}}^{\ell}, \eta^{\ell}\right)} \tag{6.1}$$

is the ratio of nonprompt objects passing the relaxed and full selection criteria, and thus serves as a per-lepton extrapolation factor between control sample yields and signal sample yields.

The total reducible background yield is thus

$$N_{\mathrm{bkg}} = \sum_{\ell \in \mathrm{3P1F}} F_\ell\left(p_{\mathrm{T}}^{\ell}, \eta^{\ell}\right) - \sum_{\ell_1, \ell_2 \in 2P2F} F_{\ell_1}\left(p_{\mathrm{T}}^{\ell_1}, \eta^{\ell_1}\right) F_{\ell_2}\left(p_{\mathrm{T}}^{\ell_2}, \eta^{\ell_2}\right). \tag{6.2}$$

The minus sign prevents double-counting of Z+2jets events in which one jet fragment is misidentified. The failing lepton candidates in the 3P1F and 2P2F control samples are assumed to truly be jet fragments or other nonprompt objects, but selection inefficiencies may cause prompt leptons to fail and contaminate the control regions with signal events. The yield of such signal events in the backgound control regions is estimated by applying the same fake factors to failing events in the ZZ signal Monte Carlo samples, and subtracted from the result of Eq. (6.2).

There are also irreducible background contributions from $t\bar{t}$Z and WWZ events, which can have four prompt leptons. Expected yields for these processes are taken from simulation.

6.2 Systematic Uncertainties

Systematic uncertainties for trigger efficiency are taken to be the difference between trigger efficiencies in data and in simulated signal events, found to be around 2% of the final event yield. Because leptons in Z $\to 4\ell$ events generally have lower p_{T},

the uncertainty increases to 4% for $Z \to 4e$ events. In both data and simulated events, trigger efficiencies are found with a tag-and-probe technique [206], performed on four-lepton events.

The lepton identification and isolation efficiencies in simulation are corrected with scaling factors derived with the tag-and-probe method, performed on $Z \to \ell^+\ell^-$ events in data and a single-Z Monte Carlo sample. To find the uncertainties associated with these corrections, the total yield is recomputed with the scaling factors varied up and down by one standard deviation of the uncertainties from the tag-and-probe method, treating all bins as correlated. The resulting changes in the $ZZ \to 4\ell$ yield, taken to be the one sigma variations resulting from lepton efficiency uncertainties, are found to be 6% in the 4e final state, 3% in the $2e2\mu$ final state, and 2% in the 4μ final state. Leptons in $Z \to 4\ell$ events tend to have lower p_T, and the tag-and-probe samples for leptons with p_T below about 15 GeV are smaller and more contaminated with nonprompt objects, so the uncertainties are larger; they are found to be 10%, 6%, and 7% for the 4e, $2e\mu$, and 4μ final states, respectively.

The uncertainty on the integrated luminosity of the data sample is 2.5% [145].

The uncertainty on lepton fake rates is 40%, which includes both statistical uncertainty and systematic uncertainties associated with the loosened lepton selections defined in Section 5.3.5 and the differences in the underlying physics processes between events in the $Z + \ell_{\text{fake}}$, 3P1F, and 2P2F control samples [73]. Statistical uncertainties arising from the limited size of the Z + X control samples are also included as a systematic uncertainty on the background yield. The total uncertainty on the background yield varies by channel but is below 1% of the expected total yield.

Uncertainties due to the effect of QCD scale on the $ZZ \to 4\ell$ acceptance are evaluated with POWHEG and MCFM, by varying the QCD scales up and down by a factor of two with respect to the default $\mu_R = \mu_F = m_{ZZ}$. Parametric uncertainties

(PDF+α_s) are evaluated according to the PDF4LHC prescription in the acceptance calculation [208], and with NNPDF3.0 in the cross section calculations. An additional theoretical uncertainty arises from scaling the $q\bar{q} \to ZZ$ and $gg \to ZZ$ simulated samples to their NNLO and NLO predicted cross sections, respectively, with the K factors described in Section 4.1.4. The corresponding change in the acceptance, 1.1%, is added to the previous theoretical errors in quadrature.

Systematic uncertainties on expected signal yield are summarized in Table 6.1. To obtain uncertainties in the inclusive fiducial and total cross sections, each uncertainty source is treated as a nuisance parameter in the fits described in Section 6.3.1. For differential cross section and other shape uncertainties, the calculation is fully redone for each uncertainty source, with the inputs shifted by one standard deviation in each direction. Variations across bins are taken to be fully correlated for each uncertainty source. Lepton and jet momentum scale and resolution uncertainties are taken to be trivial for the overall yield, but they are considered among the shape uncertainties.

Table 6.1: The contributions of each source of signal systematic uncertainty in the total yields. The integrated luminosity uncertainty and the PDF and scale uncertainties are considered separately. All other uncertainties are added in quadrature into a single systematic uncertainty. Uncertainties that vary by decay channel are listed as a range.

Uncertainty	$Z \to 4\ell$	$ZZ \to 4\ell$
Lepton efficiency	6–10%	2–6%
Trigger efficiency	2–4%	2%
MC statistics	1–2%	0.5%
Background	0.6–1.3%	0.5–1%
Pileup	1–2%	1%
PDF	1%	1%
QCD Scales	1%	1%
Integrated luminosity	2.5%	2.5%

6.3 Fiducial and Total Cross Section Calculation

Inclusive cross section measurements can be treated as simple binned counting experiments, where the bins are the three decay channels (4e, 2e2μ, and 4μ). If ν events are expected in a given bin, the probability of observing n events is given by the Poisson distribution,

$$f\left(n;\nu\right) = e^{-\nu}\frac{\nu^{n}}{n!}. \tag{6.3}$$

In a particle physics analysis like this one, ν takes the form

$$\nu = \nu_{s}\left(\vec{\theta_{s}}\right) + \nu_{b}\left(\vec{\theta_{b}}\right) = \mu\left(\vec{\theta_{s}}\right)\mathscr{L}_{int}\sigma_{SM}\epsilon + \nu_{b}\left(\vec{\theta_{b}}\right) \tag{6.4}$$

where ν_{s} and ν_{b} are respectively the expected signal and background yields, σ_{SM} is the standard model expectation for the cross section of the signal process and ϵ is our efficiency for detecting and identifying its events. The signal and background nuisance parameter vectors $\vec{\theta_{s}}$ and $\vec{\theta_{b}}$ represent hidden quantities that we do not measure directly but which affect our yields, i.e. systematic effects. The signal strength μ compares our expectation to what we actually measure:

$$\mu = \frac{\sigma_{meas}}{\sigma_{SM}}. \tag{6.5}$$

Of the variables in Eqs. (6.3) and (6.4), σ_{SM} is known from theoretical calculations, and ϵ is determined from simulation. The CMS detector is designed to measure n and $\mathscr{L}_{int}$, ν_{b} is estimated from data or simulation, and inferring σ_{meas} is a matter of finding the most likely value of the signal strength μ given the observed data. Then the measured cross section is simply

$$\sigma_{meas} = \mu\sigma_{SM}. \tag{6.6}$$

One interesting feature of this method is that σ_{SM} is used in the calculation of μ (Eq. (6.4)) and in the final cross section (Eq. (6.6)) in such a way that it cancels out,

and in fact anything proportional to the true cross section may be used. In practice, this means that the order at which σ_{SM} is calculated does not matter to the extent that higher order corrections to the kinematics of the events do not affect ϵ.

Typically, σ_{meas} in Eq. (6.6) is the fiducial cross section, the cross section for the process in a phase space similar to (typically, slightly larger than) the phase space in which the experimental analysis can in principle detect events. In the four-lepton case, the fiducial phase space is a space of $2\ell 2\ell'$ ($\ell, \ell' \in \mathrm{e}, \mu$) events defined by criteria on lepton kinematics, dilepton invariant masses, and four-lepton mass. Table 6.2 shows the fiducial definitions for both the $\mathrm{Z} \to 4\ell$ and $\mathrm{ZZ} \to 4\ell$ cross section measurements. Lepton kinematic requirements and an invariant mass requirement on all opposite-sign, same-flavor lepton pairs in the event are common to both measurements; requirements on the invariant masses of Z/γ^* boson candidates and the four-lepton system are different.

The total ZZ cross section is defined subject to no constraints except the requirement that m_{Z_1} and m_{Z_2} be between 60 and 120 GeV, which serves as the definition of a Z boson. The fiducial cross section is related to the total cross section by the branching fraction $\mathcal{B}$ to the final state in question—here, two factors of the Z/γ^* branching ratio to electron and muon pairs—and an acceptance factor $\mathcal{A}$ which is the fraction of events falling in the fiducial phase space,

$$\sigma_{fid} = \mathcal{A}\sigma_{tot} \left(\mathcal{B}\left(\mathrm{Z} \to 2\ell\right)\right)^2 . \tag{6.7}$$

The acceptance factor $\mathcal{A}$ is determined entirely from theory, and is well known [11], so it is straightforward to calculate the total cross section once the fiducial cross section is known. Calculating both fiducial and total cross sections is interesting because it effectively factorizes experimental and theoretical uncertainties. The experimental uncertainties are contained entirely in the uncertainties on ϵ, $\mathscr{L}_{int}$, and ν_b in Eq. (6.4),

which have little or no dependence on theory, while the theoretical uncertainties are contained entirely in the uncertainty on $\mathcal{A}$, which is determined with no experimental input. Thus the uncertainty on σ_{fid} is entirely experimental, and the theoretical uncertainties enter only in the uncertainty on σ_{tot}.

Table 6.2: Fiducial phase space definitions for the $Z \to 4\ell$ and $ZZ \to 4\ell$ cross section measurements. The common requirements apply to both. The $m_{\ell^+\ell^-}$ criterion is applied to all opposite-sign same-flavor lepton pairs in the event.

Measurement	Fiducial requirements
Common	$p_{\mathrm{T}}^{\ell_1} > 20\,\mathrm{GeV}$, $p_{\mathrm{T}}^{\ell_2} > 10\,\mathrm{GeV}$, $p_{\mathrm{T}}^{\ell_{3,4}} > 5\,\mathrm{GeV}$, $\left\lvert\eta^{\ell}\right\rvert < 2.5$, $m_{\ell^+\ell^-} > 4\,\mathrm{GeV}$
$Z \to 4\ell$	$m_{Z_1} > 40\,\mathrm{GeV}$, $80 < m_{4\ell} < 100\,\mathrm{GeV}$
$ZZ \to 4\ell$	$60 < m_{Z_1}, m_{Z_2} < 120\,\mathrm{GeV}$

6.3.1 Signal Strength Extraction

The signal strength is found by the method of maximum likelihood [11, 209]. The likelihood function is the product of the probability distributions across all bins,

$$L\left(\vec{\theta_s}, \vec{\theta_b}\right) = \prod_{bins} f\left(n; \nu\left(\vec{\theta_s}, \vec{\theta_b}\right)\right). \tag{6.8}$$

The most likely value of ν is the one that maximizes L. In practice, $\log L$ is typically maximized instead because it is easier to work with,

$$\frac{\partial^2 \log L}{\partial\vec{\theta_s}\partial\vec{\theta_b}} = 0. \tag{6.9}$$

This maximization is performed simultaneously for all bins, yielding a single signal strength across all channels. Systematic uncertainties enter as log-normal constraints imposed on the fit, encoded in $\vec{\theta_s}$ and $\vec{\theta_b}$. The fit is performed numerically.

6.3.2 $\mathrm{Z} \to 4\ell$ Branching Fraction

The total Z cross section can be calculated from the $\mathrm{Z} \to 4\ell$ fiducial cross section with Eq. (6.7), but it is better measured in the 2ℓ channel, where the larger branching fraction yields samples several orders of magnitude larger than the $\mathrm{Z} \to 4\ell$ sample used here. It is therefore more interesting to use $\sigma_{fid}\left(\mathrm{Z} \to 4\ell\right)$ for a measurement of the four-lepton branching fraction $\mathcal{B}\left(\mathrm{Z} \to 4\ell\right)$. After applying the acceptance correction to obtain $\sigma_{tot}\left(\mathrm{Z} \to 4\ell\right) = \sigma_{fid}\left(\mathrm{Z} \to 4\ell\right)/\mathcal{A}$, the four-lepton branching fraction is given by

$$\mathcal{B}\left(\mathrm{Z} \to 4\ell\right) = \frac{\sigma_{tot}\left(\mathrm{Z} \to 4\ell\right)}{\mathcal{C}_{80\text{–}100}^{60\text{–}120}\,\sigma\left(\mathrm{Z} \to 2\ell\right)}\mathcal{B}\left(\mathrm{Z} \to 2\ell\right), \tag{6.10}$$

where $\sigma\left(\mathrm{Z} \to 2\ell\right)$ is the dileptonic Z cross section in the 60–120 GeV mass range and $\mathcal{C}_{80\text{–}100}^{60\text{–}120}$ corrects for the fact that $\sigma\left(\mathrm{Z} \to 4\ell\right)$ is found in a mass range of 80–100 GeV.

6.4 Differential Cross Sections

Measurement of a differential fiducial cross section is also a problem of finding the most likely true distribution given observed yields in multiple bins, estimated background yields, and detector effects understood through simulation. Unlike the inclusive cross section, however, finite detector resolution leads to "smearing" effects that cause events to migrate across bins, in addition to the same inefficiencies. The mean detector-level distribution $\vec{\delta}$ is related to the true distribution $\vec{\theta}$ by a response matrix $\mathbf{R}$:

$$\vec{\delta} = \mathbf{R}\vec{\theta}. \tag{6.11}$$

The observed distribution in data $\vec{d}$ is sampled from the Poisson distribution with mean $\vec{\delta}$ independently in each bin. CMS simulation software is sufficiently sophisticated to give a good estimate of R, reproducing the real detector's resolution and smearing effects at the level of a few per cent or better for all distributions of interest.

If $\mathbf{R}$ is square and invertible, the maximum likelihood estimate (MLE) of the true distribution, $\hat{\vec{\theta}}$, is given by

$$\hat{\vec{\theta}} = \mathbf{R}^{-1}\vec{d}. \tag{6.12}$$

Even when $\mathbf{R}$ is invertible, however, it is frequently ill-conditioned, giving $\hat{\vec{\theta}}$ unphysical features like large bin-by-bin fluctuations or even negative bins as a consequence of the stochastic nature of $\vec{d}$. It is therefore necessary to use a more sophisticated procedure to ensure the differential cross section distributions obey physics-inspired constraints. The variables used for differential cross sections in this analysis are in general well-measured, so bin-to-bin fluctuations are small and the response matrices are nearly diagonal, but some bins have low occupancy which can still cause pathologies.

6.4.1 Unfolding

The technique used here is an iterative frequentist method developed in high energy physics by D'Agostini [210] and independently in other fields [211–214], as implemented in RooUnfold [215]. At iteration k, bin j of the predicted true distribution is set based on its expected contribution to all other bins, weighted by the observed data yield in each:

$$\begin{aligned} \theta_j^{(k+1)} &= \sum_i \mathbf{R}_{ij}\theta_j^{(k)}\frac{d_i}{\delta_i} \\ &= \sum_i \mathbf{R}_{ij}\theta_j^{(k)}\frac{d_i}{\sum_m \mathbf{R}_{im}\theta_m^{(k)}}. \end{aligned} \tag{6.13}$$

After several iterations, $\vec{\theta}^{(k)}$ depends only weakly on the ansatz $\vec{\theta}^{(0)}$.

The sequence will converge to the MLE for any non-pathological choice of $\vec{\theta}^{(0)}$ [216] but again the MLE often displays unphysical behavior. If $\vec{\theta}^{(0)}$ is strictly positive, $\vec{\theta}^{(k)}$ will be strictly positive for all k, and in this case $\hat{\vec{\theta}}$ (as defined in Eq. (6.12)) will be the asymptotic unfolded distribution as long as it is also strictly positive. Choosing a

smooth function for $\vec{\theta}^{(0)}$ will generally lead to smooth $\vec{\theta}^{(k)}$ for small k; typical choises include a flat initial distribution and the truth-level distribution used to construct $\mathbf{R}$ (used in this analysis). What constitutes "small" k depends on the condition of $\mathbf{R}$, but for most physics distributions of interest, including all those used in this analysis, nonphysical fluctuations do not arise until after $\vec{\theta}^{(k)}$ is close to convergence. Full regularization is therefore imposed by ceasing iteration early. For all distributions shown here, stopping after four iterations was found to obtain a result close to the asymptotic distribution without artificially increasing the bin-to-bin variance.

6.4.2 Uncertainties

The largest uncertainties in the unfolded distributions arise from the unfolding procedure itself, which can inflate statistical uncertainties present in the detector-level distributions. The correlation matrix which gives the full uncertainty—considered the statistical uncertainty of the unfolded distribution—does not have a closed form due to the nonlinearity of the method. The covariance matrix is therefore estimated by propagating the statistical error of the inputs at each iteration of the method, as laid out in Ref. [210] and improved in Ref. [215]. This procedure does not account for the bias introduced by regularization, but this is expected to be negligible relative to other systematic uncertainties for the well-modeled processes studied here.

Most systematic uncertainties are propagated through unfolding by recomputing the response matrix with the training sample shifted or reweighted to reflect a 1σ shift in the quantity in question. The uncertainty related to that quantity is taken to be the resulting shape difference in the final unfolded distribution. Systematic uncertainties are negligible compared to statistical uncertainties in most bins, as seen in Fig. 6.2, which shows the sources of shape uncertainties on the normalized differential cross section as a function of four-lepton invariant mass.

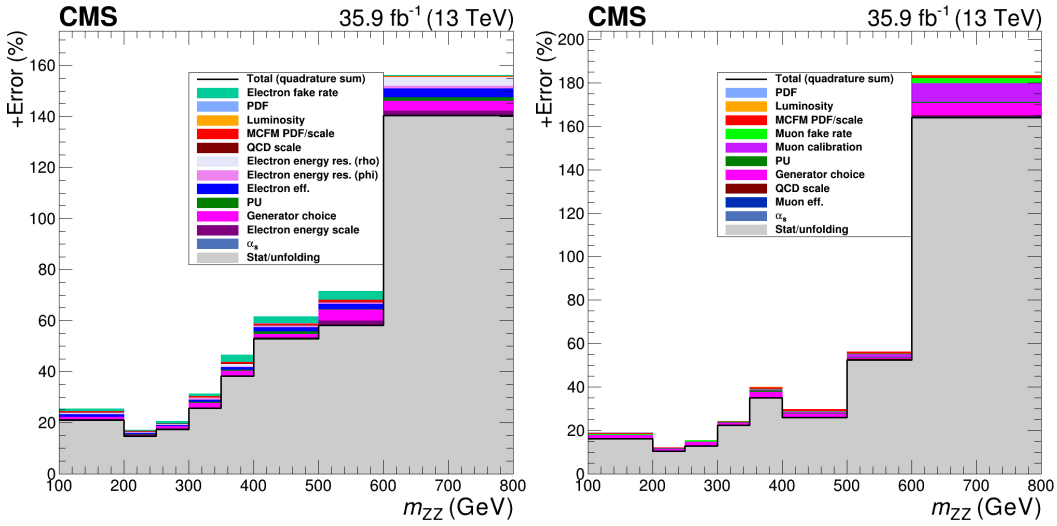

Figure 6.2: Sources of positive shape uncertainties for the normalized differential cross section as a function of four-lepton mass, for 4e events (left) and 4μ events (right). The grey histogram represents statistical errors, propagated through the unfolding procedure, and the histograms stacked on top of it represent various sources of systematic uncertainty. The thick black line represents the sum of all the uncertainties in quadrature. The systematic uncertainties are generally negligible compared to the statistical uncertainty.

6.5 VBS Signal Extraction

The VBS signal search considers events passing the selections described in Section 5.4.3. The electroweak yield is insufficient to have sensitivity at $35.9\,\text{fb}^{-1}$, even with further cut optimization, so a gradient-boosted decision tree (GBDT), implemented with the SCIKIT-LEARN package [217], is used to extract the signal. Hyperparameters of the GBDT are optimized with a grid search. Each Monte Carlo sample used in the VBS search (see Section 4.1.4) is split into a "training" subsample, used to train the GBDT, and a "test" subsample used to evaluate its performance and make templates for use in the statistical analysis. The GBDT performance is nearly the same for the test and training samples, a sign that the algorithm is not overtrained.

A number of observables have been proposed to discriminate VBS events from

background [58], of which m_{jj} and $\Delta\eta_{\mathrm{jj}}$ are the most powerful. Other commonly-used variables include $m_{4\ell}$, $\eta^{\mathrm{j}_1} \times \eta^{\mathrm{j}_2}$, $\Delta\phi_{\mathrm{Z}_1\mathrm{Z}_2}$, and the so-called Zeppenfeld variables, defined as

$$\eta_P^* = \eta_P - \frac{\eta_{\mathrm{j}_1} - \eta_{\mathrm{j}_2}}{2}, \tag{6.14}$$

where P may stand for Z_1, Z_2, or j_3, the highest-p_{T} untagged jet in the event. In addition to these "traditional" quantities, several other groups of observables have been examined, including production angles, decay angles, measures of total hadronic activity in the event, properties of individual leptons and jets and of the ZZjj system, and a discriminator designed to distinguish jets originating from quarks and gluons [218]. The hadronic activity and quark-gluon tagging variables have some discriminating power, but they differ significantly depending on the Monte Carlo generator used and were therefore considered too poorly-modeled to use. New GBDTs were trained, each with the traditional observables and one other group of observables, and the groups that improved the GBDT discrimination power significantly were retained. This procedure yielded 17 observables, including the hard process relative transverse momentum, defined as the ratio of the p_{T} of the ZZjj system to the scalar sum of the p_{T} of each object,

$$p_{\mathrm{T}}^{rel.\ hard} = \frac{p_{\mathrm{T}}^{\mathrm{ZZjj}}}{\sum_{\mathrm{Z}_1,\mathrm{Z}_2,\mathrm{j}_1,\mathrm{j}_2} p_{\mathrm{T}}}, \tag{6.15}$$

and the dijet relative transverse momentum,

$$p_{\mathrm{T}}^{rel.\ \mathrm{jj}} = \frac{p_{\mathrm{T}}^{\mathrm{jj}}}{\sum_{\mathrm{j}_1,\mathrm{j}_2} p_{\mathrm{T}}}. \tag{6.16}$$

The list of observables was further optimized by retraining the GBDT once with each variable dropped and eliminating the one with the least discriminating power. This pruning was repeated until seven observables remained, namely m_{jj}, $\Delta\eta_{\mathrm{jj}}$, $m_{4\ell}$, $\eta^*_{\mathrm{Z}_1}$, $\eta^*_{\mathrm{Z}_2}$, $p_{\mathrm{T}}^{rel.\ hard}$, and $p_{\mathrm{T}}^{rel.\ \mathrm{jj}}$. The resulting GBDT performs only marginally worse (0.2σ less expected significance on the VBS signal) than a version with all observables

included, and is faster and easier to train, simpler, and less susceptible to biases and systematic uncertainties from mismodeling.

The signal and background yields are extracted from the GBDT output spectrum with a binned maximum likelihood fit to templates from the test Monte Carlo samples. To obtain templates with better fit convergence properties, the GBDT output is mapped to the range $[0, 1]$ with the logistic transformation

$$x \to \frac{1}{1 - e^{-x}}. \tag{6.17}$$

This provides better separation between signal and background and allows uniform binning in the templates.

6.6 Anomalous Gauge Coupling Searches

The new physics represented by aGCs would generally manifest as an increase in events with high invariant mass, so it is natural to use the shape of the $m_{4\ell}$ distribution for the search. For the aTGC search, the doubly on-shell ZZ selection is used, while the aQGC search is performed with the ZZjj selection described in Section 5.4.3.

Monte Carlo samples with nonzero aTGCs are generated at grids of points in the f_4^{Z}-f_4^{γ} and f_5^{Z}-f_5^{γ} planes. In each bin of the $m_{4\ell}$ distribution, the yields at the various working points are fit to a function of the form

$$y\left(f^{\mathrm{Z}}, f^{\gamma}\right) = x_0 + x_1 f^{\mathrm{Z}} + x_2 f^{\gamma} + x_3 f^{\mathrm{Z}} f^{\gamma} + x_4 \left(f^{\mathrm{Z}}\right)^2 + x_5 \left(f^{\gamma}\right)^2 \tag{6.18}$$

where $y\left(f^{\mathrm{Z}}, f^{\gamma}\right)$ is the yield in the bin, f^{V} can be f_4^{Z} and f_4^{γ} or f_5^{Z} and f_5^{γ}, and x_i are the parameters to be fit.

A similar procedure is performed for the aQGC search. Rather than simulating a full sample for each working point, which is computationally expensive, events from MadGraph5_aMC produced at LO are used to obtain samples for nonzero values

of $f_{\mathrm{T0}}/\Lambda^4$, $f_{\mathrm{T1}}/\Lambda^4$, $f_{\mathrm{T2}}/\Lambda^4$, $f_{\mathrm{T8}}/\Lambda^4$, and $f_{\mathrm{T9}}/\Lambda^4$ by matrix element reweighting [149]. The yields in each $m_{4\ell}$ bin are fit to parabolas as a function of the five aQGC parameters separately.

A binned profile likelihood method [11] is used to derive the limits. Systematic uncertainties are taken into account by varying the number of signal and background events within their uncertainties. Exclusion limits are found by comparing the p-values of the signal hypothesis and the background only hypothesis

$$CL_s = \frac{p_{s+b}}{1 - p_b} \tag{6.19}$$

to set thresholds. Further details on the method can be found in Ref. [219]. The software for setting limits, implemented with RooStats, has been validated and used extensively by the CMS and ATLAS collaborations [220].

Chapter 7

Results

A number of measurements and analyses fall under the umbrella of four-lepton physics, and results presented in this thesis were originally made public in several journal articles and Physics Analysis Summary documents released by the CMS collaboration. The first CMS measurement of the ZZ inclusive cross section at 13 TeV used roughly half the 2015 dataset ($1.34\,\text{fb}^{-1}$) and was made public in Ref. [221] in December 2015 as one of the first measurements done on 13 TeV collision data. That analysis was expanded to use the whole $2.6\,\text{fb}^{-1}$ collected in 2015, and to include the $\text{Z} \to 4\ell$ branching fraction measurement, as reported in Ref. [222], submitted in July 2016 and published the following December. With the full 2016 dataset, the ZZ cross section and $\text{Z} \to 4\ell$ branching ratio were measured again to greater precision in Ref. [80], which also included differential cross section measurements and aTGC limits, made public in March 2017. A new paper including these measurements [223] also includes a combination of the 2015 and 2016 inclusive cross section measurements. Differential cross sections with respect to jet-related observables, and searches for EWK ZZ production and aTGCs, were reported in May 2017 in Ref. [224], with a paper on only the VBS and aQGC searches following [225]. The Higgs boson was

studied in the four-lepton final state in Refs. [226–228]. In the following, results for each topic are only shown for 2016 data, which significantly exceed the accuracy of the results from 2015 data.

7.1 Four-Lepton Yields and Inclusive Cross Sections

7.1.1 Full Spectrum

The full four-lepton invariant mass spectrum is shown in Fig. 7.1. The single-Z resonance can be seen below 100 GeV, the Higgs resonance is visible—though it is not sharply resolved with this binning—in the Z/γ^* region below $2m_Z$, where doubly resonant ZZ continuum production begins. The dilepton invariant mass spectrum is shown for both Z/γ^* candidates in Fig. 7.2 and for the Z/γ^* candidate closest to the nominal Z boson mass (Z_1) in Fig. 7.3. Figure 7.4 shows m_{Z_2} plotted against m_{Z_1} for data events representative of all four-lepton production. Clusters of events with zero ($Z \to 4\ell$ and nonresonant $\gamma^*\gamma^*$ production), one ($H \to ZZ^*$ and nonresonant $Z\gamma^*$ production), and two (nonresonant ZZ production) on-shell Z bosons can be clearly seen.

7.1.2 $Z \to 4\ell$ Resonance

Expected and observed yields for events satisfying the $Z \to 4\ell$ selection criteria ($80 < m_{4\ell} < 100$ GeV) are shown in Table 7.1. The invariant mass distribution of these events is shown in Fig. 7.5. Figure 7.6 shows m_{Z_2} plotted against m_{Z_1} for all data events consistent with $Z \to 4\ell$ production. Predictions from Monte Carlo

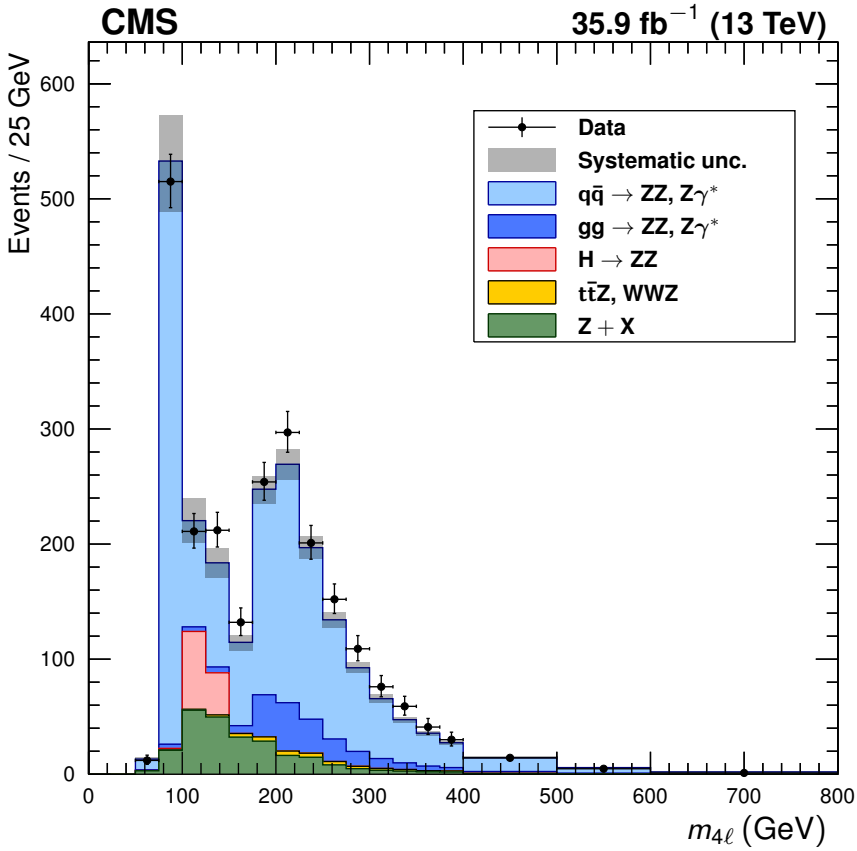

Figure 7.1: Distribution of the four-lepton invariant mass $m_{4\ell}$ of all events in the full spectrum selection. Points represent data, with statistical uncertainty bars. The stack of filled histograms represents the SM signal prediction and background estimate, with a grey band showing the sum in quadrature of the statistical and systematic uncertainties on the total expected yield.

samples generally agree well with the data, allowing us to measure the $Z \to 4\ell$ cross section and branching fraction.

The signal strength in the $Z \to 4\ell$ selection is

$$\mu = 0.980^{+0.046}_{-0.044}\,(\text{stat})^{+0.065}_{-0.059}\,(\text{syst}) \pm 0.025\,(\text{lumi}), \tag{7.1}$$

yielding a fiducial cross section

$$\sigma_{\text{fid}}\,(\text{pp} \to \text{Z} \to 4\ell) = 31.2^{+1.5}_{-1.4}\,(\text{stat})^{+2.1}_{-1.9}\,(\text{syst}) \pm 0.8\,(\text{lumi})\,\text{fb}. \tag{7.2}$$

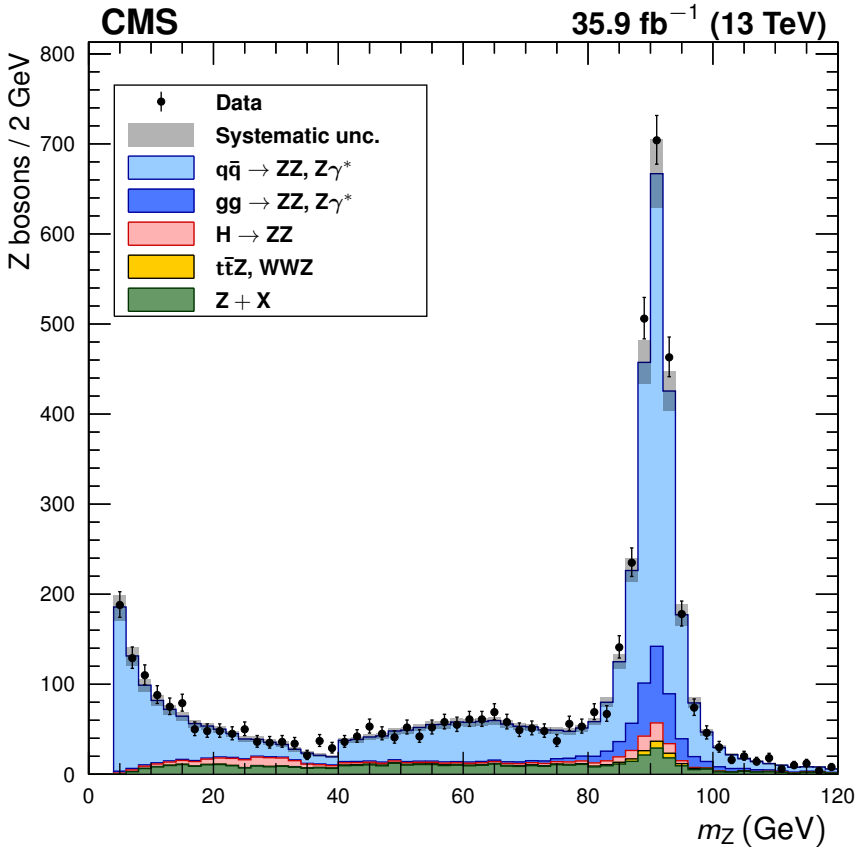

Figure 7.2: Distribution of the dilepton invariant mass of Z/γ^* candidates in all events in the full spectrum selection, regardless of whether the lepton pair is labeled Z_1 or Z_2. Points represent data, with statistical uncertainty bars. The stack of filled histograms represents the SM signal prediction and background estimate, with a grey band showing the sum in quadrature of the statistical and systematic uncertainties on the total expected yield.

Table 7.1: Observed and expected yields of $Z \to 4\ell$ events, including expected background yields, shown for each final state and summed to the total. Uncertainties are statistical, then systematic, not including the integrated luminosity uncertainty.

Final state	Expected $N_{4\ell}$	Background	Total expected	Observed
4μ	$224 \pm 1 \pm 16$	$7 \pm 1 \pm 2$	$231 \pm 2 \pm 17$	225
$2e2\mu$	$207 \pm 1 \pm 14$	$9 \pm 1 \pm 2$	$216 \pm 2 \pm 14$	206
4e	$68 \pm 1 \pm 8$	$4 \pm 1 \pm 2$	$72 \pm 1 \pm 8$	78
Total	$499 \pm 2 \pm 32$	$19 \pm 2 \pm 5$	$518 \pm 3 \pm 33$	509

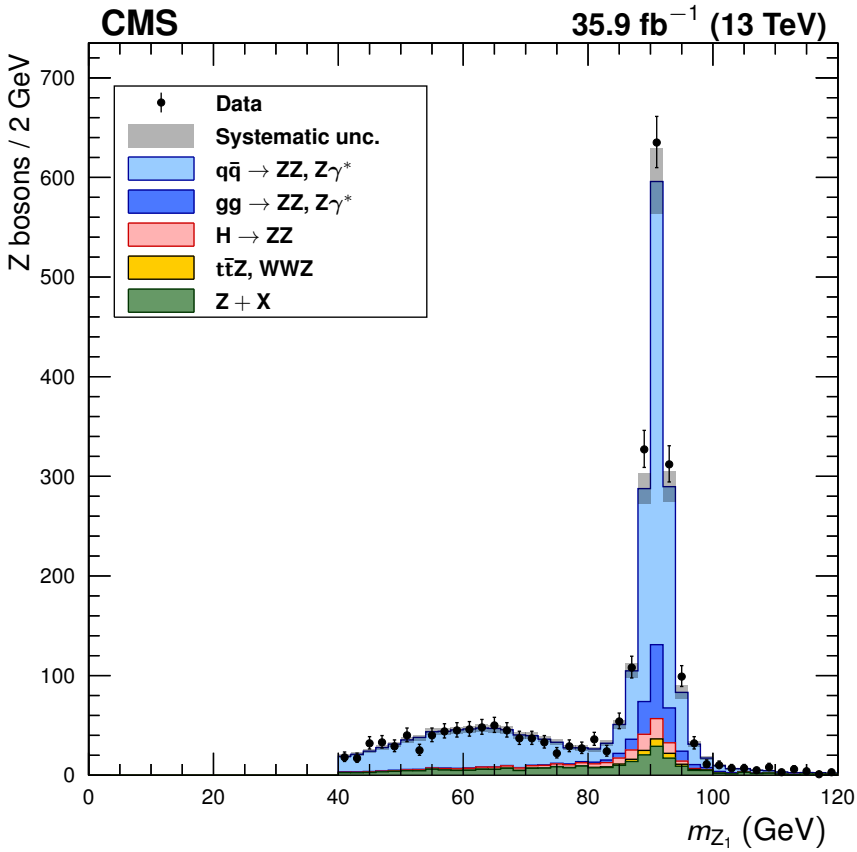

Figure 7.3: Distribution of the dilepton invariant mass of Z_1, the Z/γ^* candidate in each event closest to the nominal m_Z, in the full spectrum selection. Points represent data, with statistical uncertainty bars. The stack of filled histograms represents the SM signal prediction and background estimate, with a grey band showing the sum in quadrature of the statistical and systematic uncertainties on the total expected yield.

This is scaled by an acceptance correction factor $\mathcal{A} = 0.125 \pm 0.002$, estimated with POWHEG v2.0, to the total $Z \to 4\ell$ cross section times branching ratio,

$$\sigma(pp \to Z) \times \mathcal{B}(Z \to 4\ell) = 249 \pm 8\,(\text{stat})^{+9}_{-8}\,(\text{syst}) \pm 4\,(\text{theo}) \pm 6\,(\text{lumi})\,\text{fb}. \quad (7.3)$$

Equation (6.10) is used to calculate the branching fraction. The Z cross section times dilepton branching ratio is calculated with FEWZ v2.0 [229] at NNLO in QCD to be $\sigma(Z \to 2\ell) = 1870^{+50}_{-40}\,\text{pb}$. The Z mass window correction factor is calculated with POWHEG and found to be $C^{60\text{–}120}_{80\text{–}100} = 0.926 \pm 0.001$. Its uncertainty includes

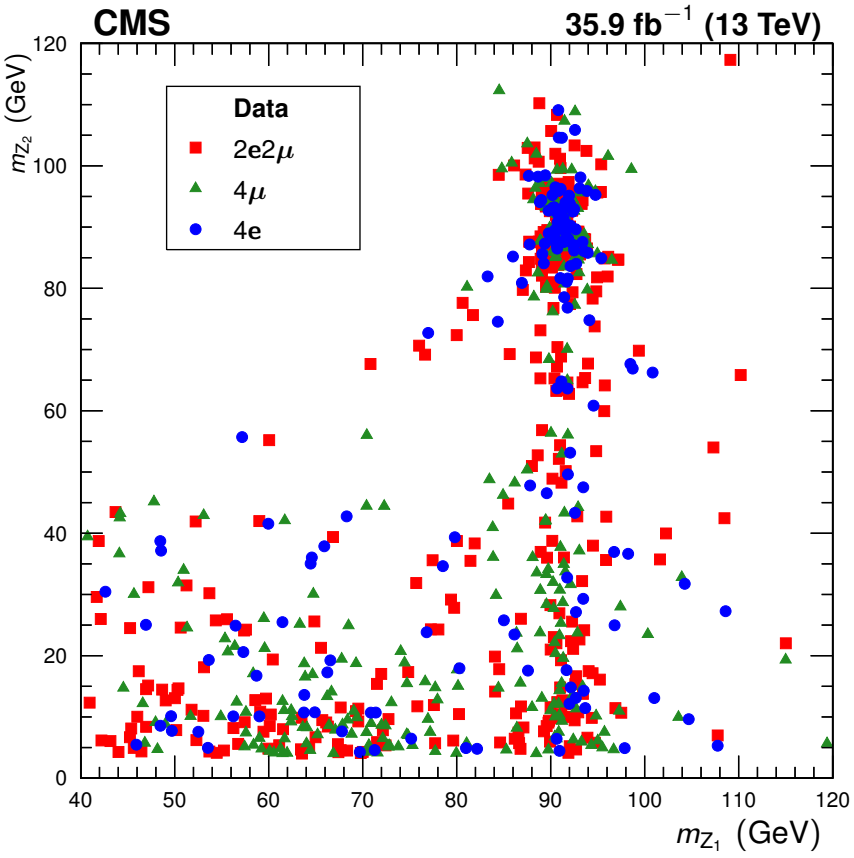

Figure 7.4: The reconstructed m_{Z_2} plotted against the reconstructed m_{Z_1} for data events in the full spectrum selection, with distinctive markers for each final state. For readability, only every fourth event is drawn. Clusters of events from different production modes are visible, as discussed in the text.

scale and PDF variations [208]. The nominal Z to dilepton branching fraction is $\mathcal{B}(\mathrm{Z} \to 2\ell) = 0.03366$ [11]. The four-lepton branching fraction is measured to be

$$\mathcal{B}(\mathrm{Z} \to 4\ell) = 4.8 \pm 0.2\,(\mathrm{stat}) \pm 0.2\,(\mathrm{syst}) \pm 0.1\,(\mathrm{theo}) \pm 0.1\,(\mathrm{lumi}) \times 10^{-6}. \quad (7.4)$$

This value is consistent with the theoretical value of 4.6×10^{-6}, calculated with MadGraph5_aMC@NLO v2.3.3, and with previous measurements from CMS and ATLAS [90, 91, 222], which had uncertainties 2–4 times larger.

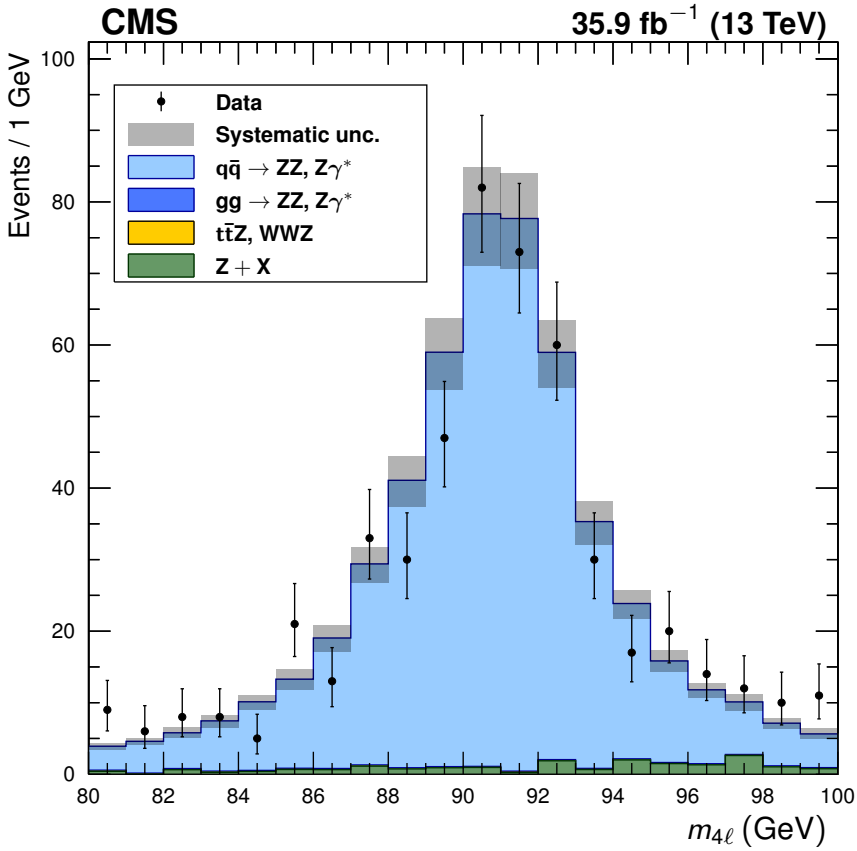

Figure 7.5: Distribution of the four-lepton invariant mass $m_{4\ell}$ of all events in the mass range $80 < m_{4\ell} < 100\,\text{GeV}$, the $Z \to 4\ell$ selection. Points represent data, with statistical uncertainty bars. The stack of filled histograms represents the SM signal prediction and background estimate, with a grey band showing the sum in quadrature of the statistical and systematic uncertainties on the total expected yield.

7.1.3 Higgs Resonance

Figure 7.7 shows the four-lepton invariant mass around the Higgs resonance, which can be clearly seen above the SM continuum background, for events passing the Higgs selection ($m_{Z_2} > 12\,\text{GeV}$, $\text{SIP}_{3D} < 4$ for all leptons). Table 7.2 shows the observed and expected yields in the mass range $118 < m_{4\ell} < 130\,\text{GeV}$. Here, SM continuum production—considered signal in all other parts of this analysis—is considered background. Figures 7.8–7.10 show the Z_1 mass, the Z_2 mass, and the scatter plot of

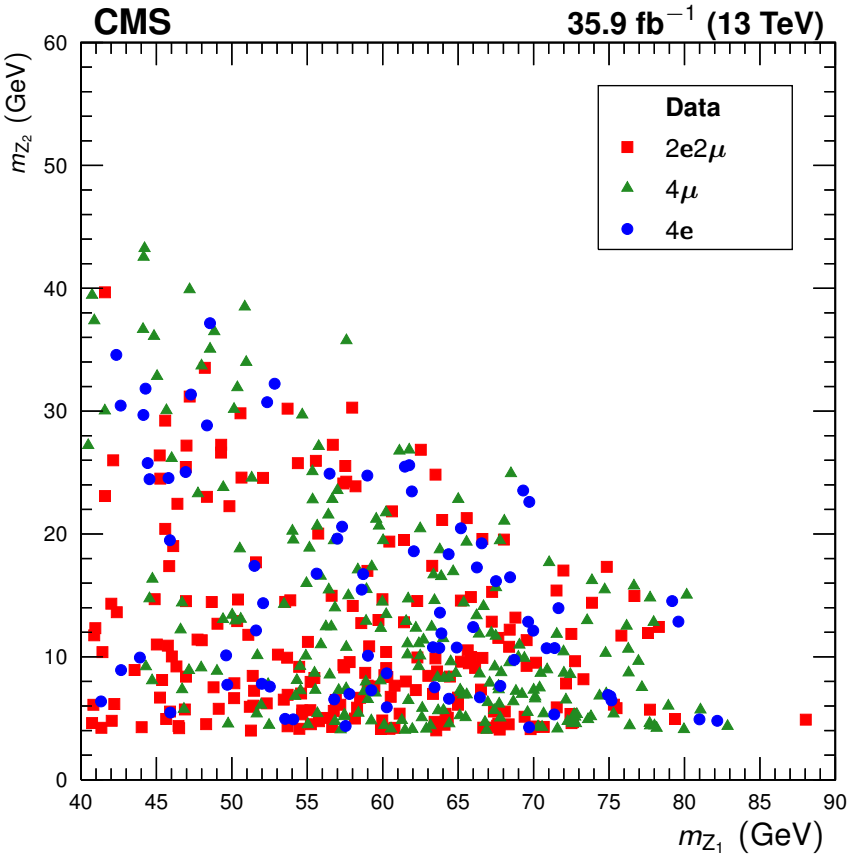

Figure 7.6: The reconstructed m_{Z_2} plotted against the reconstructed m_{Z_1} for all data events with $80 < m_{4\ell} < 100\,\text{GeV}$, with distinctive markers for each final state.

m_{Z_2} against m_{Z_1}, for events in the same four-lepton mass region around the Higgs resonance. Agreement between predictions and data is again good, allowing measurements of Higgs boson properties, couplings, and production rates. These are beyond the scope of this thesis, but were reported in Ref. [228].

7.1.4 ZZ Production

Expected and observed yields for on-shell ZZ events are shown in Table 7.3. The corresponding four-lepton and Z boson candidate invariant masses are shown in Figs. 7.11 and 7.12, respectively. Figure 7.13 shows the distribution of the number of jets (N_{jets})

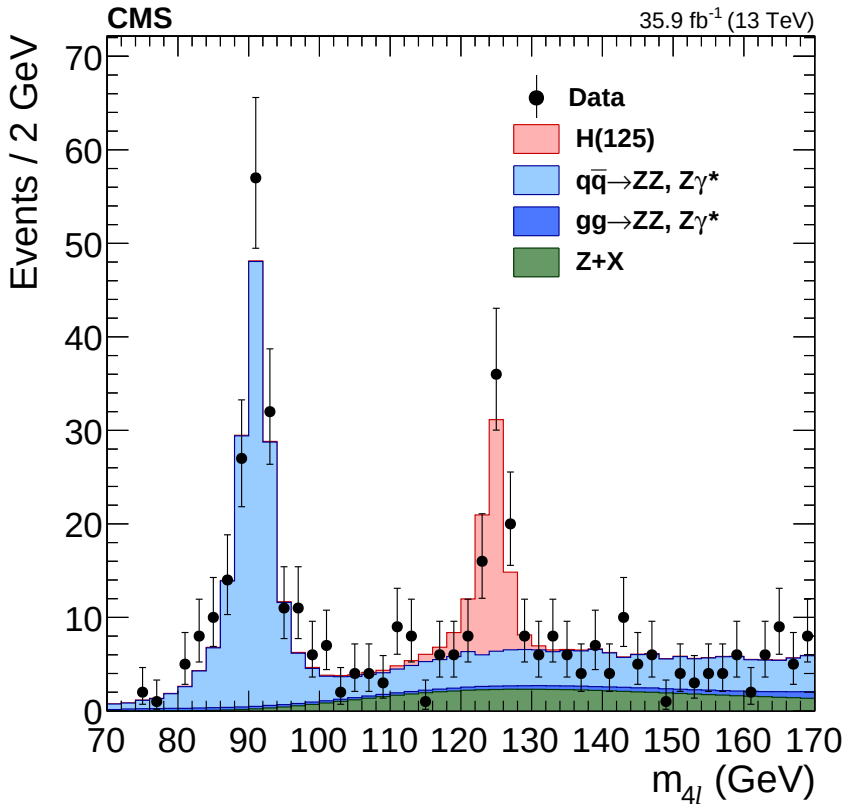

Figure 7.7: Distribution of the four-lepton invariant mass $m_{4\ell}$ for events in the Higgs selection. Points represent data, with statistical uncertainty bars. The stack of filled histograms represents the signal and SM background predictions and the reducible background estimate.

Table 7.2: Observed and expected yields of $\mathrm{H} \to \mathrm{ZZ}^* \to 4\ell$ events, including expected background yields, for events passing the Higgs selection in the mass range $118 < m_{4\ell} < 130\,\mathrm{GeV}$, shown for each final state and summed to the total. Uncertainties are statistical and systematic combined.

Final state	Expected N_{H}	SM continuum background	Z + X	Total expected	Observed
4μ	21.6 ± 1.9	$9.4^{+0.6}_{-0.7}$	$4.7^{+2.0}_{-1.8}$	35.8 ± 2.9	34
$2\mathrm{e}2\mu$	26.5 ± 2.3	$11.0^{+0.7}_{-0.8}$	$6.9^{+3.1}_{-2.9}$	$44.4^{+3.7}_{-3.6}$	41
4e	10.2 ± 1.1	3.6 ± 0.3	$1.9^{+0.8}_{-1.0}$	15.8 ± 1.6	19
Total	58.3 ± 5.0	$24.1^{+1.5}_{-1.6}$	$13.5^{+3.7}_{-3.5}$	96.0 ± 6.7	94

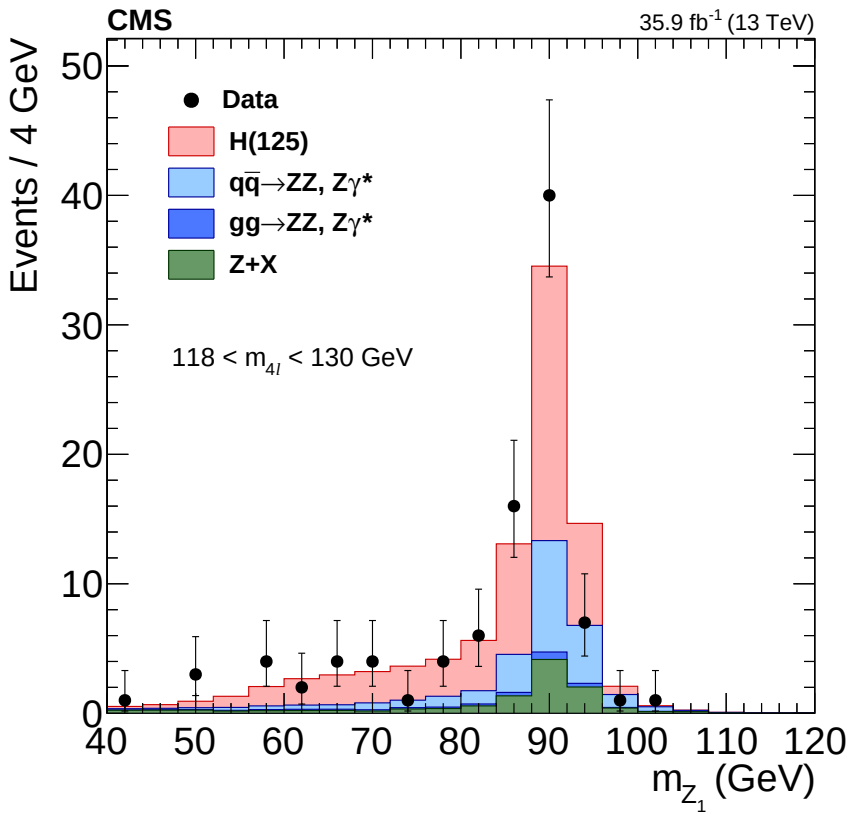

Figure 7.8: Distribution of the dilepton invariant mass of Z_1, the dilepton candidate in each event closest to the nominal m_Z, in events in the Higgs selection with $118 < m_{4\ell} < 130\,\text{GeV}$. Points represent data, with statistical uncertainty bars. The stack of filled histograms represents the signal and SM background predictions and the reducible background estimate.

in these events. The leading and subleading jet p_T are shown separately in Fig. 7.14, and the leading and subleading jet $|\eta|$ are shown separately in Fig. 7.15, for all events with at least one (leading) or two (subleading) jets. Figures 7.16 and 7.17 show the m_{jj} and $|\Delta\eta_{jj}|$ distributions for tagging jet pairs in the dijet selection. Again, agreement is good overall, indicating that the observables shown are well modeled up to the precision achievable with current data. These are the first such distributions published at $\sqrt{s} = 13\,\text{TeV}$, and statistical uncertainties are smaller than those published at any energy, allowing theorists to make more detailed comparisons to their models

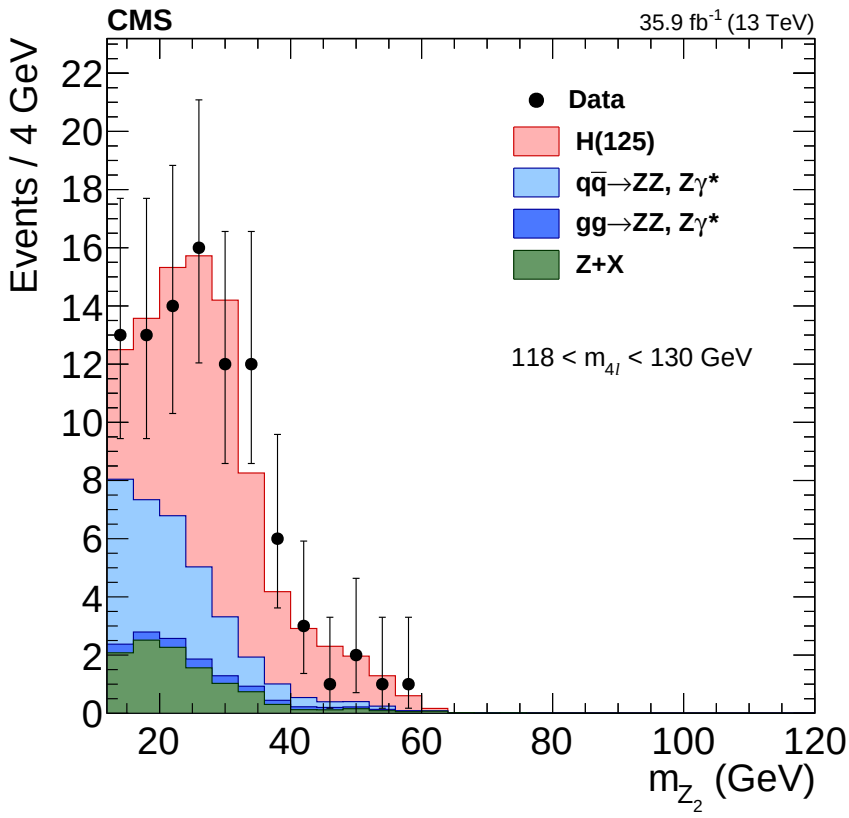

Figure 7.9: Distribution of the dilepton invariant mass of Z_2, the dilepton candidate in each event farther from the nominal m_Z, in events in the Higgs selection with $118 < m_{4\ell} < 130\,\text{GeV}$. Points represent data, with statistical uncertainty bars. The stack of filled histograms represents the signal and SM background predictions and the reducible background estimate.

and, in the case of the jet-related distributions, to QCD and shower modeling.

The yields shown in Table 7.3 and the systematic uncertainties of Table 6.1 are used as inputs to the maximum likelihood method described in Section 6.3.1 to obtain the on-shell ZZ signal strength across all four-lepton final states,

$$\mu = 1.040^{+0.033}_{-0.032}\,(\text{stat})^{+0.037}_{-0.035}\,(\text{syst}) \pm 0.026\,(\text{lumi}), \tag{7.5}$$

which gives a fiducial cross section

$$\sigma_{\text{fid}}(\text{pp} \to \text{ZZ} \to 4\ell) = 40.9 \pm 1.3\,(\text{stat}) \pm 1.4\,(\text{syst}) \pm 1.0\,(\text{lumi})\,\text{fb}, \tag{7.6}$$

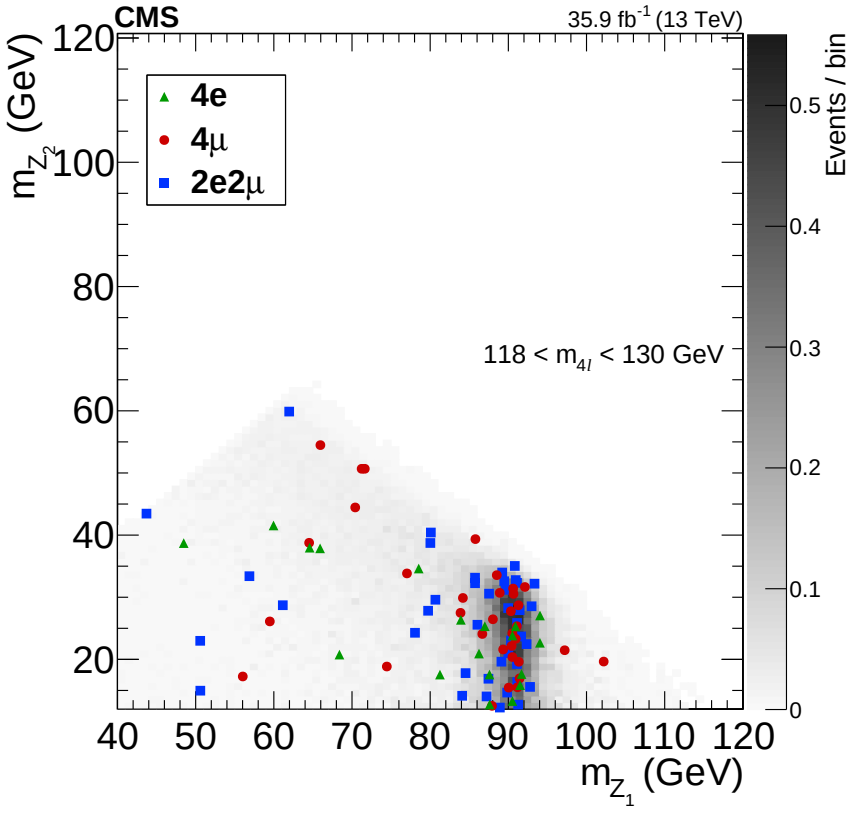

Figure 7.10: The reconstructed m_{Z_2} mass plotted against the reconstructed m_{Z_1} for data events in the Higgs selection with $118 < m_{4\ell} < 130\,\text{GeV}$, with distinctive markers for each final state. The shading represents the expected number of events in the bin.

Table 7.3: Observed and expected yields of ZZ events, including expected background yields, in the on-shell selection, shown for each final state and summed to the total. Uncertainties are statistical, then systematic, not including the integrated luminosity uncertainty.

Final state	Expected N_{ZZ}	Background	Total expected	Observed
4μ	$301 \pm 2 \pm 9$	$10 \pm 1 \pm 2$	$311 \pm 2 \pm 9$	335
$2e2\mu$	$503 \pm 2 \pm 19$	$31 \pm 2 \pm 4$	$534 \pm 3 \pm 20$	543
4e	$205 \pm 1 \pm 12$	$20 \pm 2 \pm 2$	$225 \pm 2 \pm 13$	220
Total	$1009 \pm 3 \pm 36$	$60 \pm 3 \pm 8$	$1070 \pm 4 \pm 37$	1098

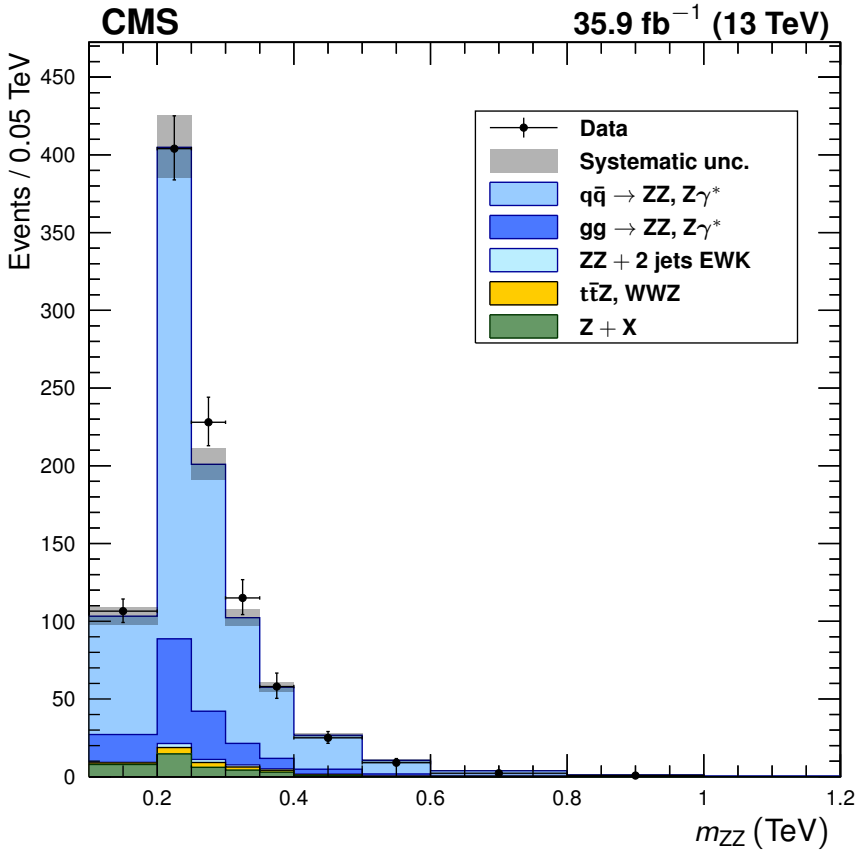

Figure 7.11: Distribution of the four-lepton invariant mass m_{ZZ} of all events in the on-shell selection. Points represent data, with statistical uncertainty bars. The stack of filled histograms represents the SM signal prediction and background estimate, with a grey band showing the sum in quadrature of the statistical and systematic uncertainties on the total expected yield.

in the $ZZ \rightarrow 4\ell$ fiducial phase space of Table 6.2. The corresponding total cross section is

$$\sigma(\mathrm{pp} \rightarrow \mathrm{ZZ}) = 17.5^{+0.6}_{-0.5}\,(\mathrm{stat}) \pm 0.6\,(\mathrm{syst}) \pm 0.4\,(\mathrm{theo}) \pm 0.4\,(\mathrm{lumi})\,\mathrm{pb}. \qquad (7.7)$$

This measurement, on 2016 data, agrees with the result of the 2015 measurement [222],

$$\sigma(\mathrm{pp} \rightarrow \mathrm{ZZ}) = 14.6^{+1.9}_{-1.8}\,(\mathrm{stat})^{+0.3}_{-0.5}\,(\mathrm{syst}) \pm 0.2\,(\mathrm{theo}) \pm 0.4\,(\mathrm{lumi})\,\mathrm{pb}. \qquad (7.8)$$

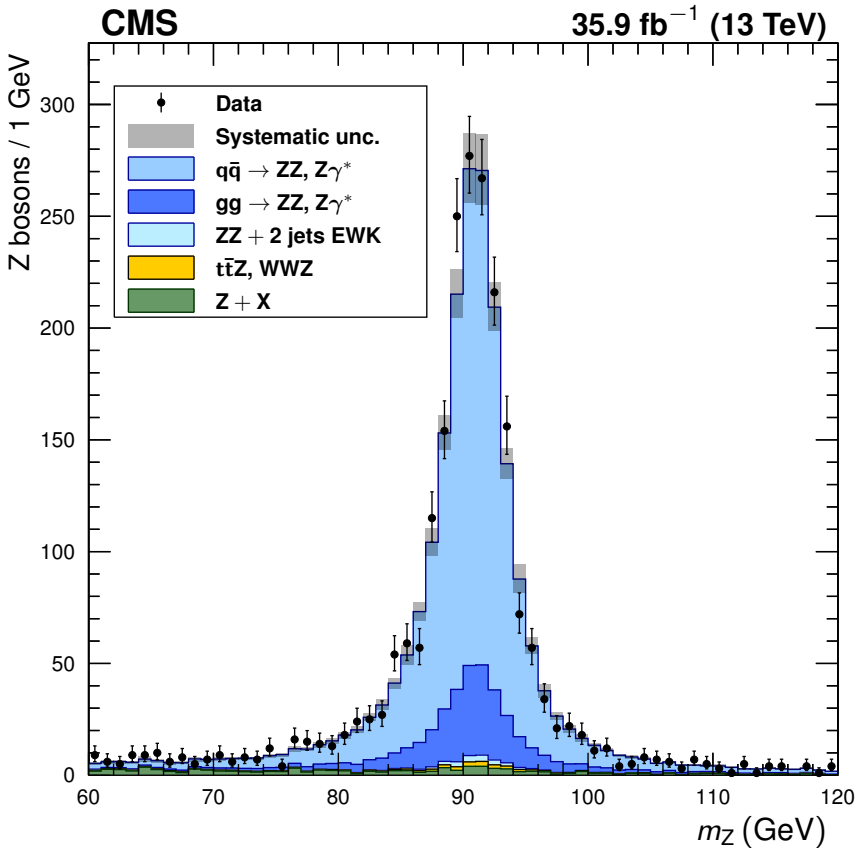

Figure 7.12: Distribution of the dilepton invariant mass of Z candidates in all events in the on-shell selection, regardless of whether the lepton pair is labeled Z_1 or Z_2. Points represent data, with statistical uncertainty bars. The stack of filled histograms represents the SM signal prediction and background estimate, with a grey band showing the sum in quadrature of the statistical and systematic uncertainties on the total expected yield.

One may combine the measurements by doing a six-bin simultaneous fit with the bins representing the same final state in 2015 and 2016 considered separately. The degree of correlation between the systematic uncertainties in the 2015 and 2016 runs is not known, but the 2015 contribution is small enough that the systematic uncertainties are dominated by those in the 2016 dataset, and the degree of correlation will have only a small effect on the measurement. We therefore do the fit twice, once treating the experimental uncertainties as fully correlated between the datasets, and again

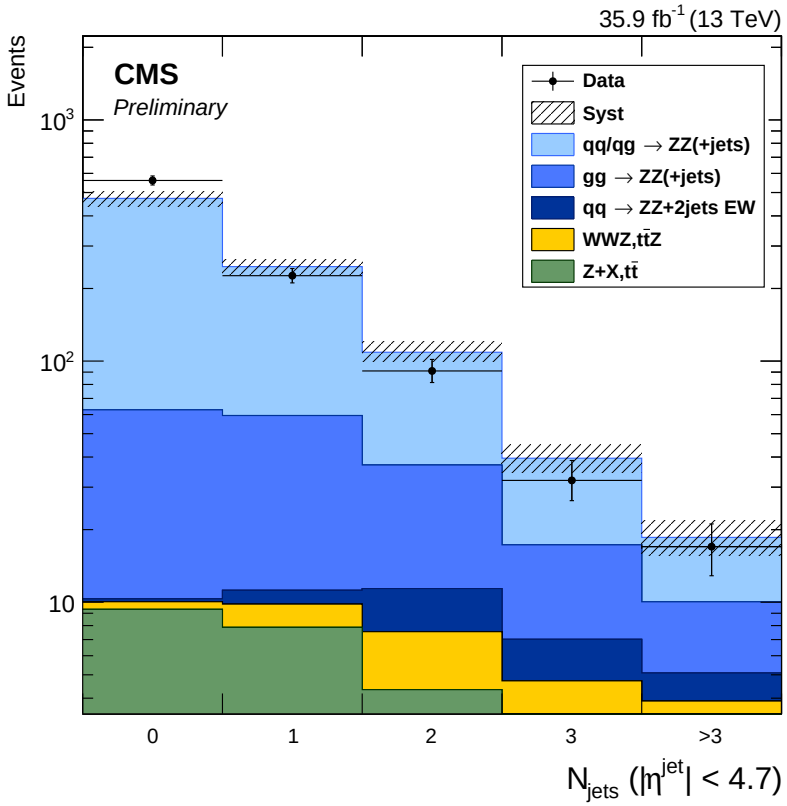

Figure 7.13: Distribution of jet multiplicity in ZZ events. Points represent data, with statistical uncertainty bars. The stack of filled histograms represents the SM signal prediction and background estimate, with a hatched band showing the sum in quadrature of the statistical and systematic uncertainties on the total expected yield.

treating them as fully uncorrelated. The small difference in the central value obtained is added linearly to the systematic error of the result. After the full combination, the "2015 + 2016" total cross section is found to be

$$\sigma(\mathrm{pp} \to \mathrm{ZZ}) = 17.2 \pm 0.5\,(\mathrm{stat}) \pm 0.7\,(\mathrm{syst}) \pm 0.4\,(\mathrm{theo}) \pm 0.4\,(\mathrm{lumi})\,\mathrm{pb}. \qquad (7.9)$$

These results can be compared to the MATRIX v1.0.0_beta4 prediction of $16.2^{+0.6}_{-0.4}$ pb, computed at NNLO in QCD, or the MCFM v7.0 prediction of $15.0^{+0.7}_{-0.6} \pm 0.2$ pb, calculated at NLO in QCD with LO gg $\to$ ZZ diagrams included. Both predictions use the NNPDF3.0 PDF sets and fixed scales $\mu_\mathrm{F} = \mu_\mathrm{R} = m_\mathrm{Z}$.

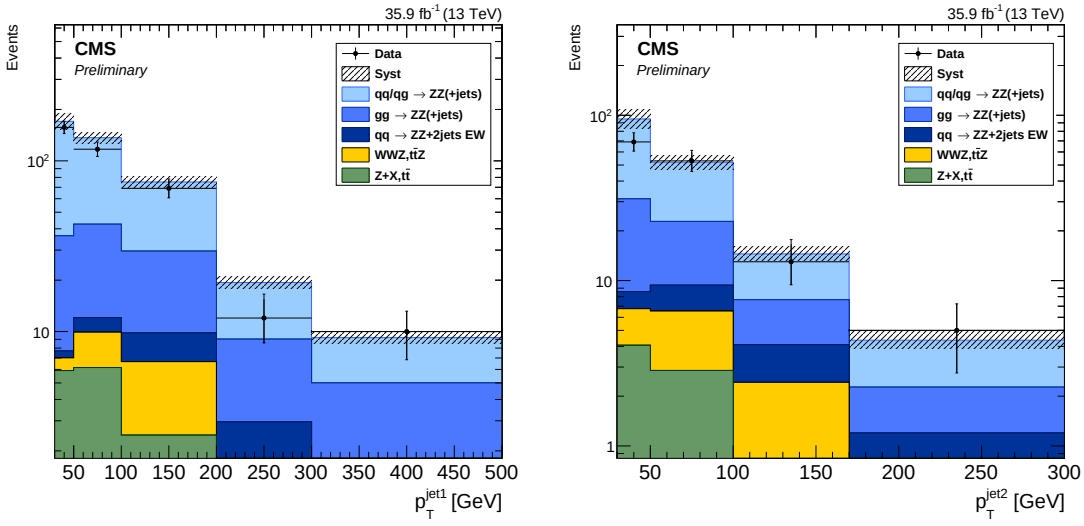

Figure 7.14: Distribution of leading (left) and subleading (right) jet p_{T} for all ZZ events with at least one jet and at least two jets, respectively. Points represent data, with statistical uncertainty bars. The stack of filled histograms represents the SM signal prediction and background estimate, with a hatched band showing the sum in quadrature of the statistical and systematic uncertainties on the total expected yield.

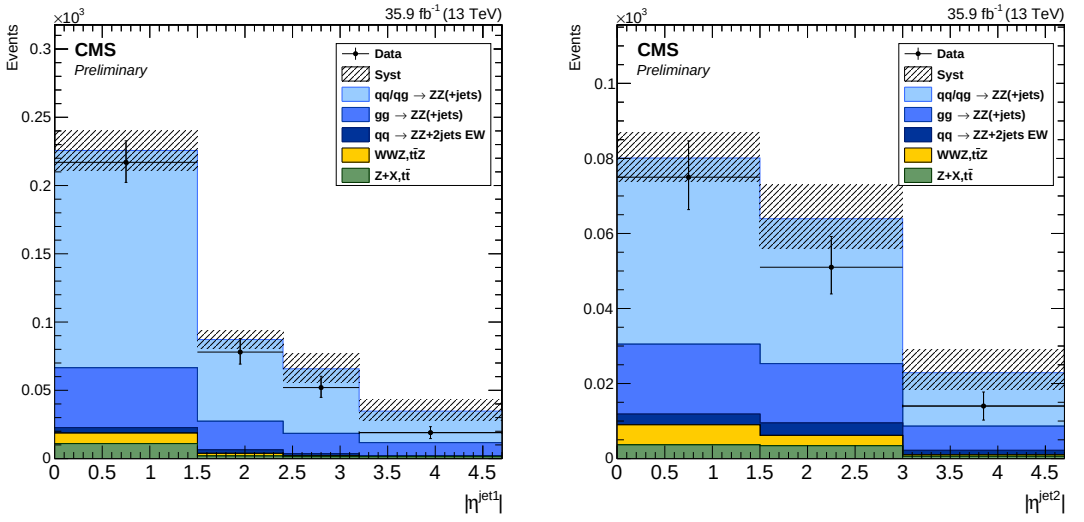

Figure 7.15: Distribution of leading (left) and subleading (right) jet $|\eta|$ for all ZZ events with at least one jet and at least two jets, respectively. Points represent data, with statistical uncertainty bars. The stack of filled histograms represents the SM signal prediction and background estimate, with a hatched band showing the sum in quadrature of the statistical and systematic uncertainties on the total expected yield.

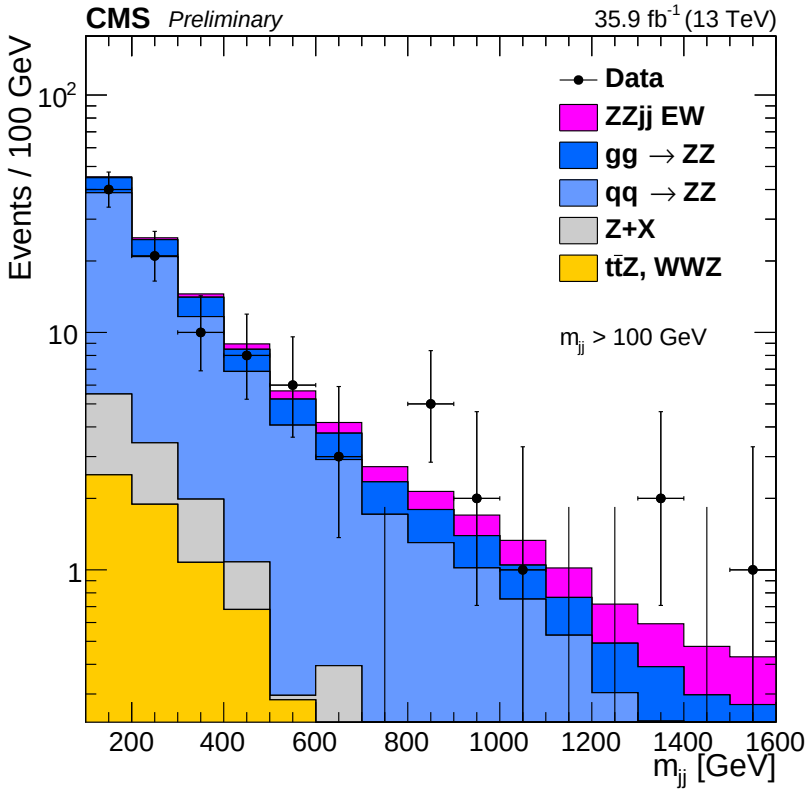

Figure 7.16: Dijet invariant mass m_{jj} of the tag jets in ZZ events passing the dijet selection ($m_{\mathrm{jj}} > 100\,\mathrm{GeV}$). Points represent data, with statistical uncertainty bars. The stack of filled histograms represents the SM signal prediction, including EWK production, and background estimate.

The total cross section is shown as a function of $\sqrt{s}$ in Fig. 7.18. Measurements from CMS [72–74, 222] and ATLAS [76, 77, 108] are compared to NLO predictions made with MCFM (with contributions from leading order gluon-gluon fusion diagrams), and NNLO predictions made with MATRIX. Results from both experiments agree with the predictions, verifying this aspect of the SM to within the measurements' uncertainties.

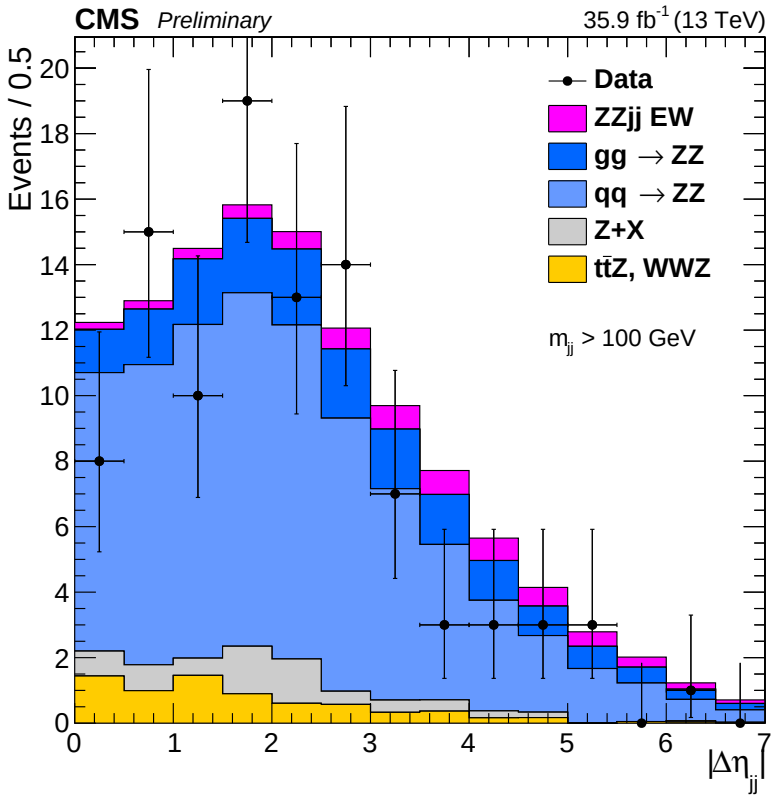

Figure 7.17: Pseudorapidity separation $|\Delta\eta_{jj}|$ of tag jets in ZZ events passing the dijet selection ($m_{jj} > 100\,\text{GeV}$). Points represent data, with statistical uncertainty bars. The stack of filled histograms represents the SM signal prediction, including EWK production, and background estimate.

7.2 Differential Cross Sections

Detector-level distributions are unfolded to calculate differential cross sections as described in Section 6.4. Figures 7.19–7.30 show measured differential cross sections and corresponding theory predictions, as functions of different observables. All distributions are normalized to the inclusive fiducial cross section, such that the integral of each is unity, including overflow bins (not shown). The observables in Figs. 7.19–7.24 consider only the four-lepton system. For the calculation of these distributions, as well as the differential cross section as a function of N_{jets} (Fig. 7.25), all events

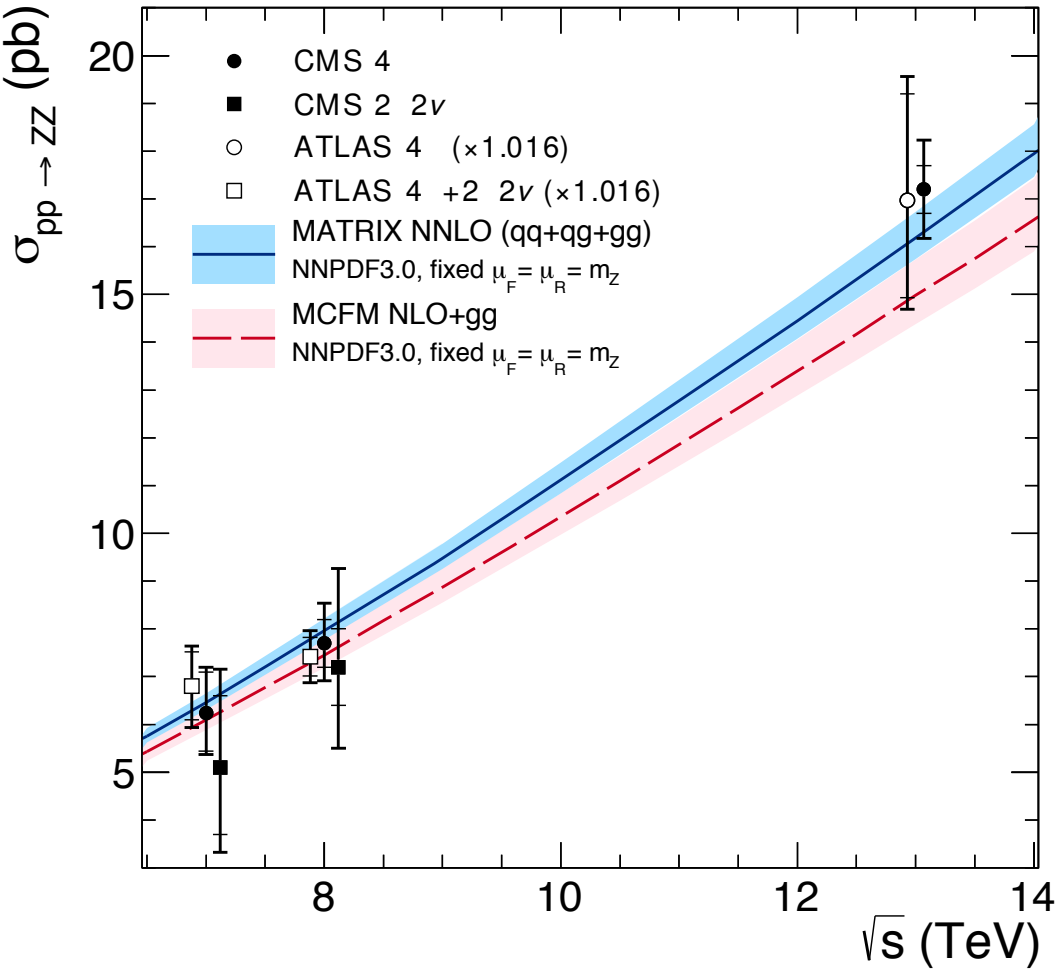

Figure 7.18: The total ZZ cross section is shown as a function of $\sqrt{s}$. Measurements from CMS and ATLAS are both shown, with the ATLAS numbers adjusted upward by 1.6% to account for differences in Z mass window choice. Points at the same center-of-mass energy are shifted slightly in the horizontal direction for clarity. Experimental measurements are compared to predictions from MCFM at NLO in QCD with additional contributions from LO gluon-gluon fusion diagrams, and MATRIX at NNLO in QCD. Both sets of predictions use the NNPDF3.0 PDF sets and fixed scales $\mu_{\mathrm{F}} = \mu_{\mathrm{R}} = m_{\mathrm{Z}}$.

passing the on-shell selection of Table 6.2 are used. Figures 7.26 and 7.27 show m_{jj} and $|\Delta\eta_{\mathrm{jj}}|$ for all ZZ events with at least two jets, while Figs 7.28 and 7.29 show p_{T} and η, respectively, for the leading jet in events with $N_{\mathrm{jets}} \geq 1$ on the left and the subleading jet in events with $N_{\mathrm{jets}} \geq 2$ on the right. In Fig. 7.30, the phase space is expanded to the full spectrum selection of Table 6.2 at both detector and true level, to show the four-lepton differential cross section through all production modes as a function of $m_{4\ell}$. Measured cross sections overall agree with the theoretical predictions within their uncertainties, which are dominated by statistical uncertainties in all bins.

7.3 Vector Boson Scattering

Figure 7.31 shows the output of the GBDT discussed in Section 6.5 for events in the dijet selection. The search procedure finds a modest excess of events compatible with VBS ZZjj signal, at the level of 2.7 standard deviations over the null hypothesis of the SM without VBS ZZ production. The expected significance is 1.6 standard deviations. This corresponds to a VBS fiducial cross section of

$$\sigma_{\mathrm{fid}}(\mathrm{pp} \to \mathrm{ZZjj(EWK)} \to 4\ell\mathrm{jj}) = 0.40^{+0.21}_{-0.16}\,(\mathrm{stat})^{+0.13}_{-0.09}\,(\mathrm{syst})\,\mathrm{fb}, \tag{7.10}$$

which is consistent with the SM prediction of $0.29^{+0.02}_{-0.03}\,\mathrm{fb}$.

7.4 Anomalous Coupling Limits

The ZZ invariant mass is shown in Fig. 7.32 for all events in the on-shell selection, with two example distributions shown for potential scenarios with nonzero aTGCs, one of which sets $f_5^{\gamma} = 0.0019$ and $f_5^{\mathrm{Z}} = 0.0015$, and the other $f_4^{\gamma} = 0.0019$ and $f_4^{\mathrm{Z}} = 0.0015$. The limit setting procedure described in Section 6.6 is applied to each aTGC parameter, with all other couplings fixed to their SM values, to yield

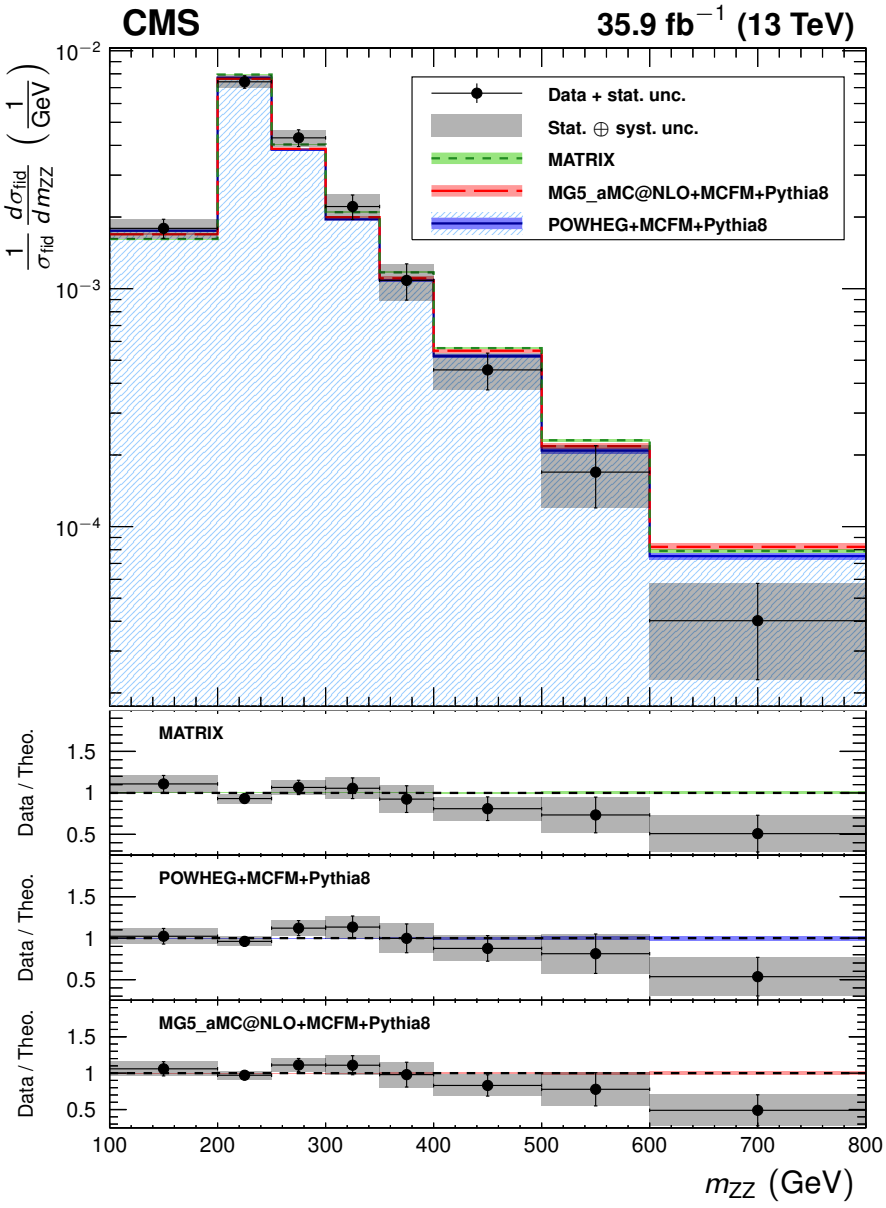

Figure 7.19: The ZZ differential cross section as a function of m_{ZZ}, normalized to the inclusive fiducial cross section. Points represent the unfolded data, with vertical bars showing the statistical uncertainty and a grey band showing the sum in quadrature of the statistical and systematic uncertainties. Blue, red, and green histograms represent the POWHEG+MCFM, MadGraph5_aMC@NLO+MCFM, and MATRIX predictions, respectively, with bands around each which represent their combined statistical, scale, and PDF uncertainties. The lower sections of the plot represents the ratio of the measured cross section to each of the predictions.

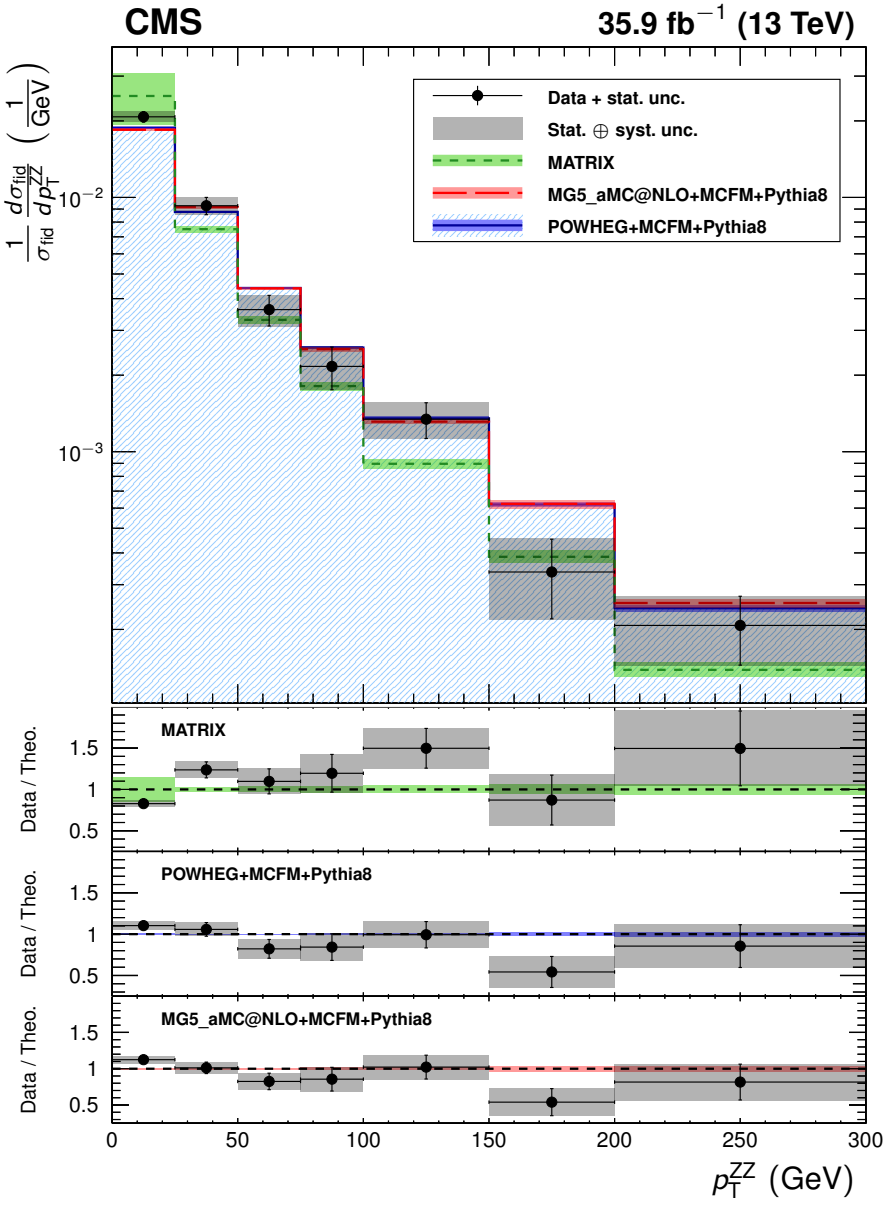

Figure 7.20: The ZZ differential cross section as a function of the four-lepton p_T, normalized to the inclusive fiducial cross section. Points represent the unfolded data, with vertical bars showing the statistical uncertainty and a grey band showing the sum in quadrature of the statistical and systematic uncertainties. Blue, red, and green histograms represent the POWHEG+MCFM, MADGRAPH5_aMC@NLO+MCFM, and MATRIX predictions, respectively, with bands around each which represent their combined statistical, scale, and PDF uncertainties. The lower sections of the plot represents the ratio of the measured cross section to each of the predictions.

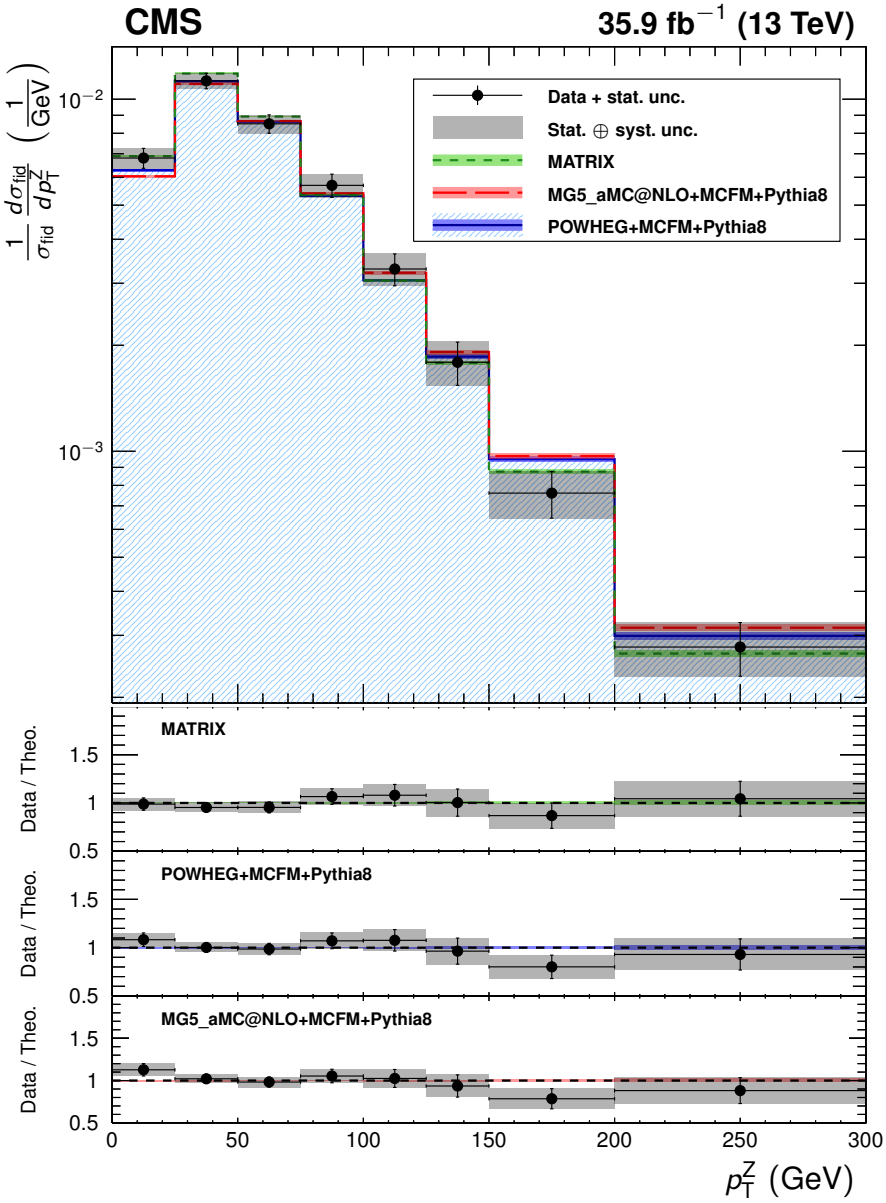

Figure 7.21: The ZZ differential cross section as a function of the p_T of both Z boson candidates, regardless of which one is Z_1 and which is Z_2, normalized to the inclusive fiducial cross section. Points represent the unfolded data, with vertical bars showing the statistical uncertainty and a grey band showing the sum in quadrature of the statistical and systematic uncertainties. Blue, red, and green histograms represent the POWHEG+MCFM, MADGRAPH5_aMC@NLO+MCFM, and MATRIX predictions, respectively, with bands around each which represent their combined statistical, scale, and PDF uncertainties. The lower sections of the plot represents the ratio of the measured cross section to each of the predictions.

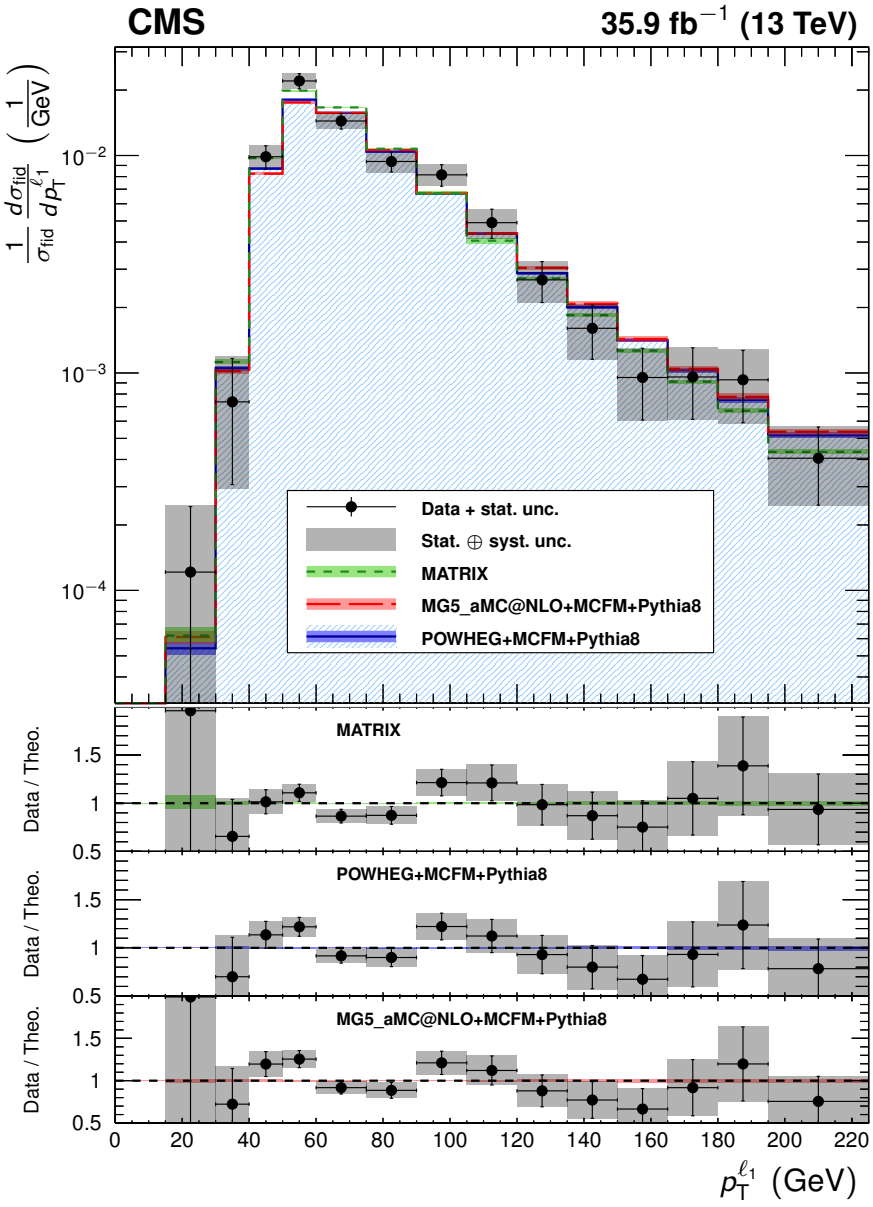

Figure 7.22: The ZZ differential cross section as a function of leading lepton p_T, normalized to the inclusive fiducial cross section. Points represent the unfolded data, with vertical bars showing the statistical uncertainty and a grey band showing the sum in quadrature of the statistical and systematic uncertainties. Blue, red, and green histograms represent the POWHEG+MCFM, MADGRAPH5_aMC@NLO+MCFM, and MATRIX predictions, respectively, with bands around each which represent their combined statistical, scale, and PDF uncertainties. The lower sections of the plot represents the ratio of the measured cross section to each of the predictions.

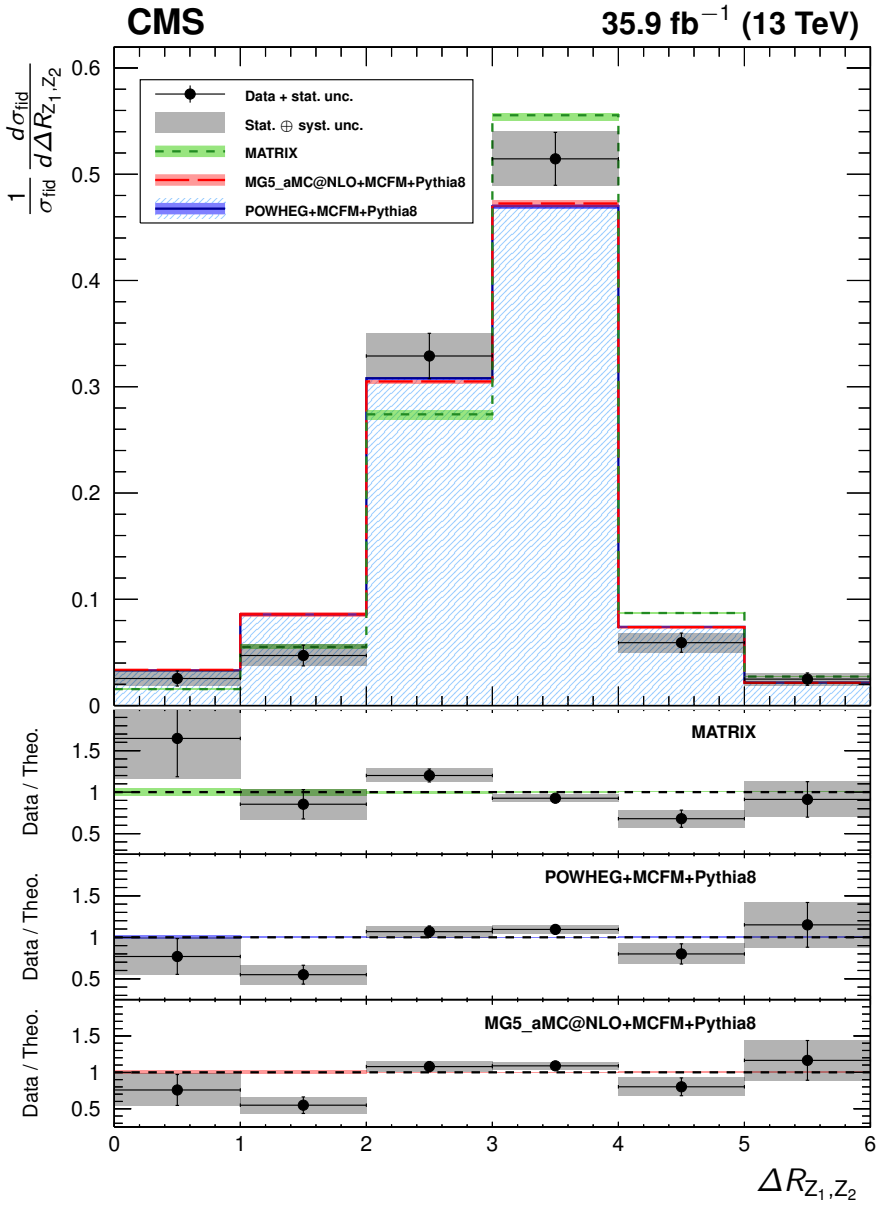

Figure 7.23: The ZZ differential cross section as a function of ΔR between the two Z bosons, normalized to the inclusive fiducial cross section. Points represent the unfolded data, with vertical bars showing the statistical uncertainty and a grey band showing the sum in quadrature of the statistical and systematic uncertainties. Blue, red, and green histograms represent the POWHEG+MCFM, MadGraph-5_aMC@NLO+MCFM, and MATRIX predictions, respectively, with bands around each which represent their combined statistical, scale, and PDF uncertainties. The lower sections of the plot represents the ratio of the measured cross section to each of the predictions.

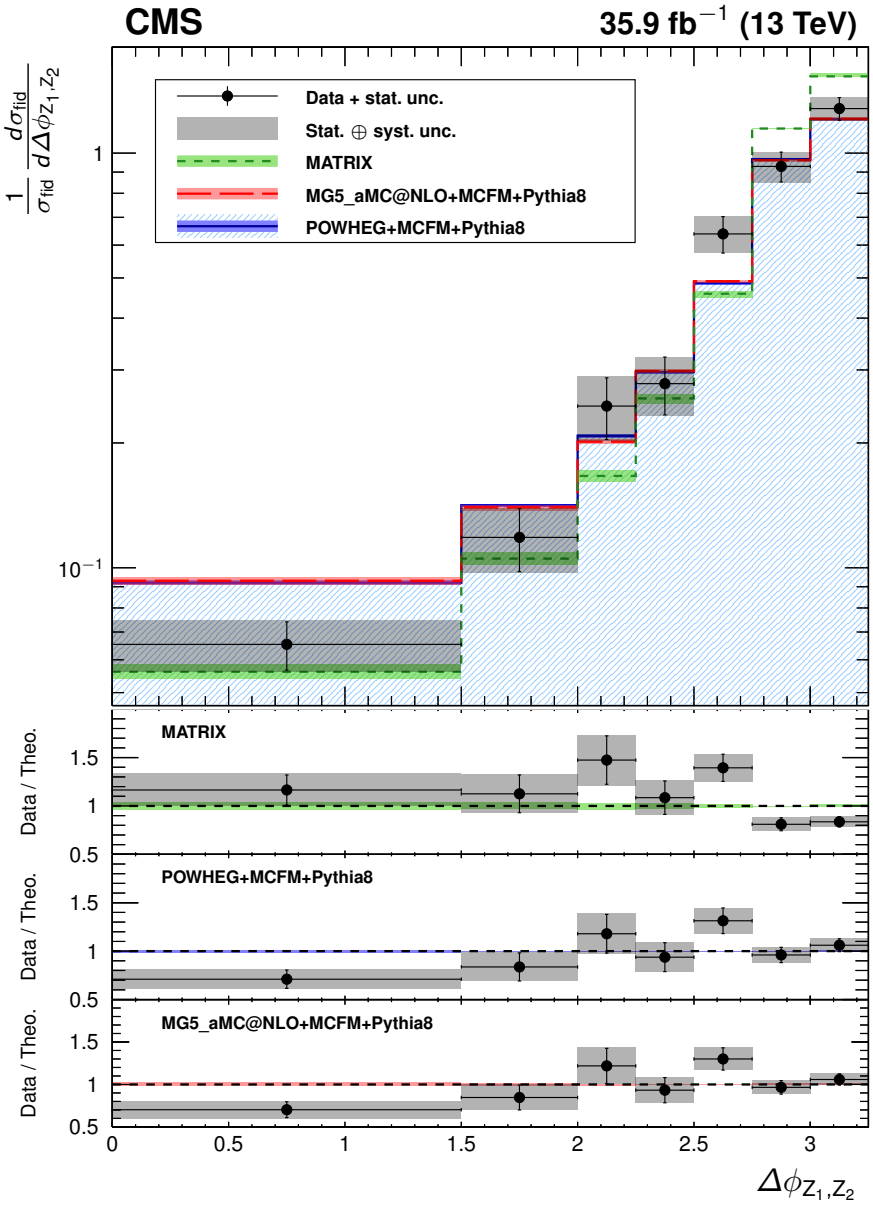

Figure 7.24: The ZZ differential cross section as a function of $\Delta\phi$ between the two Z bosons, normalized to the inclusive fiducial cross section. Points represent the unfolded data, with vertical bars showing the statistical uncertainty and a grey band showing the sum in quadrature of the statistical and systematic uncertainties. Blue, red, and green histograms represent the POWHEG+MCFM, MadGraph-5_aMC@NLO+MCFM, and MATRIX predictions, respectively, with bands around each which represent their combined statistical, scale, and PDF uncertainties. The lower sections of the plot represents the ratio of the measured cross section to each of the predictions.

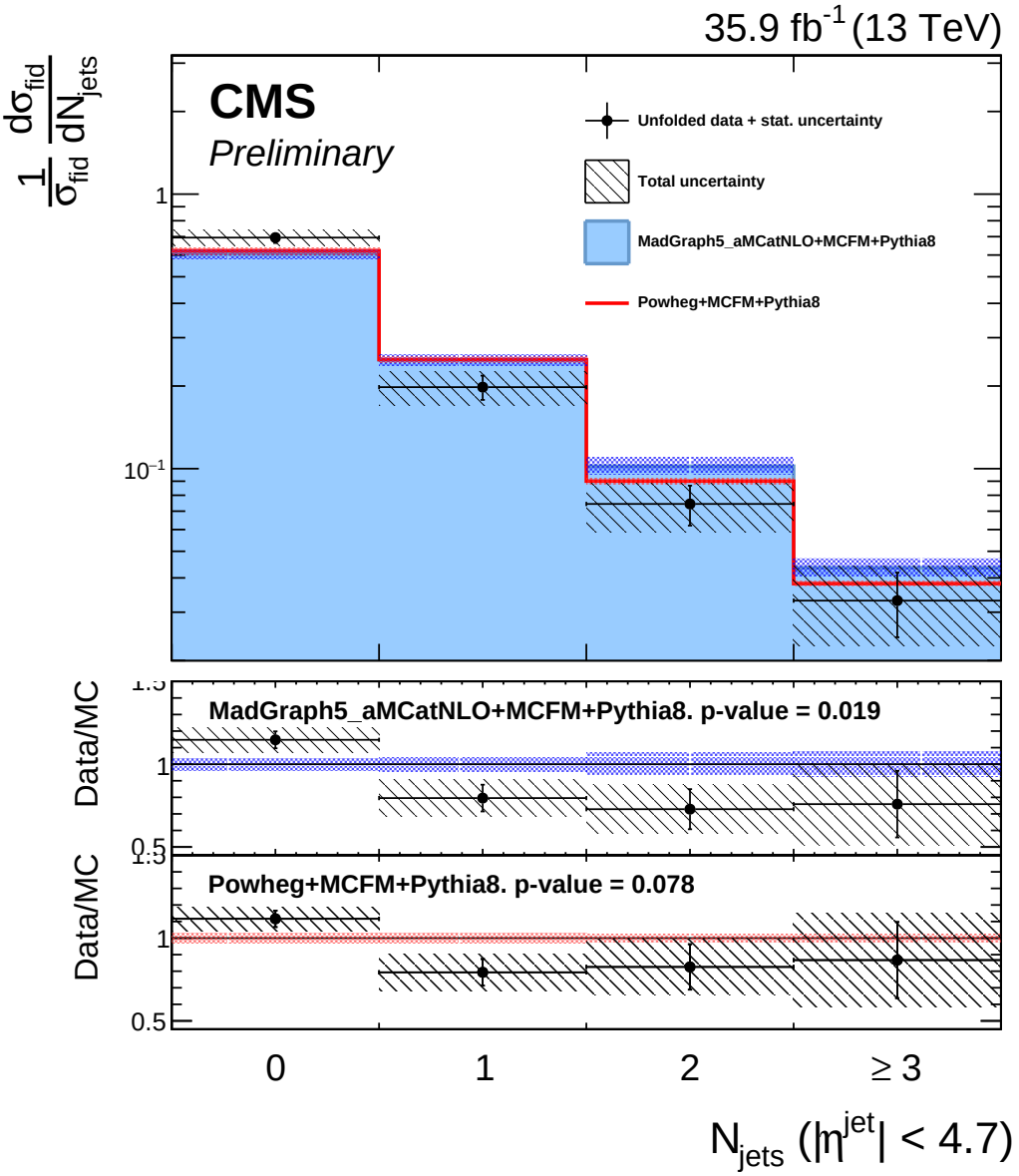

Figure 7.25: The ZZ differential cross section as a function of the jet multiplicity N_{jets}, normalized to the inclusive fiducial cross section. Points represent the unfolded data, with vertical bars showing the statistical uncertainty and a hatched band showing the sum in quadrature of the statistical and systematic uncertainties. Red and blue histograms represent the POWHEG+MCFM and MADGRAPH5_aMC@NLO+MCFM predictions, respectively, with bands around each which represent their combined statistical, scale, and PDF uncertainties. The lower sections of the plot represents the ratio of the measured cross section to each of the predictions.

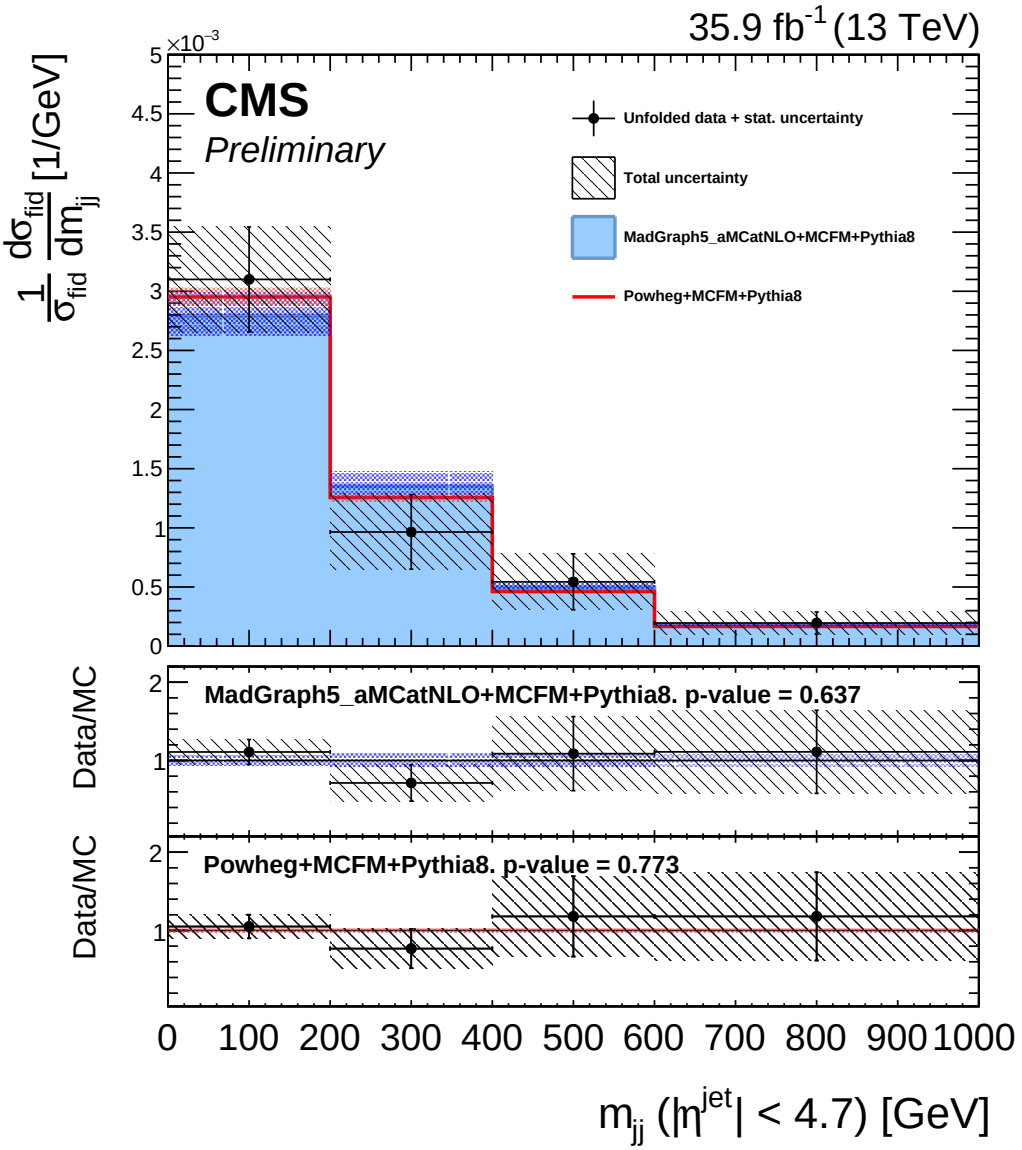

Figure 7.26: The ZZ differential cross section as a function of the invariant mass of the two highest-p_{T} jets m_{jj}, including all ZZ events with at least two jets, normalized to the inclusive fiducial cross section. Points represent the unfolded data, with vertical bars showing the statistical uncertainty and a hatched band showing the sum in quadrature of the statistical and systematic uncertainties. Red and blue histograms represent the POWHEG+MCFM and MadGraph5_aMC@NLO+MCFM predictions, respectively, with bands around each which represent their combined statistical, scale, and PDF uncertainties. The lower sections of the plot represents the ratio of the measured cross section to each of the predictions.

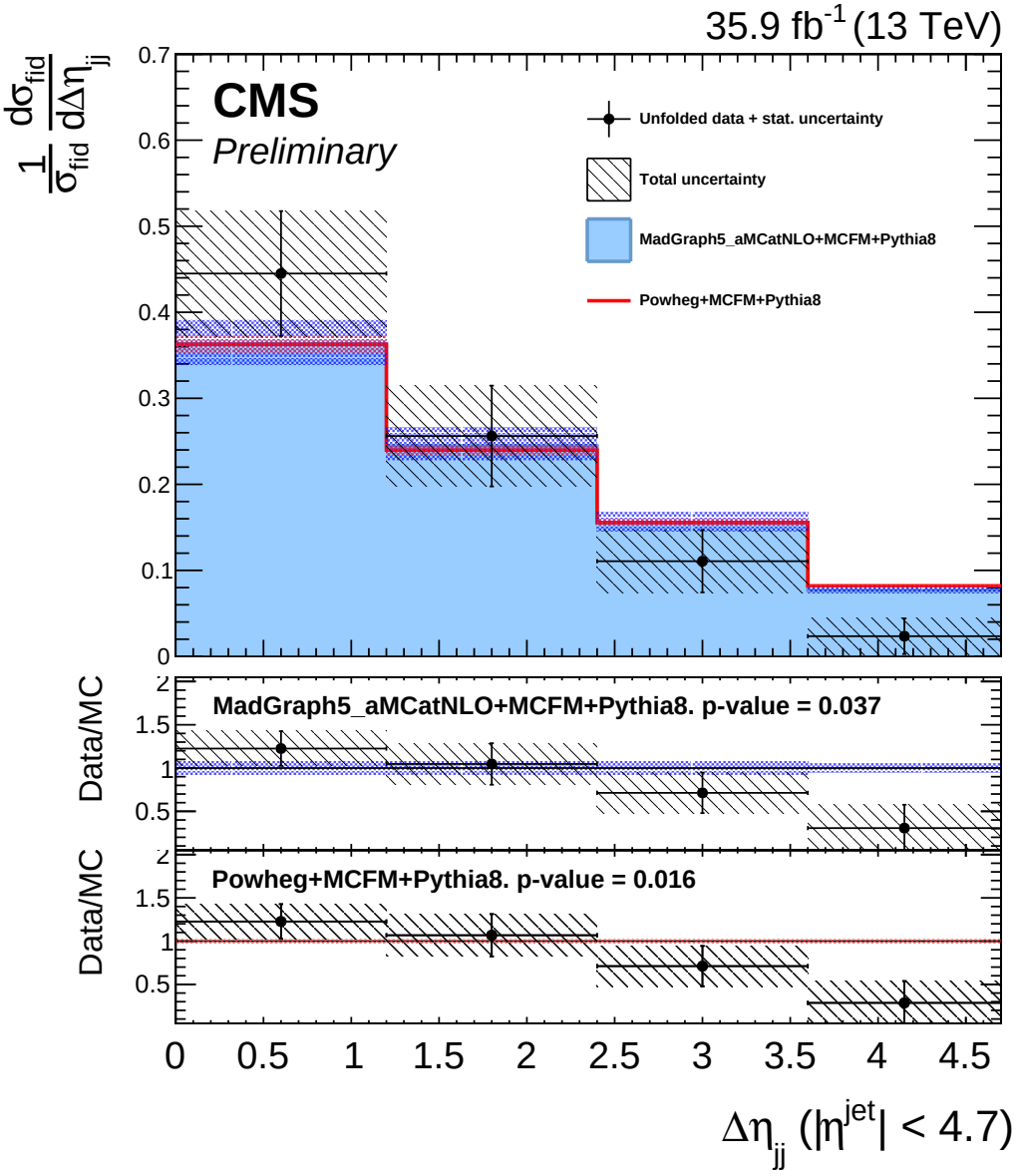

Figure 7.27: The ZZ differential cross section as a function of the absolute pseudo-rapidity separation of the two highest-p_{T} jets $|\Delta\eta_{\mathrm{jj}}|$, including all ZZ events with at least two jets, normalized to the inclusive fiducial cross section. Points represent the unfolded data, with vertical bars showing the statistical uncertainty and a hatched band showing the sum in quadrature of the statistical and systematic uncertainties. Red and blue histograms represent the POWHEG+MCFM and MADGRAPH5_aMC@-NLO+MCFM predictions, respectively, with bands around each which represent their combined statistical, scale, and PDF uncertainties. The lower sections of the plot represents the ratio of the measured cross section to each of the predictions.

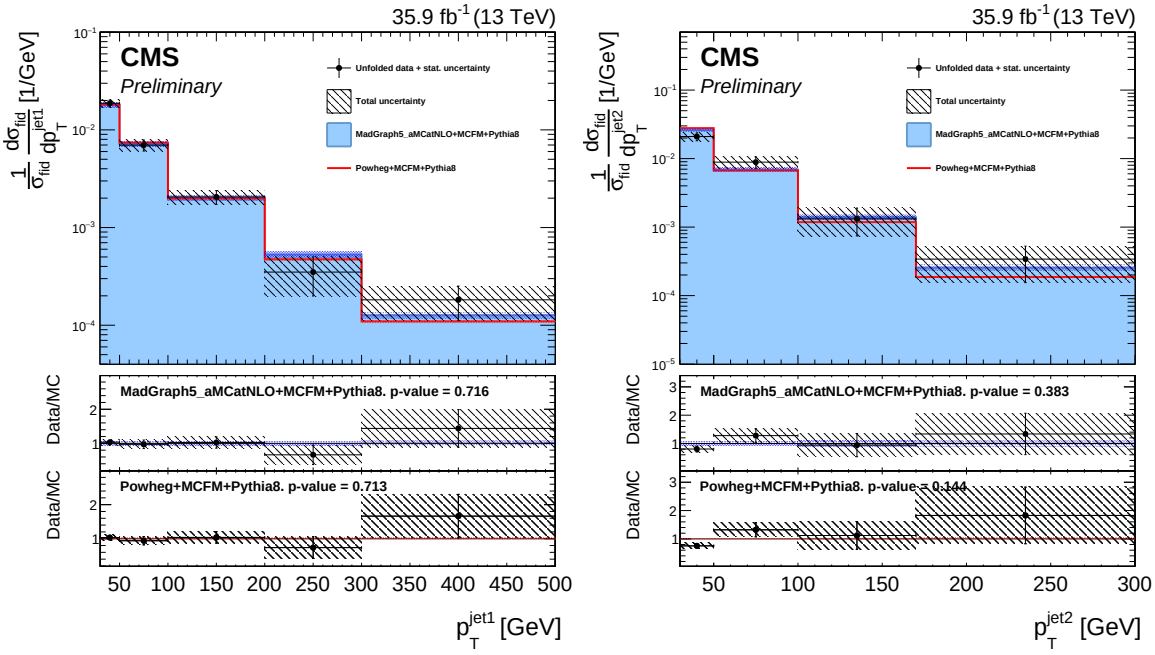

Figure 7.28: The ZZ differential cross section as a function of the leading (left) and subleading (right) jet p_{T}, in ZZ events with at least one jet and at least two jets respectively, normalized to the inclusive fiducial cross section. Points represent the unfolded data, with vertical bars showing the statistical uncertainty and a hatched band showing the sum in quadrature of the statistical and systematic uncertainties. Red and blue histograms represent the POWHEG+MCFM and MadGraph5_aMC@-NLO+MCFM predictions, respectively, with bands around each which represent their combined statistical, scale, and PDF uncertainties. The lower sections of the plots represent the ratio of the measured cross section to each of the predictions.

one-dimensional 95% CL limits,

$$\begin{aligned} -0.0012 < f_4^{\mathrm{Z}} < 0.0010, \quad -0.0010 < f_5^{\mathrm{Z}} < 0.0013, \\ -0.0012 < f_4^{\gamma} < 0.0013, \quad -0.0012 < f_5^{\gamma} < 0.0013. \end{aligned} \tag{7.11}$$

These results improve the previous CMS limits, which were the most stringent set previously, by factors of 2–3 [74] and are the most stringent limits to date on the parameters in question. Recent preliminary limits from ATLAS using 13 TeV data are 50–80% looser [230]. Two-dimensional limits are set in the f_4^{γ}-f_4^{Z} and f_5^{γ}-f_5^{Z} planes, holding all other parameters to the SM values in each calculation. One- and

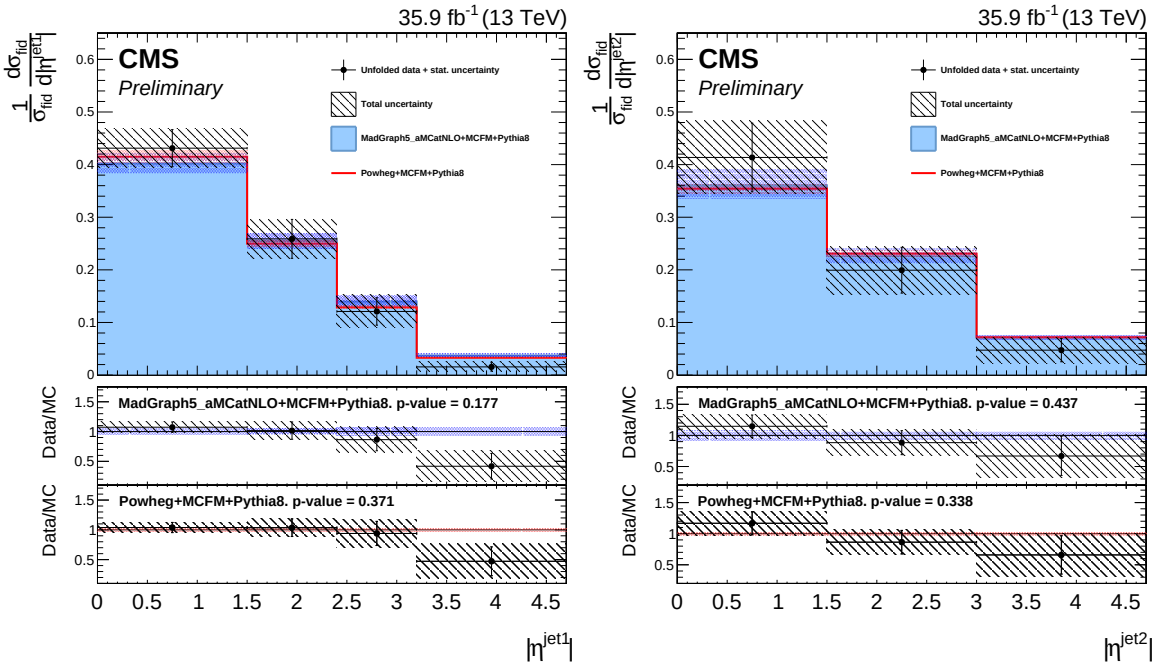

Figure 7.29: The ZZ differential cross section as a function of the leading (left) and subleading (right) jet η, in ZZ events with at least one jet and at least two jets respectively, normalized to the inclusive fiducial cross section. Points represent the unfolded data, with vertical bars showing the statistical uncertainty and a hatched band showing the sum in quadrature of the statistical and systematic uncertainties. Red and blue histograms represent the POWHEG+MCFM and MADGRAPH5_aMC@-NLO+MCFM predictions, respectively, with bands around each which represent their combined statistical, scale, and PDF uncertainties. The lower sections of the plots represent the ratio of the measured cross section to each of the predictions.

two-dimensional 95% CL limits are shown in Fig. 7.33.

No unitarizing form factor (c.f. Section 1.5.1) is applied when calculating the limits of Eq. (7.11). One way to enforce unitarity without a form factor would be to restrict the maximum ZZ invariant mass used, and set the limits considering only events with m_{ZZ} below some cutoff. The limits would then depend on the cutoff chosen, converging to the nonunitary limits when the cutoff is larger than the energies accessible in the experiment. The limit computations are repeated with multiple cutoff values, and the resulting expected and observed limits are shown in Fig. 7.34

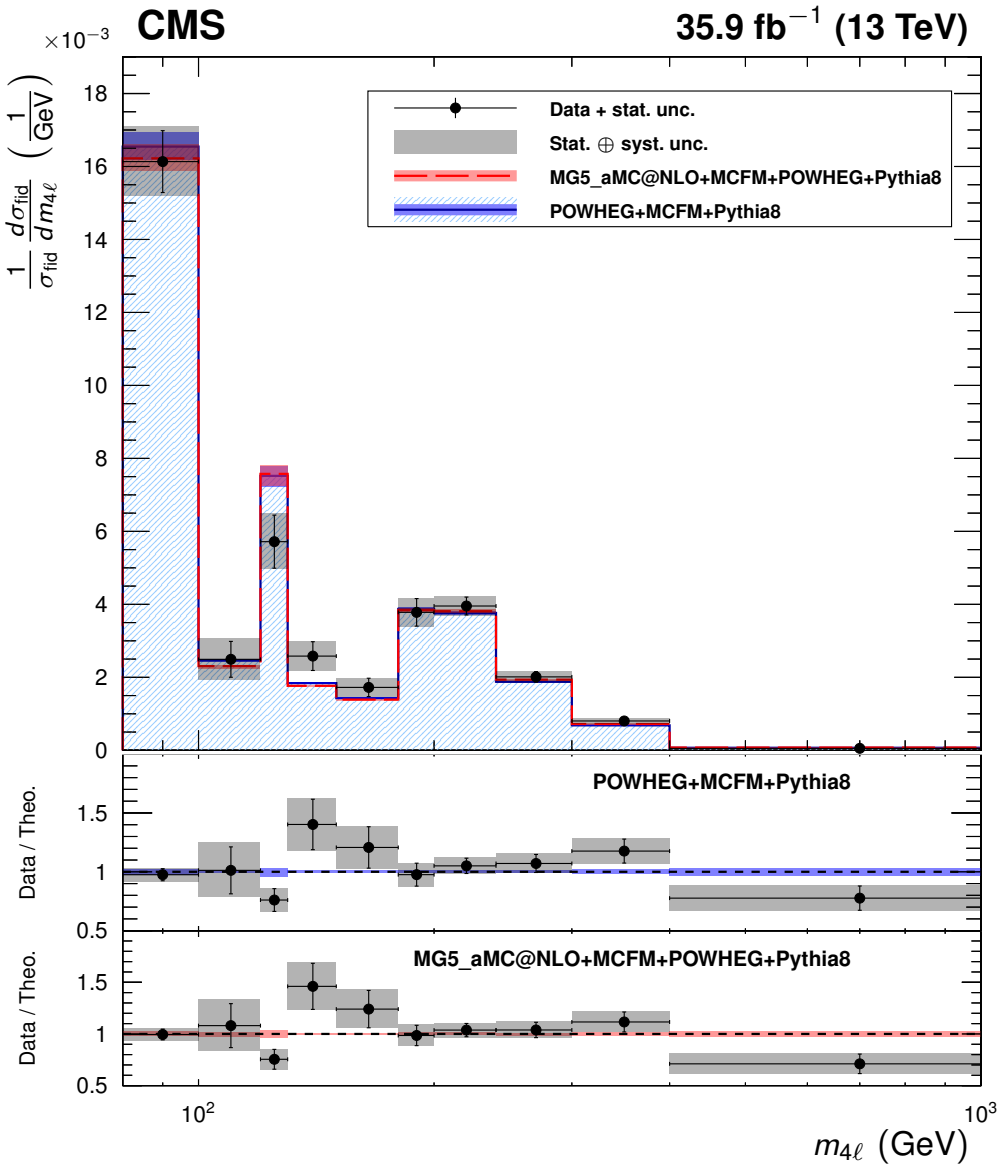

Figure 7.30: The four-lepton differential cross section as a function of $m_{4\ell}$ under the full spectrum selections, normalized to the inclusive fiducial cross section. Points represent the unfolded data, with vertical bars showing the statistical uncertainty and a grey band showing the sum in quadrature of the statistical and systematic uncertainties. Blue and red histograms represent the POWHEG+MCFM and MadGraph5_aMC@NLO+MCFM predictions, respectively, with bands around each which represent their combined statistical, scale, and PDF uncertainties. The lower sections of the plot represents the ratio of the measured cross section to each of the predictions.

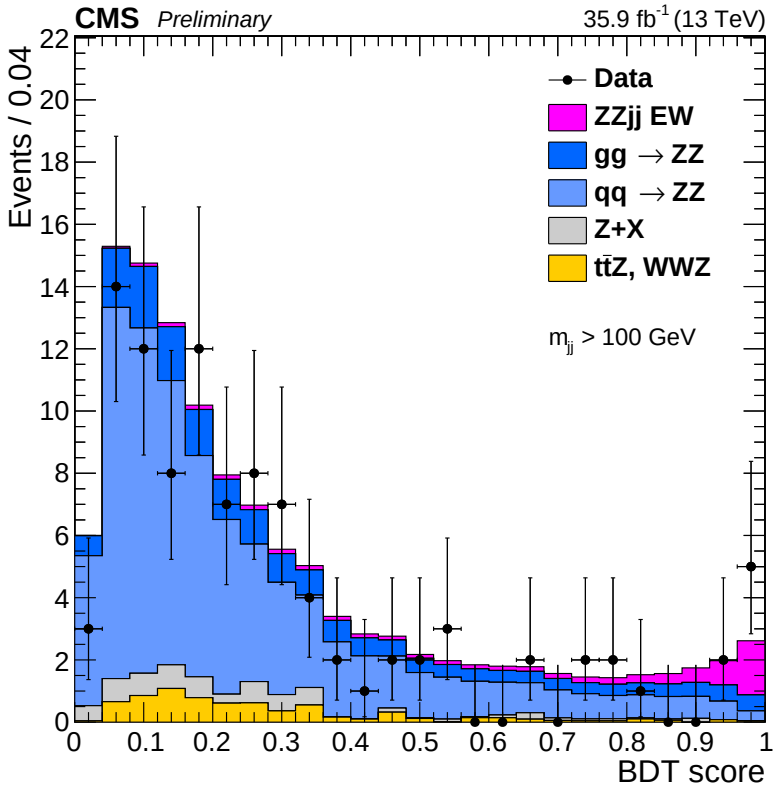

Figure 7.31: Output distribution of the VBS signal extraction GBDT, for events in the dijet selection. Points represent data, with statistical uncertainty bars. The stack of filled histograms represents the SM signal prediction and background estimate.

as a function of the maximum m_{ZZ} used.

The aQGC search proceeds the same way, but using events in the dijet selection. The observable used for limit setting is again m_{ZZ}, which is shown for these events in Fig. 7.35 along with two example distributions for scenarios with nonzero aQGCs, one with $f_{T8}/\Lambda^4 = 1\text{TeV}^{-4}$, the other with $f_{T9}/\Lambda^4 = 2\text{TeV}^{-4}$. In the aQGC search, a unitarity bound is imposed, chosen with VBFNLO [231] to be the value of m_{ZZ} at which the scattering amplitude would violate unitarity if the aQGC parameter in question were set to its 95% CL limit value. While limits are set for each parameter, all other parameters and their unitarity bounds are set to zero. The observed 95% CL limits

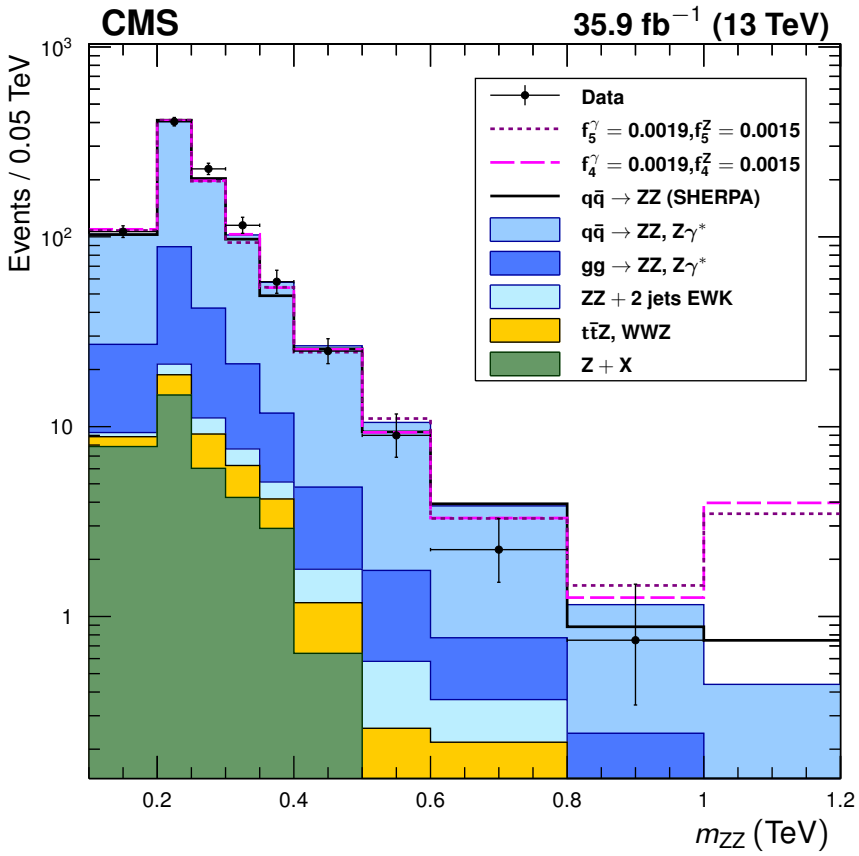

Figure 7.32: Distribution of ZZ invariant mass for all events in the on-shell selection. Points represent data, with statistical uncertainty bars. The stack of filled histograms represents the SM signal prediction and background estimate. The unfilled histograms represent two example SHERPA predictions for nonzero aTGC hypotheses (dashed) and the SHERPA SM prediction (solid), included to illustrate the shape differences between the SHERPA and POWHEG+MCFM SM predictions. The SHERPA distributions are normalized such that the SM prediction's total yield matches that of the other generators. The last bin includes the overflow contributions from events at masses above 1.2 TeV.

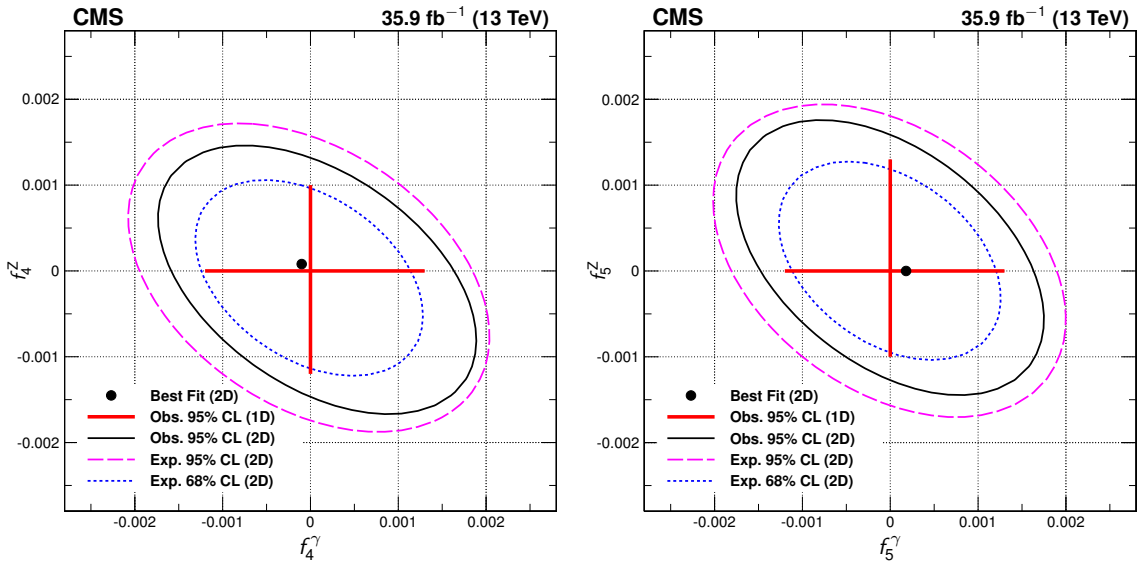

Figure 7.33: Two-dimensional observed 95% CL limits (solid contour) and expected 68 and 95% CL limits (dashed contours) in the f_4^γ-f_4^Z (left) and f_5^γ-f_5^Z (right) planes. The regions outside the contours are excluded at the corresponding confidence level. The dot is the point of maximum likelihood in the two-dimensional fits. Solid, straight lines at the center show the observed one-dimensional 95% CL limits for $f_{4,5}^\gamma$ (horizontal) and $f_{4,5}^Z$ (vertical). No form factor is used.

on the coefficients of the effective field theory operators governing ZZjj production are

$$\begin{aligned}
-0.46 &< f_{T0}/\Lambda^4 < 0.44 \quad \text{TeV}^{-4}, \\
-0.61 &< f_{T1}/\Lambda^4 < 0.61 \quad \text{TeV}^{-4}, \\
-1.2 &< f_{T2}/\Lambda^4 < 1.2 \quad \text{TeV}^{-4}, \\
-0.84 &< f_{T8}/\Lambda^4 < 0.84 \quad \text{TeV}^{-4}, \\
-1.8 &< f_{T9}/\Lambda^4 < 1.8 \quad \text{TeV}^{-4}.
\end{aligned} \tag{7.12}$$

These are the most stringent constraints to date on all five parameters, improving on the previous best by factors of 2–8 (see Section 2.3.1). This is the first time any of them have been measured in the ZZjj channel.

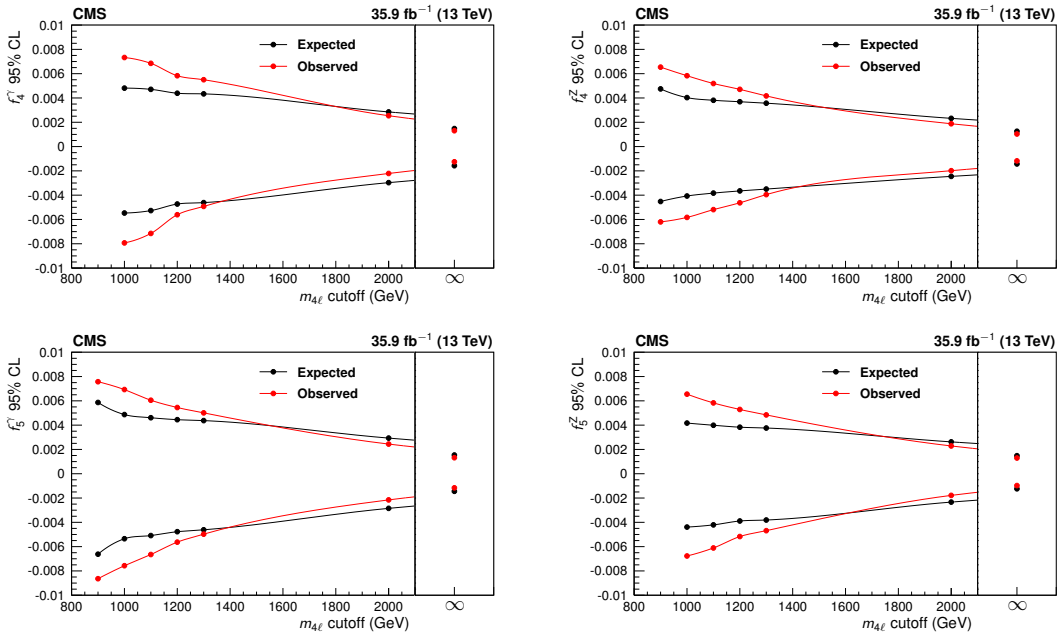

Figure 7.34: Expected and observed one-dimensional limits on the four aTGC parameters, as functions of the m_{ZZ} cutoff used to enforce unitarity. No form factor is used.

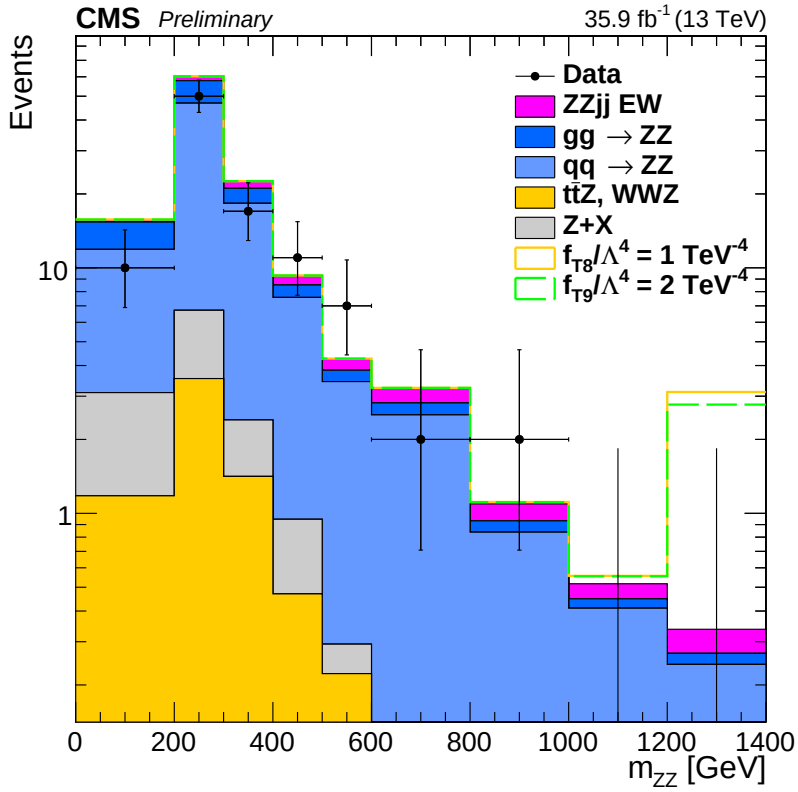

Figure 7.35: Distribution of ZZ invariant mass for events in the dijet selection. Points represent data, with statistical uncertainty bars. The stack of filled histograms represents the SM signal prediction and background estimate. The unfilled histograms represent two example MadGraph5_aMC@NLO distributions for nonzero aQGC hypotheses. The last bin includes the overflow contributions from events at masses above 1.4 TeV.

Chapter 8

Conclusions

8.1 Summary

Diboson studies in high-energy particle collisions are important probes of the electroweak sector of the standard model. In particular, measurements of resonant and nonresonant four-lepton production shed light on the couplings between the neutral gauge bosons and on the details of electroweak symmetry breaking. Decays to four charged leptons (electrons or muons) are rare, but they can be easily identified and fully reconstructed, and they represent a clean channel with low backgrounds. The LHC at CERN has generated proton-proton collisions with a center-of-mass energy of 13 TeV at record-breaking luminosities, providing an unprecedented opportunity to study such processes. The CMS detector is well designed for these measurements and collected a high-quality dataset corresponding to an integrated luminosity of $35.9\,\mathrm{fb}^{-1}$ in 2016. Several studies of four-lepton production were performed with this dataset and reported here.

Because the four-lepton channel is so clean, event selections are loose and efficiencies are high. Most backgrounds are estimated from data. The full four-lepton

spectrum includes resonant single-Z decays ($pp \to Z \to 4\ell$), resonant Higgs boson decays ($pp \to H \to 4\ell$), continuum production of a single Z boson and a nonresonant lepton pair ($pp \to Z\gamma^* \to 4\ell$), and continuum production of two on-shell ($60 < m_{\ell\ell} < 120\,\text{GeV}$) Z bosons ($pp \to ZZ \to 4\ell$).

Both inclusive and differential ZZ cross sections were measured. Inclusive cross sections were measured with a signal strength found by a maximum likelihood fit. The measured fiducial ZZ cross section, subject to the requirements of Table 6.2, is

$$\sigma_{\text{fid}}(pp \to ZZ \to 4\ell) = 40.9 \pm 1.3\,(\text{stat}) \pm 1.4\,(\text{syst}) \pm 1.0\,(\text{lumi})\,\text{fb}. \tag{8.1}$$

The total ZZ cross section, subject only to the constraint that both Z bosons be on-shell, was extrapolated with an acceptance correction and combined with the smaller ($2.9\,\text{fb}^{-1}$) dataset collected in 2015. Its measured value is

$$\sigma(pp \to ZZ) = 17.2 \pm 0.5\,(\text{stat}) \pm 0.7\,(\text{syst}) \pm 0.4\,(\text{theo}) \pm 0.4\,(\text{lumi})\,\text{pb}. \tag{8.2}$$

The $Z \to 4\ell$ branching fraction was measured for events with $80 < m_{4\ell} < 100\,\text{GeV}$ and a requirement of $m_{\ell\ell} > 4\,\text{GeV}$ for all opposite-sign, same-flavor lepton pairs, and found to be

$$\mathcal{B}\,(Z \to 4\ell) = 4.8 \pm 0.2\,(\text{stat}) \pm 0.2\,(\text{syst}) \pm 0.1\,(\text{theo}) \pm 0.1\,(\text{lumi}) \times 10^{-6}. \tag{8.3}$$

Differential cross sections were measured as functions of a number of observables including fully leptonic kinematic variables and quantities related to the production of associated jets. All results are in agreement with SM predictions.

A search was performed for fully electroweak ZZjj production using a gradient-boosted decision tree. An excess consistent with VBS was found at the level of 2.7 standard deviations above the null hypothesis (1.6σ expected). This corresponds to a measured electroweak fiducial cross section of

$$\sigma_{\text{fid}}(pp \to ZZjj(\text{EWK}) \to 4\ell jj) = 0.40^{+0.21}_{-0.16}\,(\text{stat})^{+0.13}_{-0.09}\,(\text{syst})\,\text{fb}, \tag{8.4}$$

consistent with SM predictions.

Searches were performed for anomalous triple and quartic gauge couplings. The aTGC search, considered in an effective lagrangian framework, used the invariant mass of inclusive ZZ events to set the most stringent 95% CL limits to date on ZZZ and ZZγ couplings,

$$\begin{aligned} -0.0012 < f_4^{\mathrm{Z}} < 0.0010, \quad -0.0010 < f_5^{\mathrm{Z}} < 0.0013, \\ -0.0012 < f_4^{\gamma} < 0.0013, \quad -0.0012 < f_5^{\gamma} < 0.0013. \end{aligned} \tag{8.5}$$

Two-dimensional limits were also set. The aQGC search, performed in an effective field theory parameterization with ZZjj events, set the most stringent 95% CL limits to date on several dimension-8 operators which govern quartic gauge couplings,

$$\begin{aligned} -0.46 &< f_{\mathrm{T0}}/\Lambda^4 < 0.44 \quad \mathrm{TeV}^{-4}, \\ -0.61 &< f_{\mathrm{T1}}/\Lambda^4 < 0.61 \quad \mathrm{TeV}^{-4}, \\ -1.2 &< f_{\mathrm{T2}}/\Lambda^4 < 1.2 \quad \mathrm{TeV}^{-4}, \\ -0.84 &< f_{\mathrm{T8}}/\Lambda^4 < 0.84 \quad \mathrm{TeV}^{-4}, \\ -1.8 &< f_{\mathrm{T9}}/\Lambda^4 < 1.8 \quad \mathrm{TeV}^{-4}. \end{aligned} \tag{8.6}$$

8.2 Outlook

Diboson measurements have great potential to shed further light on the SM or find deviations from it. In the long term, cross section measurements at higher center-of-mass energies are of great interest because new physics should be most obvious at high $\sqrt{s}$. With no new colliders expected in the near future[1], progress will first come in the form of precision measurements of processes that are in principle accessible now. The statistical uncertainties of the measured inclusive cross sections are now comparable

[1]The LHC may operate at $\sqrt{s} = 14\,\mathrm{TeV}$ in the near future, which would be useful but only marginally more likely to reveal new physics, in line with the marginal increase in energy.

to or smaller than the systematic uncertainties, and systematics should dominate after the inclusion of data collected in 2017, even if new techniques are developed which reduce lepton efficiency and trigger uncertainties somewhat. Systematic uncertainty reductions that may be developed in the near future have the potential to bring total experimental uncertainties down to a similar level to the theoretical uncertainties.

Differential cross sections and searches, however, will be statistically limited for some time and will benefit greatly from additional luminosity at $\sqrt{s} = 13\,\text{TeV}$. Statistical uncertainties dominate in almost all bins in the differential cross sections. Assuming no deviations from the SM, data collected in 2017 will likely be enough to allow 3σ evidence for VBS, when added to the 2016 data presented here. New data will likewise reduce the electroweak ZZ production cross section uncertainty substantially as the process' anticipated discovery draws near. The statistical power for the aGC searches comes largely from the highest-mass bins, where very few events have been observed—only three above 800 GeV and none above 1 TeV, even in the inclusive selection. Further data collection will improve these limits substantially and place stringent restrictions on BSM neutral gauge boson couplings—or discover them.

Bibliography

[1] D. J. Griffiths, *Introduction to elementary particles; 2nd rev. version*, ser. Physics textbook. New York, NY: Wiley, 2008.

[2] F. Halzen and A. Martin, *Quarks & Leptons: An introductory course in modern particle physics*. New York, USA: John Wiley & Sons, 1984.

[3] V. Barger and R. Phillips, *Collider Physics*, ser. Frontiers in physics. Avalon Publishing, 1997, ISBN: 9780201149456.

[4] M. E. Peskin and D. V. Schroeder, *An Introduction to quantum field theory*. Reading, USA: Addison-Wesley, 1995, ISBN: 9780201503975, 0201503972.

[5] J. F. Donoghue, E. Golowich, and B. R. Holstein, *Dynamics of the Standard Model*, ser. Cambridge monographs on particle physics, nuclear physics, and cosmology. Cambridge: Cambridge Univ. Press, 1992.

[6] O. W. Greenberg, "Spin and unitary-spin independence in a paraquark model of baryons and mesons," *Phys. Rev. Lett.*, vol. 13, p. 598, 20 1964. DOI: 10.1103/PhysRevLett.13.598. https://link.aps.org/doi/10.1103/PhysRevLett.13.598.

[7] S. L. Glashow, "Quarks with color and flavor," *Scientific American*, vol. 233, p. 38, 1975. http://www.jstor.org/stable/24949915.

[8] Super-Kamiokande Collaboration, "Evidence for oscillation of atmospheric neutrinos," *Phys. Rev. Lett.*, vol. 81, pp. 1562–1567, 1998. DOI: 10.1103/PhysRevLett.81.1562. arXiv: hep-ex/9807003 [hep-ex].

[9] SNO Collaboration, "Measurement of the rate of $\nu_e + d \rightarrow p + p + e^-$ interactions produced by ^8B solar neutrinos at the Sudbury Neutrino Observatory," *Phys. Rev. Lett.*, vol. 87, p. 071 301, 2001. DOI: 10.1103/PhysRevLett.87.071301. arXiv: nucl-ex/0106015 [nucl-ex].

[10] SNO Collaboration, "Direct evidence for neutrino flavor transformation from neutral current interactions in the Sudbury Neutrino Observatory," *Phys. Rev. Lett.*, vol. 89, p. 011 301, 2002. DOI: 10.1103/PhysRevLett.89.011301. arXiv: nucl-ex/0204008 [nucl-ex].

[11] Particle Data Group, C. Patrignani, *et al.*, "Review of particle physics," *Chin. Phys. C*, vol. 40, p. 100 001, 2016. DOI: 10.1088/1674-1137/40/10/100001.

[12] N. Cabibbo, "Unitary symmetry and leptonic decays," *Phys. Rev. Lett.*, vol. 10, p. 531, 1963. DOI: 10.1103/PhysRevLett.10.531.

[13] M. Kobayashi and T. Maskawa, "CP-violation in the renormalizable theory of weak interaction," *Prog. Theo. Phys.*, vol. 49, p. 652, 1973. DOI: 10.1143/PTP.49.652.

[14] J. H. Christenson, J. W. Cronin, V. L. Fitch, and R. Turlay, "Evidence for the 2π decay of the K_2^0 meson," *Phys. Rev. Lett.*, vol. 13, p. 138, 4 Jul. 1964. DOI: 10.1103/PhysRevLett.13.138.

[15] KTeV Collaboration, "Observation of direct CP violation in $K_{S,L} \to \pi\pi$ decays," *Phys. Rev. Lett.*, vol. 83, p. 22, 1999. DOI: 10.1103/PhysRevLett.83.22. arXiv: hep-ex/9905060 [hep-ex].

[16] NA48 Collaboration, "A new measurement of direct CP violation in two pion decays of the neutral kaon," *Phys. Lett. B*, vol. 465, p. 335, 1999. DOI: 10.1016/S0370-2693(99)01030-8. arXiv: hep-ex/9909022 [hep-ex].

[17] BaBar Collaboration, "Measurement of CP violating asymmetries in B^0 decays to CP eigenstates," *Phys. Rev. Lett.*, vol. 86, p. 2515, 2001. DOI: 10.1103/PhysRevLett.86.2515. arXiv: hep-ex/0102030 [hep-ex].

[18] Belle Collaboration, "Observation of large CP violation in the neutral B meson system," *Phys. Rev. Lett.*, vol. 87, p. 091 802, 2001. DOI: 10.1103/PhysRevLett.87.091802. arXiv: hep-ex/0107061 [hep-ex].

[19] LHCb Collaboration, "Observation of CP violation in $B^\pm \to DK^\pm$ decays," *Phys. Lett. B*, vol. 712, p. 203, 2012, [Corrigendum: DOI: 110.1016/j.physletb.2012.05.060]. DOI: 10.1016/j.physletb.2012.04.060. arXiv: 1203.3662 [hep-ex].

[20] LHCb Collaboration, "First observation of CP violation in the decays of B_s^0 mesons," *Phys. Rev. Lett.*, vol. 110, p. 221 601, 2013. DOI: 10.1103/PhysRevLett.110.221601. arXiv: 1304.6173 [hep-ex].

[21] E. Noether, "Invariant variation problems," trans. by M. A. Tavel, *Gott. Nachr.*, p. 235, 1918, [*Transp. Theory Statist. Phys.*, vol. 1, p. 186, 1971]. DOI: 10.1080/00411457108231446. arXiv: physics/0503066 [physics].

[22] M. Srednicki, *Quantum Field Theory*. Cambridge: Cambridge Univ. Press, 2007.

[23] S. L. Glashow, "Partial symmetries of weak interactions," *Nucl. Phys.*, vol. 22, p. 579, 1961. DOI: 10.1016/0029-5582(61)90469-2.

[24] S. Weinberg, "A model of leptons," *Phys. Rev. Lett.*, vol. 19, p. 1264, 1967. DOI: 10.1103/PhysRevLett.19.1264.

[25] A. Salam, "Weak and electromagnetic interactions," *Conf. Proc.*, vol. C680-519, p. 367, 1968.

[26] F. Englert and R. Brout, "Broken symmetry and the mass of gauge vector mesons," *Phys. Rev. Lett.*, vol. 13, p. 321, 9 Aug. 1964. DOI: 10.1103/PhysRevLett.13.321. https://link.aps.org/doi/10.1103/PhysRevLett.13.321.

[27] P. W. Higgs, "Broken symmetries and the masses of gauge bosons," *Phys. Rev. Lett.*, vol. 13, p. 508, 16 Oct. 1964. DOI: 10.1103/PhysRevLett.13.508. https://link.aps.org/doi/10.1103/PhysRevLett.13.508.

[28] G. S. Guralnik, C. R. Hagen, and T. W. B. Kibble, "Global conservation laws and massless particles," *Phys. Rev. Lett.*, vol. 13, p. 585, 20 Nov. 1964. DOI: 10.1103/PhysRevLett.13.585. https://link.aps.org/doi/10.1103/PhysRevLett.13.585.

[29] A. Alboteanu, W. Kilian, and J. Reuter, "Resonances and unitarity in weak boson scattering at the LHC," *JHEP*, vol. 11, p. 010, 2008. DOI: 10.1088/1126-6708/2008/11/010. arXiv: 0806.4145 [hep-ph].

[30] V. C. Rubin, "Dark matter in spiral galaxies," *Scientific American*, vol. 248, p. 96, 1983. DOI: 10.1038/scientificamerican0683-96.

[31] K. Garrett and G. Duda, "Dark matter: a primer," *Adv. Astron.*, vol. 2011, p. 968 283, 2011. DOI: 10.1155/2011/968283. arXiv: 1006.2483 [hep-ph].

[32] J. Ellis, "Searching for particle physics beyond the standard model at the LHC and elsewhere," *AIP Conf. Proc.*, vol. 1446, p. 9, 2012. DOI: 10.1063/1.4727987. arXiv: 1102.5009 [hep-ph].

[33] H. Georgi, H. R. Quinn, and S. Weinberg, "Hierarchy of interactions in unified gauge theories," *Phys. Rev. Lett.*, vol. 33, p. 451, 1974. DOI: 10.1103/PhysRevLett.33.451.

[34] E. Gildener, "Gauge symmetry hierarchies," *Phys. Rev. D*, vol. 14, p. 1667, 1976. DOI: 10.1103/PhysRevD.14.1667.

[35] A. J. Buras, J. R. Ellis, M. K. Gaillard, and D. V. Nanopoulos, "Aspects of the grand unification of strong, weak and electromagnetic interactions," *Nucl. Phys. B*, vol. 135, p. 66, 1978. DOI: 10.1016/0550-3213(78)90214-6.

[36] S. Mele, "The measurement of the number of light neutrino species at LEP," *Adv. Ser. Direct. High Energy Phys.*, vol. 23, p. 89, 2015. DOI: 10.1142/9789814644150_0004. http://cds.cern.ch/record/2103251.

[37] S. P. Martin, "A supersymmetry primer," in *Perspectives on Supersymmetry II*. DOI: 10.1142/9789814307505_0001. arXiv: hep-ph/9709356 [hep-ph].

[38] C. Autermann, "Experimental status of supersymmetry after the LHC run-I," *Prog. Part. Nucl. Phys.*, vol. 90, p. 125, 2016. DOI: 10.1016/j.ppnp.2016.06.001. arXiv: 1609.01686 [hep-ex].

[39] H. Georgi and S. L. Glashow, "Unity of all elementary particle forces," *Phys. Rev. Lett.*, vol. 32, p. 438, 1974. DOI: 10.1103/PhysRevLett.32.438.

[40] K. Hagiwara, R. D. Peccei, D. Zeppenfeld, and K. Hikasa, "Probing the weak boson sector in $e^+e^- \to W^+W^-$," *Nucl. Phys. B*, vol. 282, p. 253, 1987. DOI: 10.1016/0550-3213(87)90685-7.

[41] G. J. Gounaris, J. Layssac, and F. M. Renard, "New and standard physics contributions to anomalous Z and γ self-couplings," *Phys. Rev. D*, vol. 62, p. 073 013, 2000. DOI: 10.1103/PhysRevD.62.073013. arXiv: hep-ph/0003143 [hep-ph].

[42] U. Baur and D. L. Rainwater, "Probing neutral gauge boson self-interactions in ZZ production at hadron colliders," *Phys. Rev. D*, vol. 62, p. 113 011, 2000. DOI: 10.1103/PhysRevD.62.113011. arXiv: hep-ph/0008063 [hep-ph].

[43] U. Baur and E. L. Berger, "Probing the weak boson sector in $Z\gamma$ production at hadron colliders," *Phys. Rev. D*, vol. 47, p. 4889, 1993. DOI: 10.1103/PhysRevD.47.4889.

[44] C. Degrande, N. Greiner, W. Kilian, O. Mattelaer, H. Mebane, T. Stelzer, S. Willenbrock, and C. Zhang, "Effective field theory: a modern approach to anomalous couplings," *Annals Phys.*, vol. 335, p. 21, 2013. DOI: 10.1016/j.aop.2013.04.016. arXiv: 1205.4231 [hep-ph].

[45] O. J. P. Éboli, M. C. Gonzalez-Garcia, and J. K. Mizukoshi, "$pp \to jje^{\pm}\mu^{\pm}\nu\nu$ and $jje^{\pm}\mu^{\mp}\nu\nu$ at $\mathcal{O}(\alpha_{em}^6)$ and $\mathcal{O}(\alpha_{em}^4\alpha_s^2)$ for the study of the quartic electroweak gauge boson vertex at LHC," *Phys. Rev. D*, vol. 74, p. 073 005, 2006. DOI: 10.1103/PhysRevD.74.073005. arXiv: hep-ph/0606118 [hep-ph].

[46] NNPDF Collaboration, "Parton distributions from high-precision collider data," 2017. arXiv: 1706.00428 [hep-ph].

[47] A. Lazopoulos, K. Melnikov, and F. Petriello, "QCD corrections to tri-boson production," *Phys. Rev. D*, vol. 76, p. 014 001, 2007. DOI: 10.1103/PhysRevD.76.014001. arXiv: hep-ph/0703273 [hep-ph].

[48] T. Binoth, G. Ossola, C. G. Papadopoulos, and R. Pittau, "NLO QCD corrections to tri-boson production," *JHEP*, vol. 06, p. 082, 2008. DOI: 10.1088/1126-6708/2008/06/082. arXiv: 0804.0350 [hep-ph].

[49] V. Hankele and D. Zeppenfeld, "QCD corrections to hadronic WWZ production with leptonic decays," *Phys. Lett. B*, vol. 661, p. 103, 2008. DOI: 10.1016/j.physletb.2008.02.014. arXiv: 0712.3544 [hep-ph].

[50] F. J. Hasert *et al.*, "Search for elastic ν_μ electron scattering," *Phys. Lett. B*, vol. 46, p. 121, 1973. DOI: 10.1016/0370-2693(73)90494-2.

[51] UA1 Collaboration, "Experimental observation of lepton pairs of invariant mass around $95\,\mathrm{GeV}/c^2$ at the CERN SPS collider," *Phys. Lett. B*, vol. 126, p. 398, 1983. DOI: 10.1016/0370-2693(83)90188-0.

[52] SLD Electroweak Group, DELPHI Collaboration, ALEPH Collaboration, SLD Collaboration, SLD Heavy Flavour Group, OPAL Collaboration, LEP Electroweak Working Group, L3 Collaboration, "Precision electroweak measurements on the Z resonance," *Phys. Rept.*, vol. 427, p. 257, 2006. DOI: 10.1016/j.physrep.2005.12.006. arXiv: hep-ex/0509008 [hep-ex].

[53] J. M. Campbell and R. K. Ellis, "An update on vector boson pair production at hadron colliders," *Phys. Rev. D*, vol. 60, p. 113 006, 1999. DOI: 10.1103/PhysRevD.60.113006. arXiv: hep-ph/9905386 [hep-ph].

[54] J. M. Campbell, R. K. Ellis, and C. Williams, "Vector boson pair production at the LHC," *JHEP*, vol. 07, p. 018, 2011. DOI: 10.1007/JHEP07(2011)018. arXiv: 1105.0020 [hep-ph].

[55] T. Melia, P. Nason, R. Röntsch, and G. Zanderighi, "W^+W^- , WZ and ZZ production in the POWHEG BOX," *JHEP*, vol. 11, p. 078, 2011. DOI: 10.1007/JHEP11(2011)078. arXiv: 1107.5051 [hep-ph].

[56] F. Cascioli, T. Gehrmann, M. Grazzini, S. Kallweit, P. Maierhöfer, A. von Manteuffel, S. Pozzorini, D. Rathlev, L. Tancredi, and E. Weihs, "ZZ production at hadron colliders in NNLO QCD," *Phys. Lett. B*, vol. 735, p. 311, 2014. DOI: 10.1016/j.physletb.2014.06.056. arXiv: 1405.2219 [hep-ph].

[57] F. Caola, K. Melnikov, R. Röntsch, and L. Tancredi, "QCD corrections to ZZ production in gluon fusion at the LHC," *Phys. Rev. D*, vol. 92, p. 094 028, 2015. DOI: 10.1103/PhysRevD.92.094028. arXiv: 1509.06734 [hep-ph].

[58] D. Rainwater, R. Szalapski, and D. Zeppenfeld, "Probing color-singlet exchange in Z + 2-jet events at the CERN LHC," *Phys. Rev. D*, vol. 54, p. 6680, 11 Dec. 1996. DOI: 10.1103/PhysRevD.54.6680.

[59] Sjöstrand, Torbjörn and Ask, Stefan and Christiansen, Jesper R. and Corke, Richard and Desai, Nishita and Ilten, Philip and Mrenna, Stephen and Prestel, Stefan and Rasmussen, Christine O. and Skands, Peter Z., "An introduction to PYTHIA 8.2," *Comput. Phys. Commun.*, vol. 191, p. 159, 2015. DOI: 10.1016/j.cpc.2015.01.024. arXiv: 1410.3012 [hep-ph].

[60] C. Bierlich and J. R. Christiansen, "Effects of color reconnection on hadron flavor observables," *Phys. Rev. D*, vol. 92, p. 094 010, 2015. DOI: 10.1103/PhysRevD.92.094010. arXiv: 1507.02091 [hep-ph].

[61] ALEPH Collaboration, "Measurement of the $e^+e^- \to ZZ$ production cross-section at center-of-mass energies of 183 GeV and 189 GeV," *Phys. Lett. B*, vol. 469, p. 287, 1999. DOI: 10.1016/S0370-2693(99)01288-5. arXiv: hep-ex/9911003 [hep-ex].

[62] OPAL Collaboration, "Z boson pair production in e^+e^- collisions at $\sqrt{s} =$ 183 GeV and 189 GeV," *Phys. Lett. B*, vol. 476, p. 256, 2000. DOI: 10.1016/S0370-2693(00)00197-0. arXiv: hep-ex/0003016 [hep-ex].

[63] L3 Collaboration, "Z boson pair production at LEP," *Phys. Lett. B*, vol. 572, p. 133, 2003. DOI: 10.1016/j.physletb.2003.08.023. arXiv: hep-ex/0308013 [hep-ex].

[64] DELPHI Collaboration, "ZZ production in e^+e^- interactions at $\sqrt{s} = 183$–209 GeV," *Eur. Phys. J. C*, vol. 30, p. 447, 2003. DOI: 10.1140/epjc/s2003-01287-0. arXiv: hep-ex/0307050 [hep-ex].

[65] OPAL Collaboration, "Study of Z pair production and anomalous couplings in e^+e^- collisions at $\sqrt{s}$ between 190 GeV and 209 GeV," *Eur. Phys. J. c*, vol. 32, p. 303, 2003. DOI: 10.1140/epjc/s2003-01467-x. arXiv: hep-ex/0310013 [hep-ex].

[66] ALEPH Collaboration, "Measurement of Z-pair production in e^+e^- collisions and constraints on anomalous neutral gauge couplings," *JHEP*, vol. 04, p. 124, 2009. DOI: 10.1088/1126-6708/2009/04/124.

[67] CDF Collaboration, "First measurement of ZZ production in $\bar{p}p$ collisions at $\sqrt{s} = 1.96$ TeV," *Phys. Rev. Lett.*, vol. 100, p. 201 801, 2008. DOI: 10.1103/PhysRevLett.100.201801. arXiv: 0801.4806 [hep-ex].

[68] D0 Collaboration, "ZZ $\to \ell^+\ell^-\nu\bar{\nu}$ production in $p\bar{p}$ collisions at $\sqrt{s} = 1.96$ TeV," *Phys. Rev. D*, vol. 78, p. 072 002, 2008. DOI: 10.1103/PhysRevD.78.072002. arXiv: 0808.0269 [hep-ex].

[69] D0 Collaboration, "Observation of ZZ production in $p\bar{p}$ collisions at $\sqrt{s} = 1.96$ TeV," *Phys. Rev. Lett.*, vol. 101, p. 171 803, 2008, DOI: 10.1103/PhysRevLett.101.171803. arXiv: 0808.0703 [hep-ex].

[70] D0 Collaboration, "Measurement of the ZZ production cross section in $p\bar{p}$ collisions at $\sqrt{s} = 1.96$ TeV," *Phys. Rev. D*, vol. 84, p. 011 103, 2011. DOI: 10.1103/PhysRevD.84.011103. arXiv: 1104.3078 [hep-ex].

[71] CDF Collaboration, "Measurement of ZZ production in leptonic final states at $\sqrt{s}$ of 1.96 TeV at CDF," *Phys. Rev. Lett.*, vol. 108, p. 101 801, 2012. DOI: 10.1103/PhysRevLett.108.101801. arXiv: 1112.2978 [hep-ex].

[72] CMS Collaboration, "Measurement of the ZZ production cross section and search for anomalous couplings in $2\ell 2\ell'$ final states in pp collisions at $\sqrt{s} = 7$ TeV," *JHEP*, vol. 01, p. 063, 2013. DOI: 10.1007/JHEP01(2013)063. arXiv: 1211.4890 [hep-ex].

[73] CMS Collaboration, "Measurement of the pp $\to$ ZZ production cross section and constraints on anomalous triple gauge couplings in four-lepton final states at $\sqrt{s} = 8$ TeV," *Phys. Lett. B*, vol. 740, p. 250, 2015, [Corrigendum: DOI: 10.1016/j.physletb.2016.04.010]. DOI: 10.1016/j.physletb.2014.11.059. arXiv: 1406.0113 [hep-ex].

[74] CMS Collaboration, "Measurements of the ZZ production cross sections in the $2\ell 2\nu$ channel in proton–proton collisions at $\sqrt{s} = 7$ and 8 TeV and combined constraints on triple gauge couplings," *Eur. Phys. J. C*, vol. 75, p. 511, 2015. DOI: 10.1140/epjc/s10052-015-3706-0. arXiv: 1503.05467 [hep-ex].

[75] CMS Collaboration, "Measurement of the differential cross sections for pairs of Z bosons produced in association with jets in pp collisions at $\sqrt{s} = 8$ TeV," CERN, Tech. Rep. CMS-PAS-SMP-15-012, 2016. https://cds.cern.ch/record/2209215.

[76] ATLAS Collaboration, "Measurement of ZZ production in pp collisions at $\sqrt{s} = 7$ TeV and limits on anomalous ZZZ and ZZγ couplings with the ATLAS detector," *JHEP*, vol. 03, p. 128, 2013. DOI: 10.1007/JHEP03(2013)128. arXiv: 1211.6096 [hep-ex].

[77] ATLAS Collaboration, "Measurements of four-lepton production in pp collisions at $\sqrt{s} = 8$ TeV with the ATLAS detector," *Phys. Lett. B*, vol. 753, p. 552, 2016. DOI: 10.1016/j.physletb.2015.12.048. arXiv: 1509.07844 [hep-ex].

[78] ATLAS Collaboration, "Measurement of the ZZ production cross section in proton-proton collisions at $\sqrt{s} = 8$ TeV using the ZZ $\to \ell^-\ell^+\ell'^-\ell'^+$ and ZZ $\to \ell^-\ell^+\nu\bar{\nu}$ channels with the ATLAS detector," *JHEP*, vol. 01, p. 099, 2017. DOI: 10.1007/JHEP01(2017)099. arXiv: 1610.07585 [hep-ex].

[79] CMS Collaboration, "Measurement of WZ and ZZ production in pp collisions at $\sqrt{s} = 8$ TeV in final states with b-tagged jets," *Eur. Phys. J. C*, vol. 74, p. 2973, 2014. DOI: 10.1140/epjc/s10052-014-2973-5. arXiv: 1403.3047 [hep-ex].

[80] CMS Collaboration, "Measurement of the pp $\to$ ZZ production cross section, Z $\to 4\ell$ branching fraction and constraints on anomalous triple gauge couplings at $\sqrt{s} = 13$ TeV," Tech. Rep. CMS-PAS-SMP-16-017, 2017. https://cds.cern.ch/record/2256100.

[81] ATLAS Collaboration, "Evidence for electroweak production of $W^{\pm}W^{\pm}$jj in pp collisions at $\sqrt{s} = 8$ TeV with the ATLAS detector," *Phys. Rev. Lett.*, vol. 113, p. 141 803, 2014. DOI: 10.1103/PhysRevLett.113.141803. arXiv: 1405.6241 [hep-ex].

[82] CMS Collaboration, "Study of vector boson scattering and search for new physics in events with two same-sign leptons and two jets," *Phys. Rev. Lett.*, vol. 114, p. 051 801, 2015. DOI: 10.1103/PhysRevLett.114.051801. arXiv: 1410.6315 [hep-ex].

[83] CMS Collaboration, "Measurement of the cross section for electroweak production of $Z\gamma$ in association with two jets and constraints on anomalous quartic gauge couplings in proton–proton collisions at $\sqrt{s} = 8\,\text{TeV}$," *Phys. Lett. B*, vol. 770, p. 380, 2017. DOI: 10.1016/j.physletb.2017.04.071. arXiv: 1702.03025 [hep-ex].

[84] ATLAS Collaboration, "Studies of $Z\gamma$ production in association with a high-mass dijet system in pp collisions at $\sqrt{s} = 8\,\text{TeV}$ with the ATLAS detector," *JHEP*, vol. 07, p. 107, 2017. DOI: 10.1007/JHEP07(2017)107. arXiv: 1705.01966 [hep-ex].

[85] CMS Collaboration, "Measurement of electroweak-induced production of $W\gamma$ with two jets in pp collisions at $\sqrt{s} = 8\,\text{TeV}$ and constraints on anomalous quartic gauge couplings," *JHEP*, vol. 06, p. 106, 2017. DOI: 10.1007/JHEP06(2017)106. arXiv: 1612.09256 [hep-ex].

[86] CMS Collaboration, "Evidence for exclusive $\gamma\gamma \to W^+W^-$ production and constraints on anomalous quartic gauge couplings in pp collisions at $\sqrt{s} = 7$ and $8\,\text{TeV}$," *JHEP*, vol. 08, p. 119, 2016. DOI: 10.1007/JHEP08(2016)119. arXiv: 1604.04464 [hep-ex].

[87] ATLAS Collaboration, "Measurement of exclusive $\gamma\gamma \to W^+W^-$ production and search for exclusive Higgs boson production in pp collisions at $\sqrt{s} = 8\,\text{TeV}$ using the ATLAS detector," *Phys. Rev. D*, vol. 94, p. 032 011, 2016. DOI: 10.1103/PhysRevD.94.032011. arXiv: 1607.03745 [hep-ex].

[88] CMS Collaboration Collaboration, "Observation of electroweak production of same-sign W boson pairs in the two jet and two same-sign lepton final state in proton-proton collisions at 13 TeV," CERN, Tech. Rep. CMS-PAS-SMP-17-004, 2017. https://cds.cern.ch/record/2264525.

[89] ALEPH Collaboration, "Study of the four fermion final state at the Z resonance," *Z. Phys. C*, vol. 66, p. 3, 1995. DOI: 10.1007/BF01496576.

[90] CMS Collaboration, "Observation of Z decays to four leptons with the CMS detector at the LHC," *JHEP*, vol. 12, p. 034, 2012. DOI: 10.1007/JHEP12(2012)034. arXiv: 1210.3844 [hep-ex].

[91] ATLAS Collaboration, "Measurements of four-lepton production at the Z resonance in pp collisions at $\sqrt{s} = 7$ and $8\,\text{TeV}$ with ATLAS," *Phys. Rev. Lett.*, vol. 112, p. 231 806, 2014. DOI: 10.1103/PhysRevLett.112.231806. arXiv: 1403.5657 [hep-ex].

[92] LHC Higgs Cross Section Working Group Collaboration, "Handbook of LHC Higgs cross sections: 4. deciphering the nature of the Higgs sector," 2016. DOI: 10.23731/CYRM-2017-002. arXiv: 1610.07922 [hep-ph].

[93] OPAL Collaboration, DELPHI Collaboration, LEP Working Group for Higgs boson searches, ALEPH Collaboration, L3 Collaboration, "Search for the standard model Higgs boson at LEP," *Phys. Lett. B*, vol. 565, p. 61, 2003. DOI: 10.1016/S0370-2693(03)00614-2. arXiv: hep-ex/0306033 [hep-ex].

[94] DELPHI Collaboration, OPAL Collaboration, ALEPH Collaboration, LEP Electroweak Working Group, L3 Collaboration, "A combination of preliminary electroweak measurements and constraints on the standard model," 2006. arXiv: hep-ex/0612034 [hep-ex].

[95] CDF Collaboration, D0 Collaboration, "Higgs boson studies at the Tevatron," *Phys. Rev. D*, vol. 88, p. 052 014, 2013. DOI: 10.1103/PhysRevD.88.052014. arXiv: 1303.6346 [hep-ex].

[96] CDF Collaboration, D0 Collaboration, "Evidence for a particle produced in association with weak bosons and decaying to a bottom-antibottom quark pair in Higgs boson searches at the Tevatron," *Phys. Rev. Lett.*, vol. 109, p. 071 804, 2012. DOI: 10.1103/PhysRevLett.109.071804. arXiv: 1207.6436 [hep-ex].

[97] Tevatron Electroweak Working Group, CDF Collaboration, DELPHI Collaboration, SLD Electroweak and Heavy Flavour Groups, ALEPH Collaboration, LEP Electroweak Working Group, SLD Collaboration, OPAL Collaboration, D0 Collaboration, L3 Collaboration, "Precision electroweak measurements and constraints on the standard model," 2010. arXiv: 1012.2367 [hep-ex].

[98] CMS Collaboration, "Observation of a new boson at a mass of 125 GeV with the CMS experiment at the LHC," *Phys. Lett. B*, vol. 716, p. 30, 2012. DOI: 10.1016/j.physletb.2012.08.021. arXiv: 1207.7235 [hep-ex].

[99] ATLAS Collaboration, "Observation of a new particle in the search for the standard model Higgs boson with the ATLAS detector at the LHC," *Phys. Lett. B*, vol. 716, p. 1, 2012. DOI: 10.1016/j.physletb.2012.08.020. arXiv: 1207.7214 [hep-ex].

[100] CMS Collaboration, "Search for the standard model Higgs boson in the decay channel $H \to ZZ \to 4$ leptons in pp collisions at $\sqrt{s} = 7$ TeV," *Phys. Rev. Lett.*, vol. 108, p. 111 804, 2012. DOI: 10.1103/PhysRevLett.108.111804. arXiv: 1202.1997 [hep-ex].

[101] ATLAS Collaboration, CMS Collaboration, "Combined measurement of the Higgs boson mass in pp collisions at $\sqrt{s} = 7$ and 8 TeV with the ATLAS and CMS experiments," *Phys. Rev. Lett.*, vol. 114, p. 191 803, 2015. DOI: 10.1103/PhysRevLett.114.191803. arXiv: 1503.07589 [hep-ex].

[102] ATLAS Collaboration, CMS Collaboration, "Measurements of the Higgs boson production and decay rates and constraints on its couplings from a combined ATLAS and CMS analysis of the LHC pp collision data at $\sqrt{s} = 7$ and 8 TeV," *JHEP*, vol. 08, p. 045, 2016. DOI: 10.1007/JHEP08(2016)045. arXiv: 1606.02266 [hep-ex].

[103] I. Ots, H. Uibo, H. Liivat, R. Saar, and R. K. Loide, "Possible anomalous ZZγ and Z$\gamma\gamma$ couplings and Z boson spin orientation in $e^+e^- \to Z\gamma$," *Nucl. Phys.*, vol. B702, pp. 346–356, 2004. DOI: 10.1016/j.nuclphysb.2004.09.019.

[104] DELPHI Collaboration, "Study of triple-gauge-boson couplings ZZZ, ZZγ and Z$\gamma\gamma$ at LEP," *Eur. Phys. J. C*, vol. 51, p. 525, 2007. DOI: 10.1140/epjc/s10052-007-0345-0. arXiv: 0706.2741 [hep-ex].

[105] CDF Collaboration, D0 Collaboration, "Diboson physics at the Tevatron," *EPJ Web Conf.*, vol. 28, p. 06 001, 2012. DOI: 10.1051/epjconf/20122806001. arXiv: 1201.4771 [hep-ex].

[106] D0 Collaboration, "Search for ZZ and Zγ^* production in $p\bar{p}$ collisions at $\sqrt{s} = 1.96$ TeV and limits on anomalous ZZZ and ZZγ^* couplings," *Phys. Rev. Lett.*, vol. 100, p. 131 801, 2008. DOI: 10.1103/PhysRevLett.100.131801. arXiv: 0712.0599 [hep-ex].

[107] ATLAS Collaboration, "Measurement of the ZZ production cross section and limits on anomalous neutral triple gauge couplings in proton-proton collisions at $\sqrt{s} = 7$ TeV with the ATLAS detector," *Phys. Rev. Lett.*, vol. 108, p. 041 804, 2012. DOI: 10.1103/PhysRevLett.108.041804. arXiv: 1110.5016 [hep-ex].

[108] ATLAS Collaboration, "Measurement of the ZZ production cross section in pp collisions at $\sqrt{s} = 13$ TeV with the ATLAS detector," *Phys. Rev. Lett.*, vol. 116, p. 101 801, 2016. DOI: 10.1103/PhysRevLett.116.101801. arXiv: 1512.05314 [hep-ex].

[109] L. Evans and P. Bryant, "LHC machine," *JINST*, vol. 3, S08001, 2008. DOI: 10.1088/1748-0221/3/08/S08001.

[110] O. Brüning, H. Burkhardt, and S. Myers, "The Large Hadron Collider," *Prog. Part. Nucl. Phys.*, vol. 67, p. 7054, 2012. DOI: https://doi.org/10.1016/j.ppnp.2012.03.001.

[111] CMS Collaboration, "The CMS experiment at the CERN LHC," *JINST*, vol. 3, S08004, 2008. DOI: 10.1088/1748-0221/3/08/S08004.

[112] C. Lefèvre, "The CERN accelerator complex. complexe des accélérateurs du CERN," Dec. 2008, https://cds.cern.ch/record/1260465.

[113] ATLAS Collaboration, "The ATLAS experiment at the CERN Large Hadron Collider," *JINST*, vol. 3, S08003, 2008. DOI: 10.1088/1748-0221/3/08/S08003.

[114] LHCb Collaboration, "The LHCb detector at the LHC," *JINST*, vol. 3, S08005, 2008. DOI: 10.1088/1748-0221/3/08/S08005.

[115] ALICE Collaboration, "The ALICE experiment at the CERN LHC," *JINST*, vol. 3, S08002, 2008. DOI: 10.1088/1748-0221/3/08/S08002.

[116] TOTEM Collaboration, "The TOTEM experiment at the CERN Large Hadron Collider," *JINST*, vol. 3, S08007, 2008. DOI: 10.1088/1748-0221/3/08/S08007.

[117] LHCf Collaboration, "The LHCf detector at the CERN Large Hadron Collider," *JINST*, vol. 3, S08006, 2008. DOI: 10.1088/1748-0221/3/08/S08006.

[118] MoEDAL Collaboration, "The physics programme of the MoEDAL experiment at the LHC," *Int. J. Mod. Phys.*, vol. A29, p. 1 430 050, 2014. DOI: 10.1142/S0217751X14300506. arXiv: 1405.7662 [hep-ph].

[119] M. Bajko *et al.*, "Report of the task force on the incident of 19th September 2008 at the LHC," CERN, Geneva, Tech. Rep. LHC-PROJECT-Report-1168. CERN-LHC-PROJECT-Report-1168, Mar. 2009. http://cds.cern.ch/record/1168025.

[120] M. Lamont, "Status of the LHC," *Journal of Physics: Conference Series*, vol. 455, p. 012 001, 2013. http://stacks.iop.org/1742-6596/455/i=1/a=012001.

[121] Y. Papaphilippou, H. Bartosik, G. Rumolo, and D. Manglunki, "Operational beams for the LHC," 2014. arXiv: 1412.7857 [physics.acc-ph].

[122] F. Bordry and C. Pralavorio, "LHC smashes targets for 2016 run," Nov. 2016. http://cds.cern.ch/record/2235979.

[123] T. Sakuma and T. McCauley, "Detector and event visualization with SketchUp at the CMS experiment," CERN, Geneva, Tech. Rep. CMS-CR-2013-379, Oct. 2013. arXiv: 1311.4942. https://cds.cern.ch/record/1626816.

[124] CMS Collaboration, "The magnet project: technical design report," 1997. https://cds.cern.ch/record/331056.

[125] CMS Collaboration, "The CMS tracker system project: technical design report," 1997. http://cds.cern.ch/record/368412.

[126] B. Isildak, "Measurement of the differential dijet production cross section in proton-proton collisions at $\sqrt{s} = 7\,\text{TeV}$," PhD thesis, Bogazici U., 2011. arXiv: 1308.6064 [hep-ex]. https://inspirehep.net/record/1251416/files/arXiv:1308.6064.pdf.

[127] "The CMS muon project: technical design report," 1997. http://cds.cern.ch/record/343814.

[128] CMS Collaboration, "The CMS muon system in Run2: preparation, status and first results," *PoS*, vol. EPS-HEP2015, p. 237, 2015. arXiv: 1510.05424 [physics.ins-det].

[129] CMS Collaboration, "CMS technical design report for the level-1 trigger upgrade," Tech. Rep. CERN-LHCC-2013-011. CMS-TDR-12, Jun. 2013. https://cds.cern.ch/record/1556311.

[130] P. R. K. Chumney, S. Dasu, J. Lackey, M. Jaworski, P. Robl, and W. H. Smith, "Level-1 regional calorimeter trigger system for CMS," *EConf*, vol. C0303241, THHT003, 2003. arXiv: hep-ex/0305047 [hep-ex].

[131] B. Kreis and others, "Run 2 upgrades to the CMS level-1 calorimeter trigger," *JINST*, vol. 11, p. C01051, 2016. DOI: 10.1088/1748-0221/11/01/C01051. arXiv: 1511.05855 [physics.ins-det].

[132] A. Svetek, M. Blake, M. Cepeda Hermida, S. Dasu, L. Dodd, R. Fobes, B. Gomber, T. Gorski, Z. Guo, P. Klabbers, A. Levine, I. Ojalvo, T. Ruggles, N. Smith, W. Smith, J. Tikalsky, M. Vicente, and N. Woods, "The calorimeter trigger processor card: the next generation of high speed algorithmic data processing at CMS," *JINST*, vol. 11, p. C02011, 2016. DOI: 10.1088/1748-0221/11/02/C02011.

[133] J. Ero *et al.*, "The CMS drift tube trigger track finder," *JINST*, vol. 3, P08006, 2008. DOI: 10.1088/1748-0221/3/08/P08006.

[134] D. Acosta, A. Atamanchuk, V. Golovtsov, A. Madorsky, B. Razmyslovich, B. Scurlock, and S. Wang, "The track-finding processor for the level-1 trigger of the CMS endcap muon system," 1999.

[135] J. Ero *et al.*, "The CMS level-1 trigger barrel track finder," *JINST*, vol. 11, p. C03038, 2016. DOI: 10.1088/1748-0221/11/03/C03038.

[136] W. M. Zabolotny and A. Byszuk, "Algorithm and implementation of muon trigger and data transmission system for barrel-endcap overlap region of the CMS detector," *JINST*, vol. 11, p. C03004, 2016. DOI: 10.1088/1748-0221/11/03/C03004.

[137] H. Sakulin and A. Taurok, "The level-1 global muon trigger for the CMS experiment," CERN, Geneva, Tech. Rep. CMS-CR-2003-040, Oct. 2003. https://cds.cern.ch/record/687846.

[138] M. Jeitler, J. Lingemann, D. Rabady, H. Sakulin, and A. Stahl, "Upgrade of the CMS global muon trigger," *IEEE Trans. Nucl. Sci.*, vol. 62, pp. 1104–1109, 2015. DOI: 10.1109/TNS.2015.2435060.

[139] M. Jeitler *et al.*, "The level-1 global trigger for the CMS experiment at LHC," *JINST*, vol. 2, P01006, 2007. DOI: 10.1088/1748-0221/2/01/P01006.

[140] J. Wittmann, B. Arnold, H. Bergauer, M. Jeitler, T. Matsushita, D. Rabady, B. Rahbaran, and C.-E. Wulz, "The upgrade of the CMS global trigger," *JINST*, vol. 11, p. C02029, 2016. http://stacks.iop.org/1748-0221/11/i=02/a=C02029.

[141] CMS Collaboration, "The CMS high level trigger," *Eur. Phys. J. C*, vol. 46, p. 605, 2006. DOI: 10.1140/epjc/s2006-02495-8. arXiv: hep-ex/0512077 [hep-ex].

[142] S. Van der Meer, "Calibration of the effective beam height in the ISR," 1968.

[143] CMS Collaboration, "Beams scan based absolute normalization of the CMS luminosity measurement. CMS 2010 luminosity determination," 2011. https://cds.cern.ch/record/1357856.

[144] CMS Collaboration, "CMS luminosity measurement for the 2015 data-taking period," CERN, Tech. Rep. CMS-PAS-LUM-15-001, 2017. http://cds.cern.ch/record/2138682.

[145] CMS Collaboration Collaboration, "CMS luminosity measurements for the 2016 data taking period," CERN, Tech. Rep. CMS-PAS-LUM-17-001, 2017. http://cds.cern.ch/record/2257069.

[146] N. Metropolis and S. Ulam, "The Monte Carlo method," *Journal of the American Statistical Association*, vol. 44, p. 335, 1949. DOI: 10.2307/2280232. http://www.jstor.org/stable/2280232.

[147] M. Matsumoto and T. Nishimura, "Mersenne Twister: A 623-dimensionally equidistributed uniform pseudo-random number generator," *ACM Trans. Model. Comput. Simul.*, vol. 8, p. 3, 1998. DOI: 10.1145/272991.272995. http://doi.acm.org/10.1145/272991.272995.

[148] CTEQ Collaboration, "Handbook of perturbative QCD: version 1.0," *Rev. Mod. Phys.*, vol. 67, p. 157, 1995. DOI: 10.1103/RevModPhys.67.157.

[149] J. Alwall, R. Frederix, S. Frixione, V. Hirschi, F. Maltoni, O. Mattelaer, H.-S. Shao, T. Stelzer, P. Torrielli, and M. Zaro, "The automated computation of tree-level and next-to-leading order differential cross sections, and their matching to parton shower simulations," *JHEP*, vol. 07, p. 079, 2014. DOI: 10.1007/JHEP07(2014)079. arXiv: 1405.0301 [hep-ph].

[150] P. Nason, "A new method for combining NLO QCD with shower Monte Carlo algorithms," *JHEP*, vol. 11, p. 040, 2004. DOI: 10.1088/1126-6708/2004/11/040. arXiv: hep-ph/0409146 [hep-ph].

[151] S. Frixione, P. Nason, and C. Oleari, "Matching NLO QCD computations with parton shower simulations: the POWHEG method," *JHEP*, vol. 11, p. 070, 2007. DOI: 10.1088/1126-6708/2007/11/070. arXiv: 0709.2092 [hep-ph].

[152] S. Alioli, P. Nason, C. Oleari, and E. Re, "A general framework for implementing NLO calculations in shower Monte Carlo programs: the POWHEG BOX," *JHEP*, vol. 06, p. 043, 2010. DOI: 10.1007/JHEP06(2010)043. arXiv: 1002.2581 [hep-ph].

[153] T. Gleisberg, S. Hoeche, F. Krauss, M. Schonherr, S. Schumann, F. Siegert, and J. Winter, "Event generation with SHERPA 1.1," *JHEP*, vol. 02, p. 007, 2009. DOI: 10.1088/1126-6708/2009/02/007. arXiv: 0811.4622 [hep-ph].

[154] J. M. Campbell, R. K. Ellis, and W. T. Giele, "A multi-threaded version of MCFM," *Eur. Phys. J. C*, vol. 75, p. 246, 2015. DOI: 10.1140/epjc/s10052-015-3461-2. arXiv: 1503.06182 [physics.comp-ph].

[155] R. Boughezal, J. M. Campbell, R. K. Ellis, C. Focke, W. Giele, X. Liu, F. Petriello, and C. Williams, "Color singlet production at NNLO in MCFM," *Eur. Phys. J. C*, vol. 77, p. 7, 2017. DOI: 10.1140/epjc/s10052-016-4558-y. arXiv: 1605.08011 [hep-ph].

[156] G. P. Lepage, "A new algorithm for adaptive multidimensional integration," *J. Comput. Phys.*, vol. 27, p. 192, 1978. DOI: 10.1016/0021-9991(78)90004-9.

[157] M. Bahr *et al.*, "Herwig++ physics and manual," *Eur. Phys. J. C*, vol. 58, p. 639, 2008. DOI: 10.1140/epjc/s10052-008-0798-9. arXiv: 0803.0883 [hep-ph].

[158] J. Bellm *et al.*, "Herwig 7.0/Herwig++ 3.0 release note," *Eur. Phys. J. C*, vol. 76, p. 196, 2016. DOI: 10.1140/epjc/s10052-016-4018-8. arXiv: 1512.01178 [hep-ph].

[159] B. Andersson, G. Gustafson, and C. Peterson, "A semiclassical model for quark jet fragmentation," *Z. Phys. C*, vol. 1, p. 105, 1979. DOI: 10.1007/BF01450386.

[160] B. Andersson, G. Gustafson, and B. Soderberg, "A general model for jet fragmentation," *Z. Phys. C*, vol. 20, p. 317, 1983. DOI: 10.1007/BF01407824.

[161] B. Andersson, S. Mohanty, and F. Soderberg, "The lund fragmentation process for a multigluon string according to the area law," *Eur. Phys. J. C*, vol. 21, p. 631, 2001. DOI: 10.1007/s100520100757. arXiv: hep-ph/0106185 [hep-ph].

[162] Sjöstrand, T. and Skands, Peter Z., "Transverse-momentum-ordered showers and interleaved multiple interactions," *Eur. Phys. J. C*, vol. 39, p. 129, 2005. DOI: 10.1140/epjc/s2004-02084-y. arXiv: hep-ph/0408302 [hep-ph].

[163] J. Alwall *et al.*, "Comparative study of various algorithms for the merging of parton showers and matrix elements in hadronic collisions," *Eur. Phys. J. C*, vol. 53, p. 473, 2008. DOI: 10.1140/epjc/s10052-007-0490-5. arXiv: 0706.2569 [hep-ph].

[164] J. Alwall, S. de Visscher, and F. Maltoni, "QCD radiation in the production of heavy colored particles at the LHC," *JHEP*, vol. 02, p. 017, 2009. DOI: 10.1088/1126-6708/2009/02/017. arXiv: 0810.5350 [hep-ph].

[165] M. Rauch, "Vector-boson fusion and vector-boson scattering," 2016. arXiv: 1610.08420 [hep-ph].

[166] M. L. Mangano, M. Moretti, F. Piccinini, and M. Treccani, "Matching matrix elements and shower evolution for top-quark production in hadronic collisions," *JHEP*, vol. 01, p. 013, 2007. DOI: 10.1088/1126-6708/2007/01/013. arXiv: hep-ph/0611129 [hep-ph].

[167] S. Catani, F. Krauss, R. Kuhn, and B. R. Webber, "QCD matrix elements + parton showers," *JHEP*, vol. 11, p. 063, 2001. DOI: 10.1088/1126-6708/2001/11/063. arXiv: hep-ph/0109231 [hep-ph].

[168] R. Frederix and S. Frixione, "Merging meets matching in MC@NLO," *JHEP*, vol. 12, p. 061, 2012. DOI: 10.1007/JHEP12(2012)061. arXiv: 1209.6215 [hep-ph].

[169] Sjöstrand, T. and Skands, Peter Z., "Multiple interactions and the structure of beam remnants," *JHEP*, vol. 03, p. 053, 2004. DOI: 10.1088/1126-6708/2004/03/053. arXiv: hep-ph/0402078 [hep-ph].

[170] A. V. Manohar and W. J. Waalewijn, "A QCD analysis of double parton scattering: color correlations, interference effects and evolution," *Phys. Rev. D*, vol. 85, p. 114 009, 2012. DOI: 10.1103/PhysRevD.85.114009. arXiv: 1202.3794 [hep-ph].

[171] S Banerjee, "CMS simulation software," *Journal of Physics: Conference Series*, vol. 396, p. 022 003, 2012. %7Bhttp://stacks.iop.org/1742-6596/396/i=2/a=022003%7D.

[172] M Hildreth and V N Ivanchenko and D J Lange and M J Kortelainen, "CMS full simulation for run-2," *Journal of Physics: Conference Series*, vol. 664, p. 072 022, 2015. %7Bhttp://stacks.iop.org/1742-6596/664/i=7/a=072022%7D.

[173] S. Alioli, P. Nason, C. Oleari, and E. Re, "NLO vector-boson production matched with shower in POWHEG," *JHEP*, vol. 07, p. 060, 2008. DOI: 10.1088/1126-6708/2008/07/060. arXiv: 0805.4802 [hep-ph].

[174] J. M. Campbell and R. K. Ellis, "MCFM for the Tevatron and the LHC," *Nucl. Phys. Proc. Suppl.*, vol. 205, p. 10, 2010. DOI: 10.1016/j.nuclphysbps.2010.08.011. arXiv: 1007.3492 [hep-ph].

[175] A. Ballestrero, A. Belhouari, G. Bevilacqua, V. Kashkan, and E. Maina, "PHANTOM : a Monte Carlo event generator for six parton final states at high energy colliders," *Comput. Phys. Commun.*, vol. 180, p. 401, 2009. DOI: 10.1016/j.cpc.2008.10.005. arXiv: 0801.3359 [hep-ph].

[176] NNPDF Collaboration, "Parton distributions for the LHC Run II," *JHEP*, vol. 04, p. 040, 2015. DOI: 10.1007/JHEP04(2015)040. arXiv: 1410.8849 [hep-ph].

[177] CMS Collaboration, "Event generator tunes obtained from underlying event and multiparton scattering measurements," *Eur. Phys. J. C*, vol. 76, p. 155, 2016. DOI: 10.1140/epjc/s10052-016-3988-x. arXiv: 1512.00815 [hep-ex].

[178] GEANT4 Collaboration, "GEANT4: a simulation toolkit," *Nucl. Instrum. Meth. A*, vol. 506, p. 250, 2003. DOI: 10.1016/S0168-9002(03)01368-8.

[179] R. Frühwirth, "Application of Kalman filtering to track and vertex fitting," *Nucl. Instrum. Meth. A*, vol. 262, p. 444, 1987. DOI: 10.1016/0168-9002(87)90887-4.

[180] P. Billoir and S. Qian, "Simultaneous pattern recognition and track fitting by the Kalman filtering method," *Nucl. Instrum. Meth. A*, vol. 294, p. 219, 1990. DOI: 10.1016/0168-9002(90)91835-Y.

[181] W. Adam, B. Mangano, T. Speer, and T. Todorov, "Track reconstruction in the CMS tracker," 2005.

[182] CMS Collaboration, "Description and performance of track and primary-vertex reconstruction with the CMS tracker," *JINST*, vol. 9, P10009, 2014. DOI: 10.1088/1748-0221/9/10/P10009. arXiv: 1405.6569 [physics.ins-det].

[183] W. Adam, R. Frühwirth, A. Strandlie, and T. Todor, "Reconstruction of electrons with the Gaussian-sum filter in the CMS tracker at the LHC," 2005.

[184] T. Speer, K. Prokofiev, R. Fruhwirth, W. Waltenberger, and P. Vanlaer, "Vertex fitting in the CMS tracker," 2006.

[185] K. Rose, "Deterministic annealing for clustering, compression, classification, regression, and related optimization problems," *Proceedings of the IEEE*, vol. 86, p. 2210, Nov. 1998, ISSN: 0018-9219. DOI: 10.1109/5.726788.

[186] CMS Collaboration, "Particle-flow event reconstruction in CMS and performance for jets, taus, and MET," CERN, Tech. Rep. CMS-PAS-PFT-09-001, Apr. 2009. https://cds.cern.ch/record/1194487.

[187] CMS Collaboration, "Commissioning of the particle-flow event reconstruction with the first LHC collisions recorded in the CMS detector," Tech. Rep. CMS-PAS-PFT-10-001, 2010. https://cds.cern.ch/record/1247373.

[188] CMS Collaboration, "Particle-flow reconstruction and global event description with the CMS detector," vol. 12, P10003, 2017. DOI: 10.1088/1748-0221/12/10/P10003. arXiv: 1706.04965 [physics.ins-det].

[189] CMS Collaboration, "Performance of CMS muon reconstruction in pp collision events at $\sqrt{s} = 7\,\text{TeV}$," *JINST*, vol. 7, P10002, 2012. DOI: 10.1088/1748-0221/7/10/P10002. arXiv: 1206.4071 [physics.ins-det].

[190] S. Baffioni, C. Charlot, F. Ferri, D. Futyan, P. Meridiani, I. Puljak, C. Rovelli, R. Salerno, and Y. Sirois, "Electron reconstruction in CMS," *Eur. Phys. J. C*, vol. 49, p. 1099, 2007. DOI: 10.1140/epjc/s10052-006-0175-5.

[191] CMS Collaboration, "Performance of photon reconstruction and identification with the CMS detector in proton-proton collisions at $\sqrt{s} = 8\,\text{TeV}$," *JINST*, vol. 10, P08010, 2015. DOI: 10.1088/1748-0221/10/08/P08010. arXiv: 1502.02702 [physics.ins-det].

[192] G. P. Salam and G. Soyez, "A practical seedless infrared-safe cone jet algorithm," *JHEP*, vol. 05, p. 086, 2007. DOI: 10.1088/1126-6708/2007/05/086. arXiv: 0704.0292 [hep-ph].

[193] G. P. Salam, "Towards jetography," *Eur. Phys. J. C*, vol. 67, p. 637, 2010. DOI: 10.1140/epjc/s10052-010-1314-6. arXiv: 0906.1833 [hep-ph].

[194] M. Cacciari, G. P. Salam, and G. Soyez, "The anti-k_T jet clustering algorithm," *JHEP*, vol. 04, p. 063, 2008. DOI: 10.1088/1126-6708/2008/04/063. arXiv: 0802.1189 [hep-ph].

[195] M. Cacciari, G. P. Salam, and G. Soyez, "FastJet user manual," *Eur. Phys. J. C*, vol. 72, p. 1896, 2012. DOI: 10.1140/epjc/s10052-012-1896-2. arXiv: 1111.6097 [hep-ph].

[196] CMS Collaboration, "Study of pileup removal algorithms for jets," Tech. Rep. CMS-PAS-JME-14-001, 2014. https://cds.cern.ch/record/1751454.

[197] CMS Collaboration, "Jet energy scale and resolution in the CMS experiment in pp collisions at 8 TeV," *JINST*, vol. 12, P02014, 2017. DOI: 10.1088/1748-0221/12/02/P02014. arXiv: 1607.03663 [hep-ex].

[198] M. Cacciari, G. P. Salam, and G. Soyez, "The catchment area of jets," *JHEP*, vol. 04, p. 005, 2008. DOI: 10.1088/1126-6708/2008/04/005. arXiv: 0802.1188 [hep-ph].

[199] M. Cacciari and G. P. Salam, "Pileup subtraction using jet areas," *Phys. Lett. B*, vol. 659, p. 119, 2008. DOI: 10.1016/j.physletb.2007.09.077. arXiv: 0707.1378 [hep-ph].

[200] CMS Collaboration, "Determination of jet energy calibration and transverse momentum resolution in CMS," *JINST*, vol. 6, P11002, 2011. DOI: 10.1088/1748-0221/6/11/P11002. arXiv: 1107.4277 [physics.ins-det].

[201] CMS Collaboration, "Missing transverse energy performance of the CMS detector," *JINST*, vol. 6, P09001, 2011. DOI: 10.1088/1748-0221/6/09/P09001. arXiv: 1106.5048 [physics.ins-det].

[202] CMS Collaboration, "Performance of the CMS missing transverse momentum reconstruction in pp data at $\sqrt{s} = 8$ TeV," *JINST*, vol. 10, P02006, 2015. DOI: 10.1088/1748-0221/10/02/P02006. arXiv: 1411.0511 [physics.ins-det].

[203] CMS Collaboration, "Performance of missing energy reconstruction in 13 TeV pp collision data using the CMS detector," CERN, Tech. Rep. CMS-PAS-JME-16-004, 2016. http://cds.cern.ch/record/2205284.

[204] CMS Collaboration, "Electron reconstruction and identification at $\sqrt{s} = 7$ TeV," CERN, Tech. Rep. CMS-PAS-EGM-10-004, 2010. https://cds.cern.ch/record/1299116.

[205] CMS Collaboration, "Performance of electron reconstruction and selection with the CMS detector in proton-proton collisions at $\sqrt{s} = 8$ TeV," *JINST*, vol. 10, P06005, 2015. DOI: 10.1088/1748-0221/10/06/P06005. arXiv: 1502.02701 [physics.ins-det].

[206] CMS Collaboration, "Measurement of the inclusive W and Z production cross sections in pp collisions at $\sqrt{s} = 7$ TeV," *JHEP*, vol. 10, p. 132, 2011. DOI: 10.1007/JHEP10(2011)132. arXiv: 1107.4789 [hep-ex].

[207] CMS Collaboration, "Measurement of the properties of a Higgs boson in the four-lepton final state," *Phys. Rev. D*, vol. 89, p. 092 007, 2014. DOI: 10.1103/PhysRevD.89.092007. arXiv: 1312.5353 [hep-ex].

[208] J. Butterworth *et al.*, "PDF4LHC recommendations for LHC Run II," *J. Phys. G*, vol. 43, p. 023 001, 2016. DOI: 10.1088/0954-3899/43/2/023001. arXiv: 1510.03865 [hep-ph].

[209] G. Bohm and G. Zech, *Introduction to statistics and data analysis for physicists*. DESY, 2010, ISBN: 9783935702416. https://books.google.ch/books?id=aQBHcgAACAAJ.

[210] G. D'Agostini, "A multidimensional unfolding method based on Bayes' theorem," *Nucl. Instrum. Meth. A*, vol. 362, p. 487, 1995. DOI: 10.1016/0168-9002(95)00274-X.

[211] A. P. Dempster, N. M. Laird, and D. B. Rubin, "Maximum likelihood from incomplete data via the EM algorithm," *J. R. Stat. Soc. B*, vol. 39, p. 1, 1977, ISSN: 00359246. http://www.jstor.org/stable/2984875.

[212] L. B. Lucy, "An iterative technique for the rectification of observed distributions," *Astron. J.*, vol. 79, p. 745, Jun. 1974. DOI: 10.1086/111605.

[213] W. H. Richardson, "Bayesian-based iterative method of image restoration," *J. Opt. Soc. Am.*, vol. 62, p. 55, Jan. 1972. DOI: 10.1364/JOSA.62.000055. http://www.osapublishing.org/abstract.cfm?URI=josa-62-1-55.

[214] L. A. Shepp and Y. Vardi, "Maximum likelihood reconstruction for emission tomography," *IEEE Transactions on Medical Imaging*, vol. 1, p. 113, Oct. 1982, ISSN: 0278-0062. DOI: 10.1109/TMI.1982.4307558.

[215] T. Adye, "Unfolding algorithms and tests using RooUnfold," in *Proceedings, PHYSTAT 2011 Workshop on Statistical Issues Related to Discovery Claims in Search Experiments and Unfolding, CERN, Geneva, Switzerland 17–20 January 2011*, CERN, Geneva: CERN, 2011, p. 313. DOI: 10.5170/CERN-2011-006.313. arXiv: 1105.1160 [physics.data-an]. https://inspirehep.net/record/898599/files/arXiv:1105.1160.pdf.

[216] Y. Vardi, "Empirical distributions in selection bias models," *Ann. Statist.*, vol. 13, p. 178, Mar. 1985. DOI: 10.1214/aos/1176346585. http://dx.doi.org/10.1214/aos/1176346585.

[217] F. Pedregosa, G. Varoquaux, A. Gramfort, V. Michel, B. Thirion, O. Grisel, M. Blondel, P. Prettenhofer, R. Weiss, V. Dubourg, J. Vanderplas, A. Passos, D. Cournapeau, M. Brucher, M. Perrot, and E. Duchesnay, "Scikit-learn: Machine learning in Python," *J. Mach. Learn. Res.*, vol. 12, p. 2825, 2011.

[218] CMS Collaboration Collaboration, "Performance of quark/gluon discrimination in 8 TeV pp data," CERN, Tech. Rep. CMS-PAS-JME-13-002, 2013. https://cds.cern.ch/record/1599732.

[219] G. Cowan, K. Cranmer, E. Gross, and O. Vitells, "Asymptotic formulae for likelihood-based tests of new physics," *Eur. Phys. J. C*, vol. 71, p. 1554, 2011, [Erratum: DOI: 10.1140/epjc/s10052-013-2501-z]. DOI: 10.1140/epjc/s10052-011-1554-0. arXiv: 1007.1727 [physics.data-an].

[220] CMS Collaboration and ATLAS Collaboration, "Combination of results from the ATLAS and CMS experiments on anomalous triple gauge couplings in ZZ production from pp collisions at a centre-of-mass energy of 7 TeV at the LHC," CERN, Tech. Rep. CMS-PAS-SMP-15-001. ATLAS-CONF-2016-036, 2016. https://cds.cern.ch/record/2202807.

[221] CMS Collaboration, "Measurement of the ZZ production cross section in $\ell\ell\ell'\ell'$ decays in pp collisions at $\sqrt{s} = 13\,\text{TeV}$," Tech. Rep. CMS-PAS-SMP-15-005, 2015. https://cds.cern.ch/record/2114822.

[222] CMS Collaboration, "Measurement of the ZZ production cross section and $\text{Z} \to \ell^+\ell^-\ell'^+\ell'^-$ branching fraction in pp collisions at $\sqrt{s} = 13\,\text{TeV}$," *Phys. Lett. B*, vol. 763, p. 280, 2016. DOI: 10.1016/j.physletb.2016.10.054. arXiv: 1607.08834 [hep-ex].

[223] CMS Collaboration, "Measurements of the $\text{pp} \to \text{ZZ}$ production cross section and the $\text{Z} \to 4\ell$ branching fraction, and constraints on anomalous triple gauge couplings at $\sqrt{s} = 13\,\text{TeV}$," 2017, submitted to *Eur. Phys. J. C*. arXiv: 1709.08601 [hep-ex].

[224] CMS Collaboration, "Measurements of differential cross sections and search for the electroweak production of two Z bosons produced in association with jets," Tech. Rep. CMS-PAS-SMP-16-019, 2017. https://cds.cern.ch/record/2264556.

[225] CMS Collaboration, "Measurement of vector boson scattering and constraints on anomalous quartic couplings from events with four leptons and two jets in proton-proton collisions at $\sqrt{s} = 13\,\text{TeV}$," 2017, accepted by *Phys. Lett. B*. arXiv: 1708.02812 [hep-ex].

[226] CMS Collaboration, "Studies of Higgs boson production in the four-lepton final state at $\sqrt{s} = 13\,\text{TeV}$," Tech. Rep. CMS-PAS-HIG-15-004, 2016. https://cds.cern.ch/record/2139978.

[227] CMS Collaboration, "Measurements of properties of the Higgs boson and search for an additional resonance in the four-lepton final state at $\sqrt{s} = 13\,\text{TeV}$," Tech. Rep. CMS-PAS-HIG-16-033, 2016. https://cds.cern.ch/record/2204926.

[228] CMS Collaboration, "Measurements of properties of the Higgs boson decaying into the four-lepton final state in pp collisions at $\sqrt{s} = 13\,\text{TeV}$," 2017, accepted by *JHEP*. arXiv: 1706.09936 [hep-ex].

[229] R. Gavin, Y. Li, F. Petriello, and S. Quackenbush, "FEWZ 2.0: a code for hadronic Z production at next-to-next-to-leading order," *Comput. Phys. Commun.*, vol. 182, p. 2388, 2011. DOI: 10.1016/j.cpc.2011.06.008. arXiv: 1011.3540 [hep-ph].

[230] ATLAS Collaboration, "ZZ $\to \ell^+\ell^-\ell'^+\ell'^-$ cross-section measurements and aTGC search in 13 TeV pp collisions with the ATLAS detector," 2017. http://cds.cern.ch/record/2263045.

[231] K. Arnold *et al.*, "VBFNLO: a parton level Monte Carlo for processes with electroweak bosons," *Comput. Phys. Commun.*, vol. 180, p. 1661, 2009. DOI: 10.1016/j.cpc.2009.03.006. arXiv: 0811.4559 [hep-ph].